

Versuchsanstalt für Wasserbau  
Hydrologie und Glaziologie  
der Eidgenössischen  
Technischen Hochschule Zürich

---

**Mitteilungen**

**216**

**Variations of the surface ice motion of Gorner-  
gletscher during drainages of the ice-dammed  
lake Gornersee**

Patrick Riesen

Zürich, 2011

Herausgeber: Prof. Dr. Robert Boes

*Zitiervorschlag für VAW-Mitteilungen:*

Riesen, P. (2011).

Variations of the surface ice motion of Gornergletscher during drainages of the ice-dammed lake Gornersee.

*Mitteilungen* 216, Versuchsanstalt für Wasserbau, Hydrologie und Glaziologie (VAW), R. Boes, Hrsg., ETH Zürich.

Im Eigenverlag der  
Versuchsanstalt für Wasserbau,  
Hydrologie und Glaziologie  
ETH Zürich  
CH-8092 Zürich

Tel.: +41 - 44 - 632 4091  
Fax: +41 - 44 - 632 1192  
e-mail: [info@vaw.baug.ethz.ch](mailto:info@vaw.baug.ethz.ch)

Zürich, 2011

ISSN 0374-0056

## Preface

The drainage of glacier-dammed lakes poses one of the greatest and far reaching glacier-related hazards. Glacier-dammed lakes have the tendency to drain rapidly once an initial drainage path is established. A typical example of such a lake is Gornersee, located at the confluence between Gorner- and Grenz-gletscher, above Zermatt, Valais. During the outburst of a glacier-dammed lake, an enormous amount of lake water drains into the glacier bed within a short time period. According to the diurnal flow variations and motion events observed on Alpine glaciers so far, a sudden water input into the bed increases the sub-glacial water pressure and enhances the basal ice motion through sliding. The ice-flow speed significantly increases as the basal water pressure approaches the ice overburden pressure and the glacier sole decouples from the bed. The sub-glacial water input due to the lake drainage is generally much larger than the input due to melt water. Therefore, ice-flow changes may be caused that are not observable under the usual hydrological conditions. Furthermore, the ice dynamics near a glacier-dammed lake are important because the motion of the ice dam may control the water discharge from the lake and may play a role in the triggering of the lake outburst. Therefore, knowledge of ice-flow dynamics in the vicinity of a glacier-dammed lake contributes to understanding the triggering mechanisms of an outburst.

To study the impact of the drainage of Gornersee on the dynamics of Gornergletscher, high-frequency surface ice-flow measurements were carried out simultaneously with hydrological measurements. The surface ice motion of Gornergletscher was traditionally measured at stakes with geodetic survey techniques. For the first time these measurements were complemented with high-resolution ice displacement measurements using a ground-based portable real aperture radar interferometer. During the lake drainage, surface ice motion changes were recorded on 20 min time intervals downstream a glacier section covering 2 km distance from Gornersee. The agreement of this method with results from in-situ marker measurements was satisfactory, indicating that this technique has application potential for future glaciological research. During the drainage the water level measured in boreholes was consistently high near flotation level, suggesting that the elevated sub-glacial water pressure enhanced basal ice motion and sub-glacial cavity formation. An intriguing observation was a reversing ice motion recorded at one of the surveyed stakes. The cause to the reversal of the ice-flow direction was difficult to explain. This unexpected observed ice-flow characteristics were the main motivation of this doctoral thesis.

An important contribution of the author is the formulation of a higher-order viscoelastic flow law for polycrystalline ice allowing stress dependence on strain, strain rate and strain acceleration. With this constitutive law, creep deformation of ice including the initial elastic, delayed elastic (primary creep) and stationary (secondary creep) creep regimes can be described. The viscoelastic material description was considered to describe recoverable transient ice deformation responses on short time scale events as the lake drainages. With a numerical modeling study the author investigated which load and unload sequences (mimicking lake level variations) were required to generate the observed reversal of surface ice motion using the viscoelastic constitutive law. The conclusion was that the observed magnitude of the reversing displacement could only be reproduced by much larger loads than what could be inferred from the observed lake level changes. The main conclusion of the author is that the non-steady creep response of the ice has a marginal effect on the observed reversal of the ice displacement. Instead, it is proposed that this abrupt ice-flow direction change might be due to an uplift and lowering of the ice dam due to blocked sub-glacial water drainage.



# Contents

Preface . . . . .	i
Abstract . . . . .	ix
Zusammenfassung . . . . .	xi
Notation . . . . .	xiii
<b>1 Introduction</b>	<b>1</b>
1.1 Outbursts of Gornersee: A bulk categorization . . . . .	2
1.2 Objectives . . . . .	3
1.3 Organization . . . . .	3
<b>I Investigation of ice flow observations on Gornergletscher</b>	<b>5</b>
<b>2 Local to regional impact of Gornersee on Gornergletscher</b>	<b>7</b>
2.1 Data acquisition and processing . . . . .	7
2.1.1 Position estimates via automated tachymeter . . . . .	8
2.1.2 Position estimates via differential GPS . . . . .	8
2.1.3 Accuracy of the position measurements . . . . .	9
2.2 Consistent displacements and velocities using Kalman filtering . . . . .	9
2.3 Observed key ice motion events at selected locations . . . . .	12
2.3.1 Spatial variability of vertical ice motion . . . . .	18
2.4 Surface ice flow velocities and strain-rates . . . . .	21
2.4.1 Horizontal strain-rates along flow lines and transects . . . . .	23
2.4.2 Estimated vertical strain-rates compared to observed vertical motion . . . . .	26
2.5 Discussion . . . . .	28
<b>3 Ice flow changes during the drainage of Gornersee</b>	<b>29</b>
3.1 Introduction . . . . .	29
3.2 Field methods . . . . .	30
3.3 Numerical model . . . . .	31
3.4 Results (I): Observations . . . . .	33
3.5 Results (II): Modeling . . . . .	35
3.5.1 Modeling of the ice flow changes . . . . .	36
3.6 Discussion . . . . .	39
3.7 Conclusion . . . . .	41

<b>4</b>	<b>Surface ice motion measured with an interferometric radar</b>	<b>43</b>
4.1	Introduction . . . . .	43
4.2	Field Methods . . . . .	44
4.2.1	Surface ice motion measurements . . . . .	45
4.3	Results . . . . .	46
4.3.1	Drainage of Gornerssee . . . . .	46
4.3.2	Surface ice displacements . . . . .	47
4.4	Discussion . . . . .	51
4.4.1	Influence of Gornerssee drainage on the surface ice motion . . . . .	53
4.5	Conclusions . . . . .	54
<b>II</b>	<b>Constitutive modelling of transient viscoelastic creep of ice</b>	<b>55</b>
<b>5</b>	<b>Theory of a thermo-viscoelastic constitutive model for ice</b>	<b>57</b>
5.1	Introduction . . . . .	57
5.2	Theoretical Background . . . . .	58
5.2.1	Basis of Formulation and Prerequisites . . . . .	58
5.2.2	Form of Constitutive Relation for Isotropic Materials . . . . .	61
5.2.3	Glen's flow law for ice . . . . .	66
5.3	Ice as thermoelastic modified second order isotropic material . . . . .	66
5.3.1	The Modified Second Order Fluid . . . . .	66
5.3.2	The Thermoelastic Modified Second Order Isotropic Material . . . . .	67
5.3.3	Thermodynamic Restrictions . . . . .	67
5.3.4	Constitutive Function for the Thermo-Viscoelastic Modified Second Order Isotropic Material (TMSOIM) . . . . .	74
5.4	Summary . . . . .	76
<b>6</b>	<b>Viscoelastic creep responses in uni-directional shearing</b>	<b>79</b>
6.1	Introduction . . . . .	79
6.2	Constitutive relations . . . . .	80
6.2.1	Glen's flow law . . . . .	81
6.2.2	The modified second order fluid model . . . . .	81
6.3	The elastic modified second order isotropic material . . . . .	82
6.4	Unidirectional flow of the EMSOIM . . . . .	84
6.4.1	Numerical implementation . . . . .	86
6.5	Results . . . . .	87
6.5.1	Creep under step function load . . . . .	87
6.5.2	Fading elasticity . . . . .	89
6.6	Discussion . . . . .	91
6.6.1	Viable ranges of $\mathbb{H}$ and $\mathbb{K}$ . . . . .	91
6.6.2	Relevance of acceleration effects ( $\mathbb{H} > 0$ ) . . . . .	91
6.7	Final remarks . . . . .	92

6.8	Addendum: Fit to experimental creep data . . . . .	93
<b>7</b>	<b>Simulating reversing ice motion as recoverable creep</b>	<b>97</b>
7.1	Observed ice motions with reversing displacement component . . . . .	97
7.2	Modelled reversing deformation in uni-directional shearing . . . . .	99
7.3	Discussion . . . . .	101
<b>8</b>	<b>Conclusions</b>	<b>105</b>
	References . . . . .	107
	Acknowledgements . . . . .	113
	Curriculum Vitae . . . . .	115

# List of Figures

1.1	Overview map of Gornergletscher and Gornerseel. . . . .	2
1.2	Idealized lake water level decreases and schematic classification of drainages . . . . .	3
2.1	Jump correction of a marker displacement time series . . . . .	10
2.2	Kalman filter example on synthetic data. . . . .	12
2.3	Summerly surface flow velocities on Gornergletscher . . . . .	13
2.4	Locations L1-L4 for discussion of ice displacement trajectories in Figures 2.5-2.8. . . . .	13
2.5	Ice displacement and velocity of a L1-marker during drainages O1-O3 . . . . .	15
2.6	Ice displacement and velocity of a L2-marker (drainages O1-O3) . . . . .	16
2.7	Ice displacement and velocity of a L3-marker (drainages O1-O3) . . . . .	17
2.8	Ice displacement and velocity of a L4-marker (drainages O1-O3) . . . . .	18
2.9	Local calculation of daily vertical uplift magnitude . . . . .	19
2.10	Spatial variation of daily vertical surface uplift during days -1 to 4 of drainages O1 and O3 . . . . .	20
2.11	Contour maps of normalized horizontal surface flow speed . . . . .	22
2.12	Map locations of streamlines, transects and intersection points used for strain-rates analysis . . . . .	23
2.13	Horizontal strain-rate $\dot{\epsilon}_h$ along three streamlines and three transects (drainage O1) . . . . .	24
2.14	Horizontal strain-rate $\dot{\epsilon}_h$ along three streamlines and three transects (drainage O3) . . . . .	25
2.15	Measured vertical velocity compared to vertical velocity expected due to ice deformation. . . . .	27
3.1	Map of Gornerseel and Gornergletscher with inset map of ice dam area . . . . .	30
3.2	Lake water level and horizontal flow velocities during Gornerseel drainage 2006 . . . . .	33
3.3	Lake water level and horizontal flow velocities during Gornerseel drainage in 2004 . . . . .	35
3.4	Initial flow field computation and comparison to measurements . . . . .	37
3.5	Modelled flow velocities and <i>C</i> -configuration in scenarios 1 and 2 (2006) . . . . .	38
3.6	Modelled flow velocities and <i>C</i> -configuration in scenarios 1 and 2, (2004) . . . . .	39
3.7	Modelled flow velocities and <i>C</i> -configuration including lake water pressure and basal motion (combined scenario 2006) . . . . .	41
4.1	Map of Gornergletscher showing field settings and scan sector of interferometer . . . . .	44
4.2	Lake water level and borehole water levels during Gornerseel drainage 2008 . . . . .	47
4.3	Displacement maps from six 5 h-interferograms taken during drainage 2008 . . . . .	48
4.4	Errors between displacements measured at in-situ markers and the interferometer . . . . .	49
4.5	Cumulative displacements (interferometer vs. in-situ markers) at reference markers . . . . .	51
4.6	Cumulative displacements (interferometer vs. in-situ markers) at transect 813-816 . . . . .	52

4.7	Displacements of in-situ markers at transect 813-816 . . . . .	53
6.1	Problem geometry of one-directional shearing flow down an inclined plate . . . . .	84
6.2	Non-dimensional velocity and displacement at slab surface for either $\mathbb{H}$ or $\mathbb{K} = 0$ . . . . .	88
6.3	Non-dimensional velocity and displacement at slab surface for $\mathbb{H}$ and $\mathbb{K}$ non-zero . . . . .	89
6.4	Non-dimensional velocity and displacement at slab surface for $\mathbb{H}$ , $\mathbb{K}$ and $c$ non-zero . . . . .	90
6.5	Change of the dimensionless numbers $\mathbb{H}$ and $\mathbb{K}$ as functions of the time scale . . . . .	92
6.6	Experimental creep curves from constant load experiments from the literature . . . . .	94
6.7	Primary and secondary uni-axial creep modelled using the EMSOIM . . . . .	95
7.1	Ice motion trajectories R1 and R2 with reversing motion components . . . . .	98
7.2	Use of uni-directional shearing model for creep recovery simulation. . . . .	99
7.3	Loading functions and resulting deformation as functions of time with $\mathbb{H}$ , $\mathbb{K}$ , and $c$ estimated in Sect. 6.8 . . . . .	101
7.4	Reversing ice motions R1 and R2 reproduced using the uni-directional shearing model . . . . .	102

# List of Tables

2.1	Records of ice displacement measurements on Gornergletscher . . . . .	7
2.2	Parameters for kinematic processing of GPS data with “Track”. . . . .	8
3.1	Direction-dependent position errors of flow measurements via tachymeter . . . . .	31
4.1	Key characteristics of the Gamma Portable Radar Interferometer (GPRI) . . . . .	45
4.2	Start and end times of six 5 h-interferograms . . . . .	47
4.3	Error norms of displacement differences (interferometer vs. in-situ markers) for different processings . . . . .	50
4.4	Detailed errors of displacement differences at reference markers . . . . .	50
5.1	Mean least-square estimates on the parameters $\mu$ and $\alpha_1$ for the MSOFM . . . . .	76
6.1	Definitions of kinematic tensor quantities in Eulerian notation . . . . .	81
6.2	Values for parameters of different constitutive equations from literature . . . . .	83

## Abstract

Gornergletscher is a large valley glacier formed by the confluence of two flow tributaries descending from the heights of the Monte-Rosa massif located in southern Switzerland. Gornergletscher is about 5 km long and up to 400 m thick at the center of flow convergence. Upstream of the confluence, where the two tributaries actually meet, the ice-marginal lake Gornersee exists. In most cases, Gornersee starts to fill by melt water retention in spring. Meanwhile, below the adjacent Gornergletscher, an extensive system of subglacial conduits and channels starts to form and transport melt water as well. A connection of the lake water with the basal discharge system eventually allows Gornersee to drain subglacially. This phenomenon is known to occur at other glaciers as well, but Gornersee provides an ideal study case due to the recurrence of the drainage every early summer. The filling and drainage of such an ice-dammed lake does not leave the adjacent glacier unaffected. Due to the drastic amounts of lake water passing through the subglacial hydrological system in short time, the basal conditions and intermittent water storage are strongly affected. The basal motion of the ice is very sensitive to such changes in the subglacial properties, and development of temporal and spatial variations of the ice motions, directly observable at the ice surface, are the immediate consequences. Vice versa, details on the lake drainage process can be inferred from the changes of the surface ice flow. In this thesis, temporal and spatial variations of the surface ice flow of Gornergletscher during several drainages of Gornersee are reported and analyzed. The ice flow changes are compared for different lake drainage events, as the diverse character of the drainages of Gornersee lead to variable impacts on the surface ice displacements and flow velocities of Gornergletscher. In one drainage event, a pronounced impact on the flow of Gornergletscher was apparently absent. Then, the discharge of lake water from Gornersee to the base of Gornergletscher was essentially limited by superficial outflow. Nevertheless, changes of the direction of ice movement and flow velocities solely caused by the pressure imposed on the ice due to the presence of the lake are identified in the course of this work. The application and release of such forces are then conjectured to be responsible for intriguing retrograde ice displacements observed in the vicinity of Gornersee. However, the glacier ice is commonly considered a purely viscous material, under which circumstances a reversal of the flow motion can not occur. A viscoelastic constitutive model of the ice rheology is thus developed. A constitutive equation for the ice in the form of a higher-order Rivlin-Ericksen material is proposed and tested. Finally, the possibility of recoverable displacements being solely caused by relaxation of the ice deformation is examined in the response of shearing flow subject to time-dependent loading/unloading. The model can not support the presumptions on the reversing displacements under expected stress conditions and for reasonable parameters of the viscoelastic ice rheology.



## Zusammenfassung

Gornergletscher ist ein grosser Talgletscher, geformt vom Zusammenfluss zweier Gletscher am Fusse des Monta-Rosa Massivs in der südlichen Schweiz. Gornergletscher hat eine Länge von knapp 5 km und ist bis zu 400 m dick im Zentrum der Konfluenz der Eisflüsse. Oberhalb der Konfluenz, wo die beiden Gletscher zusammentreffen, existiert der eis-gestaute Gornersee. Üblicherweise füllt sich der Gornersee im Frühling durch Schmelzwasser. Zeitgleich dazu entwickelt der Gornergletscher ein subglaziales System aus Abflusskanälen welches auch Schmelzwasser transportiert. Eine Verbindung des Wassers vom Gornersee zu diesem subglazialen Abflusssystem ermöglicht dessen Entleerung. Dieses Phänomen beobachtet man auch an anderen Gletschern, jedoch zeichnet sich Gornersee speziell zur Untersuchung dieses Vorgangs aus, da die See-Entleerung sich jährlich wiederholt. Die Entstehung und Entleerung des eis-gestauten Sees hat einen spürbaren Einfluss auf den benachbarten Gletscher. Der Transport von grossen Mengen des Wasser aus dem See durch das subglaziale Kanalsystem in kurzer Zeit beeinflusst die Bedingungen und Zwischenspeicherung von Wasser am Gletscherbett beträchtlich. Die Bewegung des Gletschereises am Bett reagiert direkt auf die Veränderungen der subglazialen Eigenschaften und die Entstehung von zeitlichen und räumlichen Schwankungen der Eisbewegung, erkennbar an der Gletscheroberfläche, ist die Folge. Andererseits, von den Veränderungen der Eisbewegung kann auch auf den Entleerungsprozess des Gletschersees rückgeschlossen werden. In dieser Abhandlung werden die räumlichen und zeitlichen Veränderungen der Fliessbewegung vom Gornergletscher während wiederholter Entleerungen des Gornersees erfasst und untersucht. Die Änderungen der Fliessbewegungen während verschiedener Seeausbrüche werden verglichen, da der Einfluss des Seeausbruchs auf die Bewegung des Gornergletschers sehr differenziert ausgefallen ist. Während einer besonderen Entleerung des Gornersees schien es, dass der Ausbruch des Sees keinen Einfluss auf die Eisbewegungen hatte. Dies war der Fall, als der Abfluss des Wassers in den Untergrund des Gletschers durch ein oberflächliches Abfliessen kontrolliert wurde. Trotzdem konnten Veränderungen in der Bewegung und Geschwindigkeit des Eisfliessens in dieser Arbeit erkannt werden. Es wird festgestellt dass diese Bewegungsänderungen durch den Druck, der vom gestauten Seewasser auf das umliegende Eis ausgeübt wird, verursacht wird. Diese Druckspannungen werden als Ursache von speziellen Fliessbewegungen nahe des Gornersees, welche sich durch eine ausgeprägte Wende der Fliessrichtung auszeichnen, angesehen. Jedoch wird Gletschereis im üblichen Sinne als viskoses Material behandelt. Unter solchem Materialverhalten kann keine umkehrbare Bewegung erzeugt werden. Deshalb wird ein viskoelastisches Materialgesetz für Gletschereis entwickelt. Das Gesetz wird formuliert als ein sogenanntes Rivlin-Ericksen Material höherer Ordnung. Letztlich wird die Möglichkeit, dass diese speziellen Fliessbewegungen aus der Erholung der Deformation des Eises nach einer aufgebrauchten Spannung entstehen, behandelt. Das Modell kann diese Annahme, unter Voraussetzung erwarteter Spannungsbedingungen und Werte der Parameter der viskoelastischen Rheologie des Eises nicht bekräftigen.



# Notation

Calculus	Description	
$a, \alpha, A, a, \mathbf{A}, \dots$	Indices, scalars, constants	
$\mathbf{a}, a_i$	Tensors of 1st rank (Vectors)	
$\mathbf{A}, A_{ij}$	Tensors of 2nd rank (Matrices)	
$\mathbf{B}, B_{ijk\dots}$	Tensors of third rank or higher	
$\mathbf{I} = \delta_{ij}$	Identity tensor / Kronecker symbol	
$\varepsilon_{ijk}$	Levi-Civita tensor	
$\text{tr}(\mathbf{A}), A_{ii}$	Trace of $\mathbf{A}$	
$\det(\mathbf{A})$	Determinant of $\mathbf{A}$	
$\mathbf{A}'$	Deviatoric part of $\mathbf{A}$ , as $\mathbf{A}' = \mathbf{A} - \frac{1}{3} \text{tr}(\mathbf{A})$	

Symbol	Description	Units
$\mathbf{X} = (X, Y, Z)$	Particle coordinates in the reference configuration	m
$\mathbf{x} = (x, y, z)$	Position coordinates in the present configuration	m
$\text{Grad}(\mathbf{A}), \partial\mathbf{A}/\partial\mathbf{X}$	Gradient of $\mathbf{A}$ with respect to the reference configuration	
$\text{grad}(\mathbf{A}), \partial\mathbf{A}/\partial\mathbf{x}$	Gradient of $\mathbf{A}$ with respect to the present configuration	
$\mathbf{t}$	Cauchy stress tensor	Pa
$\eta$	Entropy	$\text{Pa m}^3 \text{K}^{-1}$
$\varepsilon$	Internal energy	$\text{Pa m}^3 (\hat{=} \text{J})$
$\mathbf{F}, \partial\mathbf{x}/\partial\mathbf{X}$	Deformation gradient	
$\mathbf{L} = \text{grad}(\mathbf{v})$	Spatial velocity gradient	$\text{m d}^{-1}$
$\mathbf{D} = \frac{1}{2}(\mathbf{L} + \mathbf{L}^T)$	Symmetric component of $\mathbf{L}$	$\text{m d}^{-1}$
$\mathbf{W} = \frac{1}{2}(\mathbf{L} - \mathbf{L}^T)$	Skew-symmetric component of $\mathbf{L}$	$\text{m d}^{-1}$
$\mathbf{O}$	Orthogonal rotation matrix	
$\mathbf{A}_{(n)}$	Nth Rivlin-Ericksen tensor	
$\mathbf{C}$	Right Cauchy-Green deformation tensor	
$\mathbf{B}$	Left Cauchy-Green deformation tensor	
$\mathbf{E}$	Finger strain tensor	

In the following we define some operator symbols which will be used frequently in the text. For clear presentation we also denote the equivalent operations in index notation.

The scalar (dot) product of two vectors is

$$\mathbf{a} \cdot \mathbf{b} = a_i b_j \delta_{ij} = a_i b_i.$$

The vector (cross) product of two vectors is

$$\mathbf{a} \times \mathbf{b} = a_i b_j \varepsilon_{ijk},$$

with the Levi-Civita tensor (e.g. Hutter and Jöhnk, 2004)

$$\varepsilon_{ijk} := \begin{cases} 1 & \text{if } (ijk) \text{ is a cyclic permutation of } (123) \\ -1 & \text{if } (ijk) \text{ is an anti-cyclic perm. of } (123) \\ 0 & \text{otherwise.} \end{cases}$$

The tensor product of two  $N$ -dimensional vectors is

$$\mathbf{a} \otimes \mathbf{b} = \begin{pmatrix} a_1 b_1 & a_1 b_2 & a_1 b_3 & \dots \\ a_2 b_1 & a_2 b_2 & \dots & \dots \\ \vdots & \vdots & \ddots & \vdots \\ \dots & \dots & \dots & a_N b_N \end{pmatrix},$$

for  $i, j \in \{1 \dots N\}$ .

Multiplication (composition) of two square tensors is

$$\mathbf{A}\mathbf{B} = A_{ik} B_{kl}$$

The scalar product of two tensors (tensor contraction) is

$$\mathbf{A} * \mathbf{B} = A_{ij} B_{kl} \delta_{jl} \delta_{ik} = A_{ij} B_{ij} := \text{tr}(\mathbf{A}\mathbf{B}^T).$$

# Chapter 1

## Introduction

Recent observations of significant retreat and melt of glaciers, degradation of permafrost and accelerated erosion processes indicate a highly sensitive environment in polar, alpine and sub-alpine areas. The observed changes are commonly linked to global warming trends, and further drastic changes in glacial and periglacial environments can be expected. As such, the likeliness of increased melt water production and increased variability of melt water supply are of due importance (e.g. Schoof, 2010). In glaciated environments, melt water can be naturally dammed by topographic obstacles or glacier ice, leading to the formation of lakes. Evidently, changes of thaw conditions, melt water production and surface topography may evoke increased formation and appearance of such ice/debris-dammed lakes. A flood wave produced by an outburst of retained lake water has the ability to cause damage on nearby human activity and civilization. Thus, potentially dangerous lakes need to be assessed. The evaluation and risk assessment requires understanding of formation, triggering and flooding processes. In most cases of such a glacier lake outburst flood (GLOF), interaction between the dammed lake water and the blocking glacier is of major concern, since, ultimately, the outburst is triggered by the time the lake water can pass the barrier, i.e., the glacier. The passage may happen superficially, as the lake water over-spoils ice and debris; or else, a subglacial pathway is established. Certainly, combination of superficial and subglacial water evacuation is possible. An alpine, temperate glacier has its own distinct subglacial melt water drainage system, which evolves with seasonal (melt-)water input variation. The system is pronounced and most efficient during melt season. However, large additional amounts of water routed into the drainage system in a short time due to a subglacial lake outburst may overcharge the drainage system. Increase of basal water pressure, dispersion, and storage of water at the glacier bed are expected. These processes modulate the basal motion of the ice which, in turn enhances surface ice motion (e.g. Iken and Bindschadler, 1986; Iken et al., 1983; Iken and Truffer, 1997). Hence, measurements and analysis of glacier surface uplift and variation of surface ice motion during GLOFs indirectly ascertain information on the associated dynamics and contribute significantly to the understanding of subglacial processes and GLOFs.

The ice-dammed marginal lake, Gornersee, located in the southern Swiss Alps (Fig. 1.1), provided an excellent opportunity to study the drainage phenomenon (which is also termed jökulhlaup, stemming from Icelandic). Repeated surveys of the Gornersee jökulhlaup were conducted in 2004-2008, and targeted to establish knowledge of important aspects of the drainage phenomena. The research project in this thesis is a complement of three main targets: (i) study of the glacier drainage system and hydraulic properties, accomplished in the thesis and work of Werder (2009), (ii) investigation of seismic activity within the ice and association with the subglacial drainage, described in the thesis of Walter (2009), and (iii) measurements and analysis of disturbances of the surface ice motion of Gornergletscher during the Gornersee drainage. This thesis deals with the latter target and completes the intensive studies on Gornergletscher.

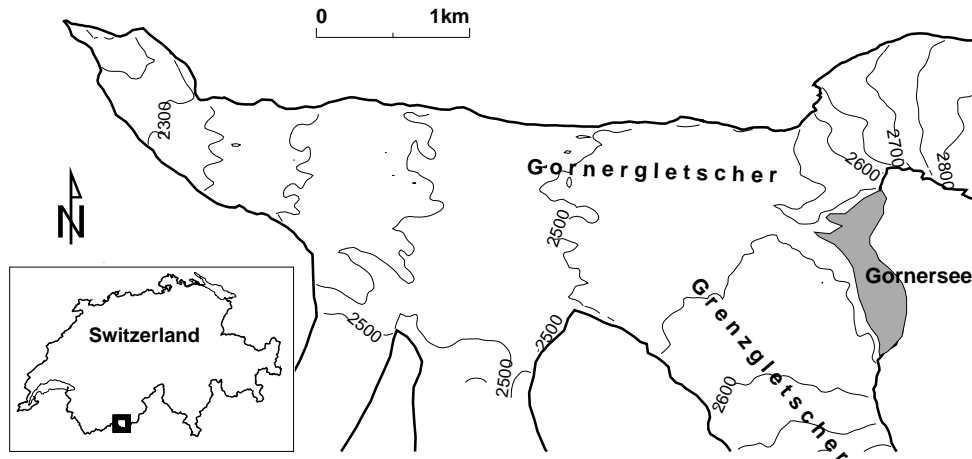


Figure 1.1: Overview map of Gornergletscher and Gonersee.

## 1.1 Outbursts of Gonersee: A bulk categorization

The repeated outbursts of Gonersee observed at Gornergletscher differed substantially from each other. Accordingly, their impact on the surface ice flow of Gornergletscher varied and numerous features were observed. Also, similarities between different impacts were detected and attempts undertaken to expose interrelations. At this point, the five glacial lake outburst events are categorized into three general types of drainages. This categorization is optional and not a standard convention, therefore it may not apply directly to other glacial lake outbursts. The highly variable nature of the lake outburst itself and the almost certain topographic differences of Gonersee to other glacial lakes, prevent such a generalization. This categorization is used to facilitate reference to key observations in the context of a specific outburst (type). In Figure 1.2, different lake water level curves as functions of time are drawn schematically. The glacial lake outbursts on Gonersee are categorized according to the decrease and curvature of such measured lake water levels following the initial increase (filling).

**Type O1** Initially, the lake water level decreases very rapidly. The subsequent evolution is followed by phases with irregular intensity of lake level decrease. The outburst is likely initiated by the ice dam surrounding the lake going partially or completely afloat. This provides an escape to discharge large amounts of water within a short time. The glacial lake outbursts of 2004 and 2007 belong to this category.

**Type O2** The O2 drainage is characterized by superficial overflow of the lake water. The lake water level exceeds the elevation of the ice dam locally, without occurrence of flotation. The spilled lake water overflows the ice surface. In the case of Gornergletscher, the draining water was conducted into a nearby moulin, and subsequently evacuated subglacially. If the lake drains by superficial overflow, the decrease of lake water level is slow and the rate of decrease approximately constant. A complete drainage by overflow occurred in 2006.

**Type O3** For this category, the lake water level decreases progressively, and the rate of decrease is largest towards the end of the drainage. The leakage of lake water enlarging a major drainage channel into the ice, due to energy dissipation causing melt of the ice, is suspected to be responsible for progressively increasing outflow. The drainage events of 2005 and 2008 belong to this type.

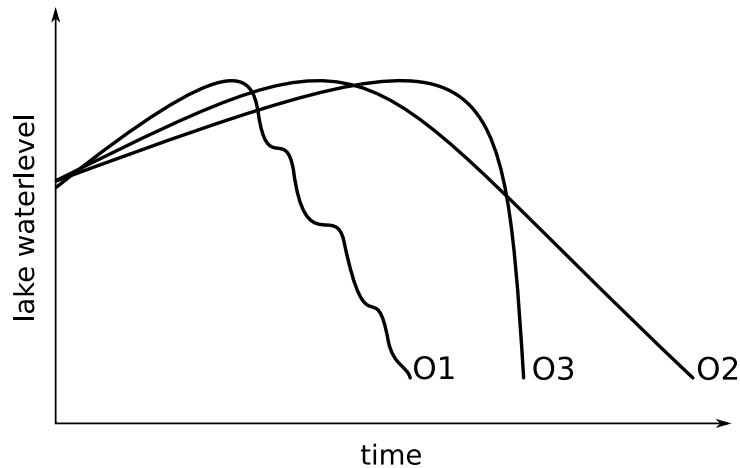


Figure 1.2: Glacial lake outbursts are schematically classified with regard to the curvature of lake water level decrease (O1-O3).

## 1.2 Objectives

This thesis aims to accomplish the following objectives:

From the repeated field surveys and measurements on Gornergletscher, a sound catalogue of ice displacements and flow velocities is acquired. From the catalogue, key ice flow perturbations and distinct patterns are identified and interpreted in relation to the drainage phenomenon. Also, the variation of ice flow disturbances caused by the impact of the subglacially draining lake water is analyzed.

In recent work related to Gornergletscher and the drainage of Gornersee (Sugiyama et al., 2007a), exceptional ice displacement with a reversing motion component was identified and analyzed. The interpretation of the reversing motion originating from basal processes due to the lake drainage was not sufficiently conclusive, neither was the explanation of the motion in terms of purely elastic recovery of the displacement. Sugiyama et al. (2007a) then hypothesized considering the ice as a viscoelastic material and analyzing the capability of viscoelastic recovery of the displacement.

Motivated by this hypothesis, a viscoelastic material model applicable to ice is constructed in an attempt to address the question, whether, or to what extent, ice rheological properties beyond viscous deformation need to be considered when drastic ice flow variations occur in a short time. However, the model is not specifically designed for the particular application to Gornergletscher, rather the constitutive model is a formulation of a very general viscoelastic relation. Therefore, an additional motivation and objective is that the model may be applicable to other situations.

## 1.3 Organization

According to the objectives, the thesis is organized in two parts:

**Part I:** The first part of this thesis compiles the field methods and measurements of the ice motion of Gornergletscher. A result of this work was the publication of two manuscripts in peer-reviewed journals. These are embedded as chapters (Chapters 3 and 4).

Chapter 2 deals with surface ice motion measurements and summarizes results in relation to drainage characteristics and to local versus regional variations of the impacts on the ice flow.

In chapter 3, the observations of changes of ice flow velocities in the periphery of Gornersee are described, and the influence of the lake water pressure boundary condition is identified. The observed flow changes are interpreted with the help of a three-dimensional ice-flow model.

Chapter 4 presents and discusses large-scale measurements of ice displacements at Gornergletscher conducted with a novel interferometric radar device. The manuscript highlights these results and examines the 2008 outburst of Gornersesee.

**Part II:** In this part, the constitutive theory of the viscoelastic model is elucidated (Chapter 5). This theoretical chapter is primarily formed from a lecture given by K. Hutter specially tailored to continuum formulations of a viscoelastic ice rheology.

In Chapter 6, the viscoelastic constitutive equation is numerically implemented and solved for uni-directional, transient flow. Creep and recovery responses generated by the proposed viscoelastic constitutive equation are numerically investigated. This chapter also forms a manuscript published in a peer-reviewed journal.

Chapter 7 uses again the viscoelastic model to test for viscoelastic creep and possible recovery of elapsed displacement in the situation of Gornergletscher.

A conclusion on the studies and results is presented in chapter 8.

## **Part I**

# **Investigation of ice flow observations on Gornergletscher**



## Chapter 2

# Local to regional impact of Gornersee on the surface ice motion of Gornergletscher

Between 2004-08 an area of about 3 km<sup>2</sup> of the ice surface of Gornergletscher, covering the part of Gornergletscher from the immediate lake shore of Gornersee down to the confluence of Gornergletscher with additional southern tributaries (Fig. 1.1) was intensely and repeatedly surveyed. The movement of the surface ice, and the spatial variability of its displacement was tracked with the help of a dense network of markers. The markers, aluminum stakes drilled into the ice, were equipped with either optical (Laser) or autonomous (GPS) sensors, and marker positions were recorded at sampling intervals in the range of 30 s to 1 h. The marker positions were processed to derive consistent ice displacement trajectories and flow velocity estimates. This chapter briefly explains the processing strategies common to all measurements. Thereafter, a comparative summary is given on the typical flow observations characterizing the drainage classes established in Section 1.1.

### 2.1 Data acquisition and processing

Thanks to the annual recurring of the Gornersee and the five-year project, it was possible to observe repeated glacial lake outbursts of Gornersee. Data sets of surface ice displacements at high temporal resolution were obtained for each observed Gornersee outburst event during these years. In Table 2.1, the corner dates of the intervals are indicated, in which ice displacement data is available of each survey year. The amounts of data acquired are substantial. However, the analysis and presentation of ice displacement measurements within this thesis is restricted to the existence periods of Gornersee, i.e., the time periods of the filling and drainage of Gornersee. These intervals constitute approximately a period of 14 to 30 days (mostly June/July) in each year. The setup of the survey, operation and stake marker locations varied slightly from year to year. For specific survey setups and further descriptions the reader can refer to the field methods sections 3.2 and 4.2 of the published manuscripts (Chapters 3 and 4). In the following, details on the acquisition and processing of the data not explicitly described in the published manuscripts (Chapts. 3 and 4) are documented.

Year	Record Begin	Record End
2004	10 June	11 July
2005	12 May	16 September
2006	26 April	12 August
2007	26 April	11 September
2008	24 April	26 June

Table 2.1: Begin and End dates of annual ice displacement measurement records on Gornergletscher.

“Track” Command	Value	Unit
MODE	short	
SITE_STATS ( $\sigma$ , noise)	(20, 0.01)	m
BACK_TYPE	smooth	
BF_SET	5 10	
OUT_SIG_LIMIT	0.03	m
INTERVAL	120	sec
CUT_OFF	10	deg

Table 2.2: Parameters for kinematic processing of GPS data with “Track”.

### 2.1.1 Position estimates via automated tachymeter

The majority of the in-situ markers was tracked by help of an automated tachymeter (Leica TCA 1800) situated on a rock-ledge north of the confluence area (see Fig. 3.1), overlooking Gornergletscher. At the beginning of the survey the tachymeter was calibrated to the plumb line direction and the markers were located manually with the tachymeter optics. The tachymeter then electronically determined horizontal and vertical azimuth, and detected the relative distance to the marker as the phase shift of an electromagnetic wave emitted and received, reflected in between at the marker’s prismatic reflector. Once the set of initial azimuth directions and distances to all markers was measured, the tachymeter operated autonomously and detected new azimuth and distance values of a marker by helical searching starting from the orientation of the tachymeter according to the marker’s previous measurement readings. The tachymeter was in this mode of operation during day and night and automatically sampled new readings for all markers at every hour. New readings could not be detected at every hour for each marker, as the measurement was strongly influenced by weather and visibility conditions. The tachymeter also measured a set of fixed markers (reference markers) at known azimuth and distances during each hourly measurement cycle. Correction values for horizontal/vertical azimuth and distance measurements for the markers located on the ice were determined from these referential readings in each measurement cycle. After the survey, the tachymeter readings were converted to Cartesian coordinates. The conversion requires knowledge of the exact position of the tachymeter, which was determined by GPS using the precise point positioning (PPP) online processing service provided by Natural Resources Canada (2008).

### 2.1.2 Position estimates via differential GPS

In each survey, five markers were equipped with GPS receivers instead of prism reflectors. We used the Leica GPS500 system and Leica 502 or 1200 antennas. A sixth receiver was located close to the tachymeter station and served as reference station for the relative positioning of the other sites located on the glacier (see Figures 3.1 and 4.1). The GPS500 system measures code, pseudo-range and phase signals. The positioning was done based on the L1/L2 carrier phase measurements and phase signals were processed using integer ambiguity fixing strategies (see e.g. Hofmann-Wellenhof et al., 2001), implemented in commercial and academic software. In 2004 and 2005, the data acquired with the Leica GPS500 systems was processed with the commercial Leica GeoOffice/SKI-Pro software. The processing strategy was a static mode, and single positions were estimated from 1 hour sessions every 3 hours. The sampling frequency in one session was 0.033 Hz. The processing of the data from these two years was carried out by S. Sugiyama and A. Bauder. In the years 2006 to 2008, the field setups of the GPS markers were upgraded with additional solar panel and battery capacity and the receivers were run in continuous mode at a sampling frequency of 0.033 Hz. Those data sets were processed in kinematic mode using the software “Track” from GAMIT/GLOBK (Chen, 1998; King, 2004). “Track” also estimates positions based on the L1/L2 phase signals and the fixing of the carrier phase wavelengths biases to integers, although it uses its own processing strategy and is adapted to determine a kinematic trajectory from the position estimates by a built-in Kalman filtering procedure. In Table 2.2, the parameters for the

processing are documented. Please refer to the “Track” documentation (see <http://geoweb.mit.edu/simon/gtgk/help/track.hlp.htm>) for the explanation of the parameters. Here it is merely mentioned that the estimation of the positions was constrained by the ‘a priori’ statistics (SITE\_STATS parameter). This parameter sets the internal noise level in “Track”, which allowed to constrain the position trajectories (King, 2004). The binary executable of “Track” was embedded in a custom script to automate the repeated processing of large data sets (30 to 120 d at chunks of 24 h length) as batch jobs. All the data was archived in standard RINEX format using the TEQC conversion tool (Estey and Meertens, 1999).

### 2.1.3 Accuracy of the position measurements

The position estimates obtained from the surveys via automated tachymeter or differential GPS have associated errors which are briefly discussed in this paragraph. The azimuth precision of the tachymeter (Leica TCA 1800) according to the manufacturer is  $3 \cdot 10^{-4}$  degrees, while the distance measurements are as accurate as  $1 \text{ mm} \pm 1 \text{ mm/km}$ . The automated tachymeter and the described measurement technique is based on previous studies on other glaciers. It was shown that the accuracy of the azimuth estimates is about ten times less the device precision. According to Bassi (1999) and Gudmundsson et al. (2000), the azimuth errors correspond to  $\pm 3 \text{ cm}$  in horizontal direction (transverse to the line of sight of the device), and  $\pm 5 \text{ cm}$  in the vertical. In Bucher (2007), the measurements and associated errors were re-analyzed in more detail and it was shown that the absolute errors are larger; up to  $\pm 40 \text{ cm}$  in the horizontal, and even larger in the vertical. However, the measurements were sampled at a repeat interval of one hour providing up to 24 measurements per day, which helps to reduce the errors (see also Sect. 3.2). This is sufficient to allow detection of displacement changes on a diurnal scale, possibly by a few hours at maximum.

Concerning the position estimates by GPS, the manufacturer indicates a precision of  $\pm 1 \text{ cm}$  in the horizontal (not direction-dependent), and about  $\pm 2 \text{ cm}$  in the vertical. For kinematic positioning, the error in the height estimate is slightly larger, about  $\pm 4 \text{ cm}$ . The positions were sampled at high-resolution, every 2 min (Tab. 2.2). The GPS measurements provide more accurate position estimates than by automated tachymeter and were also used to check the trajectories and displacements of ‘conventional’ markers located close to a marker equipped with a GPS-receiver. The filtering of (all) the displacement time series as described in the next section, further reduces the variance of the position estimates and adds to an increased reliability of the determined ice motion trajectories.

## 2.2 Consistent displacements and velocities using Kalman filtering

The raw position trajectories from the output of either data set (tachymeter or GPS) were further processed in a common strategy to obtain consistent displacement trajectories and accurate velocity estimates. First, jumps and dislocations in the trajectories were addressed. From time to time, the aluminum poles onto which the prisms/receivers were mounted had to be shortened, as the ice surface decreased due to melt and the poles thus increased in height above the ice surface. Occasionally, the marker had to be repositioned. Such interventions resulted in jumps occurring in the temporal evolution of the marker motion. The dislocations were removed in all three Cartesian components by placing the trajectory following a dislocation onto a continued direction estimated from a linear regression of the displacement preceding the dislocation, as shown in Figure 2.1. The data interval for the linear regression was chosen manually. Removal of dislocations and sometimes of outlier points was documented and archived for each marker.

The obtained displacement trajectories originate from two measurement and processing strategies, i.e. tachymeter or GPS, thus the data inherits different characteristics and measurement errors. To estimate optimal (smooth) displacement trajectories and associated flow velocities from the available data in an identical, consistent way, we employed a discrete Kalman filter (Kalman, 1960). The Kalman filter was

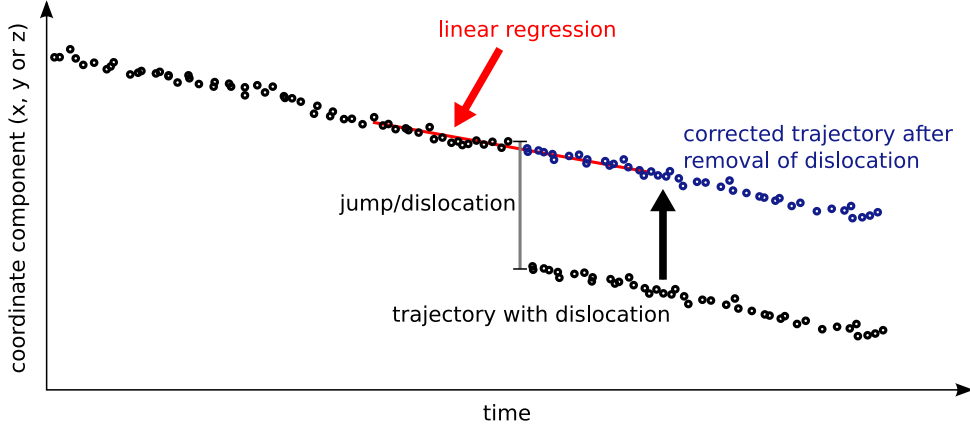


Figure 2.1: Correction of a jump of the marker trajectory in the Cartesian component/time-space.

constructed to simulate the acceleration of the marker motion as a random walk process. The filter predicts optimal, smooth displacement estimates with exact velocities. Before the actual filter model is described, the essentials of the Kalman filter based on the notes of Welch and Bishop (2006) are briefly recapitulated.

Consider a certain process which evolves over time and can be described at an actual time  $k$ , called the current state, by a set of  $n$  variables. The set of variables is the state vector  $\mathbf{x}_k$ . To describe the underlying process, the linear difference equation

$$\mathbf{x}_k = \mathbf{M}\mathbf{x}_{k-1} + \mathbf{w}_{k-1}, \quad (2.2.1)$$

is used, where the  $n \times n$  matrix  $\mathbf{M}$  is the evolution model, relating the state  $\mathbf{x}_{k-1}$  at the previous time  $k-1$  to the state at the current time step  $k$ . The vector  $\mathbf{w}_{k-1}$  represents the process noise. Say, we have measured different variables at stake  $k$ ; they are collected in the measurement vector  $\mathbf{z}_k$ . In general,  $\mathbf{z}_k$  has the length  $m \neq n$ , but is related to the current state as

$$\mathbf{z}_k = \mathbf{K}\mathbf{x}_k + \mathbf{v}_k, \quad (2.2.2)$$

with the  $m \times n$  matrix  $\mathbf{K}$ , termed forward model, and  $\mathbf{v}_k$  is the measurement noise. We now define an *a priori* state estimate  $\mathbf{x}_k^a$  based on information of the process prior to time step  $k$ , and an *a posteriori* state estimate  $\mathbf{x}_k^p$ , deduced from a measurement  $\mathbf{z}_k$ . These estimates are related via

$$\mathbf{x}_k^p = \mathbf{x}_k^a + \mathbf{G}(\mathbf{z}_k - \mathbf{K}\mathbf{x}_k^a), \quad (2.2.3)$$

with the  $m \times n$  matrix  $\mathbf{G}$ , known as the *Kalman gain* (Welch and Bishop, 2006). We further define the *a priori* and *a posteriori* error covariances,  $\mathbf{S}^a$  and  $\mathbf{S}^p$  as

$$\mathbf{S}^a = E \left[ (\mathbf{x}_k - \mathbf{x}_k^a)(\mathbf{x}_k - \mathbf{x}_k^a)^T \right], \quad \text{and} \quad \mathbf{S}^p = E \left[ (\mathbf{x}_k - \mathbf{x}_k^p)(\mathbf{x}_k - \mathbf{x}_k^p)^T \right]. \quad (2.2.4)$$

It is now possible to select  $\mathbf{G}$  in equation (2.2.3) in a form that an *a posteriori* estimate of the state  $\mathbf{x}^p$  and covariance  $\mathbf{S}^p$  can be obtained by the following equations:

$$\mathbf{G} = \mathbf{S}^a \mathbf{K}^T (\mathbf{K} \mathbf{S}^a \mathbf{K}^T + \mathbf{R})^{-1}, \quad (2.2.5)$$

$$\mathbf{x}_k^p = \mathbf{x}_k^a + \mathbf{G}(\mathbf{z}_k - \mathbf{K}\mathbf{x}_k^a), \quad (2.2.6)$$

$$\mathbf{S}^p = \mathbf{S}^a - \mathbf{G} \mathbf{K} \mathbf{S}^a, \quad (2.2.7)$$

where  $\mathbf{R}$  is a measurement error covariance matrix. Equations (2.2.5) to (2.2.7) are the *Discrete Kalman filter measurement update equations* (Welch and Bishop, 2006). From these *a posteriori* estimates, a new *a priori* state can be predicted using the *Discrete Kalman filter time update equations*,

$$\mathbf{x}_k^a = \mathbf{M}\mathbf{x}_{k-1}^p, \quad (2.2.8)$$

$$\mathbf{S}^a = \mathbf{M}\mathbf{S}_{k-1}^p \mathbf{M}^T + \mathbf{S}, \quad (2.2.9)$$

where  $\mathbf{S}$  describes the process noise covariance (i.e., the error of the state model). The discrete Kalman filter operator is complete with the above pair of equation sets, which forms a predictor-corrector scheme. A new state  $\mathbf{x}_k^a$  of the process considered is predicted for time step  $k$  with equations (2.2.8) and (2.2.9). This *a priori* prediction is then improved (corrected) by incorporating an actual measurement at time  $k$  via equations (2.2.5) to (2.2.7). From the corrected state estimate  $\mathbf{x}_k^p$  a new prediction for the next time step  $k + 1$  is obtained using again the time update equations (2.2.8) and (2.2.9). This recursive scheme indicates that the prediction of a new state can be given solely from the previous *a posteriori* estimate, and the dependence on former states is implicit, there is no explicit operation on all former states when predicting a new estimate. Due to the design of  $\mathbf{G}$  in (2.2.5), the Kalman filter operates in such way that it minimizes the *a posteriori* error covariance  $\mathbf{S}^p$ . The Kalman filter's predictor-corrector system can be started with initial *a posteriori* guesses, thus, initial values for  $\mathbf{x}_{k-1}^p$  and  $\mathbf{S}_{k-1}^p$  need to be prescribed.

For the intended Kalman filter, the process to be modeled is the position change of a marker as function of time. Let us denote by  $x(t)$  one of the Cartesian components of the actual marker position (The Kalman filter is applied to each component independently). The state vector  $\mathbf{x}$  has three components: position, velocity and acceleration as

$$\mathbf{x} = (x, v, a). \quad (2.2.10)$$

The random acceleration model gives the motion  $x$  and the velocity  $v$  as functions of the acceleration  $a$  and time  $t$  as

$$x(a) = \int_{t_1}^{t_2} \int_{t_1}^{t'} a dt' dt = \frac{1}{2} a \Delta t^2 \quad \text{and} \quad v(a) = \int a dt = a \Delta t, \quad (2.2.11)$$

where  $\Delta t = t_2 - t_1$  is the current time step. The evolution model  $\mathbf{M}$  is constructed from the linearization around the current state, i.e., the partial derivatives of the Jacobian matrix:

$$\mathbf{M}_k = \begin{bmatrix} \frac{\partial x_i}{\partial x_j} \end{bmatrix}_k = \begin{bmatrix} \frac{\partial x}{\partial x} & \frac{\partial x}{\partial v} & \frac{\partial x}{\partial a} \\ \frac{\partial v}{\partial x} & \frac{\partial v}{\partial v} & \frac{\partial v}{\partial a} \\ \frac{\partial a}{\partial x} & \frac{\partial a}{\partial v} & \frac{\partial a}{\partial a} \end{bmatrix}_k \quad (2.2.12)$$

Thus, if the time steps are equal, then  $\mathbf{M}_k = \text{const}$ , for all  $k$ . In the process model, only relations  $x = x(a)$ , and  $v = v(a)$  are defined, whereas the inverse relations  $a = \hat{x}(x)$  or  $a = \hat{v}(v)$  are undefined. Evaluating the Jacobian (2.2.12), we obtain the upper triangular matrix

$$\mathbf{M}_k = \begin{bmatrix} 1 & \Delta t_k & \frac{1}{2} \Delta t_k^2 \\ 0 & 1 & \Delta t_k \\ 0 & 0 & 1 \end{bmatrix}. \quad (2.2.13)$$

Since we only measured positions, the measurement vector  $\mathbf{z}$  is a scalar ( $m = 1$ ), hence the forward model  $\mathbf{K}$  is simply  $(1, 0, 0)$ . The state error  $\mathbf{S}$  has the form

$$\mathbf{S} = \begin{bmatrix} s_x & 0 & 0 \\ 0 & s_v & 0 \\ 0 & 0 & s_a \end{bmatrix}, \quad (2.2.14)$$

where  $s_x$ ,  $s_v$  and  $s_a$  represent errors in the state model when estimating the position, velocity and acceleration. To obtain exact estimates of positions and velocities, it is important to set  $s_x = s_v = 0$ . By this, the velocity estimate will correspond to the exact analytic derivative of the estimated position trajectory. The coefficient  $s_a$  is used as a tuning coefficient, and it constrains the random acceleration. In general, the measurement error covariance matrix  $\mathbf{R}$  is a  $m \times m$  matrix, however, in this case, since  $m = 1$ , it reduces to a scalar,  $R$ . After having defined  $\mathbf{M}$ ,  $\mathbf{K}$ ,  $\mathbf{S}$  and  $R$ , we can start the filter at  $k = 0$  with initial estimates for  $\mathbf{x}_{-1}^p$  and  $\mathbf{S}_{-1}^p$ . In  $\mathbf{x}_{-1}^p$ , initial values for position, velocity and acceleration are needed. A good choice is to take the first position estimate, some arbitrary velocity and zero acceleration. Since these initial guesses are not exact, the initial error covariance  $\mathbf{S}_0^p$  should be set according to equation (2.2.14) with non-zero values on the diagonal. The choice is not very crucial, it is solely used to advise the filter about

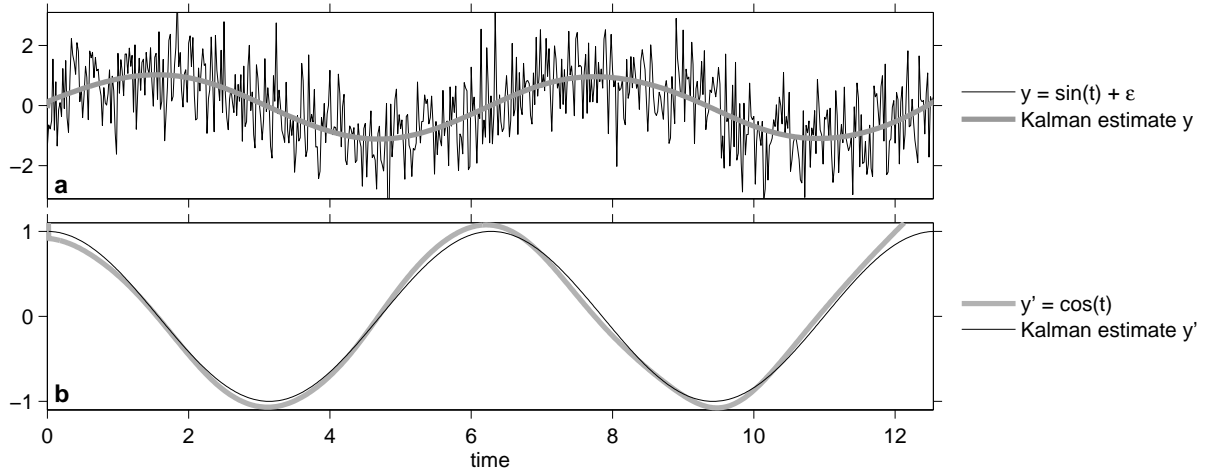


Figure 2.2: Kalman filter example on synthetic data.

the non-exactness of the initial guesses. The Kalman filter is then run forward and backward in time and returns a least-square solution to the problem.

The filter is now illustrated on synthetic data. In Figure 2.2a, a sine function  $y(t) = \sin(t) + \varepsilon$  is shown on the time interval  $t \in [0, 4\pi]$  with normally distributed noise  $\varepsilon$  overprinted. The noise  $\varepsilon$  has standard deviation  $\sigma = 1$ , which is directly assigned the measurement error in the Kalman gain equation (2.2.5), thus  $R = 1$ . Running the filter with a state error matrix  $\mathbf{S} = \text{diag}(0, 0, s_a = 0.02)$  and initial values  $\mathbf{x}_{-1}^p = (1, 0, 0)$  and  $\mathbf{S}_{-1}^p = \text{diag}(1, 1.1, 0.1)$ , a smooth sinusoidal signal is recovered (Fig. 2.2a, grey solid). The Kalman filter also returns the first derivative  $y'$ , which recovers very well a cosine function (Fig. 2.2b, thin solid), corresponding to the first derivative of the initial, noise-free sine function. Discrepancies at the beginning (due to forward run) and end of the time interval (due to backward run) emanate from the recursive nature of the filter: its performance evolves with increasing state estimates and is less accurate on the few initial state estimates. By this example, the smoothing performance and simultaneous, favorable output of first derivatives (i.e. velocities) of the smoothed series is nicely demonstrated.

As already mentioned, the filter was applied separately on each Cartesian component time series of a marker, and the non-zero state error component  $s_a$  was used as tuning coefficient to adjust smoothness of the temporal displacement and velocity trajectories. For almost all applications, the values of  $R = 0.05$  m and  $s_a = 0.8$  m/d<sup>2</sup> were used. Only at a few markers, a value of  $s_a = 1.5$  m/d<sup>2</sup> with increased smoothing, was applied. Note that  $s_a$  was not varied between the Cartesian component time series of a single marker.

### 2.3 Observed key ice motion events at selected locations

In Figure 2.3, surface flow velocities are depicted to convey an impression of the general flow regime of Gornergletscher. Flow velocity vectors at different locations depict mean summer surface flow speeds (taken from April-September). Flow speeds strongly decrease in the downstream direction on Grenzgletscher tributary, indicating a compressive flow regime. The inflow of Gornergletscher is slow, which is due to a slowly progressing uncoupling of Gornergletscher, caused by recent shrinkage and reduced mass flux from upstream areas of Gornergletscher. The particular location of Gornerssee right in the confluence apex of the two tributaries Gornergletscher and Grenzgletscher determines the orientation of ice flow direction with respect to the lake margin. There is considerable variation of flow speed and direction along the western, ice-marginal boundary of Gornerssee due to the converging flow of the two tributaries. This issue slightly complicates the interpretation of the ice motions and impact of a subglacial GLOF on Gornergletscher. In Figure 2.4, four reference locations, marked L1-L4, are indicated. In the following, ice motions characteristic to these locations are displayed and the local

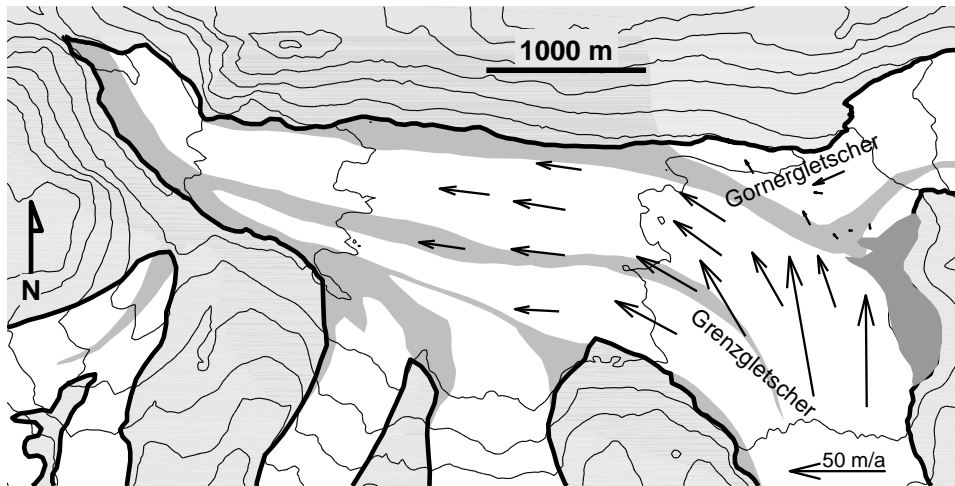


Figure 2.3: Summer surface flow velocities (April-September) on Gornergletscher.

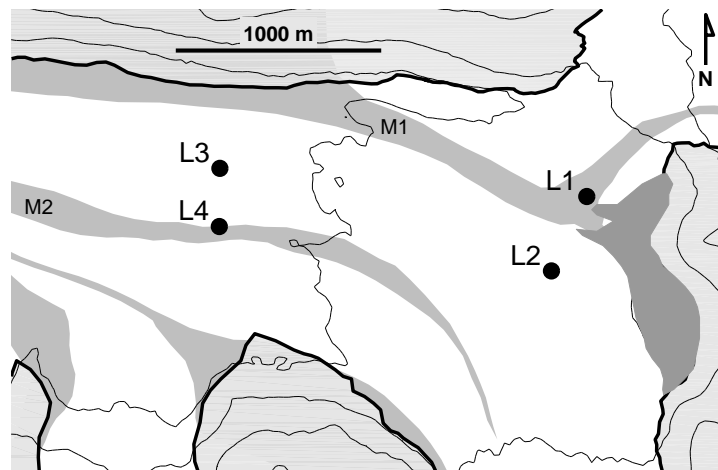


Figure 2.4: Locations L1-L4 for discussion of ice displacement trajectories in Figures 2.5-2.8.

impact of different drainages O1-O3 is discussed. Figures 2.5-2.8 depict horizontal ice displacement trajectories, vertical motion and horizontal velocity of referential markers pivotal to the locations L1-L4 and different outbursts O1-O3. The lake drainages differed in the amount of water stored in the lake and released afterward, as well as in the time it took to drain the water (subglacially). The figures clearly illustrate the varying impact of drainage on the considered locations and local ice flow. The time axes of the coordinate series (vertical motion/horizontal velocity) refer to the days before/after the beginning of the lake water level decrease. Day zero refers to the time of maximum lake water level immediately before the start of the decrease. Days prior to the drainage are counted negative, whereas consecutive days during the drainage are assigned positive numbers. The ice motions displayed refer to equivalent time intervals encompassing -5 d to +9 d of the time of maximum lake water level in each drainage O1-O3.

The referential marker L1 situated in the vicinity of the northern lake shore (Fig. 2.4) moved approximately westward prior to day 0 (Fig. 2.5a1). As soon as the lake water level started to decrease, the ice surface began to rise slightly and horizontal ice motion also increased noticeably (Fig. 2.5b1, c1). At the same time, the ice rather moved towards NW in the horizontal plane. This NW-directed movement was terminated and immediately reversed to a SW direction on days 4-5 while, simultaneously, the ice surface lowered again. During these days, horizontal velocities were largest, indicating that the ice returned

faster from the NW excursion than it turned into it previously during days 0-3. When looking at Figures 2.5a2-c2, a3-c3, one notes that the NW-excursion and subsequent SW-reversion of the respective ice motion are less pronounced during the O2 or O3 outbursts. In O2, a tiny NW-excursion of  $\sim 2$  cm of the ice movement had already begun on day -1 and then the ice reversed its motion to a SW direction for a small fraction ( $\sim 1$  cm) afterward, then proceeded to move in a West direction again. For the O3 drainage, the depicted L1 marker motion showed a similar motion towards NW, which continued throughout the drainage period. The motion did not obviously reverse at all (Fig. 2.5a3). In any case, ice displacements at the L1-markers are quite small; nevertheless, noticeable differences in flow speed, vertical uplift and the level of lateral motion (horizontal) indicate symptomatic features of each drainage.

At referential marker L2, a general movement towards NW at a moderate speed of about 0.08 m/d was observed during drainage O1. After the beginning of the lake water level decrease in O1, the ice motion deviated from the usual trajectory, increasingly bending towards West (Fig. 2.6a1). This Westward divergence of the ice motion correlates well with a moderate uplift which reached a maximum of about 10 cm on the late evening of day 3 (Fig. 2.6b1). Then, the direction of the motion of the marker reverted to  $\sim N$  and it appears that the marker resumed moving on a trajectory in line with the direction of ice motion preceding day 0. Horizontal flow speed increased considerably, and rather abruptly at day 1. The peak speed, a twofold increase of flow speed magnitude compared to pre-drainage conditions, occurred at day 3 late, simultaneously to maximum vertical uplift and maximum lateral excursion of horizontal motion. No such lateral motion, or any other peculiar movement of the L2-marker is apparent during the O2 drainage (Fig. 2.6). Unfortunately, to make matters worse, the displacement motion record was corrupted (horizontal and vertical motion) by an oscillatory signal with  $\sim 1$  d period. This is artificial and reflects the daily movement of the pillar on which the automated tachymeter was installed. The movement is caused by thermal effects, i.e. diurnal warming and nightly cool-down of the aluminum pillar construction and was not compensated for due to failure of the automatic plumb line recalibration of the tachymeter during the respective survey (the signals were recorded in 2006). The erroneous oscillation becomes more pronounced with increasing distance from the tachymeter (see also markers L3 and L4; Figs. 2.7 and 2.8).

For the O3 drainage, the horizontal ice motion of referential marker L2 had already started to accelerate two days in advance to day 0, as indicated by the progressively increasing velocity at days -2 to 0(1) (Fig. 2.6c3). This is in sharp contrast to drainage O1, where the horizontal ice motion began to accelerate about 1 d after the beginning of the lake water level decrease (Fig. 2.6c1). The differing increase of horizontal velocity seems to be a feature usable to discriminate between O1 and O3 drainages, provided the lake water level evolution is known. Flow speed increasing prior to day 0 strongly suggests leakage of lake water and a perturbation of the subglacial drainage system at an early stage, i.e. already before the direct observation and measurement of decreasing lake water level at the surface. Flow speeds increasing posterior to day 0 do characterize the abrupt impact of the drainage O1. The motion of marker L2 also deviates slightly in the West direction during days -1 to 2 (Fig. 2.6a3), whereas a subsequent return of the trajectory is poorly developed or not recognized. In addition, vertical uplift of the ice is far less pronounced than in O1 (Fig. 2.6b3 vs. b1). Thus, the amount of lateral diversive horizontal ice motion correlates with the magnitude of surface uplift (vertical motion).

At reference marker L3, located downstream of the confluence on the flow center line between moraines M1 and M2 (Fig. 2.4), the flow is directed virtually to the West. At this location, the horizontal displacement of the L3-marker did not show exceptional motions after day 0 of any drainage O1-O3 (Fig. 2.7). The trajectories seemed to move steadily in the down-glacier direction. However, substantial impact of the subglacial perturbation becomes apparent when examining the vertical ice motion and horizontal velocities: Large surface uplifts correlating with moderate to large increases of flow velocity were present. The O1 drainage was characterized by moderate surface uplift of  $\sim 25$  cm on day 4. The vertical motion was accompanied by a twofold increase of horizontal flow velocity (Fig. 2.7b1, c1). At marker L3, both the rising of the ice surface and the horizontal acceleration of flow initiated after the lake water level started to decrease, i.e. on day 1. The drainage O2 does not seem to affect the ice motion. Unfortunately, artificial fluctuations due to the malfunctioning tachymeter were also present here, and corrupted the

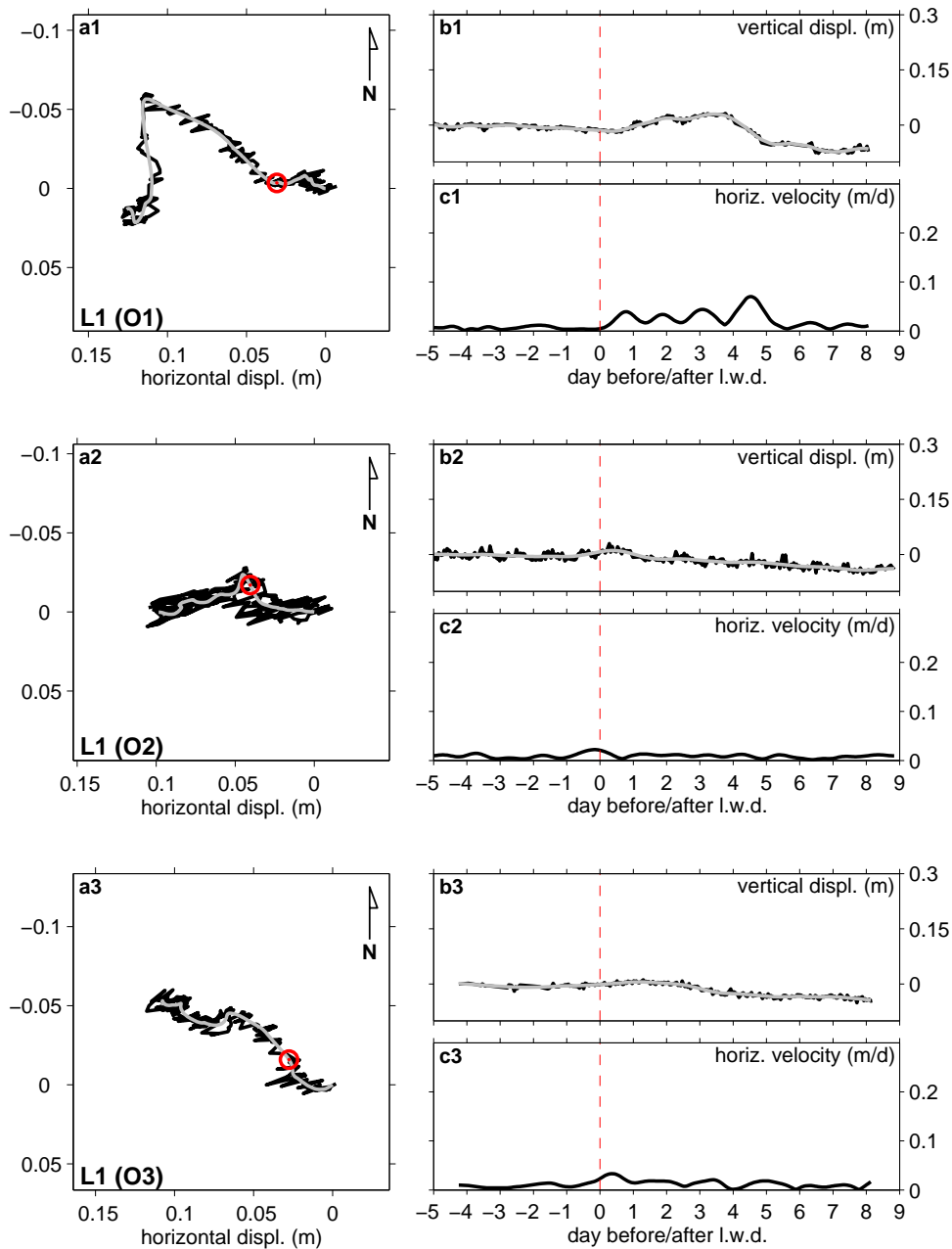


Figure 2.5: Horizontal ice displacement trajectory (a), vertical motion (b) and horizontal velocity (c) of referential marker L1 (Fig. 2.4) during the different drainages O1-O3 (Sect. 1.1). The circle in sub-panels a1-a3 and vertical dashed lines in sub-panels b1-b3/c1-c3 indicate day 0, the onset of lake water level decrease (l.w.d.).

displacement signal, especially in the vertical axis (Fig. 2.7b2).

Uplift of the ice surface was most pronounced in drainage O3 (Fig. 2.7), with amplitude of  $\sim 40$  cm on day 2 of the drainage. Also, a simultaneous increase of horizontal flow velocity by a factor 3 occurred concurrently (Fig. 2.7c3). Also at marker L3 the ice flow had started to accelerate before the lake water level had notably decreased, which again confirms the subglacial impact of leaking lake water prior to day 0. Note the contrast of vertical uplift and simultaneous speed-up of flow velocities between drainages O1 and O3: In drainage O1, both markers L2 and L3 experienced similar increases of flow speed and significant vertical uplift (Figs. 2.6 and 2.7, b1-c1). In drainage O3, there is considerable variance of

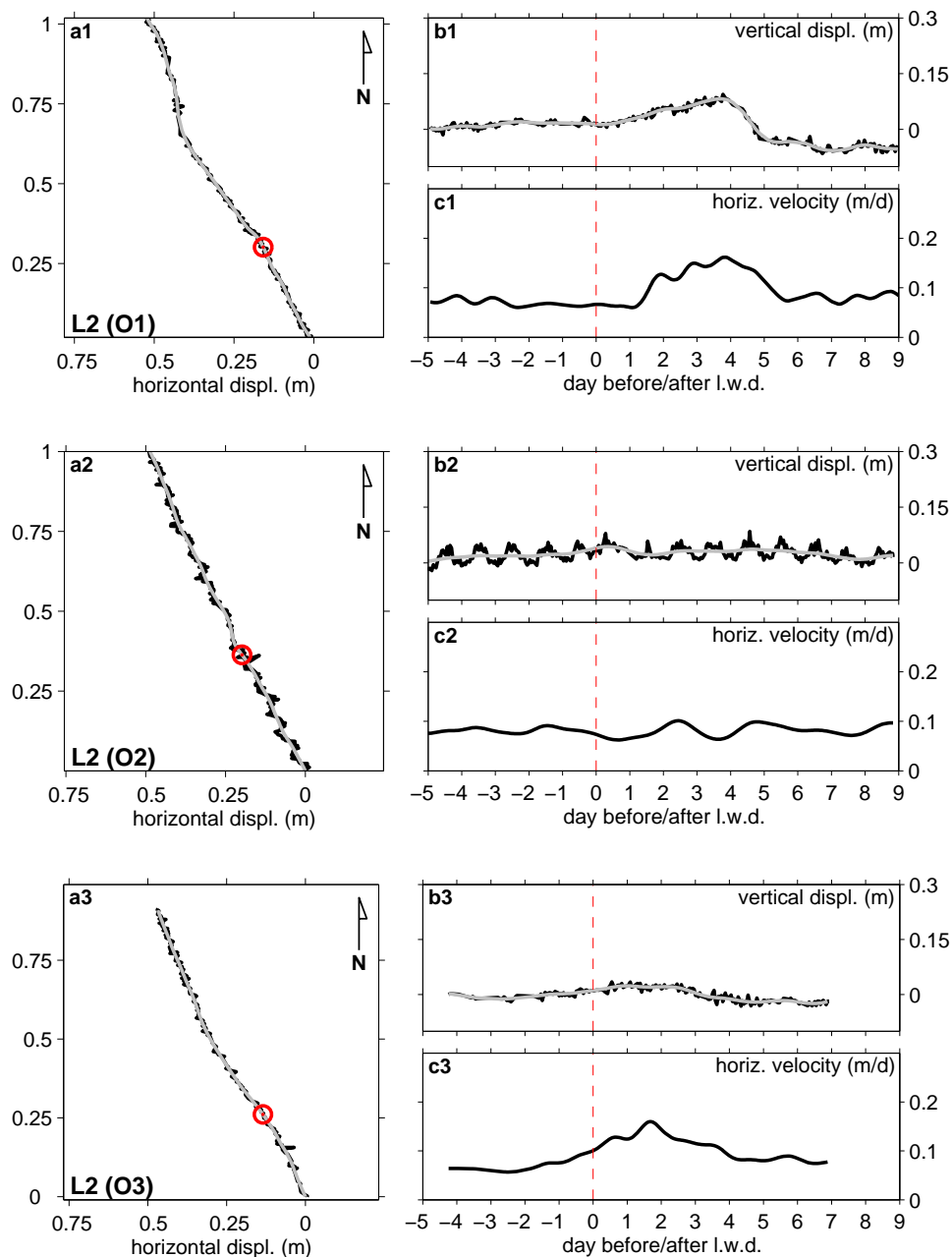


Figure 2.6: Same as Figure 2.5 , but for reference marker L2 (Fig. 2.4).

flow speed increase and vertical uplift between markers L2 and L3; a remarkable increase of flow speed and uplift is observed at marker L3, whereas a modest speed-up and virtually no uplift occurred to marker L2. A very similar picture is given by the motion, flow velocity and vertical uplift of marker L4, which is located off the center flow on moraine M2 (Fig. 2.4). Increase of horizontal flow speed and concurrent uplift of the ice surface very much resemble the equivalent time series of the nearby marker L3 (Fig. 2.8b-c vs. Fig. 2.7b-c). However, there is a major difference in the horizontal motion between the L3 and L4 markers. In Figure 2.7a3, marker L3 continually moves towards NW. While moving about 1.2 m towards West, marker L3 also gradually moved about 0.2 m towards North. By contrast, marker L4 (Fig. 2.8a3) moved about 0.75 m principally towards the West. In fact, during that time, marker L4 even moved fractionally towards South. However, at 0.75 m displacement, there is a rapid displacement offset towards North, whereafter the marker continues to move in the Northwest direction, only now similarly to marker L3. These 'side-way' motions (Sugiyama et al., 2010) strongly resemble the lateral motions

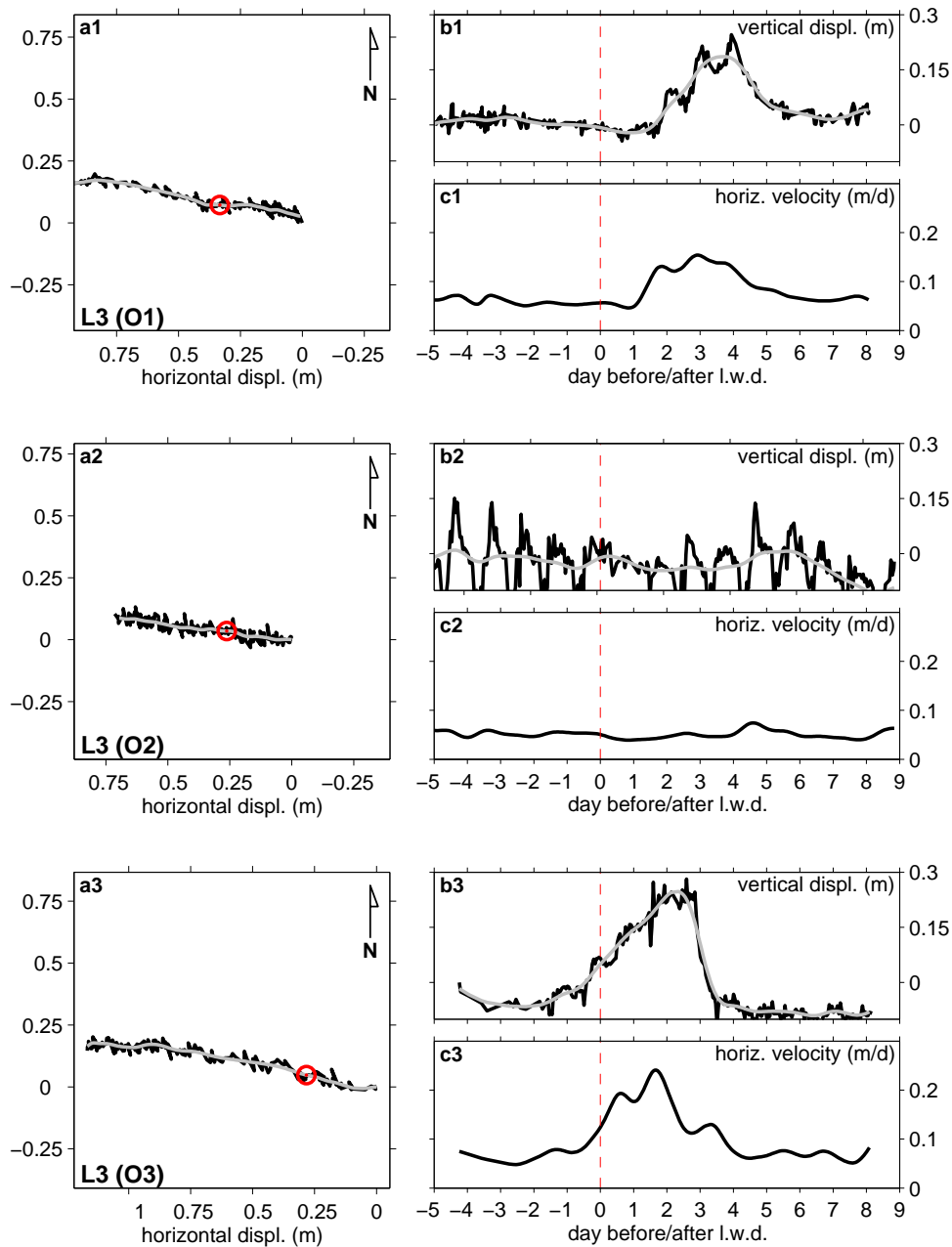


Figure 2.7: Same as Figure 2.5, but for marker L3 (Fig. 2.4).

of the L2-marker but are even more pronounced, especially in the O3-drainage (Fig. 2.8a3).

The local ice flow changes presented do not illustrate the full spectrum of spatial and temporal diversity of the variable impact of the Gornersee subglacial drainage on the ice flow of Gornergletscher. For example, pronounced side-way, lateral ice motion deflections were also observed in the L3-region at markers located close to the glacier margin. This issue is however discussed in Sugiyama et al. (2010). Thus, the figures 2.5-2.8 compiled the motion events observed during different Gornersee drainages and simultaneously indicated the spatial variability of ice flow changes. Further details on respective locations and distinct ice motions will be highlighted and discussed in the successive sections.

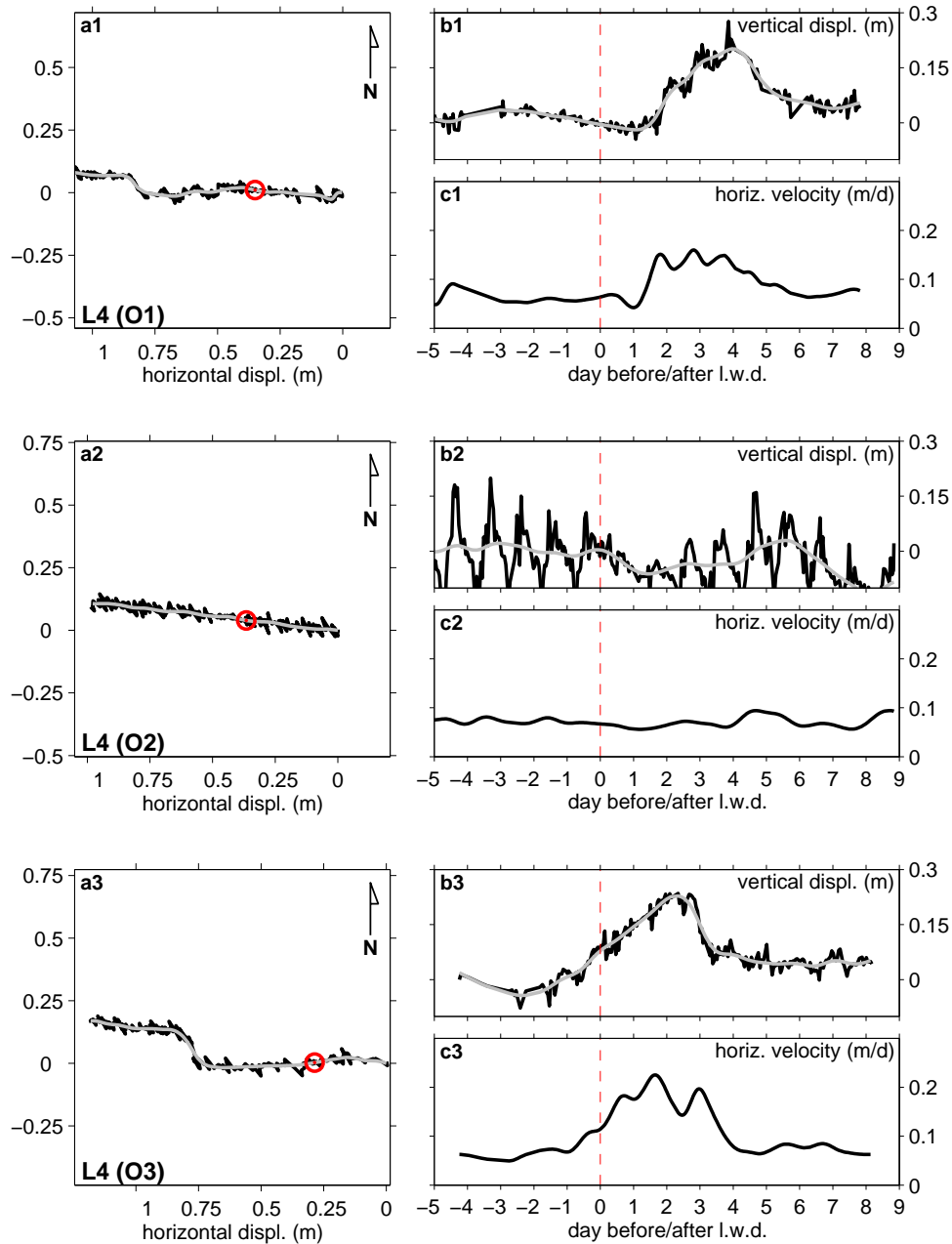


Figure 2.8: Same as Figure 2.5, but for marker L4 (Fig. 2.4).

### 2.3.1 Spatial variability of vertical ice motion

As already noted, large variation of vertical motion were present not only between the different drainages but also between the various referential markers presented. To illustrate the rather pronounced spatial differences of vertical motion, a series of the daily surface uplift magnitudes during the drainages O1 and O3 was computed. To calculate the uplifts, the trajectories of vertical motion at a range of markers were normalized by subtracting a best fit linear trend function. The linear trend function was estimated from a reduced set of the data points present in the 14 d intervals ( $\pm 7$  d of day 0 of drainage), where only data-points before ( $< \text{day } -1$ ) and after ( $> \text{day } 4$ ) the periods of major uplifts and flow accelerations (days -1 to 4) were considered. Then, mean uplifts were computed from the detrended time series of vertical motion for each of the six days -1 to 4. This procedure is sketched graphically in Figure 2.9.

Figure 2.10 shows the spatial distribution of the daily surface uplift magnitudes  $u_i$  at selected markers

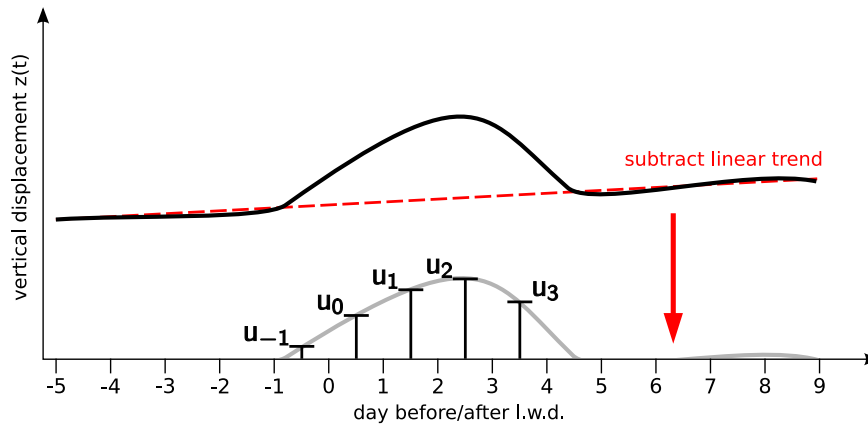


Figure 2.9: Illustration of the calculation of daily vertical uplift magnitude at a marker location. A linear trend (red dashed line) is computed from the data present before day -1 and after day 4, and then subtracted from the vertical displacement (black solid). From the normalized displacement (grey solid), the mean vertical motion magnitude  $u_i$  is then computed for each day  $i \in [-1, \dots, 4]$ .

(according to Figure 2.9) across the area of Gornergletscher. The magnitudes of uplift are drawn in a map at the marker locations as rectangles or circles, where the type of symbol refers to the drainage O1 or O3, respectively. The size of the symbol indicates the magnitude of vertical uplift (see legends in Fig. 2.10a).

On day -1, no particular significant vertical uplift occurred yet, neither in drainage O1, nor in O3 (Fig. 2.10a). On day 0 of drainage O1, one marker located close to Gornersee indicates some vertical motion. Surprisingly, in drainage O3, two markers located in the main flow region between the two moraines M1 and M2, about 2 km downstream of Gornersee, indicate moderate vertical uplift already on day 0 (Fig. 2.10b). The vertical motion drastically increases at the markers on the lower portion of Gornergletscher during days 1 and 2 of drainage O3, indicating a pronounced uplift of the ice surface below the confluence. Then, on day 3, the uplift magnitudes on the two markers are again very small, which suggests an abrupt lowering of the ice surface (Fig. 2.10e). Contrarily, in drainage O1, the markers on Gornergletscher ice do not show such a localized vertical uplift signal during days 1-3 of the drainage. Rather, the sizes of all marker symbols (O1: rectangles) seem to increase gradually during days 1-3, and then decrease again on day 4 (Fig. 2.10f), which suggests uniform elevation and subsequent decrease of the ice surface of Gornergletscher across a wide area, especially covering the lake vicinity and the center confluence area. These observations reveal the striking difference between the impact character of drainages O1 and O3.

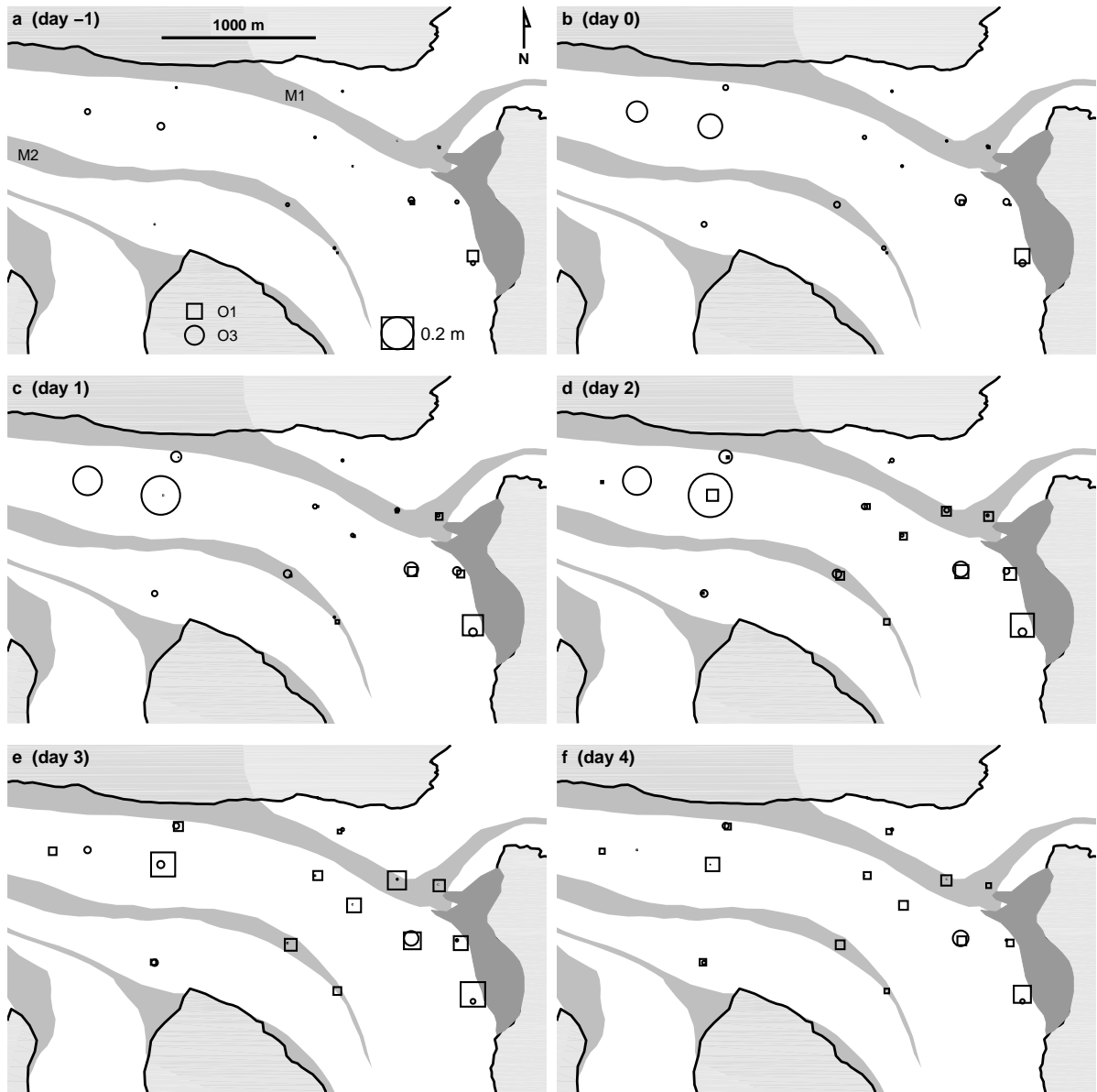


Figure 2.10: Spatial distribution of daily vertical ice surface uplift during drainages O1 and O3 (days -1 to 4). The symbols (rectangles, circles) refer to the drainage (O1 or O3, legend in sub-panel a), and are drawn at selected marker locations. The magnitude of uplift is indicated by the size of the symbol (see sub-panel a).

## 2.4 Surface ice flow velocities and strain-rates

To obtain an overall impression of the large-scale impact of each drainage, i.e. over the whole investigated region of Gornergletscher, the sparse marker flow velocities were interpolated onto a regular grid of points in order to obtain area-wide maps of flow velocities. A grid of points defining the discrete map was regularly distributed within the largest polygon defined by the marker locations. On this regular grid, component-wise, horizontal velocity fields were then computed by multiple linear regression. The regression is defined as follows: At each grid point, the scalar horizontal velocity component  $v$  is described by the linear equation

$$v = b_0 + b_1 x + b_2 y, \quad (2.4.1)$$

where  $\mathbf{G} = (x, y)$  are the coordinates of the grid point and  $\mathbf{b} = (b_0, b_1, b_2)$  is a vector of regression coefficients. Equation (2.4.1) is a planar parametric surface equation of the form  $f(x, y) - v = 0$ . An optimal guess of the coefficients  $b_i$  is obtained via multiple linear regression, where a set of equations like (2.4.1) is solved. In matrix form, this can be written as

$$\begin{bmatrix} v_1 \\ v_2 \\ \vdots \\ v_N \end{bmatrix} = \begin{bmatrix} 1 & x_1 & y_1 \\ 1 & x_2 & y_2 \\ \vdots & \vdots & \vdots \\ 1 & x_N & y_N \end{bmatrix} \begin{bmatrix} b_0 \\ b_1 \\ b_2 \end{bmatrix}, \quad (2.4.2)$$

or else, in shorter notation,

$$\mathbf{V} = \hat{\mathbf{X}} \mathbf{b}, \quad (2.4.3)$$

with the matrix  $\hat{\mathbf{X}}$  consisting of the column vectors  $[\mathbf{1} \ \mathbf{x} \ \mathbf{y}]$ , where  $\mathbf{x}$  and  $\mathbf{y}$  are  $N \times 1$  vectors of the marker (horizontal) position components and  $\mathbf{1}$  is a  $N \times 1$  identity vector. The scalar  $N$  refers to the number of units of input variables  $(x_i, y_i)$  and the measurement variable  $v_i$ , where  $i \in [1, \dots, N]$ . At each grid point within the polygon, the system of  $N$  equations (2.4.3) is thus formed using  $N$  available marker positions (input variables  $x_i, y_i$ ) and respective velocities (dependent variable  $v_i$ ) and solved for  $\mathbf{b}$ . Note that the velocities stem from the outputs of the Kalman filtering of the marker trajectories. With  $\mathbf{b}$  computed, an optimal velocity estimate  $v$  at the grid point  $\mathbf{G}$  is obtained by evaluating (2.4.1). In the regression algorithm, at every grid point we use *all* available marker position/velocities measurements ( $N = \text{const}$ ). However, the regression equations are weighted by the inverse fourth power of the distance between the corresponding marker position and the grid point at which the regression is currently performed. By this approach, measurements of velocity/marker positions closer to the current grid point are weighted far stronger than measurements distant from the grid point, yet at every grid point all presently available flow speed information from the surroundings is taken into account, rather than just flow speed information close-by, as for a simple neighbour interpolation scheme. For grid points very close to a marker position, the estimated velocity  $v$  approaches the measured marker velocity due to the pronounced weighting routine. Sweeping the weighted regression algorithm across all grid points, a smooth distribution is obtained for the horizontal velocity component  $v$ . The regression is repeated for the other horizontal velocity component. Since the markers generally did not measure the positions/velocities at exactly the same time instances, all position and velocity time series of the markers were to be interpolated onto the same discrete vector of time steps. Then, the regression algorithm was performed twofold on each time step, the final result being thus a temporal series of pairs of maps of horizontal flow velocity components.

In Figure 2.11, contour maps of normalized horizontal flow velocity magnitude are displayed. The velocities are normalized as  $(v_h - v_0)/v_0$ , where  $v_0$  is a reference velocity field, and  $v_h$  is the mean horizontal flow velocity of a single day. The reference velocity field  $v_0$  was computed as the mean horizontal velocity from the days -7 to -2 and 5-7 of the 14 d interval considered (see Sect. 2.3). From the 14 d interval, the days not mentioned beforehand are the days most influenced by the drainage of Gornersee, which is why they were omitted from the computation of  $v_0$ . Thus, the normalization by  $v_0$  will emphasize the anomalous flow regime during the main days of the drainage. Each sub-panel in Figure 2.11 shows the distribution of  $(v_h - v_0)/v_0$  on a selected day particularly characteristic for the respective drainage O1,

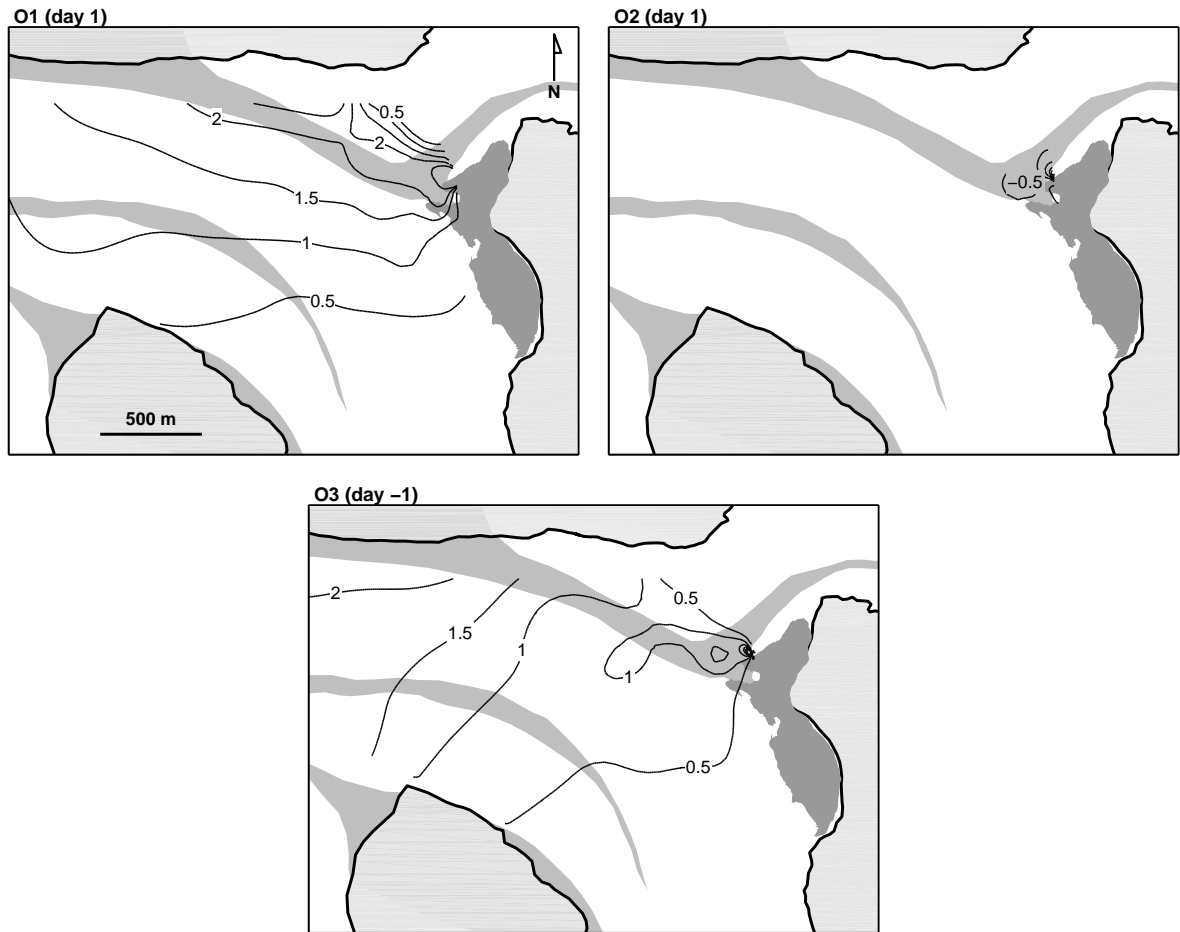


Figure 2.11: Contour maps of normalized horizontal surface flow speed magnitude,  $v_h$ . Horizontal flow speeds were normalized as  $(v_h - v_0)/v_0$ , where  $v_0$  is a reference velocity (see text). Of each drainage, mean  $(v_h - v_0)/v_0$  of a particular day of the respective drainage is displayed.

O2, or O3. Positive (negative) contour labels indicate a relative increase (decrease) in velocity. For example, a label of 2 indicates the velocity  $v_h$ , to have a magnitude corresponding to three-fold the reference velocity,  $v_0$ .

In drainage O1, after the lake water level started to decrease on day 0, a significant increase of the flow speed developed on day 1 (Fig. 2.11, O1). The contour lines are oriented approximately E-W, i.e., in line with the main flow direction (to the West) below the confluence. The contours originate at the western tip of Gornersee and cross the entire confluence area downstream. The relative change of velocity increases towards the northern moraine separating the Gornergletscher tributary. The maximum speed of the flow anomaly is thus a three-fold increase of flow speed. The obvious alignment of the contour of the three-fold increase (label 2) along the northern moraine (Fig. 2.11, O1), suggests that the flow velocities increased equally across the entire confluence and main flow direction, but differentially in the direction perpendicular to the principal flow direction (in North direction). These unusual flow speeds then decreased again and fully diminished on days 3-4 of drainage O1.

During drainage O2, a particular anomalous horizontal flow field evolving as a consequence to the lake drainage, was almost absent (Fig. 2.11, O2). A minor impact occurred only right at the tip of Gornersee. There, the flow velocities decreased slightly on day 1, after the lake had started to drain (on day 0). This very local disturbance is supposedly correlated with movement of the ice towards a sinkhole formed by melt and enlargement of a moulin, into which the lake water disappeared (see also Sect. 6.5). During drainage O3, the ice flow speeds were influenced in another striking manner (Fig. 2.11, O3).

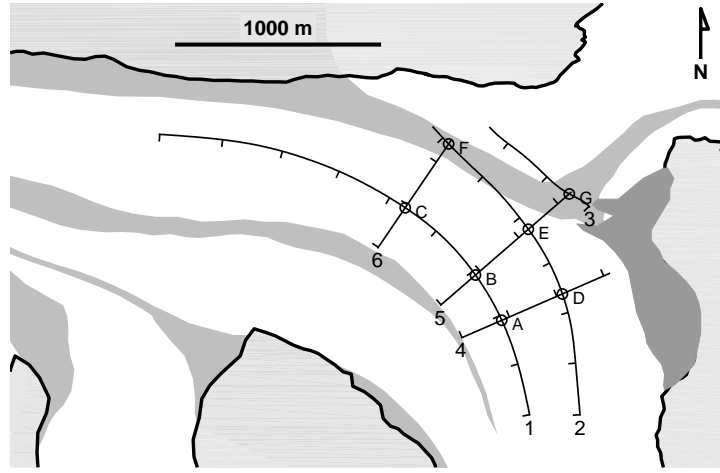


Figure 2.12: Streamlines (1-3) and transects (4-6) used for display of horizontal strain-rate  $\dot{e}_h = \dot{e}_{xx} + \dot{e}_{yy}$  in Figures 2.13 and 2.14. Ticks along streamlines and transects indicate distances in 250 m intervals. Intersection points are labeled A-G and are also indicated in Figures 2.13 and 2.14.

In drainage O3, the differential increase of flow speeds was already pronounced on day -1, prior to the superficial decrease of lake water level. This indicates that the lake water leaking from Gornersee already impacted the ice flow of Gornergletscher prior to day 0 and the actual decrease of lake water level. In the area below the confluence, about  $\sim 1.5$ -2 km distant from Gornersee, anomalous surface flow speeds increased up to a factor 3 on day -1. The contour lines are aligned approximately perpendicular to the main flow direction and indicate increasing flow speeds in the downstream direction (Fig. 2.11, O3). The relative increase in flow speed is fairly uniform across the width of Gornergletscher, while the flow speed deviations increase remarkably in the down-glacier direction. The resulting downstream gradient of the accelerated flow is in remarkable contrast to the gradient oriented in the S-N direction in drainage O1 (Fig. 2.11, O1).

### 2.4.1 Horizontal strain-rates along flow lines and transects

When performing the multiple linear regression algorithm described in the previous Section 2.4, horizontal strain-rates can be readily computed as

$$\dot{e}_{xx} = \frac{\partial u}{\partial x}, \quad \dot{e}_{yy} = \frac{\partial v}{\partial y}, \quad (2.4.4)$$

where  $u$  and  $v$  are the horizontal velocity components obtained from the regression method at each grid point, and  $x$ ,  $y$  are the coordinate axes. The strain-rates  $\dot{e}_{xx}$  and  $\dot{e}_{yy}$  were obtained simultaneously during the computations of the maps of flow velocities. Due to the rather unspectacular regional impact of the drainage O2, presentation of horizontal strain-rates was considered not worthwhile, which is why O2 is disregarded in the following. Only the differential impact of the O1/O3 drainages is further analyzed. In the following we consider the magnitude of the horizontal strain-rate,  $\dot{e}_h = \dot{e}_{xx} + \dot{e}_{yy}$ , along selected streamlines and transects normal to the streamlines, to assess the prevailing deformation regime. The projection of  $\dot{e}_h$  onto these streamlines and cross-sections will tell us where the ice experiences enhanced deformations and straining due to the spatial variation of the flow velocity modulations induced by the lake drainage. Compressive strain-rates are taken positive, while negative strain-rates indicate tensile/extensive conditions. Three representative streamlines, estimated from the mean summer surface flow velocity distribution, as well as three transects normal to these flow lines, were chosen. The six segments are depicted in Figure 2.12. Note that streamlines 2 and 3 are not aligned exactly with the medial moraine M1 of Gornergletscher. Due to the decreasing delivery of ice from the Gornergletscher tributary, the flow of Grenzgletscher dictates the converging flow; the ice mass delivered by Grenzgletscher slowly

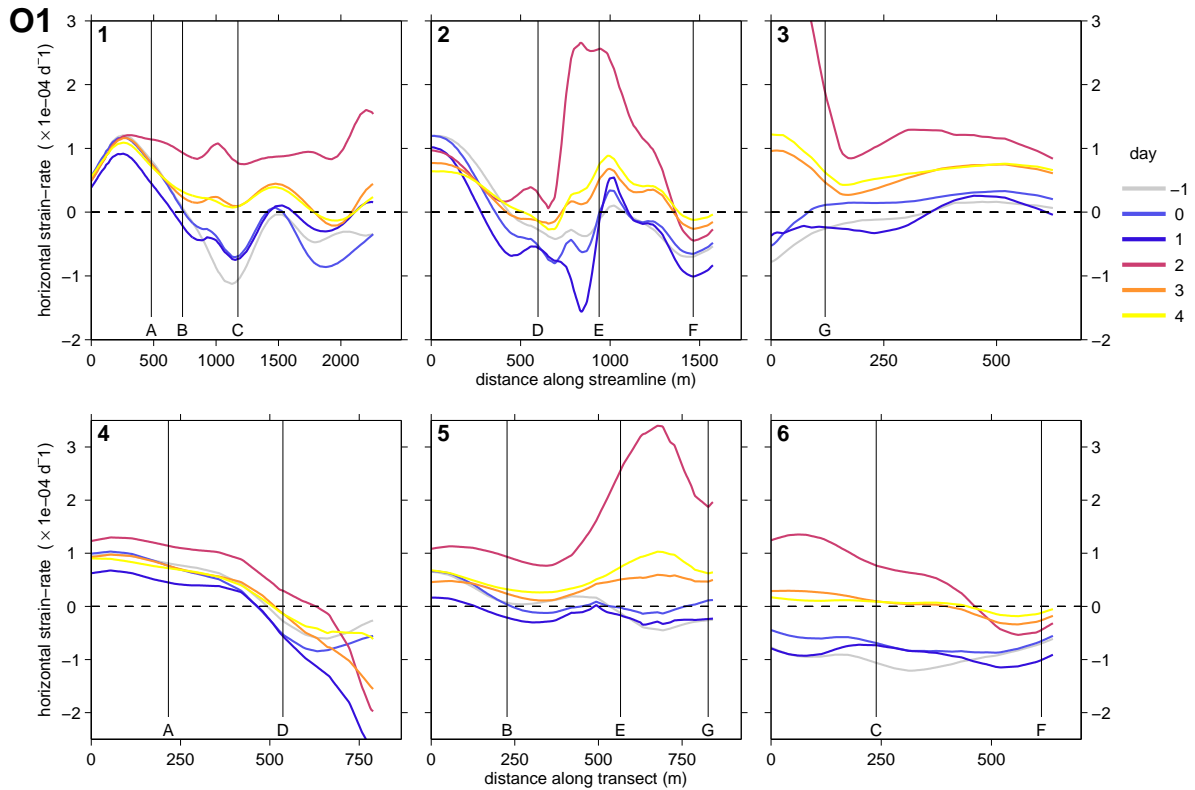


Figure 2.13: Horizontal strain-rate  $\dot{\epsilon}_h$  as function of distance on streamlines 1-3 and on transects 4-6 (Fig. 2.12), during days -1 to 4 of the O1 drainage. The dashed line indicates zero strain-rate; positive strain-rates are compressive, negative strain-rates are tensile. Vertical lines refer to intersection points traversed along the streamlines/transects.

spreads out into the entire confluence, thereby pushing aside the morainal ice and Gornergletscher, which is why the surface ice flow regime intersects the medial moraine.

In Figure 2.13,  $\dot{\epsilon}_h$  as function of the distance along the segments 1-6 is displayed. The results of Figure 2.13 refer to drainage O1. On streamline 1, horizontal strain-rate  $\dot{\epsilon}_h$  was compressive and decreased steadily along the streamline down to intersection point B, on day -1. Below B,  $\dot{\epsilon}_h$  then became negative; the deformation field changing to extension. Strain-rates were increasingly extensive downstream passed intersection point C, to about 1200 m distance. This streamline segment corresponds to the region of strongest curvature of the ice flow. The switch from a compressive to extensive regime (with another intermediate compression) in the downstream direction is explained by the curvature of the flow. Roughly said, the ice flows down into the confluence from a sloping tributary and slows down (compression). Due to the channel curvature, the ice flow rotates (generating extension) and is then forced to flow into the narrowing channel (intermediate decrease of extension), where it accelerates again slightly (another extension). Within the first two days of drainage (days 0-2), the deformation became substantially compressive along the entire length of streamline 1 (Fig. 2.13). On days 3-4, the compression relaxed again and  $\dot{\epsilon}_h$  dropped noticeably. The segment of streamline 1 between points B and C, with initial extensive strain-rates  $\dot{\epsilon}_h$ , experienced drastic compression on day 2 of drainage O1. On streamline 2,  $\dot{\epsilon}_h$  also increased significantly on that day (Fig. 2.13, 2). The most pronounced increase of  $\dot{\epsilon}_h$  occurred between intersection points D and F on this streamline. During days -1 to 4,  $\dot{\epsilon}_h$  decreased, increased and again decreased consistently along the segment between points D and F, except that a permanent compression was present at  $\sim 1000$  m, which is where the streamline traverses the moraine (Fig. 2.13, 2). On streamline 3, upstream of intersection point G,  $\dot{\epsilon}_h$  increased considerably on day 2 of the drainage O1 (Fig. 2.13, 3). Thus, the ice experienced strong compression near Gornersee and decreasing compression with increasing distance from it. On transect 4,  $\dot{\epsilon}_h$  generally decreases with increasing distance and becomes

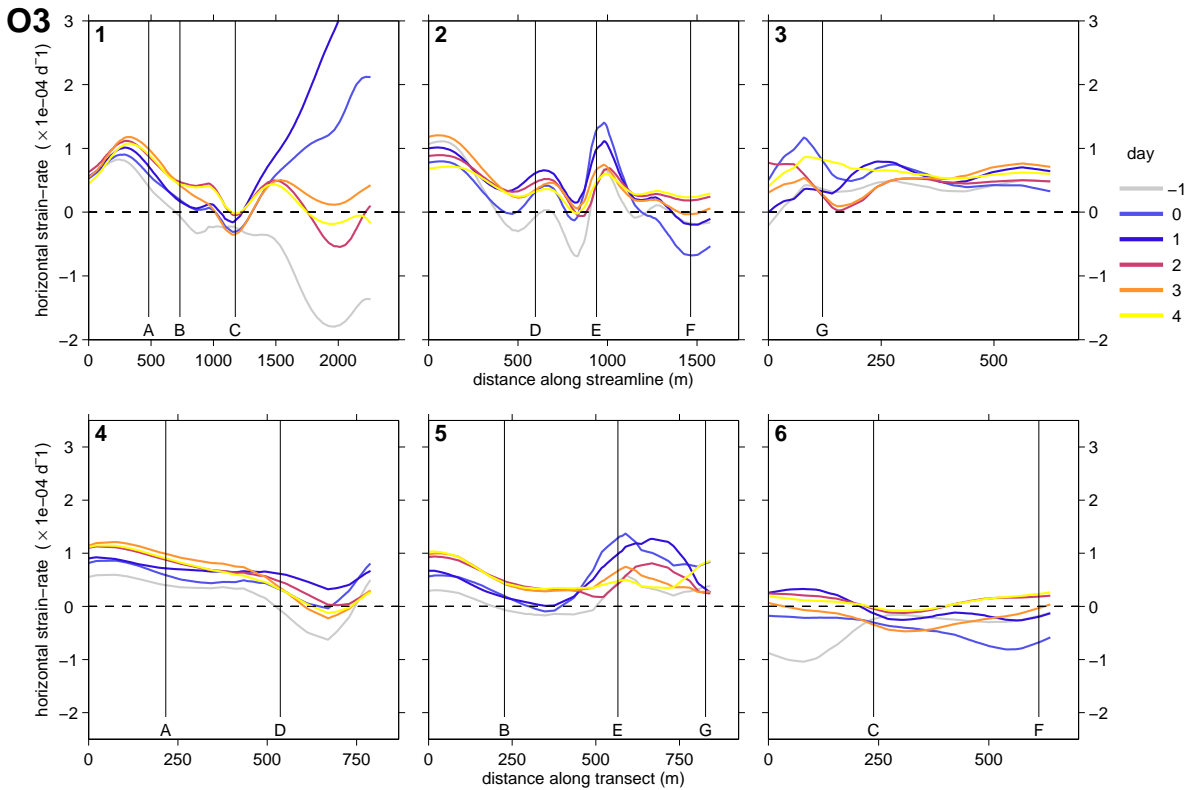


Figure 2.14: Same as Figure 2.13, but for drainage O3.

extensive at about 500 m distance, right before traversing intersection point D. On days -1 and 0,  $\dot{\epsilon}_h$  then increased again with increasing distance and nearness to Gornersee. The change of  $\dot{\epsilon}_h$  along transect 4 during the subsequent days 1 and 2 showed two noticeable features: First,  $\dot{\epsilon}_h$  decreased considerably to very tensile strain-rates of about  $-2 \times 10^{-4}/d$  near to Gornersee, i.e. at the end of the transect, on day 1. Second,  $\dot{\epsilon}_h$  increased considerably across the width of the transect on day 2, and the transition from compressive to extensive strain-rates moved past point D, closer towards Gornersee. On days 3-4, the profile of  $\dot{\epsilon}_h$  relaxed again and the variation of  $\dot{\epsilon}_h$  along the transect became again similar to the profile of day -1 (Fig. 2.13, 4). Along transect 5,  $\dot{\epsilon}_h$  is rather small. The transect actually intersects streamline 1 at point B, which is where the transition of compressive to tensile deformation occurs (see Fig. 2.13, 1). On day 2, the ice experienced compressive deformation along the complete transect with an increase of  $\dot{\epsilon}_h$  to  $1 \times 10^{-4}/d$  at intersection point B, while when moving closer to intersection point E,  $\dot{\epsilon}_h$  increased by another factor of 3. This maximum compressive strain-rate occurred again in the vicinity of Gornersee and the moraine between points E and G (Fig. 2.13, 5). On transect 6,  $\dot{\epsilon}_h$  is tensile along the entire length of the transect on days -1 to 1. Then, on day 2, an increase of  $\dot{\epsilon}_h$  to substantially compressive strain-rates occurred, similar to transect 5. The increase of  $\dot{\epsilon}_h$  along transect 6 decreases towards point F and is larger in the proximity of point C, i.e. the intersection with streamline 1.

In drainage O3, the variation of  $\dot{\epsilon}_h$  along the different streamlines and transects was radically different (Fig. 2.14). On streamline 1, no major variation of  $\dot{\epsilon}_h$  was experienced on days -1 to 4 on the streamline segment down to the lowest intersection point C. However, at downstream point C, the ice suddenly experienced substantial compression on the first days 0 and 1 of drainage O3. This is in sharp contrast to the drainage O1, where  $\dot{\epsilon}_h$  was compressive and of similar magnitude along most of streamline 1, including the portion upstream of C. The compressive strain-rates relaxed again during the following days 2-4 but remained rather high compared to the tensile  $\dot{\epsilon}_h$  of day -1 (Fig. 2.14, 1). Along streamline 2, the change of  $\dot{\epsilon}_h$  indicates a moderate compression nearby Gornersee, at intersection points D and E (Fig. 2.14, 2). Close to point E,  $\dot{\epsilon}_h$  increased (days 0-1) and subsequently decreased (days 2-4), while close to point F, the variation of  $\dot{\epsilon}_h$  through these days is reversed; the strain-rate first decreased (days 0-

1) and then increased (days 2-3). On streamline 3, upstream of point G, which is very close to Gornerssee,  $\dot{e}_h$  increased slightly on day 0. Afterwards, a decrease of  $\dot{e}_h$  on days 2-3 alternates with an increase of  $\dot{e}_h$  on day 4 (Fig. 2.14, 3). During drainage O3, the variations of  $\dot{e}_h$  along the transects 4-6 were also considerably smaller than during drainage O1 (Fig. 2.14, 4-6). On transects 4 and 5, the general trend was an increase of  $\dot{e}_h$  during days 0-1, which was then followed by a decrease of  $\dot{e}_h$  on days 2-4, in the vicinity of Gornerssee, i.e. passed intersection points D and E, respectively. At distances lower than  $\sim 500$  m, i.e. before passing the points D and E of the transects 4 and 5,  $\dot{e}_h$  increased further on days 2-4. On the lowermost transect 6, the ice to the left of streamline 1, before the transect traverses point C, exhibited a moderate compression (Fig. 2.14, 6). None of the streamlines and transects displayed showed similar striking variations of  $\dot{e}_h$  as observed during the drainage O1, except for the lower part of streamline 1.

## 2.4.2 Estimated vertical strain-rates compared to observed vertical motion

From the local marker motions L1-L4 (Figs. 2.5- 2.8) and the vertical motions displayed in Figure 2.10, it was inferred that the surface of Gornergletscher was lifted substantially during either drainage O1 or O3 (Fig. 2.10). Generally, ice is assumed incompressible (e.g. Schulson and Duval, 2009). Thus, for an incompressible material, strong horizontal compression of the ice provokes increased vertical straining, due to the constraint  $\dot{e}_{xx} + \dot{e}_{yy} + \dot{e}_{zz} = 0$ . If one assumes vertical strain-rate to be constant over the ice depth, it is related to the vertical velocity,  $w$  at the ice surface, as

$$\dot{e}_{zz} = \frac{\partial w}{\partial z}, \quad \iff \quad w = \int_0^h \dot{e}_{zz} \delta z = \dot{e}_{zz} h + C \quad (2.4.5)$$

where  $h$  is the ice thickness, and  $C$  is an integration constant, which, if  $h = 0$ , can be immediately identified with a vertical velocity at  $h = 0$ , i.e., at the base of the glacier. We assume that the vertical velocity at the base of the glacier is zero ( $C = 0$ ). That means that no separation ( $C > 0$ ) or melt of the basal ice ( $C < 0$ ) occurs (this latter case is not considered). However, we now test whether assuming  $C = 0$  is reasonable by the following procedure: The velocity  $\dot{e}_{zz} h = -\dot{e}_h h$  gives an estimate of the fraction of the vertical velocity which is due to vertical thickening/thinning of the ice compensating the horizontal deformations due to incompressibility. If  $w$  is the measured vertical velocity, and we have  $w \approx -\dot{e}_h h$ , we may suppose the measured vertical velocity to be essentially caused by vertical deformation of the ice. This would indicate that  $C \rightarrow 0$ . On the other hand, if  $w$  is rather different from  $-\dot{e}_h h$ , the vertical motion is influenced by other processes than solely vertical deformation. This possibly includes uplift of the whole ice column due to separation from the base, which would suggest  $C > 0$ . In Figure 2.15 this hypothesis is tested at the intersection points A-G (Fig. 2.12), for the two drainages O1 and O3.

The plots display the daily mean of measured  $w$  at the surface (and interpolated to the intersection points by the regression method described in Sect. 2.4) as open circles at days -1 to 4 of the drainages O1 and O3, respectively. Open grey circles indicate positive vertical velocity (i.e. surface uplift), whereas black open circles refer to negative measured vertical velocity  $w$ . The filled circles represent the quantity  $\dot{e}_h h$  and are inversely color-referenced; i.e. a black filled circle corresponds to  $\dot{e}_h h < 0$ , and grey filled circles indicate  $\dot{e}_h h > 0$ . To compute  $\dot{e}_h h$  at the points A-G, the ice thickness  $h$  at A-G was required, which was estimated from available digital elevation models (DEMs) of the glacier surface and bed (e.g. Riesen et al., 2006).

If the open circles are balanced by filled circles of opposite color and equivalent area, the result is  $w - \dot{e}_h h \approx 0$ . If the discrepancy between respective open and filled circles is large, one has  $w - \dot{e}_h h \neq 0$ . The former case (i.e. open circle has a counterpart of opposite color and similar area) suggests that the measured vertical velocity can be sufficiently explained by vertical straining compensating the horizontal deformations ( $C = 0$  in equation (2.4.5) is reasonable). The latter state (i.e. open and filled circles differ greatly) indicates that the measured vertical velocity can not be explained solely by vertical straining of the ice ( $C > 0$  in equation (2.4.5) presumably). In that case, other processes are supposedly responsible for the observed vertical ice motion rather than vertical straining of the ice.

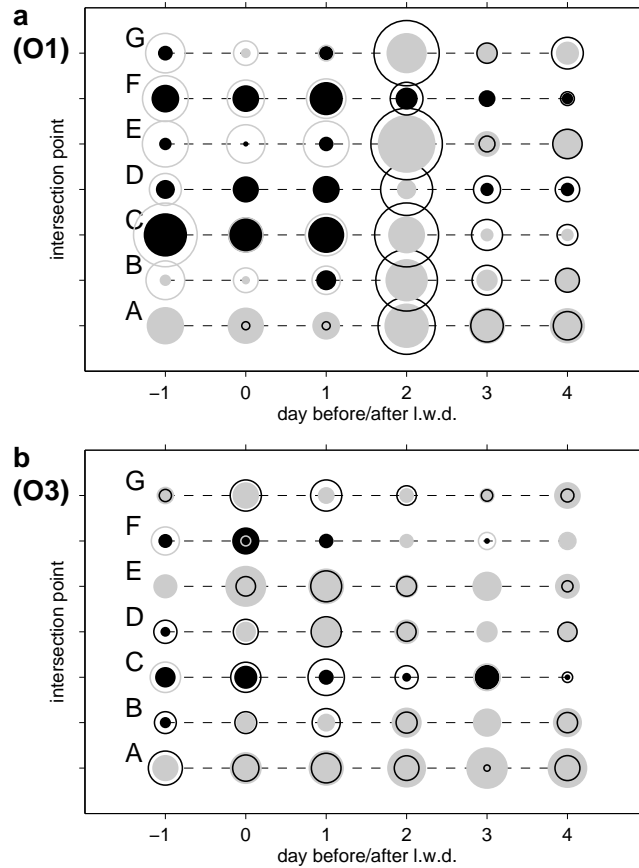


Figure 2.15: Comparison of measured vertical velocity (open circles) to  $\dot{e}_h h$  (closed circles), which is vertical ice velocity expected due to vertical ice deformation, at intersection points A-G (Fig. 2.12). Open circles represent measured vertical velocity  $w$ , where  $w < 0$  is grey and  $w > 0$  is black. Closed circles, i.e. vertical velocity  $\dot{e}_h h$  based on ice thickening/thinning due to horizontal deformation is inversely color-referenced;  $\dot{e}_h h < 0$  is black,  $\dot{e}_h h > 0$  is grey.

The filled and open circles at days -1 to 2 of drainage O1 appear larger than those during the same days of drainage O3 (Fig. 2.15a,b). This correlates well to the significant vertical motions observed during drainage O1 and already described so far. Due to the strong differences in horizontal velocities, considerable vertical straining compensating the horizontal deformations is present, which is indicated by the abundance and considerable sizes of the filled circles in Figure 2.15a. However, the velocities due to vertical straining only partially match the measured vertical velocities. Largest discrepancies between vertical velocity  $w$  and that due to the vertical straining,  $\dot{e}_h h$ , occurred at intersection point E during days -1 to 1 and at all points A-G on day 2. There, the open circles are hardly balanced by filled circles. This suggests the vertical uplift may be caused by basal separation of the ice. Vertical straining of the ice in reaction to the strong horizontal compressions is obviously not sufficient to explain the vertical velocities, though at other points, i.e. C, D and F, vertical ice deformation matches well the measured ice velocities. In the case of drainage O3 (Fig. 2.15b), the sizes of the circles are considerably smaller, indicating smaller vertical velocities and also smaller possible vertical ice deformation. The absence of considerable discrepancies allows one to suspect that vertical motions due to basal separation or the like would not play a great role. The balancing of open/filled circles is coherent across most days of the drainage.

## 2.5 Discussion

The preceding sections reviewed both the localized impact of the different subglacial drainages of Gornerssee and the regional, large-scale changes of ice motion and flow velocities induced by the drainages. Immediately, one realizes that only the drainages O1 and O3 seriously disturbed the motion of Gornergletscher on both local and regional scales. In drainage O2 the lake water nonetheless travelled down Gornergletscher almost completely subglacially; only the lake water was not directly evaded subglacially from the lake basin, but routed to the subglacial environment by a superficial by-pass (i.e. the overspill into a nearby moulin). This process did not lead to a sudden or progressively increasing discharge of lake water, but to a rather constant rate of lake water discharge. If there is no sudden or progressively increasing transfer of water to the subglacial drainage system of the glacier, no considerable impact can be expected. This is confirmed by the absence of any significant alteration of the surface ice motion of Gornergletscher. It appears that neither the time series of the horizontal flow motion, velocity and vertical motion of the referential markers L1-L4 (local scale), nor the maps of regional velocity variations indicated any significant impact of the drainage O2. During drainages O1 and O3, where lake water discharged directly to the subglacial environment of Gornergletscher, the subglacial drainage system of Gornergletscher was almost certainly overstressed. When the basal system is forced to accommodate the additional water, subglacial conditions (i.e. water storage, detention periods of lake water, basal water pressure, basal lubrication) are strongly modulated. These are properties which govern the basal motion of Gornergletscher and indirectly the flow motion observed at the ice surface. The documented ice flow perturbations showed exceptional variations which reflect the different characters of the lake drainages and their impact on the subglacial environment. In drainage O1, flow velocities, strain-rates and surface elevation increased considerably across most of the area of Gornergletscher. Vertical uplift increased first close to Gornerssee and then at subsequent later time at increasing distance from the lake. Similarly, largest changes of strain-rates occurred in the central confluence or at close distance to Gornerssee. The comparison of vertical velocities to vertical ice deformation compensating the horizontal ice deformations indicated that the vertical motions are only partially attributed to the ice deformation. Some considerable vertical motion of the ice may be due to lake water penetrating the basal environment and separating the ice from the sole. In drainage O1, the origin of the basal perturbation was at Gornerssee, and the range of influence enlarged in the down-glacier direction as more and more water entered the drainage system and was presumably dispersed along the base of Gornergletscher. It is recognized that drainage O3 was associated with striking changes of flow velocities, vertical surface uplift and horizontal strain-rates only on the part of Gornergletscher below the confluence area. The flow variations in the vicinity of Gornerssee were almost negligible, or, at least considerably less pronounced than during O1. It is somewhat intriguing that no, or negligible, vertical motion was observed in the confluence and periphery of Gornerssee during O3. Furthermore, the minor vertical motions can be sufficiently explained by vertical ice deformation. It suggests that any intrusion of water to the glacier bed was minor or completely absent. In the O3 case, the water presumably crossed the confluence area without interrupting the local subglacial conditions severely. How this was achieved is not fully clear. The water may have travelled en-glacially, or possibly in a very localized channel. The impact of the O3 drainage effectively occurred at rather large distance from Gornerssee, and only slowly propagated upstream, towards Gornerssee.

## Chapter 3

# Ice flow changes during the drainage of Gornersee

This chapter is published in a slightly modified form as:

Riesen, P., Sugiyama, S., and Funk, M. (2010). The influence of the presence and drainage of an ice-marginal lake on the ice flow of Gornergletscher, Switzerland. *J. Glaciol.*, 56(196):278-286.

**Abstract** Gornergletscher, Switzerland, is located adjacent to the marginal Gornersee that periodically drains. We measured ice flow velocities of the glacier during two drainage events of the lake, in 2004 and 2006. The common feature of these two events was that during both, Gornersee filled to its maximum level and then overflowed. The events differed in that in 2004 Gornersee rapidly drained via a sudden subglacial connection, whereas in 2006, the lake water continued to overflow and slowly discharged into a nearby moulin. We analyzed the changes in ice flow velocities in the vicinity of Gornersee during the two drainage events, using a three-dimensional ice flow model which is able to (i) simulate locally variable enhanced basal motion of the ice, and (ii) account for the load and release of water pressure exerted on the ice covered by the lake. We demonstrate that the key features of the observed flow changes can be reproduced adequately in the numerical model by considering these two effects as the main mechanisms. We interpret the 2006 flow changes to be dominated by the release of lake water pressure acting on the ice during the lake drainage. The 2004 ice flow changes can be explained by enhanced basal motion, and the impact of the lake water pressure provides certain clues to some observations insufficiently explained by enhanced basal motion.

### 3.1 Introduction

A glacier-dammed marginal lake fills until the water reaches a certain threshold at which the lake water connects to the subglacial drainage system, allowing it to drain. The drainage is of unstable nature (Nye, 1976) and may lead to potentially hazardous flooding in the glacier outlet stream. The phenomenon, termed *jökulhlaup* (e.g. Björnsson, 1992), drives large amounts of water into the basal environment of the adjacent glacier within a short time, causing a strong perturbation of subglacial water flow. Increased water pressure and temporary water storage at the glacier bed locally enhance basal motion, which is reflected in increased surface flow speeds (e.g. Iken, 1981; Sugiyama and Gudmundsson, 2004). Anderson et al. (2005) emphasized the coherence between the speed-up of Kennicott Glacier and the drainage of Hidden Creek Lake (HCL), whereas Walder et al. (2005, 2006) discussed the response of the ice dam in the vicinity of HCL to its filling and drainage.

Gornergletscher, Switzerland, is a valley glacier located in the southern Swiss Alps. At the place where it meets Grenzletscher, an even larger tributary, it dams the ice-marginal lake, Gornersee (Fig. 3.1). Gornersee originates from melt water retention during spring and usually drains in early summer. The bottom of Gornersee is essentially ice, except for along the eastern lake border, where the lake floor is formed by a steep slope of morainal debris plunging westward into the lake. We observed five drainage

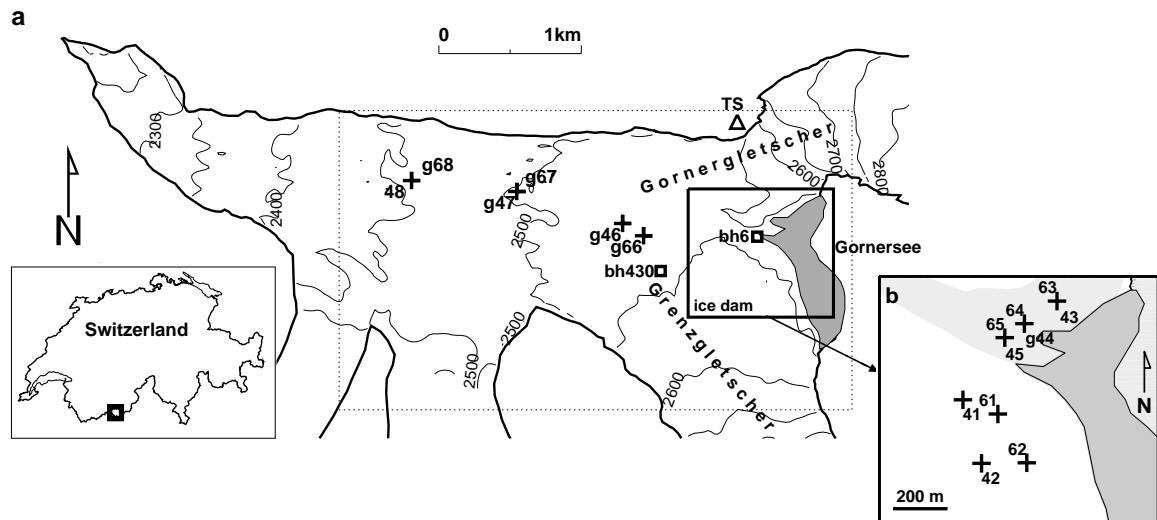


Figure 3.1: (a) Map of Gornersee (grey) and Gornergletscher with contour lines of ice surface elevation (solid, 50 m intervals), glacier margin (thick solid), location of the tachymeter and nearby GPS reference station (triangle TS), boreholes *bh430* and *bh6* (squares) and ice flow measurement locations (crosses). The dotted box indicates the geographic coverage of Figures 3.4-3.7. (b) Zoom panel of the box in Fig. 3.1a (*Ice dam*) indicating the measurement locations in the ice dam area. For identification, we label an individual marker with an integer composed of the respective survey year (first digit: 4 or 6) and an individual number (2nd digit). A 'g' in front of the integer indicates a GPS-equipped marker.

events of Gornersee in past years (2004-2008). Results on the impact of individual Gornersee jökulhlaups on the ice flow and hydrology of Gornergletscher have been published in Huss et al. (2007) and Sugiyama et al. (2007a, 2008). The results from passive seismic surveys are described in Walter et al. (2008), and Werder et al. (2009) and Werder and Funk (2009) give details on extensive dye tracing experiments performed during the observed Gornersee drainage events.

In this paper, we further examine the interaction between draining lake and damming glacier using field measurements and numerical modeling. We measured ice flow velocities of Gornergletscher in the vicinity and down-glacier of the Gornersee marginal lake during the 2004 and 2006 drainage events and studied the observed changes in flow speed and direction during these distinct events. To reproduce and interpret the observed flow changes we used a full Stokes three-dimensional numerical ice flow model, which is able to treat local variations in basal motion as well as the effect of the lake water pressure acting on the ice. To detect and corroborate the mechanisms responsible for the observed flow changes, we carried out different flow simulations with adjustments in the model boundary conditions.

## 3.2 Field methods

We measured the ice flow of Gornergletscher by surveying the displacements of eight poles (markers) installed in the ice. Five markers (41-45 in 2004, 61-65 in 2006) were located in the vicinity of Gornersee (henceforth *ice dam*, Fig. 3.1b). These markers were equipped with optical survey prisms. Every hour, an automated tachymeter estimated distance and both horizontal and vertical angles from the prisms' reflectance patterns. This tachymeter was situated on the rock ledge at the northern margin of the glacier (Fig. 3.1a, TS). We fixed multiple reference prisms onto rock outcrops along the glacier margin to carry out an atmospheric correction for the angle and distance readings. The relative azimuth and distance data were then converted to absolute coordinate positions. For the optical survey, the position errors are dependent on the tachymeter orientation (Table 3.1). The error is larger in the down-glacier (east-west)

Orientation:	East-West	North-South
$SD$	35	2
$SE_{N=50}$	4.9	0.3
$SE_{N=150}$	2.8	0.2
$SE_{N=300}$	2.0	0.1

Table 3.1: Absolute position errors (in cm) for the optical ice flow measurements (tachymeter) with standard deviation ( $SD$ ) and standard error from the mean ( $SE = SD/\sqrt{N}$  for  $N = \{50, 150, 300\}$  repeated measurements)

direction than in the cross-glacier (north-south) direction, due to increased influence of vertical tilt errors of the tachymeter device in this axis. The absolute position error of 35 cm in the down-glacier direction is large but diminishes for repeated measurements. Within 3-4 days, when  $N=50$  position estimates are acquired, it decreases to about 5 cm. For our studies,  $N$  is in the range of 50 – 350, hence the error becomes even smaller. Also, the ice displacement at the key markers 41-42 (61-62) is approximately aligned with the axis of minor errors. Three markers (46-48 in 2004, 66-68 in 2006) were also installed about 1 to 2.5 km down-glacier of Gornerssee (Fig. 3.1a). These stakes moved down-glacier, i.e., principally west, and differential GPS receivers (Leica500) at those marker locations were used in order to overcome the low accuracy of the tachymeter in the down-glacier direction. The GPS reference station was installed close to the tachymeter. We recorded 1 h sessions of L1+L2 phase signals every 3 hours at 1/30 Hz sampling rate. We processed the GPS data in static differential mode relative to the reference station, using commercial software provided by Leica. The error of the position estimates using GPS is  $\pm 1$  cm in the horizontal, and independent of orientation.

Note that the data of an individual marker was acquired by either GPS or tachymeter and is not the result of a combined survey. However, we compared trajectories of poles installed side by side and surveyed by either GPS or tachymeter. These data sets were generally coherent, inspiring confidence in the trajectories obtained by means of the optical survey. The two-component horizontal flow velocity  $\mathbf{v} = (v_1, v_2)$  of an individual stake was computed in a least-squares sense from fitting the linear equations  $\mathbf{x}_1 = v_1 \mathbf{t}$  and  $\mathbf{x}_2 = v_2 \mathbf{t}$ , with  $\mathbf{x}_1(\mathbf{t})$ , and  $\mathbf{x}_2(\mathbf{t})$  being  $N \times 1$  vectors of the horizontal components of the positions, and  $\mathbf{t} = [t_1, \dots, t_N]$  being a  $N \times 1$  vector of time steps during the time interval  $\Delta t = t_N - t_1$ , in which the position coordinates were measured. Thus, the velocities  $v_1$  and  $v_2$  correspond to the slopes of linear fits to the stake's horizontal displacement components in the interval  $\Delta t$ .

In addition to the geodetic measurement, we also measured basal water pressure in boreholes drilled to the glacier bed using a hot water drilling system. In each borehole, a vibrating wire pressure sensor (Geokon Model 4500) connected to a logger at the glacier surface was operated at a sampling interval of 10 min. We show data from borehole *bh430* which was used in 2004, and from borehole *bh6* used in 2006, their respective locations are depicted in Figure 3.1. Also, the lake water level was recorded using a Keller PAA-36W pressure transducer with 10 min sampling interval.

### 3.3 Numerical model

We solve the balance equations for incompressible, isothermal steady Stokes flow as

$$-\operatorname{div}(\mathbf{t}) + \nabla p = \rho \mathbf{g}, \quad (3.3.1)$$

$$\operatorname{div}(\mathbf{v}) = 0, \quad (3.3.2)$$

where  $\rho=900 \text{ kg m}^{-3}$  is the density of ice,  $\mathbf{g}$  is the gravitational acceleration and  $\mathbf{t}$  is now the deviatoric stress tensor with  $\operatorname{tr}(\mathbf{t}) = 0$ . The fields to solve for are velocity  $\mathbf{v}$  and pressure  $p$ . The constitutive relation adopted for the stress is a power law of the form

$$\mathbf{t} = \nu(\mathbf{D})\mathbf{D} \iff \nu(\mathbf{D}) = A^{-\frac{1}{n}} \left( \frac{1}{2} \operatorname{tr}(\mathbf{D}\mathbf{D}) \right)^{\frac{1-n}{2n}}, \quad (3.3.3)$$

where  $\mathbf{D} = \frac{1}{2}(\text{grad}(\mathbf{v}) + \text{grad}(\mathbf{v})^T)$  is the strain-rate tensor,  $n$  is the power law exponent and  $A$  is the constant rate factor. The problem (3.3.1)-(3.3.3) was solved by adapting the variable viscosity  $\nu(\mathbf{D})$  through a Newton-Raphson iteration scheme until convergence of the velocities was achieved, starting from an initially uniform viscosity distribution or previously determined solution. A penalty method was used for the incompressibility constraint. The model is implemented in the commercial Finite Elements software MSC.Marc (Marc, 2005) and has been used and validated in previous studies (Gudmundsson, 1994, 1999; Raymond and Gudmundsson, 2005; Helbing, 2005). In all computations we used  $n = 3$  and  $A = 75 \text{ (MPa)}^{-3} \text{ a}^{-1}$  (Gudmundsson, 1999).

From a digital elevation model (DEM), acquired in September 2004 using airborne photogrammetry, and radio echo sounding (RES) measurements of the bed topography (see Sugiyama et al., 2008), we generated a mesh representing the Gornergletscher geometry. The model domain includes the confluence area and the lower tongue of Gornergletscher. The domain does not cover the entire glacier system with the Grenzgletscher and Gornergletscher tributaries due to a lack of bed geometry information upstream of the confluence. On the two-dimensional transverse sections where the model boundary traverses the Grenzgletscher and Gornergletscher tributaries, we prescribed fixed flow velocities as inflow boundary conditions at the element nodes. These flow velocities were derived from two-dimensional cross-section flow fields, separately computed on identical geometries as the inflow faces using the implementation of two-dimensional glacier flow in a cross-section of Sugiyama et al. (2007b) with equivalent parameters  $n$  and  $A$ . The two-dimensional flow fields at the inflow boundaries were tuned so that the computed surface flow speed profiles matched nearby available measurements of annual surface flow velocities. Note that the model of Sugiyama et al. (2007b) was solved using a finite differences grid. The nodal velocities input to the finite element model were interpolated from the separately computed flow fields, then translated to the three-dimensional model faces, aligned to the mean slope of the glacier surface at the transverse section, and oriented in the main flow direction. The slopes were determined from the DEM.

In the vertical, the mesh consisted of six layers of elements (3330 total) of decreasing thickness towards the bottom. A Dirichlet condition  $\mathbf{v} = \mathbf{0}$  was applied at the bottom nodes of the sixth element layer and at all marginal nodes. The glacier bed is represented by the plane consisting of the upper faces of the sixth layer elements. Note that this sixth layer of elements has no physical meaning otherwise, but we will refer to it as 'bed layer' from now on. We applied a parametrization of basal motion by utilizing deformation of the bed layer elements. In that way, the basal velocity  $u_b$  at the glacier bed, i.e., at an upper face of an element of the bed layer, corresponded to

$$u_b = \frac{d}{\nu} \tau_b, \quad (3.3.4)$$

where  $d$  is the element thickness,  $\nu$  is the element viscosity (can also be regarded as a drag coefficient) and  $\tau_b$  is the basal shear stress. We used a Newtonian rheology with  $\nu = \text{const}$  for the bed layer elements and substituted  $C = d/\nu$  into Equation (3.3.4), thus the linear relation for the basal boundary condition was incorporated as

$$u_b = C \tau_b \quad \iff \quad \tau_b = \frac{1}{C} u_b. \quad (3.3.5)$$

Since we only solved for velocities and computed stresses separately, we controlled the simulation of the influence of the lake drainage directly through enhancement or reduction of basal velocities. Thus, we increased or decreased  $C$  in subsets of the bed layer elements to locally soften or harden the bed layer rheology, as the bed layer elements viscosity  $\nu$  is inversely proportional to  $C$ . The thickness of the bed layer (elements) is small compared to the overburden ice thickness, but a moderate thickness was needed when large deformations of the elements occurred. We used a uniform thickness of  $d=10$  m, which is about 3% of the maximum ice thickness in the central confluence. Another description of this parametrization of basal motion can be found in Vieli et al. (2000). The glacier surface was treated as a free surface with  $\mathbf{t} \cdot \mathbf{n} = 0$ , where  $\mathbf{n}$  is the surface normal. On the upper element faces within the lake domain, we described distributed pressure loads in order to simulate the effect of the lake water pressure

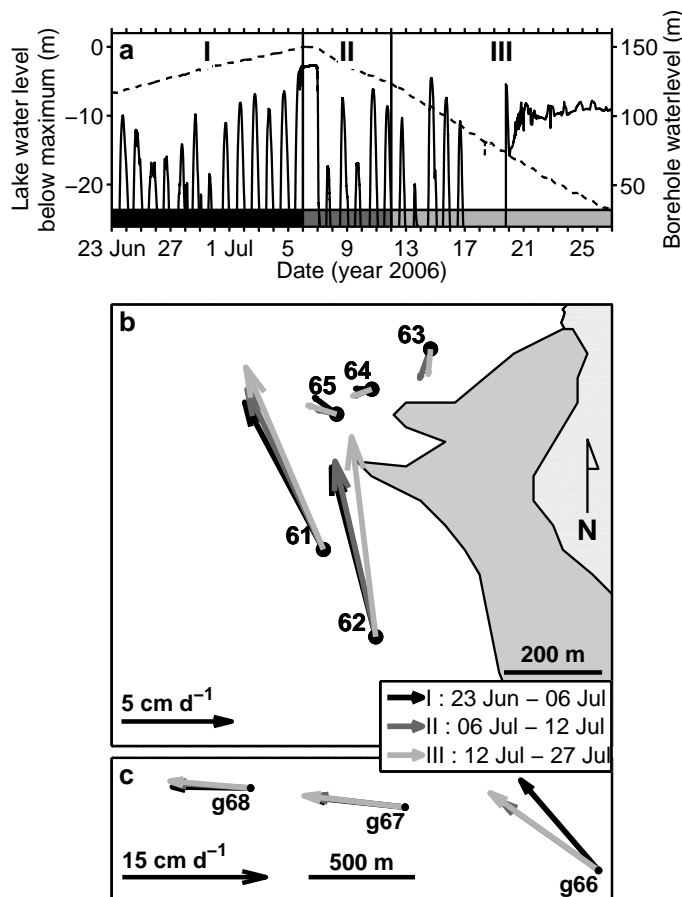


Figure 3.2: (a) Measured lake water level (dashed) and water level in the borehole *bh6* (solid) during the drainage of Gornersee in 2006. The drainage event is subdivided into the three intervals I – III as indicated by the shaded bars and vertical lines (thin solid). (b) Vector plot of horizontal flow velocities observed in the ice dam during the three intervals I – III. (c) Vector plot of horizontal flow speeds observed down-glacier of the ice dam during the three intervals I – III.

acting on the ice surface covered by the lake water. The load normal to an element face was calculated as the pressure  $p_f = \rho_w g (h_l - h_f)$ , where  $\rho_w = 10^3 \text{ kg m}^{-3}$  is the density of water and  $h_f$  is the mean elevation of the upper element face  $f$ , and  $h_l$  is the lake water level elevation.

### 3.4 Results (I): Observations

We observed perturbations of the ice flow within the ice dam of Gornergletscher during both lake drainage events (in 2006 and 2004; Figs 3.2 and 3.3, respectively). Each drainage event was analyzed in a discrete sequence of three successive time intervals: before (I), during (II) and towards the end (III) of the drainage. Figures 3.2a and 3.3a show the evolution of lake water level, and borehole water level as measured during the drainages of Gornersee. Vector plots of the flow velocities measured during the three intervals are shown in Figures 3.2b and 3.3b (ice dam), and in Figures 3.2c and 3.3c (down-glacier). Note that in the following we consider the unexpected drainage event first, and discuss the drainage of 2006 before the event of 2004.

### 2006 drainage event

On July 5 2006, the lake reached a volume of about  $4 \times 10^6 \text{ m}^3$  and had a water level that corresponded to overflow of the ice dam at the westernmost corner of Gornerssee. The overflowing water discharged into a small moulin located close to borehole *bh6* (Fig. 3.1). The superficial lake outflow filled the moulin and balanced the filling of the lake and the lake water level did not increase further until July 7, when it started to decrease. Between the lake and the drainage moulin, the lake water carved a gorge, 5 to 10 m wide, 100 m long and 30 m deep into the ice by the time the lake was fully drained. During the drainage period of more than 20 days, the rate of decrease of the lake water level was approximately constant. We consistently observed the water draining into the moulin shaft, so we assume that the lake drained completely via overflow into the moulin. It appears that no other significant subglacial connection existed. The borehole water level in *bh6* shows diurnal fluctuations with an amplitude greater than 80 m and with peak magnitude increasing from June 25 to July 5. The period of high water level without fluctuations between July 5 and 7 coincided with constant lake water level height, then the borehole water level dropped suddenly on July 7. This is consistent with the beginning of the lake water level decrease and initiation of the drainage of Gornerssee.

From the interval I to II (denoted as  $I \rightarrow II$ ) we observed a clockwise rotation of the flow vector and a slight increase in speed at the markers 61 and 62. In  $II \rightarrow III$  the rotation of the flow direction continued and flow speed increased again noticeably. Note that at marker 61 the rotation of flow direction proceeds gradually during  $I \rightarrow II \rightarrow III$ , whereas at marker 62 the incremental rotation in  $II \rightarrow III$  is more pronounced. For the intervals II – III, the measured flow velocities at 63–65 are insignificantly larger than in I. Down-glacier of the ice dam, markers g67 and g68 did not show any significant changes in flow direction. Marker g66 showed a counter-clockwise rotation in  $I \rightarrow II$  and a slight increase in speed in  $II \rightarrow III$  (Fig. 3.2c).

### 2004 drainage event

In 2004, the drainage began in a way similar to the 2006 event, i.e., following the overflow of the ice dam on July 1 (Sugiyama et al., 2007a). However, the superficial outflow ceased shortly afterward and by early morning of July 3 the lake water level decreased noticeably. Within five days (July 2 to 7), most of the lake water drained. We suspect that the lake water invaded the subglacial environment of Gornergletscher at the southwestern lake border (East of markers 41–42, Fig. 3.1b). Located close to *bh6*, two excavated en-glacial channels were observed during inspection of the lake floor after the drainage (Sugiyama et al., 2008). Unfortunately, in the evening of July 5, ice blocks broke the cable to the pressure transducer that was recording the lake water level, which resulted in the data stoppage (Fig. 3.3a). The borehole *bh430* in the central confluence indicates a clear perturbation of the subglacial conditions starting on July 2, when the amplitude of diurnal water level variations of about 150 m (interval I) abruptly changed to 25 m variations in the interval II. The water level remained at a consistently high level during most of the intervals II and III; meanwhile the lake water level went down. Then, the borehole water level abruptly dropped below 200 m on July 7, apparently marking the termination of the drainage. The diurnal oscillations in basal water level recovered again from July 9 onwards.

Figure 3.3b shows the measured flow velocities on the ice dam during the lake drainage of 2004. Note that markers 41 and 42 were located further away from Gornerssee than markers 61 and 62 (2006). In  $I \rightarrow II$ , the ice flow speed increased considerably and the flow direction rotated counter-clockwise (down-glacier) at 41 and 42. In the same interval, the flow speeds strongly increased at the markers g44 and 45 (Fig. 3.3b). In  $II \rightarrow III$ , the sense of rotation of the ice flow direction reversed towards Gornerssee at all markers 41 to 45. At markers 43–45, the rotation was so large in that the ice changed to flow directly towards Gornerssee. At the markers 42, 43 and g44, flow speeds were highest in interval III, whereas at 41 and 45 flow speeds decreased again after the maximum in II. Down-glacier of the ice dam the measured flow velocities increased by 20–70% during the interval II at all three locations g46, g47 and 48 (Fig. 3.3c). At markers g46 and g47, the increase in flow velocities was accompanied by a deflection

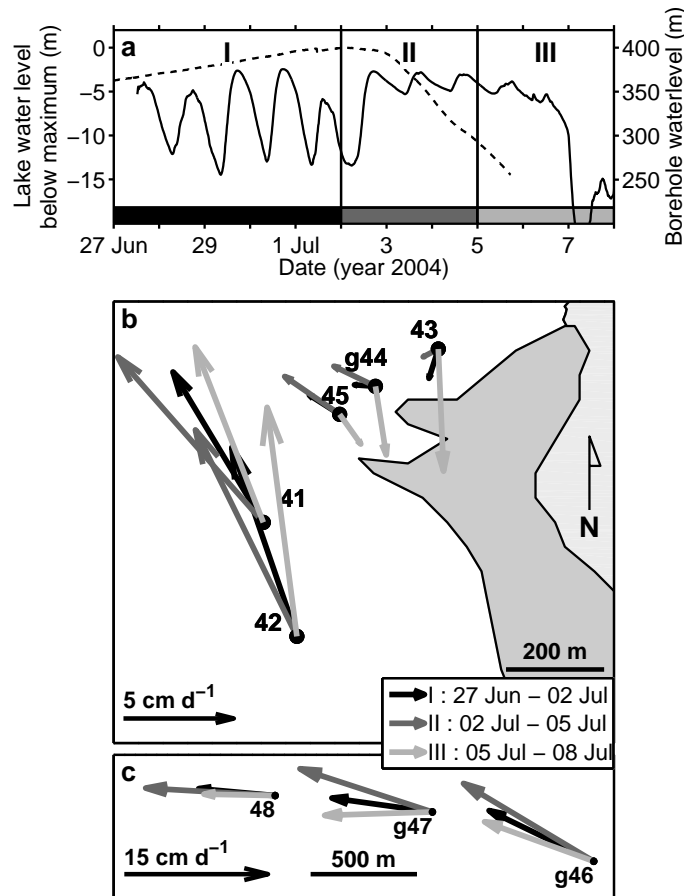


Figure 3.3: (a) Measured lake water level (dashed) and water level in the borehole *bh6* (solid) during the drainage of Gornersee in 2004. The drainage event is subdivided into the three intervals I – III as indicated by the shaded bars and vertical lines (thin solid). (b) Vector plot of horizontal flow velocities observed in the ice dam during the three intervals I – III. (c) Vector plot of horizontal flow speeds observed down-glacier of the ice dam during the three intervals I – III.

of the ice flow direction towards the north and subsequent return during interval III. In III, the flow speed decreased to a magnitude as in interval I at all three markers.

### 3.5 Results (II): Modeling

We conducted preliminary tests in order to clarify the model sensitivity to the applied boundary conditions and to estimate the errors due to numerical discretization. We varied the prescribed inflow boundary velocity distributions by both magnitude and orientation and affirmed that the computed flow regimes of Gornergletscher would not be compromised by those boundary conditions. We then constructed an additional mesh with higher vertical resolution (6105 elements, 11 layers) and verified the results of surface flow velocities. The model used is low-resolution but produces admissible horizontal surface flow regimes with requested minimal computation times. We performed many model runs (>2000) to systematically investigate how the free manipulation of  $C$  at different local patches of the bed layer affects the ice flow regime. Since the basal boundary condition (3.3.5) is linear, the variation in  $C$  operates on the magnitude of velocities, and changes in direction of the flow are caused mainly by influences of the geometry of Gornergletscher. Thus, although many degrees of freedom are introduced through the free manipulation of  $C$  in every cell of the bed layer, the low complexity of the basal condition ensured that

the model behaviour delivered reproducible results,<sup>1</sup>

### Initial flow conditions

For the subsequent simulations, an adequate flow field of Gornergletscher was required as initial configuration. To obtain the initial flow conditions, we optimized the computed flow solution based on all available surface flow speed observations for the period April to September 2006. The optimization was achieved by manually adjusting  $C$  in local subsets of basal elements. Varying  $C$  amounts to alteration of the model boundary conditions and produces systematic changes of the orientation and magnitude of the residual error vectors of the mismatch between observed and modeled flow velocities. The fitness of the distribution of  $C$  and the computed flow field is best estimated in terms of systematic errors and we seek a representative flow field where the length of the sum of normalized error vectors is minimal. The sum of normalized error vectors (SNE) is computed as

$$\mathbf{R} = \frac{1}{N} \sum_{i=1}^N \frac{\mathbf{v}_i^m - \mathbf{v}_i^c}{v_i^m}, \quad (3.5.1)$$

where  $\mathbf{v}_i^m$  is the measured horizontal flow velocity,  $\mathbf{v}_i^c$  is the computed equivalent, and  $v_i^m$  is the magnitude of the measured flow speed at the  $i$ th stake location of a total of  $N$  stakes. For a random distribution of error vectors  $\mathbf{R}_i$ , the length  $R = |\mathbf{R}|$  approaches zero when  $N \rightarrow \infty$  (Gudmundsson, 1999).

The initial flow field solution is given in Figure 3.4a, together with the settings of  $C$  of the bed layer elements in Figure 3.4b. For this flow field,  $R$  is 0.003. For comparison purposes,  $R$  is 0.112 for a distribution with uniform  $C=11.5 \text{ (MPa)}^{-1} \text{ a}^{-1} \text{ m}$ . The computed flow field is in good agreement with the observed one. The major discrepancies actually occur in the ice dam area on the side of Grenzgletscher tributary. Gudmundsson (1999) calculated flow fields for the confluence of Unteraargletscher and obtained similar residual discrepancies between modeled and observed flow regime in the confluence area, though the error vectors point towards the junction and not down-glacier. His model systematically overestimated the down-glacier component of the flow, whereas in our model it is underestimated. Although Gudmundsson's model did not incorporate basal motion, our results did not change when we excluded basal motion ( $C = 0 \equiv 10^{-8}$ ). However, the residual differences are not obstructive to the intended simulations. We provide additional remarks on those discrepancies in the discussion section.<sup>2</sup>

### 3.5.1 Modeling of the ice flow changes

Based on the initial flow field, we reproduced the flow velocities observed during the three intervals I to III of the two drainage events by considering the following two scenarios:

**Scenario 1:** The distribution of  $C$  presented in Fig. 3.4b remained unchanged. We applied a load of lake water pressure corresponding to the highest lake water level reached in the interval I, then reduced the lake water load in the drainage intervals II and III according to the decrease in lake water level measured during each period.

**Scenario 2:** The initial situation of interval I remained the same as in scenario 1, except that the lake water pressure was not considered at all. Flow field solutions for the two subsequent intervals II and III were obtained by readjusting  $C$  locally.

<sup>1</sup> There are no explicit arguments for the selection of the spatially varying  $C$  in the bed layer, as  $C$  is a free tuning parameter. However, because no non-linearity is considered in relation (3.3.5) of the bed layer, other influences than enhancement of the flow speeds are minimized. Distributions of  $C$  in the subsequent computations are justified if they can be reasonably related to the lake drainages and observed flow measurements, otherwise they might be considered as arbitrary modifications.

<sup>2</sup> The initial distribution of  $C$  is somewhat arbitrary. The discrepancies of observed to modeled flow velocities can only be compensated for by adjustment of  $C$  as it is the only tuning parameter. However, if the distribution of  $C$  would be totally irregular and random, it would not be justified. The distribution in Fig. 3.4 is more or less smooth. In most parts,  $C = 10\text{--}20 \text{ (MPa)}^{-1} \text{ a}^{-1} \text{ m}$  was set. Along the south-western border of Gornersee,  $C$  was modified to a higher degree, which is discussed in Sect. 3.6.

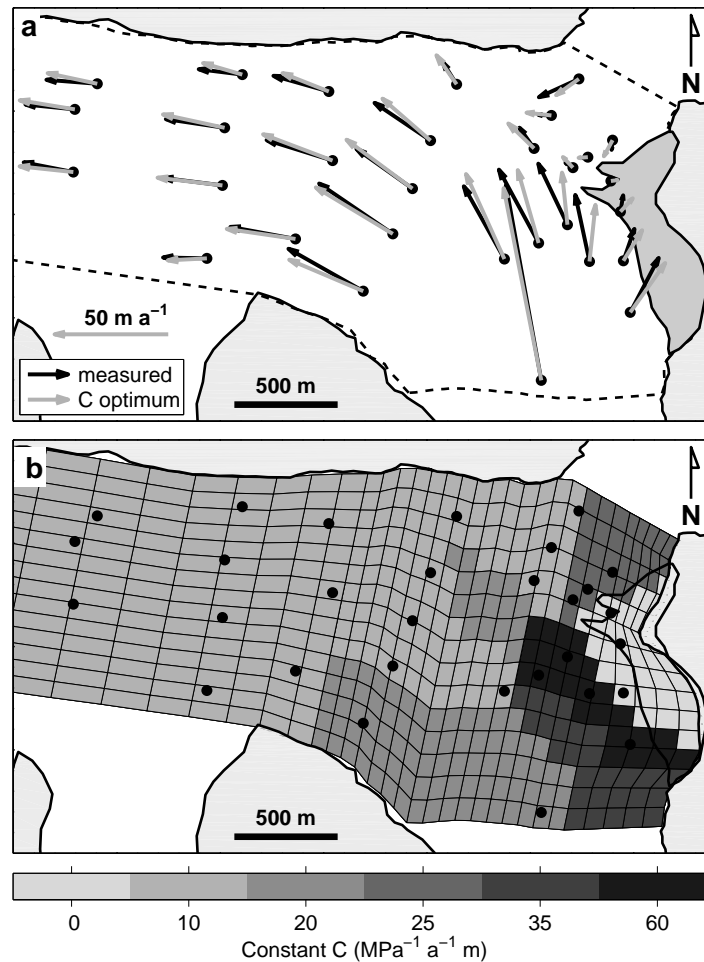


Figure 3.4: (a) Comparison of measured (black) and optimum calculated (grey) summer (2006) horizontal flow velocities at a set of  $N=30$  stakes. The model domain outline is indicated by a dashed line. (b) View from above of the bed layer elements and the spatial settings of the constant  $C$  used for the flow field computation in (a). The black dots correspond to the velocity measurement markers as in (a), and the outline of Gornerssee is indicated.

Note that in both scenarios, the computed flow changes result from the sequence of snapshots of flow regimes which conform to different prescribed boundary conditions of lake water pressure or various  $C$ -values. In the following we discuss the plausibility of the applied changes in the boundary conditions.

### Scenarios 1 and 2 for the drainage in 2006

In Scenario 1, when the lake water load is released, at markers 61 and 62 and, to a lesser extent, at marker 63, the ice flow direction rotates towards Gornerssee during I  $\rightarrow$  II  $\rightarrow$  III (Fig. 3.5a). Meanwhile, flow velocity magnitudes increase some fractional 2-5% at markers 62 and 63. When comparing the computed flow velocities according to scenario 1 (Fig. 3.5a) to those of the observations (Fig. 3.2b), we find agreement on the clockwise flow azimuth rotation for markers 61 and 62. However, in the model, the increase of the flow velocities at markers 61 and 62 in I  $\rightarrow$  II  $\rightarrow$  III is much less pronounced.

In the results of Scenario 2, the enhanced flow speeds at markers 61 and 62 in III can be better captured when changing the  $C$ -distribution of the bed layer elements in the vicinity of Gornerssee. The changes applied to  $C$  are depicted in Figure 3.5c and 3.5d, where the grey scale refers to the factor by which the value of  $C$  was increased or decreased relative to the initial configuration of Figure 3.4b. The increase of  $C$  (from 0 to 1 (MPa<sup>-1</sup> a<sup>-1</sup> m) in the lake area for interval II (Fig. 3.5c) and the increase of  $C$  by a

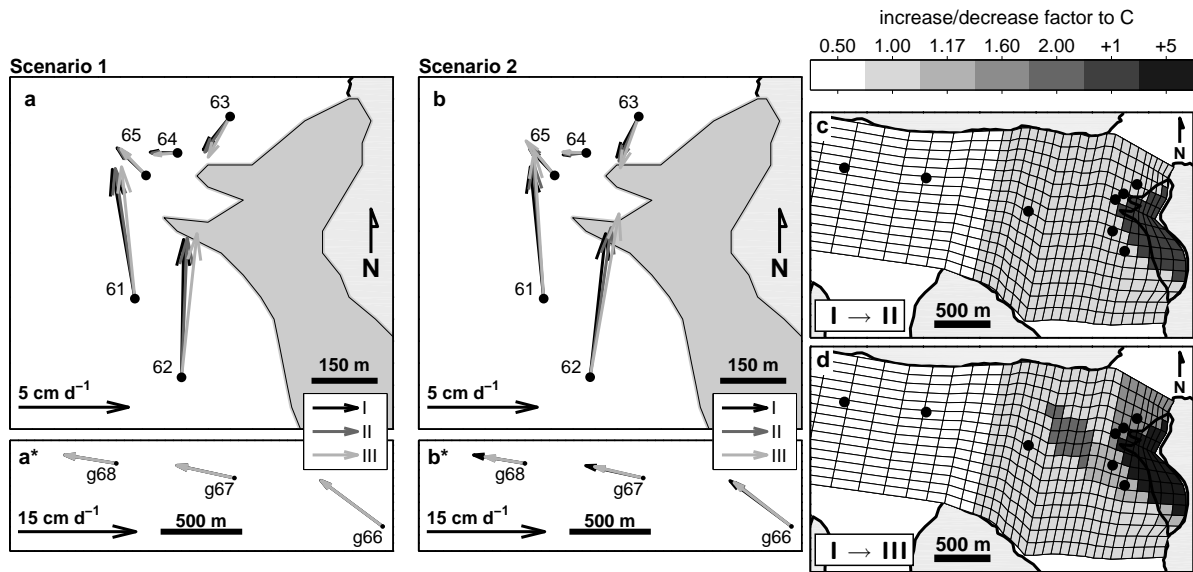


Figure 3.5: (a) Computed flow velocities from Scenario 1 for the 2006 lake drainage. The velocity of interval I includes the full lake water pressure, which is removed in two steps of -6 m and -18 m in the intervals II and III, respectively. (b) Computed flow velocities from Scenario 2 for the lake drainage in 2006. (c, d) Relative changes applied to the initial  $C$ -configuration (Fig. 3.4b) to reproduce the velocities of intervals II and III from Scenario 2 given in b. The changes are expressed in the factor of increase or decrease of  $C$ . The colors referenced to '+1' and '+5' indicate that  $C$  was set from zero ( $\sim 10^{-8}$ ) to 1 or 5.

factor of 1.6 along the southwestern border of Gornersee and by 2.0 in the central confluence (Fig. 3.5d) gradually enhance the flow velocities at markers 61 and 62 and match the observed speed increase during the sequence  $I \rightarrow II \rightarrow III$ . However, a change of flow direction, i.e., the rotation (clockwise) towards Gornersee, could hardly be introduced. We reduced  $C$  to half its value in the broad area down-glacier of the confluence area (Fig. 3.5c, d). The lowering of  $C$  relaxes the longitudinal coupling between the ice flow below the confluence and the ice dam area and decreases the down-glacier component of the ice flow in the ice dam area, hence the slight up-glacier rotation noticeable in  $I \rightarrow II \rightarrow III$ . The decrease of  $C$  below the confluence results in lower velocities at markers g68 and g67 (intervals II, III), which is inconsistent with the observations (Fig. 3.5b\* vs. 3.2c). It was not possible to obtain a distribution of  $C$  where the modeled flow velocities were fully consistent in both the ice dam area and down-glacier of the confluence because the rotation of flow directions in the ice dam area is less influenced by local enhancement/lowering of  $C$ . It was possible to modify the flow directions via use of the aforementioned (non-local) longitudinal coupling effect but this is barely supported by the observations.

#### Scenarios 1 and 2 for the drainage in 2004

The results from the model scenarios 1 and 2 corresponding to the drainage event of 2004 are given in Figure 3.6. In Scenario 1 where we considered only the release of lake water pressure acting on the ice surface, the impact is minor, also at markers 41 and 42 (Fig. 3.6a). This is because the locations of markers 41 and 42 were about 100 m to the west of their equivalents 61 and 62 in 2006. At this distance from the lake, the influence of the lake water pressure becomes small. The changes in flow speed and direction observed in  $I \rightarrow II \rightarrow III$  (Fig. 3.3b) cannot be reproduced in Scenario 1. The markers are situated beyond the noticeable influence of the lake water pressure. This indicates that counter-clockwise excursion of the flow direction from I to II, observed at the markers 41 to 45, does not relate to the influence of the lake water pressure.

In Scenario 2 (Fig. 3.6b, b\*) we captured the dominant speed increase of  $I \rightarrow II$  in the modeled flow

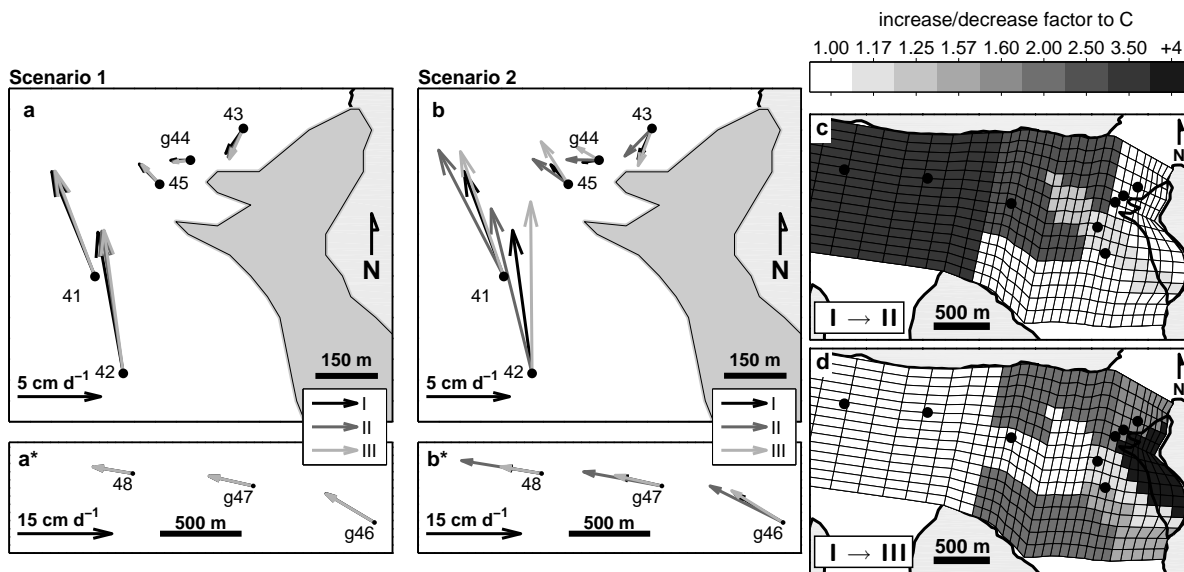


Figure 3.6: (a) Computed flow velocities from Scenario 1 for the 2004 lake drainage. The velocity of interval I includes the full lake water pressure, which is removed in two steps of  $-14$  m and  $-10$  m in the intervals II and III, respectively. (b) Computed flow velocities from Scenario 2 for the lake drainage in 2004. (c, d) Relative changes applied to the initial  $C$ -configuration (Fig. 3.4b) to reproduce the velocities of intervals II and III from Scenario 2 given in b. The changes are expressed in the factor of increase or decrease of the multiplier  $C$ . The color referenced to '+4' indicates that the multiplier  $C$  was set from zero ( $\sim 10^{-8}$ ) to 4.

velocities, as featured at markers 41, 42, g44, 45 and g46 to 48. The changes applied to  $C$  for  $I \rightarrow II$  are given in Figure 3.6c. On the southwestern border of Gornersee,  $C$  was increased by a factor 1.2 and down-glacier of the ice dam by 2.5 to 3.5. The area of enhanced basal motion thus incorporates the southwestern border of Gornersee and extends northwest into the central confluence and northern part of Gornergletscher and then down-glacier to the lower tongue. Though we have only shown three marker locations situated along the center flowline, other measurements confirm that the observed speed-up of  $I \rightarrow II$  (Fig. 3.3c) takes place across the whole width of the lower tongue.

In interval III we restored  $C$  to its initial setting in the area down-glacier of the ice dam (Fig. 3.6d). Note that this would result in flow speeds at markers 41 and 42 similar to interval I (Fig. 3.6b, b\*). To be consistent with the observations of interval III, we must retain enhanced flow velocities while the ice flow direction rotates up-glacier (clockwise) at those markers. This was achieved by further enhancement of  $C$  in the lake vicinity and along the inflow tributaries of Grenzletscher and Gornergletscher (Fig. 3.6d).

## 3.6 Discussion

### Mismatch of initial flow field in the ice dam area

In the computation of the initial flow field configuration, the largest discrepancies between modeled and measured flow velocities occurred in the ice dam area. Everywhere else the agreement between measured and observed velocities was good. We observed that the orientation of flow velocities in the ice dam area was significantly better matched when (i) increasing  $C$  considerably in the lower reaches of Gornergletscher, and/or (ii) increasing the vertical resolution of the model. The effect of (i) was an intensified longitudinal coupling between the ice dam area and the lower tongue, so the ice was pulled down-glacier. We know that on Gornergletscher the ice viscosity and thus the flow regime are influenced by a massive core of cold ice which is advected down-glacier along the center flowline of Grenzletscher

(Eisen et al., 2009). This was not considered in our model, but we speculate that cold rigid ice along the glacier central flow produces a drag on the ice dam area. An increased vertical resolution (11-layer mesh) further reduced the mismatch between measured and computed flow velocities in the dam area but was not considered due to inferior computational efficiency.

### Scenario modeling

We considered two mechanisms by which the drainage of an ice-marginal lake affects the ice flow of the adjacent glacier: the load and release of lake water pressure arising from the filling and drainage, and enhanced basal motion caused by the subglacial drainage. We observed the simultaneous change in flow directions and increase of flow velocities at markers 61 and 62 during the lake drainage 2006. In the modeling of those flow changes, when considering only the effect of decreasing lake water pressure, we were not able to capture the observed speed increase; not even when modifying the  $C$ -distribution and thus influencing basal conditions, the observed rotation of the ice flow could be reproduced. In Figure 3.7, we display a third scenario for 2006, in which the release of lake water pressure is combined with adjustments of  $C$ . In this case, we were not required to modify  $C$  below the confluence to reproduce the observed up-glacier clockwise rotation, as this event is now attributed to the impact of the lake water pressure. Besides the two initial days of the drainage, neither the borehole water level measurements in *bh6* and in other boreholes (e.g. Werder and Funk, 2009), nor the monotonic flow velocities observed below the ice dam (Fig. 3.2c) indicate the spreading of a pronounced subglacial perturbation. The subglacial conditions were likely affected close to the region where the moulin shaft reached the glacier bed, which we estimate to be somewhere between *bh6* and marker *g66* (Fig. 3.1). In the combined scenario, the essential changes of  $C$  do correspond to that location, so we assume that enhanced basal motion only played a role local to the ice dam area in the case of the 2006 lake drainage. We showed that the rotation of the ice flow due to decreasing lake water pressure yields the correct changes in flow direction and is a controlling mechanism affecting the ice flow in the ice dam area. For the Gornersee drainage in 2006, the observed flow changes found in  $I \rightarrow II \rightarrow III$  are thus caused by the release of the lake water pressure acting on the ice and locally enhanced basal motion. Due to the slow, superficial drainage of 2006 and the absence of a pronounced subglacial perturbation, the effect of the release of lake water pressure could be identified.

In interval II of 2004, the borehole water level in *bh430* was high and then decreased monotonically between July 5 to 7, dropping sharply on July 7. Also, in the ice dam the basal water pressure was high before July 6 (Sugiyama et al., 2008, Fig. 7). In interval II, the lake water presumably overcharged the subglacial drainage system of Gornergletscher and is certainly responsible for disturbed subglacial conditions, inducing broadly enhanced basal motion. For  $I \rightarrow II$ , the observations of strongly increased flow velocities in both the ice dam area and the lower tongue can be corroborated with the plausible modeling results (Fig. 3.6b-c). We assume that the lake water influenced the ice flow during the drainage of 2004 in a similar manner as in 2006 as the maximum lake water level was similar at the two drainage events. Nevertheless, the results indicate that the markers 41 and 42 were less influenced by the lake water due to the increased distance from Gornersee and also because the impact of enhanced basal motion was overwhelming. The reversal in flow direction with an almost complete switch in flow direction from west to (south-)east was observed in  $II \rightarrow III$  (Fig. 3.3b), i.e., at *g44* and *45*. This feature is absent in the model results. Also, we do not think the further enhancements applied to  $C$  in Figure 3.6d provide a plausible interpretation for  $II \rightarrow III$ . In the current model, we could not find an appropriate configuration of the constant  $C$  to reproduce these changes. The linear relation in the basal boundary condition may be insufficient. Errors in the bed topography may also play a role. Referring to the same part of the ice dam and the drainage in 2004, Sugiyama et al. (2007a) mentioned that changes in longitudinal stress can produce the reversal of the ice motion, but changes in basal conditions (basal motion and separation, sediment deformation) did not provide a sufficient explanation. Sugiyama et al. also mention that the reverse motion correlates with the increase or decrease in lake discharge, which is closely connected to the lake water level. We conjecture that the flow change  $II \rightarrow III$  with the unexplained observations

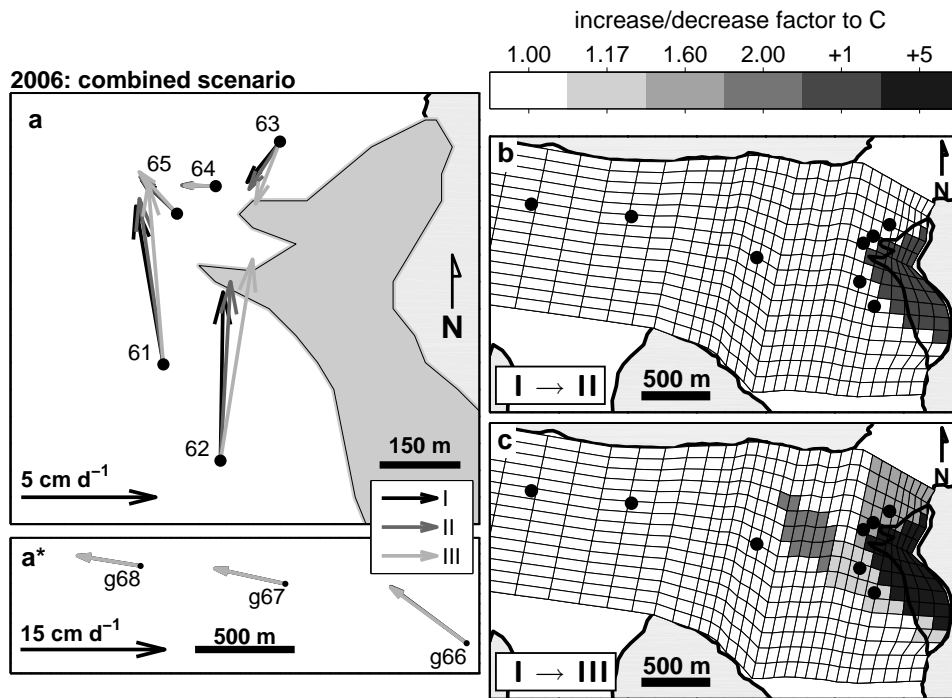


Figure 3.7: (a) Computed flow velocities for a combined Scenario in 2006. The velocity of interval I includes the full lake water pressure, which is removed in two steps of -6 m and -18 m in the intervals II and III, respectively. (b, d) Relative changes applied to the initial  $C$ -configuration (Fig. 3.4b) to reproduce the velocities of intervals II and III. The colors referenced to '+1' and '+5' indicate that  $C$  was set from zero ( $\sim 10^{-8}$ ) to 1 or 5.

at markers 43-45 may be influenced by further implications due to the effect of lake water pressure not captured in the current model. When the lake fills to its maximum possible size as in both 2006 and 2004, the lake water pressure can perturb the ice flow at a distance of up to 300 m from Gornersee. The lake emptied significantly faster in 2004 than in 2006. In 2004, the lake drained in less than five days, whereas in 2006, the drainage took place over 20 days. The rate of decrease of the lake water level, the change of stress conditions in the ice dam and fracturing of the ice further influence the ice in the lake vicinity. It may be worthwhile to analyze the ice flow as part of a transient study considering a time-dependent, possibly elastic response of the ice to explain the presence (absence) of the reversal in flow direction at markers 43-45 (63-65) in 2004 (2006) with variable loading/unloading test cases.

### 3.7 Conclusion

We studied ice flow changes on Gornergletscher during two drainage events of Gornersee in 2004 and 2006. We used a three-dimensional numerical flow model and produced scenarios of ice flow changes through adjusting the boundary conditions of spatially non-uniform basal motion and loading/unloading of lake water on the ice covered by the lake.

For each drainage event, we compared the results of the numerical experiments to our observations and identified the major mechanism generating the flow observations. The slow lake drainage of 2006 had a minor, local impact on the basal conditions and the ice flow changes were dominated by the release of the lake water load. In 2004, the draining lake water rapidly entered the subglacial environment and perturbed the basal conditions, locally enhancing basal motion of Gornergletscher.

The lake water pressure acting on the ice surface of the adjacent ice dam has not, until now, been con-

sidered as having a relevant influence on the ice flow during a glacial lake drainage event so far. We demonstrated that changes in lake water pressure load do have a notable and varying effect on the ice flow. The lake water pressure also affects the local stress conditions in the ice dam. Further experiments investigating the response of the ice dam to variable time-dependent loads and enhanced constitutive properties of the ice (i.e., elasticity, damage) may provide further information on the role of the ice dam.

## Chapter 4

# Surface ice motion of Gornergletscher measured with an interferometric radar

This chapter is published in a slightly modified form as:

Riesen, P., Strozzi, T., Bauder, A., Wiesmann, A., and Funk, M. (2011). Short-term surface ice motion variations measured with a ground-based portable real aperture radar interferometer. *J. Glaciol.*, 57(201):53-60.

**Abstract** We report measurements using a portable real aperture radar (Gamma Portable Radar Interferometer, GPRI) for interferometric imaging of the surface ice motion on Gornergletscher, Switzerland, during the drainage of the adjacent ice-marginal lake Gornersee. The GPRI tracked the surface ice motion in line of sight over an area of  $\sim 3 \text{ km}^2$  down-glacier of Gornersee almost continuously during the drainage event. The displacement maps derived from the acquired interferograms capture the spatial distribution of the surface ice motion. Due to fast acquisition times of the microwave images, the GPRI was able to record sub-daily variations of the ice displacements, most likely caused by the impact of the Gornersee drainage on the ice motion of Gornergletscher. In-situ point measurements of the ice displacement agree reasonably well with the results obtained by the GPRI and highlight the use of the GPRI for high-resolution measurements of glacier surface ice motion.

### 4.1 Introduction

Variations in surface ice motion within hours to a day have been observed on numerous glaciers (e.g. Iken, 1977; Sugiyama and Gudmundsson, 2004). To analyze such behaviour, an important aspect is to obtain accurate information on the surface ice motion. Traditional standard geodetic methods such as differential GPS or optical laser measurements (i.e. an automated tachymeter) are state of the art in field glaciology and have been applied in numerous studies. With these methods, detailed temporal information on the ice displacement at local observation points on the glacier can be obtained. To analyze the ice-flow regime of a glacier one usually requires a network of observation points equipped with optical mirrors or GPS receivers. The setup and maintenance of such a flow survey network can become costly if the target glacier is large and possibly difficult to access. For 20 years, space-borne interferometric synthetic aperture radar (InSAR) imaging has been successfully used to observe surface elevation (i.e. generation of digital elevation models) and the flow of ice streams and ice sheets in remote areas such as Antarctica and Greenland (e.g. Fahnestock et al., 1993; Joughin et al., 1995, 1996, 1998; Mohr et al., 1998; Bamber et al., 2000). In those studies, differential repeat-pass interferometry techniques (D-InSAR) were mainly used (Bamler and Hartl, 1998). Nowadays, space-borne SAR imagery can resolve cells as low as a few m in azimuth and ground range directions. Notably, the investigation period is restricted to the time the satellite passes and revisits the target on appropriate orbits, which limits temporal resolution to one or several particular days (ESA, 2007).

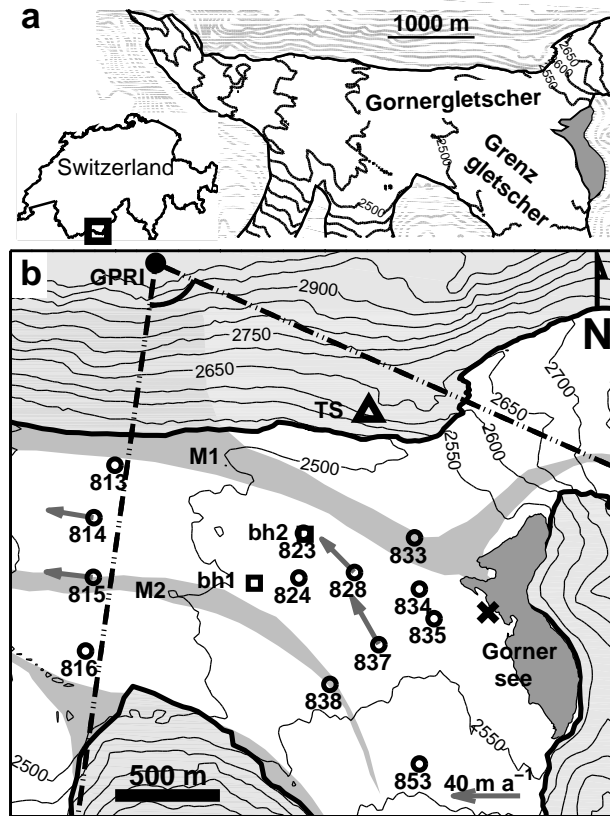


Figure 4.1: (a) Geographic position of the field site with overview of the tongue of Gornergletscher with 50 m surface elevation contours and Gornersee (dark grey). (b) Detailed map of the study area on Gornergletscher with 50 m surface elevation contours, debris covered moraines M1 and M2 (grey), local ice displacement measurement points (circles), site of GPS reference and tachymeter (triangle TS), boreholes bh1 and bh2 for water level measurements (squares), GPRI location (dot), scan-sector (dot-dashed), and location of an excavated subglacial drainage channel (cross). The arrows at markers 814, 815, 828 and 837 indicate annual ice flow velocities.

Here we apply a novel ground-based and portable real aperture radar device (Werner et al., 2008) for interferometric imaging of the surface ice motion of an Alpine glacier. The Gamma Portable Radar Interferometer (GPRI) is able to acquire phase signal images of the observation area at a repeat interval as low as 20 min. We employed the GPRI on Gornergletscher, Switzerland (Fig. 4.1a) in order to monitor sub-daily to daily variations of the surface ice motion of Gornergletscher. These variations in surface ice motion were triggered by the subglacial drainage of the adjacent marginal, ice-dammed lake Gornersee. We present ice displacement maps derived from the GPRI interferograms and analyze the performance of the radar device for remote sensing of surface ice motions of a glacier on spatial and temporal scales lower than in conventional D-InSAR applications. We compare the radar displacements against local in-situ ice displacement measurements. To complete the study, a brief discussion of the observed displacements in relation to the drainage phenomena is given.

## 4.2 Field Methods

Gornergletscher is located in southern Switzerland and is the name-giving tributary to the ablation tongue formed by the confluence of Gornergletscher and Grenz gletscher (Fig. 4.1). Gornergletscher features two distinct moraines (M1 and M2 in Fig. 4.1b) of which the medial moraine M1 is severely displaced to the northern margin of Gornergletscher due to the thinning and decreased mass delivery from Gorner-

Operating frequency	17.2 GHz
Wavelength	0.0176 m
Acquisition time	< 20 min
Operational range	0.1 - 6 km
Antenna fan-beam	0.4 × 60°
Transmit bandwidth	200 MHz
Range resolution	0.75 m
Azimuth length	2.06 m
Azimuth resolution	14 m at 2 km
Precision	2 mm along look direction

Table 4.1: Key characteristics of the Gamma Portable Radar Interferometer (GPRI)

gletscher tributary. At the junction of the two tributaries, about 5 km upstream of the terminus, the ice-marginal lake, Gornersee is located (Fig. 4.1b). The yearly subglacial drainage of Gornersee by the adjacent Gornergletscher was investigated extensively during the years 2004 to 2008 (Huss et al., 2007; Sugiyama et al., 2007a, 2008; Walter et al., 2008; Werder et al., 2009; Werder and Funk, 2009; Riesen et al., 2010).

#### 4.2.1 Surface ice motion measurements

We installed the GPRI during the drainage of Gornersee in June 2008 and surveyed the surface ice motion of Gornergletscher across an area of about 3 km<sup>2</sup> of the glacier surface downstream of Gornersee. As the radar was in operation, we carried out in-situ ice displacement measurements at 13 marker positions located approximately within the target survey area.

The GPRI was constructed by Gamma Remote Sensing (GRS). It operates at 17.2 GHz, which is higher than the space-borne SAR operating frequency of 1 to 10 GHz. Detailed characteristics of the GPRI are summarized in Table 4.2.1. The GPRI is designed as a portable system, the device is mounted on a tripod and is promptly installed in remote areas, provided power supply can be ensured. The GPRI acquires a microwave image of the target area of 90° azimuth range in about 20 min. The device carries a secondary receiver antenna at slightly different look direction than the primary antenna. The simultaneous acquisition of pairs of microwave images permits generation of a DEM of the surveyed topography alongside the displacement measurements.

The analysis of the GPRI microwave images follows differential interferometry processing techniques (e.g. Bamler and Hartl, 1998; ESA, 2007), which includes phase-unwrapping, filtering, conversion of the phase-difference signal to scalar displacements, and geolocalization. All these tasks were carried out by GRS. Multiple subsequent images can be integrated into an interferogram as long as the images remain sufficiently coherent. In this way, GRS produced displacement maps based on 5 h interferograms.

In space-borne InSAR imaging the device is located high above the target. Thus, the vector of the line of sight direction (LOSD) is dominated by the elevation difference between satellite and ground, and is assumed to be the same for all resolution cells (interferogram pixels) of the interferogram, since the lateral extent (azimuthal and ground range) is much smaller. For ground-based interferometry using the GPRI, this does not apply, since the elevation difference between device and target area may be similar or smaller than the operational range. Thus, for the ground-based GPRI survey, each resolution cell is assigned an individual LOSD vector on which the phase signal is determined.

We intended to monitor the spatial variations of the ice motion at the ice dam (the confluence area in the vicinity of Gornersee). The radar was targeted at the principal area at a distance of 0 to 1200 m from Gornersee, laterally confined by the two moraines, M1 and M2 (Fig. 4.1b). In the same area the in-situ ice displacement measurements were carried out. Figure 4.1b shows the locations of 13 markers set up

for the local ice motion measurements; for orientation purposes the mean annual ice flow directions are indicated in the primary target area at stakes 837 and 828.

The markers used for the in-situ ice-displacement measurements were ice-anchored aluminum poles equipped with optical mirrors. From the mirror reflectance pattern of each marker, the tachymeter automatically determined azimuth and relative distance at a sampling interval of 1 h. The readings were corrected for atmospheric refraction by using fixed reference markers installed at known positions along the glacier margin, thus covering different distances and azimuth directions. From the angular records and the known position of the tachymeter, the positions of the markers and the resulting displacement trajectories were calculated. The accuracy of the positions estimates is about  $\pm 5$  cm. A detailed account of the survey technique and associated error estimates is given by Gudmundsson et al. (2000) and Riesen et al. (2010).

In order to compare the in-situ measured displacements to the displacements observed by the radar, we chose nine reference markers (823, 824, 828, 833-835, 837-838, 853) at which we additionally installed corner reflectors. This enabled identification of the marker locations in the radar interferograms, as the steel panel reflectors are highly reflective.

Three markers, viz. 824, 834 and 837 (Fig. 4.1b), were equipped with GPS receivers (Leica GPS500) instead of optical mirrors. Simultaneously, a fixed GPS reference site, located close to the tachymeter, was operated. We performed a differential GPS analysis and processed the data in kinematic mode with a sampling interval of 2 min using the software, "Track" (Chen, 1998; King, 2004). The accuracies of the positions estimated by kinematic GPS are on the same order as those estimated optically by the tachymeter (Riesen et al., 2010). The exact positions of the tachymeter, the GPS reference station and the GPRI were determined with GPS precise point positioning (PPP) (Natural Resources Canada, 2008). In this way, a consistent frame of reference for all position estimates was provided, minimizing translation errors.

In addition, an ultrasonic ranger device was operated at the location of marker 837, continuously measuring surface ablation during the lake drainage/radar survey time. Each day, we also recorded the local ice melt at each of the marker locations. The ice surface motion measurements were supplemented by measurements of subglacial water pressure in boreholes, which were drilled to the glacier bed and equipped with pressure sensors.

## 4.3 Results

### 4.3.1 Drainage of Gornersee

Gornersee filled continuously until 20 June when, at 7am (CEST), a decrease of lake water level was noticed. Indeed, the lake water level started to decrease around midnight of 20 June (Fig. 4.2). Gornersee drained more and more rapidly and emptied in less than 4 d. After the lake was fully drained we inspected the lake basin and detected a large channel ( $>15$  m diameter) at the southwestern lake shore plunging into the ice of Grenzgletscher in the southwest direction (Fig. 4.1, cross). The level of the channel roof was  $\sim 5$  to 10 m lower than the surface elevation of the surrounding ice dam.

Before 14 June, the water level in the boreholes, bh1 and bh2 synchronously fluctuated diurnally with comparable amplitude (Fig. 4.2). On 15 June, the water level in borehole bh1 dropped almost 100 m, continued to oscillate diurnally, and then rose again sharply on 17 June, remaining at high level until 23 June. In borehole bh2, the diurnal oscillations were interrupted on 15 June and the water level increased slowly until 23 June without significant fluctuations. From 23 June onwards, the water level started to fluctuate again diurnally, with large amplitude variation in borehole bh1, and small amplitude variation in bh2.

These observations suggest the subglacial drainage system was undergoing some change already before the decrease of lake water level was observed on 20 June. Presumably, the disruption of the diurnal

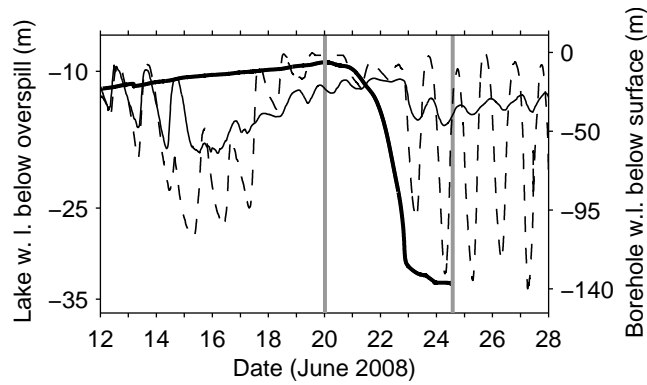


Figure 4.2: Evolution of lake water level (thick solid curve) of Gornersee and water level (w.l.) in boreholes bh1 (dashed curve) and bh2 (thin solid curve). The interval between the two vertical lines (solid grey) marks the duration of the lake drainage.

borehole water level fluctuations on 15 June and the successive increase of the water levels were caused by lake water subglacially leaking from Gornersee prior to the superficial decrease of lake water level on 20 June. We suppose, the leakage developed into a subglacial channel, which accomplished the complete drainage of Gornersee within 4 d (20 to 24 June). Most likely, the aforementioned excavated channel was the opening of this major drainage channel.

### 4.3.2 Surface ice displacements

The GPRI was in operation between 21 June, 8pm and 25 June, 12am. Due to failure caused by current peaks in the power supply, the device did not operate between June 23, 9am, and June 24, 6pm. From 55 h of operation time we obtained 44 h of useful data, which corresponds to 133 20 min interferograms. As main product, GRS produced several 5 h interferograms from these data.

In Figure 4.3, the displacement maps derived from six 5 h interferograms are presented. The corresponding acquisition time information is given in Table 4.2.

In the map of Figure 4.3a, the displacement pattern resembles a typical map of glacier flow velocities, i.e. the largest displacements are located up-most on Grenzgletscher. The displacement magnitude decreases along the moraine M2 (in the along-flow direction) and towards the margins (in the cross-flow direction). Generally, the ice moves towards the GPRI (positive displacements). But down-glacier of the confluence area where the LOSD becomes aligned normal to the principal direction of the ice motion (now to the west), the GPRI did not detect any motion. In Figure 4.3c, i.e. on the evening of 20 June, the situation changed significantly. Below the confluence, strong negative displacements were recorded between the two moraines, M1 and M2. Along the LOSD in the cross-flow direction, a transition of negative to positive displacements occurs across the moraine M2. This displacement anomaly is also present in Figure 4.3d and then starts to diminish in Figure 4.3e. In the confluence/ice dam area, i.e. the

Map	Start Time (CEST)	End Time (CEST)
a	21 June 10:29 pm	22 June 03:49 am
b	22 June 12:27 pm	22 June 05:37 pm
c	22 June 08:01 pm	23 June 00:52 am
d	22 June 10:51 pm	23 June 03:43 am
e	23 June 03:19 pm	23 June 07:41 am
f	25 June 03:00 am	25 June 08:11 am

Table 4.2: Acquisition time periods for the 5 h interferograms underlying the displacement maps of Figures 4.3a-f

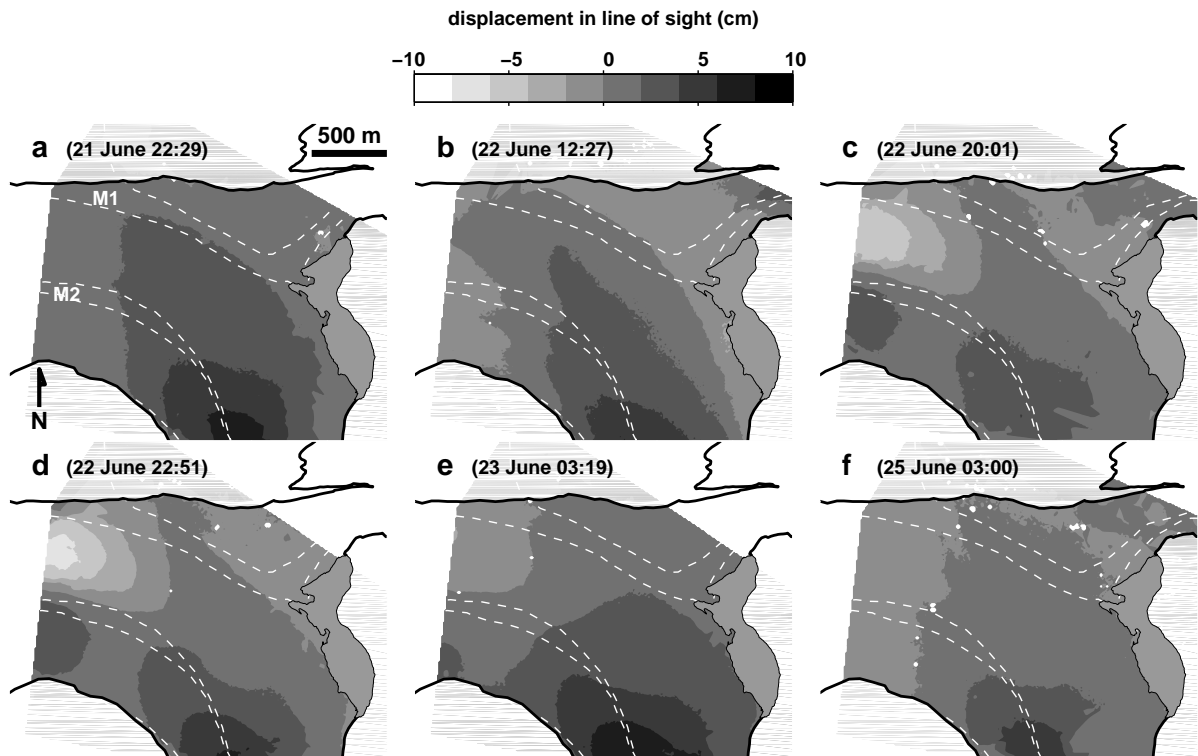


Figure 4.3: (a-f) Displacement maps derived from six 5 h interferograms. Negative displacement is away from the radar on the line of sight direction (LOSD) whilst positive displacement is towards the radar on the LOS. Dashed white curves indicate the side margins of the moraines, M1 and M2. Date and start times are indicated

primary target area, the observed displacements were small and varied marginally. We expected to record larger displacements in the ice dam area according to other drainage events from the previous years, 2004 and 2007 (e.g. Sugiyama et al., 2007a), in which the surface ice motion regime was perturbed more conspicuously. In summary, we observed two clear signals: minor displacements and changes in the confluence and lake vicinity area, and striking displacement variations down-glacier below the confluence area.

### Comparison to in-situ measured displacements

In the following, we refer to the displacements measured by the radar as *observed* displacements, whereas the displacements obtained from in-situ markers are referred to as *measured* displacements. The corner reflectors attached to the nine reference markers already mentioned were easily identified in the interferograms due to the high reflectivity of the steel panels. The flow velocities of Gornergletscher in the target area are below  $1 \text{ m d}^{-1}$ , thus, none of the markers was displaced more than 0.7 m in any direction while any interferogram was integrated. Thus, for localization of the corner reflector positions in the radar interferogram, the locations of the markers were treated as constant. Therefore, each marker location corresponded to the interferogram pixel in which the reflection from the corner reflector was identified. During a 5 h interferogram interval, five positions of a marker were usually measured by the tachymeter, whereas at a marker equipped with a GPS receiver, 150 data points were acquired during the same time span. From the array of  $j = 1 \dots N$  measured positions at a marker, denoted as vector  $\mathbf{x} = x_i^j$ , we determined the actual measured 3D displacement vector during the interferogram (IF) time,  $\Delta t_{IF}$  as

$$\mathbf{d}_m = \mathbf{v} \Delta t_{IF}, \quad (4.3.1)$$

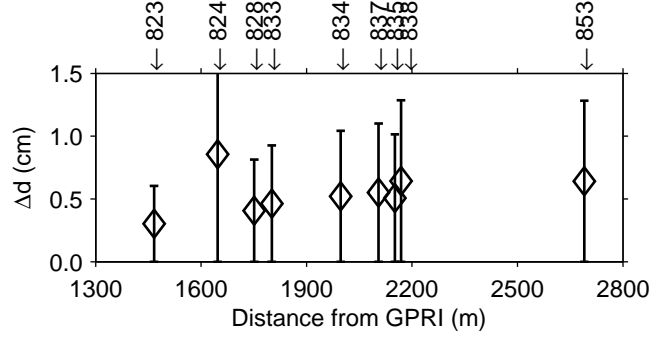


Figure 4.4: Mean values of the absolute differences ( $\Delta d$ ) between the 'observed' displacement (as measured by the GPRI in line of sight direction, LOSD) and 'measured' displacement (as obtained at the in-situ marker positions and projected onto LOSD) from the six 5 h interferograms at each of the nine reference markers. Error bars correspond to 1 standard deviation.

where  $\mathbf{v}$  is the velocity vector, of which the components,  $v_i$  were estimated as least-square fits of linear polynomials,  $x_i^j = v_i t_i^j$  to the data points,  $\mathbf{x}$  in each of the spatial components  $i \in [1, 2, 3]$ .

For each marker, we computed the LOSD unit vector  $\mathbf{e}^*$  as the normalized difference between the position of the GPRI and the average of the measured positions. Projecting  $\mathbf{d}_m$  onto  $\mathbf{e}^*$  yields the scalar component of  $\mathbf{d}_m$  in the direction of the line of sight as

$$\mathbf{d}_m^* = \mathbf{d}_m \cdot \mathbf{e}^*, \quad (4.3.2)$$

which can be directly compared to the observed displacements of the GPRI. However, it was not guaranteed that at every marker all points ( $N=5$ ; or  $N=150$  for GPS markers) were available, as sometimes data points were missing due to malfunction or low visibility. Because the in-situ measurements were sometimes sparse at several marker locations, we decided to compute the displacement vector at a marker from the acquired positions within the interferogram time enlarged by additional  $\pm 3$  h of buffering time. In this way, a few more data points, acquired before and after the 5 h interferogram interval, were incorporated, increasing  $N$  slightly. Due to the uncertainties of the individual marker position estimates, the estimate of a displacement vector from these very sparse data points might not be representative. Using an enlarged time interval with more data points and fitting the velocity vector using equation (4.3.1) to the data improves the estimate, provided the time interval is not enlarged too much. This is the reason why we fitted a velocity vector to the data and then scaled the velocity by the interferogram time  $\Delta t_{IF}$ , to estimate  $\mathbf{d}_m$  in equation (4.3.1). We tried different lengths of additional buffer time and found that the agreement between  $\mathbf{d}_m^*$  and the observed displacement from the GPRI (denoted henceforth by  $d^*$ ) is best when using  $\pm 3$  h of buffer time (section "Error Analysis").

### Ablation correction

Changes of the ice surface motion of Gornergletscher in June are a combination of ice displacement and surface melt. From the diurnal melt signal of the ultrasonic ranger and the local melt measurements at each marker we constructed simple melt functions to estimate the melt component during an interferogram. The (negative) melt component could then be added to  $\mathbf{d}_m$  of each marker if desired.

### Verification and Error Analysis

In the following, we compare the scalar projections,  $\mathbf{d}_m^*$  of the marker displacements against the displacements extracted from the GPRI maps (= distribution of  $d^*$ ) by quantifying the discrepancies,  $\Delta d = |\mathbf{d}_m^* - d^*|$  in detail. In Figure 4.4, we depict the mean of  $\Delta d$  from the six available displacement

Ablation correction	filtered Interferogram	unfiltered Interferogram	Error estimates (cm)
	×		$\bar{\sigma}=0.16$ , $\bar{e}=0.54$
×	×		$\bar{\sigma}=0.26$ , $\bar{e}=0.62$
		×	$\bar{\sigma}=0.31$ , $\bar{e}=0.65$
×		×	$\bar{\sigma}=0.33$ , $\bar{e}=1.12$

Table 4.3: Mean standard deviations,  $\bar{\sigma}$  and mean absolute errors,  $\bar{e} = \overline{|\Delta d|}$  of the differences between 'observed' displacement (as measured by the GPRI in line of sight direction, LOSD) and the 'measured' displacement (as measured at the in-situ marker positions and projected onto LOSD). The values refer to the results when different data combinations as indicated by the crosses are used.

Marker	$\overline{d_m^*}$ (cm)	$\bar{e}$ (cm)	$\bar{e}_r$ (%)	$\alpha$ (°)
853	4.52	0.64	14.2	17.2
823	1.43	0.30	21.2	36.5
838	2.94	0.64	21.8	6.4
828	1.79	0.41	22.7	16.2
837	2.17	0.55	25.3	2.2
835	1.88	0.51	27.0	15.4
834	1.68	0.52	31.1	6.7
824	1.24	0.86	69.2	37.8
833	0.10	0.46	467.2	21.5

Table 4.4: Mean values of observed absolute displacements,  $|\overline{d_m^*}|$ , mean absolute errors,  $\bar{e} = \overline{|\Delta d|}$  and mean relative error,  $\bar{e}_r$  from the six interferograms, relative to the 'measured' displacement projected onto LOSD, at each marker. The horizontal angle,  $\alpha$  between  $\mathbf{e}^*$  and the mean horizontal marker displacement direction is also indicated

maps at each marker, with  $\pm 1$  standard deviation,  $\sigma$ , the markers being sorted in increasing distance from the GPRI. The error magnitude increases slightly with increasing distance from the GPRI, but this trend is not significant. We compared the measured  $d_m^*$  with the observed,  $d^*$  displacement in several different combinations, i.e., (1) marker displacements extracted from the filtered (smoothed) interferograms, (2) additionally correcting the displacements for ablation, (3) extracting the observed displacements from the unfiltered (raw) interferograms, and (4) again including a correction for the ablation. The error estimates from these 'processing strategies' are shown in Table 4.3.

We notice that lowest standard deviations and smallest mean errors are achieved when settling with the default product, i.e., the filtered interferograms and not incorporating an ablation correction. The agreement between observed and measured displacements is acceptable, despite the considerable variance. The mean of the absolute displacements,  $|\overline{d_m^*}|$  at a marker ranges between 1 and 5 cm and that of the differences,  $\Delta d$  is between 0.5 and 1 cm, which corresponds to relative errors between 16 % and 30 % (Table 4.4). The mean relative error of the differences at all stakes excluding 833 is 29 %. The best agreement between measured and observed displacement was obtained at marker 853 (Table 4.4), which is located up-most on Grenzgletscher (Fig. 4.1b), where flow velocities are highest and thus displacements are largest.

In Table 4.4 we also indicated the angle of incidence,  $\alpha$  between the horizontal LOSD and the mean displacement vectors for each stake. There is no clear correlation indicating that displacements are better measured when LOSD and flow directions are aligned. The alignment therefore plays a minor role.

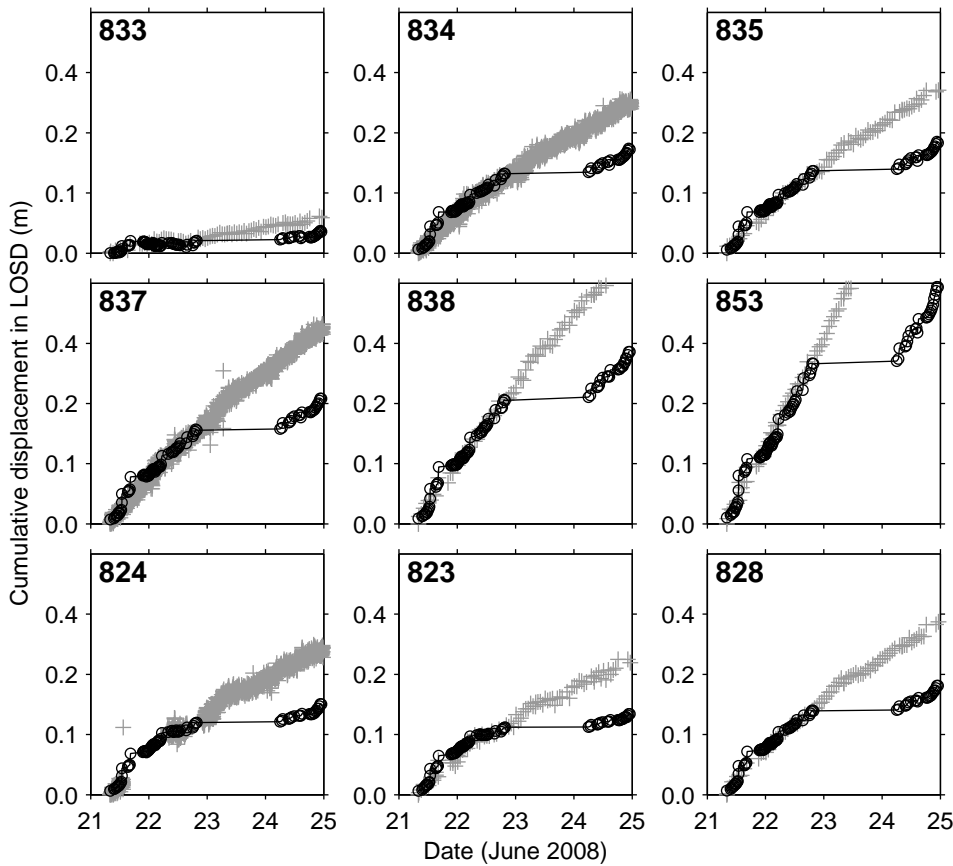


Figure 4.5: Cumulative observed ( $d^*$ , black solid, circles) and measured ( $d_m^*$ , grey crosses) displacements in LOSD during four days (21-24 June) at nine (reference) markers.

### Cumulative displacements

The GPRI was operated almost continuously. We hence extracted the scalar displacements at the marker locations from the chain of 133 interferograms and plotted in Figures 4.5 and 4.6 the resulting cumulative displacements together with the marker displacement projected onto the LOSD. Note that in Figure 4.6, the observed displacements were extracted from the interferograms at the pixels closest to the marker positions. Cumulative observed and measured displacements are in good agreement. The observed displacements are offset by 1 d on 23 June due to the interruption of the GPRI operation on 23-24 June. On 22 June, displacements decrease significantly at markers 813 and 814, while at markers 815 and 816 the displacements increase slightly (Fig. 4.6). This event is well captured by both GPRI and traditional marker measurements. It is the same signal as the displacement anomaly below the confluence, present in the displacement maps of Figures 4.3c, d and the change of displacement has a magnitude of about 10 cm within 0.5 d. This perturbation can be clearly captured by the GPRI.

## 4.4 Discussion

We have seen that observed and measured displacements show disparities up to 30%. The markers were located in the confluence region of Gornergletscher, which is the region where glacier flow is slowest and thus small displacements were recorded both by the GPRI and at the marker locations. However, the agreement is better in regions of Gornergletscher where larger displacements were measured (i.e., at markers 853 and 813-816, although at 813-816 displacements could not be directly compared). We had been aware of the slow flow in the confluence, but expected more significant disturbances of the sur-

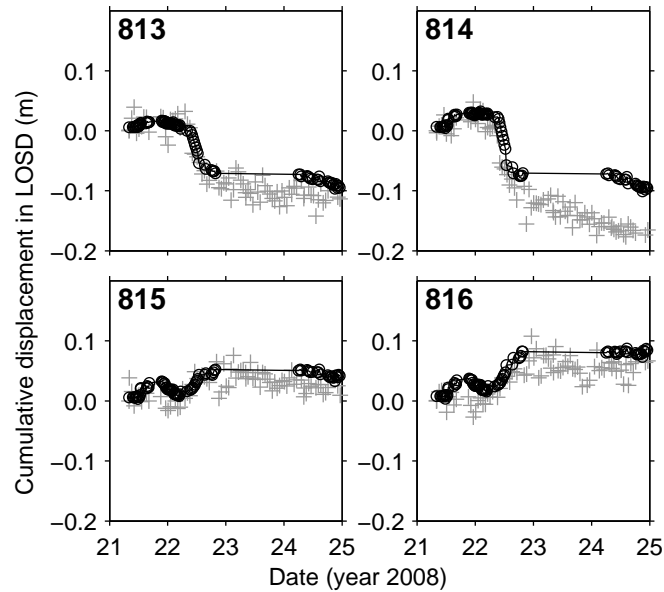


Figure 4.6: Cumulative observed ( $d^*$ , black solid, circles) and measured ( $d_m^*$ , grey crosses) displacements in LOSD during four days (21-24 June) at the four markers 814-816 outside the GPRI scan sector. The observed displacements are extracted from the interferogram pixels nearest to the marker locations.

face ice motion in the confluence and lake vicinity area (i.e. pronounced surface uplift as during the drainage event of 2004; Sugiyama et al., 2008). Small displacements occur because of the slow flow of Gornergletscher and the unspectacular influence of the lake drainage on the ice flow within the ice dam/confluence area of Gornergletscher. During 5 to 8 h, the surface ice motion within the target area of Gornergletscher is a few cm at most. Thus, the actual measured displacements are on the order of the accuracy of the position estimation of the tachymeter and GPS for such a short time period. This explains why standard deviations are large and why the best agreement was observed where the largest displacement was measured.

The melt rates were on the order of  $5 \text{ cm d}^{-1}$ . In fact, the large surface melt lowered the coherence of successive interferograms computed with more than 2 h integration-time interval during daytime (afternoon). Thus, the 5 h interferograms and displacement maps presented in Figure 4.3 were primarily obtained during evening and night time (except for the interferogram of Fig. 4.3b), when the melt was essentially absent and the inclusion of an ablation correction did not provide data enhancement. Therefore, we did not include any ablation correction when computing the displacements in LOSD from the measured displacements at the markers for comparison with the 5 h GPRI displacements. On the other hand, for the computation of cumulative displacements as those shown in Figures 4.5 and 4.6 successive interferograms with time intervals of 20 min were computed, with good coherence also during daytime. Below the confluence, the impact of the lake drainage was much more pronounced and resulted in displacements of the ice surface on the order of about 10 cm within a few hours. The GPRI measurements in that area could not directly be compared with the in-situ ice-displacement measurements as the GPRI scan sector did not overlap the markers 813-816. Nonetheless, the agreement between cumulative displacements in LOSD extracted from the closest interferogram pixel to the measured marker displacement projected onto the LOSD is indeed satisfactory. The GPRI was clearly able to capture this perturbation both temporally and in spatial dimensions. The resulting displacement maps of Figure 4.3a-f provide detailed information on the spatial distribution of the displacement changes below the confluence, filling the gap of information in the area between the markers 823, 824 and 813-816.

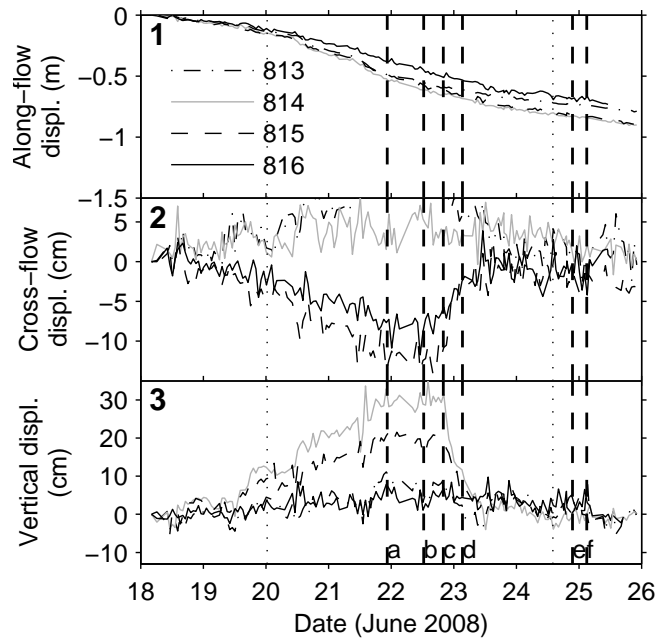


Figure 4.7: Displacements (displ.) along (1) the mean ice flow direction, (2) the cross-flow direction, and in (3) the vertical direction, at the markers 813-816. The dashed vertical lines labeled a-f correspond to the start times of the interferograms given in Figures 4.3.

#### 4.4.1 Influence of Gornersee drainage on the surface ice motion

It is known that disturbances of the glacier's subglacial environment by increased water input affects the basal motion of the glacier ice, which contributes substantially to the surface ice motion (e.g. Iken and Bindenschadler, 1986; Iken, 1981; Sugiyama and Gudmundsson, 2004). The observed and measured changes in surface ice motion on Gornergletscher are thus most likely linked to changes in basal water pressure and temporary water storage in the subglacial drainage system, as induced by the drainage of Gornersee. It drained before the lake water level approached the level of flotation of the ice dam into one major subglacial channel. The impact of the lake drainage on the flow of Gornergletscher in the confluence/ice dam area was minor; only a slight increase of displacement was determined, but surface uplifts or damaging of the lake border was not detected. This may indicate that the water traveled through the confluence area entirely en-glacially and only reached the glacier bed down-glacier of the confluence area, which is where the lake drainage had a very pronounced effect.

It is intriguing that the GPRI detected opposite displacements across Gornergletscher in the area below the confluence. To elucidate the observation of the GPRI, we refer to the displacements measured at the profile of markers 813-816 across Gornergletscher (Fig. 4.1b). In Figure 4.7 we plotted the along-flow (1), cross-flow (2) and vertical (3) components of the displacement trajectories of the markers 813-816. The along-flow direction of each marker refers to the mean flow direction at each marker. From 20 to 23 June, all markers moved slightly faster down-glacier (Fig. 4.7a). During the same time, markers 815 and 816 showed an excessive cross-flow excursive motion (towards south) of the order of 10 cm, while markers 813 and 814 seemed to move slightly in the opposite direction (towards north) (Fig. 4.7b). However, 815 and 816 do not move much in the vertical direction, whilst 813 and 814 show an uplift of almost 30 cm from 18-22 June (Fig. 4.7c). In the evening of 22 June, the vertical uplift of markers 813 and 814 drops significantly and the ice motion at markers 815 and 816 reverses to the opposite cross-flow direction (towards north), resuming its initial trajectory. This moment of opposite ice surface motion was recorded by the GPRI and is visible in the displacement maps recorded on 22 June (Fig. 4.3c-d). The anomalous signal recorded by the GPRI corresponds to the combined signal of surface down-drop (away from the GPRI, resulting in negative displacements) and cross-flow motion (towards the GPRI, resulting

in positive displacements) in the radar look direction across the lower tongue of Gornergletscher; the moraine M2 is separating these two motion events. The origin of this anomalous ice motion is not clear. It is treated in detail in the recent article by Sugiyama et al. (2010).

## 4.5 Conclusions

We measured the surface ice motion of Gornergletscher during the drainage of the adjacent Gornensee using a real aperture radar interferometer (GPRI). The lake drainage induced local variations in the ice surface motion of Gornergletscher. We could successfully detect the ice displacement variations with the GPRI. The agreement with local in-situ ice displacement measurements is satisfactory and shows that the GPRI produces reliable results. It can be well used for measuring ice displacement variations over a large area and over short time scales of a day to a few hours. In the Gornergletscher confluence area, the ice motion anomaly traveled at lowest velocities. There, the velocities were on the order of  $0.1 \text{ m d}^{-1}$ . This is about the lower limit of velocity at which an ice motion event can be tracked with an acceptable error of  $\sim 10\%$ . Our study showed the approximate lower resolution limit of the GPRI. Nevertheless, the range of application is wide. Definitely, perturbations of the ice motion which produce displacements and travel at speeds higher than  $0.1 \text{ m d}^{-1}$  can be tracked by the GPRI with high accuracy on the sub-daily scale. An upper limit of travel speed is given by the range/azimuth resolution, i.e, which is about  $50 \text{ m d}^{-1}$ . This (theoretical) upper limit is influenced by the loss of coherence due to ablation and should be assessed by further field measurements.

## **Part II**

# **Constitutive modelling of transient viscoelastic creep of ice**



# Chapter 5

## A thermomechanical solid viscoelastic model for transient creep of ice

This chapter compiles the results of a lecture held by K. Hutter specifically covering the constitutive theory of viscoelastic models of polycrystalline ice in glaciology.

### 5.1 Introduction

A continuum thermodynamic formulation of the material behavior of poly-crystalline glacier ice is proposed, in which the material exhibits elastic properties as well as viscous effects that account for primary and secondary creep. The intention is to provide a formulation for describing flow processes in glaciers which show significant changes on time scales of a few hours to a week. Surface flow measurements in the immediate vicinity and down-glacier of the ice-dammed lake Gornersee, Switzerland, have shown rapid changes and relatively fast return to 'normality' during the subglacial outburst of the lake water.

Interpretation of these measurements (see Sugiyama et al., 2007a, 2008) suggest that enhanced basal motion, caused by the excess water supply to the subglacial environment cannot fully explain the observations. It was therefore suggested that elastic effects may as well be responsible for the relatively rapid response of the ice. However, elasticity alone may equally be insufficient to explain the mentioned flow changes. Because the typical time scale of the observations is from a few hours to several days, our conjecture has been here to suspect that primary creep may play a significant role in explaining the observations. Many experiments (e.g. Glen, 1952, 1955; Steinemann, 1958; Mellor and Smith, 1967; Mellor and Testa, 1969) show primary creep to be effective in conducted creep tests, for approximate durations of a few hours to a few days, which is of a similar order of the lake outburst duration.

There exist models in the literature attempting to describe ice as a non-linear viscous fluid. Morland and Spring (1981) have proposed a rheological equation that relates stress, stress rates, strain rates and strain accelerations, and demonstrate for uni-axial compression that their proposed constitutive relations are capable to reproduce primary, secondary and tertiary creep of isotropic ice. Morland (1979) has already shown that by omitting stress rates in such a stress-deformation relation, the reproduction of constant strain-rate experiments is not possible and tertiary creep may be lost. This has been made explicit by McTigue et al. (1985) for an incompressible second grade fluid, which reduces to Newtonian behavior when second order effects are ignored. This was the reason for Man and Sun (1987) to propose two alternative second grade fluid models, which reduce to a non-Newtonian Glen-type flow law when ignoring second grade effects. Their descriptions of constitutive relations for a modified second order fluid is our starting point. However, because Man and Sun only look at creep and dismiss elastic effects in their proposed constitutive relations, we add to their basic constitutive postulate for stress, the elastic strain contribution and also thermal effects. We add a temperature dependence which was formerly ignored by Man and Sun. So,

$$\mathbf{t} = \hat{\mathbf{t}}(\mathbf{E}, \mathbf{A}_{(1)}, \mathbf{A}_{(2)}, T, \text{grad}(T)),$$

where,  $\mathbf{t}$ ,  $\mathbf{E}$ ,  $\mathbf{A}_{(1)}$ ,  $\mathbf{A}_{(2)}$ ,  $T$ ,  $\text{grad}(T)$  are stress, strain, strain rate, strain acceleration, temperature and temperature gradient, is the constitutive class, on which the thermodynamic formulation is based. We propose the most simple relation for the stress tensor on strain and shall reduce this dependence to a linear Hookean behavior of a density-preserving material with vanishing (bulk) compressibility. Moreover, the above constitutive class will be restricted by ad-hoc assumptions which make the mathematical proof of the thermodynamic behavior performed by Man and Sun (1987) applicable to this case. This is achieved by postulating that  $\mathbf{t}$  does not depend on  $\text{grad}(T)$  and the heat flux does not depend on  $\mathbf{E}$  and  $\mathbf{A}_{(1,2)}$ . Further, an interaction dependence of the thermodynamic potential on  $\mathbf{E}$  and  $\mathbf{A}_{(1,2)}$  is ignored. These simplifications are conjectured to be permissible; they make the mathematical analysis almost trivial and still preserve the essential properties, namely (i) inclusion of elasticity effects, which, paired with the viscous effects, allow for relaxation phenomena, and (ii) use of the second grade fluid concept to account for primary and secondary creep effects in the context of an extended Glen flow law. This assigns the transient response observed in the measured flow velocities to two effects, each of which can be separately studied by putting the parameters of the other effect to zero or keeping both present.

In the ensuing analysis we provide first a brief account on the kinematics, dynamics and constitutive behaviour of a classical continuum. This material can be found in any text on Continuum Mechanics (e.g. Hutter and Jöhnk, 2004). Then, we present the thermodynamic analysis for the Thermoelastic Modified Second Order Isotropic Material, which is a special form of a second grade fluid that is a slight generalization of the second order fluid proposed by Sun (1987).

## 5.2 Theoretical Background

### 5.2.1 Basis of Formulation and Prerequisites

#### Deformation

To describe motion, deformation and strain as viewed in the methods of continuum mechanics, we recall some prerequisites which will be used in further sections when constructing a constitutive relation for describing the material behaviour of ice. We will work in three-dimensional real Euclidian space with standard basis  $\mathbf{e}_i$ , where  $\mathbf{e}_i$  with  $i \in \{1, 2, 3\}$  are unit vectors in three dimensions of a rectangular Cartesian coordinate system in an inertial frame. Within this system, the vector  $\mathbf{X} = X_i \mathbf{e}_i$  refers to the position of a material particle inside a body  $B_0$  with initial configuration at time  $\tau = t_0$ , called the *reference configuration*<sup>1</sup>. If the body  $B_0$  and its particles have changed their configuration through time and reached the *present configuration* with new body shape  $B_t$  at time  $\tau = t$ , then the material particle  $\mathbf{X}$  has attained the new position  $\mathbf{x} = x_i \mathbf{e}_i$ . In general we have  $\mathbf{X} = X_\alpha \mathbf{e}_\alpha$  and  $\mathbf{x} = x_i \mathbf{e}_i$ , respectively, where the basis  $\mathbf{e}_\alpha$  with  $\alpha \in \{1, 2, 3\}$  may be distinct from the basis  $\mathbf{e}_i$ . For simplicity, we often use the same Cartesian basis  $\mathbf{e}_i$  in describing both the reference and present configurations. The motion of a particle from its reference to the present configuration is identified by the function  $\chi(\mathbf{X}, t)$ . Thus,  $\mathbf{x} = \chi(\mathbf{X}, t)$  is the coordinate triple of the particle position in the present configuration, whereas  $\mathbf{X} = \chi(\mathbf{X}, t_0)$  is the identity mapping of the particle position in terms of its coordinates in the reference configuration. This concept states two different views of the material particle.

The particle velocity  $\mathbf{v}$  and acceleration  $\mathbf{a}$  can be either calculated as

$$\mathbf{v} = \hat{\mathbf{v}}(\mathbf{X}, t) = \dot{\chi}(\mathbf{X}, t), \quad (5.2.1)$$

$$\mathbf{a} = \hat{\mathbf{a}}(\mathbf{X}, t) = \ddot{\chi}(\mathbf{X}, t), \quad (5.2.2)$$

<sup>1</sup>We employ the Einstein summation convention according to which summation over doubly repeated indices is understood (eg.  $\delta_{ii} = \delta_{11} + \delta_{22} + \delta_{33}$  for  $i = [1, 2, 3]$ )

or

$$\mathbf{v} = \hat{\mathbf{v}}(\chi^{-1}(\mathbf{X}, t)) = \mathbf{v}(\mathbf{x}(t), t), \quad (5.2.3)$$

$$\mathbf{a} = \hat{\mathbf{a}}(\chi^{-1}(\mathbf{X}, t)) = \frac{\partial \mathbf{v}}{\partial t} + \frac{\partial \mathbf{v}}{\partial \mathbf{x}} \frac{\partial \mathbf{x}}{\partial t} = \frac{\partial \mathbf{v}}{\partial t} + \text{grad } \mathbf{v} \cdot \mathbf{v}. \quad (5.2.4)$$

Direct dependence of the motion function  $\chi$  on  $\mathbf{X}$  as in (5.2.1) and (5.2.2), is referred to as material (Lagrange) formulation. Moreover, we have used the superimposed dot to designate the time derivative holding the particle  $\mathbf{X}$  fixed. We shall also use the equivalent notation of the material derivative ( $\dot{\phantom{a}}$ ) as  $\frac{\partial(\cdot)}{\partial t} + v_j \cdot (\cdot)_{,j}$ , where  $\mathbf{v} \hat{=} v_j$  is the velocity. In what follows we shall employ the same symbol to denote the functional dependence of a physical variable upon different independent variables, e.g.  $\mathbf{v} = \mathbf{v}(\mathbf{X}, t) = \mathbf{v}(\mathbf{x}, t)$ . This notation is only permissible if, in each instance, the set of independent variables is clearly defined. In the Lagrange notation a material particle is identified by its position  $\mathbf{X}$  in the reference configuration. The spatial (Euler) description, given in (5.2.3) and (5.2.4), refers to the present position  $\mathbf{x}$  of a particle. The velocity (5.2.3) is therefore determined from the actual variables  $(\mathbf{x}, t)$ . In the spatial formulation, the variable  $\mathbf{x}$  of a material particle  $\mathbf{X}$  is a function of time  $t$ , as  $\mathbf{x} = \chi(\mathbf{X}, t) = \mathbf{x}(t)$  and we use the chain rule of differentiation to calculate the acceleration in (5.2.4).

A measure to describe the changes in shape, length and volume, undergone by the particles of the material body  $B$  during their motion, is described by the *deformation gradient*

$$\mathbf{F} = \frac{\partial \chi(\mathbf{X}, t)}{\partial \mathbf{X}} = \text{Grad } \chi(\mathbf{X}, t) = \text{Grad } \mathbf{x}. \quad (5.2.5)$$

Note that we use Grad (grad) when differentiation is with respect to  $\mathbf{X}$  ( $\mathbf{x}$ ). This also holds for Div (div) or Curl (curl). The transformations of an incremental line element  $d\mathbf{X}$  into  $d\mathbf{x}$  and of a particle  $\mathbf{X}$  into  $\mathbf{x}$  are thus given by

$$d\mathbf{x} = \mathbf{F}(\mathbf{X}, t)d\mathbf{X}, \quad \text{and} \quad \mathbf{x} = \int_{t_0}^t \mathbf{F}(\mathbf{X}, t)dt, \quad (5.2.6)$$

where the integration is along the particle trajectory and  $t_0$  is the time in the initial reference configuration. Similar expressions for the transformations of a surface element  $d\mathbf{A}$ , or volume element  $d\mathbf{V}$  exist and read

$$d\mathbf{a} = J\mathbf{F}^{-T}d\mathbf{A}, \quad (5.2.7)$$

$$d\mathbf{v} = Jd\mathbf{V}, \quad (5.2.8)$$

where  $J := \det \mathbf{F}$  and  $\mathbf{F}^{-T} = (\mathbf{F}^{-1})^T$ , (see e.g. Hutter and Jöhnk, 2004, Chap.1). It is important to note that we must demand the motion function  $\chi$  to be continuously differentiable for  $\mathbf{F}$  being invertible and  $\det \mathbf{F} > 0$ .

The *spatial velocity gradient*  $\mathbf{L}$  is defined as

$$\mathbf{L} = \frac{\partial \mathbf{v}}{\partial \mathbf{x}} = \text{grad } \mathbf{v}. \quad (5.2.9)$$

The deformation gradient  $\mathbf{F}$  by definition is a spatial derivative with respect to the position in the reference configuration, whereas the spatial velocity gradient  $\mathbf{L}$  refers to the present configuration  $\mathbf{x}$ , and is a gradient quantity in the spatial formulation. Nevertheless,  $\mathbf{L}$  and  $\mathbf{F}$  can be related as follows

$$\mathbf{L} = \frac{\partial \mathbf{v}}{\partial \mathbf{x}} = \frac{\partial^2 \mathbf{x}}{\partial t \partial \mathbf{X}} \frac{\partial \mathbf{X}}{\partial \mathbf{x}} = \frac{\partial \mathbf{F}}{\partial t} \mathbf{F}^{-1} = \dot{\mathbf{F}} \mathbf{F}^{-1}. \quad (5.2.10)$$

Thus, the right-hand side of (5.2.10) gives us a measure of  $\mathbf{L}$  in the material description.

Further,  $\mathbf{L}$  can be decomposed into two tensors as

$$\mathbf{L} = \mathbf{D} + \mathbf{W}, \quad (5.2.11)$$

with

$$\mathbf{D} = \frac{1}{2}(\mathbf{L} + \mathbf{L}^T), \quad (5.2.12)$$

$$\mathbf{W} = \frac{1}{2}(\mathbf{L} - \mathbf{L}^T). \quad (5.2.13)$$

$\mathbf{D}$  is symmetric ( $\mathbf{D} = \mathbf{D}^T$ ), and is a rate measure of pure stretch or shortening (*stretching tensor*). The tensor  $\mathbf{W}$  is skew-symmetric ( $\mathbf{W} = -\mathbf{W}^T$ , *vorticity tensor*), and quantifies the rate of rotation. This becomes clear if we look at a motion where we move from the reference configuration to the present configuration by a simple *rigid body rotation*. Thus, we may write this motion as  $\mathbf{x} = \mathbf{Q}(t)\mathbf{X}$ , where  $\mathbf{Q}(t)$  is an orthogonal matrix ( $\mathbf{Q}^{-1} = \mathbf{Q}^T$ ). We show that

$$\mathbf{F} = \frac{\partial \mathbf{x}}{\partial \mathbf{X}} = \mathbf{Q}, \quad (5.2.14)$$

$$\mathbf{L} = \dot{\mathbf{F}}\mathbf{F}^{-1} = \dot{\mathbf{Q}}\mathbf{Q}^T, \quad (5.2.15)$$

$$\mathbf{D} = \frac{1}{2}(\dot{\mathbf{Q}}\mathbf{Q}^T + \mathbf{Q}\dot{\mathbf{Q}}^T) = \mathbf{0}, \quad (5.2.16)$$

$$\mathbf{W} = \frac{1}{2}(\dot{\mathbf{Q}}\mathbf{Q}^T - \mathbf{Q}\dot{\mathbf{Q}}^T) = \dot{\mathbf{Q}}\mathbf{Q}^T, \quad (5.2.17)$$

using (5.2.6), (5.2.10), and the identity  $\dot{\mathbf{Q}}\mathbf{Q}^T = -\mathbf{Q}\dot{\mathbf{Q}}^T$ . True strain measures must not include proportions of rigid body rotations. Other expressions in terms of the deformation gradient  $\mathbf{F}$  exist, for which the rate of rotation is eliminated for any general rigid body motion.

The mentioned properties of  $\mathbf{F}$  allow its unique polar decomposition, from which such measures can be derived (see e.g. Hutter and Jöhnk, 2004). They are

$$\mathbf{C} = \mathbf{F}^T\mathbf{F}, \quad (5.2.18)$$

the *right Cauchy-Green deformation tensor*, and

$$\mathbf{B} = \mathbf{F}\mathbf{F}^T, \quad (5.2.19)$$

the *left Cauchy-Green deformation tensor*. For these, the identity matrix  $\mathbf{I}$  emerges under a general rigid body motion  $\mathbf{x} = \mathbf{Q}(t)(\mathbf{X} - \mathbf{X}_m) - \mathbf{c}(t)$ , where  $\mathbf{Q}(t)$  is any orthogonal tensor,  $\mathbf{X}_m$  is a rotation center and  $\mathbf{c}(t)$  is a translation vector. The right Cauchy-Green deformation tensor (5.2.18) is in material formulation; consequently, the left Cauchy-Green deformation tensor (5.2.19) refers to the spatial description. We can construct a strain measure by

$$\mathbf{E} = \frac{1}{2}(\mathbf{B} - \mathbf{I}) = \frac{1}{2}(\mathbf{F}\mathbf{F}^T - \mathbf{I}), \quad (5.2.20)$$

which is known as the *spatial strain tensor*, or Finger strain tensor.

## Relative Deformation

Relative deformation describes the deformation of a material particle between the present configuration at time  $t$  and an earlier past configuration at time  $\tau < t$ . Consequently, the motion from the reference position at  $t_0$  to the position at  $\tau$  is not considered. Only the recent *relative motion*  $\chi_{t,\tau}$  of the material particle between the present time  $t$  and the past time  $\tau$  is preserved. We write the *relative deformation gradient* as

$$\mathbf{F}_{t,\tau} = \mathbf{F}(\tau)\mathbf{F}^{-1}(t), \quad \text{or} \quad (F_{t,\tau})_{ij} = F_{i\alpha}(\tau)F_{\alpha j}^{-1}(t), \quad (5.2.21)$$

which measures the deformation of a material particle between the times  $t$  and  $\tau$ . The relative deformation gradient is a composition of the deformation gradient describing the epoch  $t_0 \rightarrow \tau$ , and the inverse material deformation gradient  $\mathbf{F}$  for  $t \rightarrow t_0$ . Note that the relative deformation gradient now corresponds to a spatial formulation and the relative motion and respective relative deformation are described backwards into the past. The total time derivative of the relative quantities are, hence, defined for times  $\tau$  between the past and the present configuration. We can formulate an important relation of the spatial velocity gradient  $\mathbf{L}$ , which is defined at the present time  $t$ . With the help of (5.2.10) and by evaluating the relative deformation gradient  $\mathbf{F}_{t,\tau}$  at  $\tau = t$ , the spatial gradient becomes

$$\mathbf{L} = \left. \frac{\partial \mathbf{F}_{t,\tau}}{\partial \tau} \right|_{\tau=t} \mathbf{F}_{t,\tau}^{-1} \Big|_{\tau=t} = \dot{\mathbf{F}}_{t,\tau} \Big|_{\tau=t} \mathbf{I} = \dot{\mathbf{F}}_{t,t}. \quad (5.2.22)$$

$\mathbf{F}$  must be evaluated at time  $t$  after differentiation with respect to  $\tau$ , hence  $\dot{\mathbf{F}}_{t,t}$ , whereas the second term in (5.2.22) reduces to the identity matrix, because, if  $\tau = t$ , then  $\mathbf{F}_{t,t} = [\mathbf{F}(t)\mathbf{F}^{-1}(t)]^{-1} = \mathbf{I}^{-1} = \mathbf{I}$ , according to (5.2.21).

Similarly, the relative right Cauchy-Green deformation tensor is formed, and its time derivative, evaluated at time  $\tau = t$  is the *first* Rivlin-Ericksen tensor

$$\mathbf{A}_{(1)}(t) = \left. \frac{\partial \mathbf{C}_{t,\tau}}{\partial \tau} \right|_{\tau=t} = \dot{\mathbf{C}}_{t,\tau}|_{\tau=t} = \dot{\mathbf{C}}_{t,t}. \quad (5.2.23)$$

The  $n$ th time derivative  $\partial^n \mathbf{C}_{t,\tau} / \partial \tau^n |_{\tau=t}$  defines the Rivlin-Ericksen tensor of order  $n$ . Those may also be constructed by the recurrence relation as stated by Truesdell and Noll (2004)

$$\mathbf{A}_{(n+1)} = \dot{\mathbf{A}}_{(n)} + \mathbf{L}^T \mathbf{A}_{(n)} + \mathbf{A}_{(n)} \mathbf{L}, \quad (5.2.24)$$

thus, by using (5.2.12) and the fact that  $\mathbf{A}_{(0)} = \mathbf{I}$ ,

$$\mathbf{A}_{(1)} = \mathbf{L} + \mathbf{L}^T = 2\mathbf{D}, \quad (5.2.25)$$

$$\mathbf{A}_{(2)} = 2(\dot{\mathbf{D}} + \mathbf{L}^T \mathbf{D} + \mathbf{D} \mathbf{L}), \quad (5.2.26)$$

are the first and the second Rivlin-Ericksen tensors.

### Balance laws

A body composed of material particles and subjected to motion must fulfill the fundamental balance laws of mass, momentum and energy. In continuum theories of fluid dynamics, these laws are commonly expressed in the spatial (Euler) formulation as

$$\dot{\rho} + \rho \operatorname{div}(\mathbf{v}) = 0 \quad (\text{mass}), \quad (5.2.27)$$

$$\rho \dot{\mathbf{v}} = \operatorname{div}(\mathbf{t}) + \rho \mathbf{f} \quad (\text{momentum}), \quad (5.2.28)$$

$$\rho \dot{\varepsilon} = -\operatorname{div}(\mathbf{q}) + \mathbf{t} * \mathbf{D} + \rho r \quad (\text{energy}). \quad (5.2.29)$$

In (5.2.27),  $\rho$  is the specific density of the body or material particle and  $\mathbf{v}$  is the velocity vector. Mass balance states that the change in density of the considered material body must balance any material flux into the body. The momentum balance (5.2.28) states that the time rate of change of momentum, here expressed as mass per unit volume multiplied by the acceleration, must equal the sum of external body force  $\rho \mathbf{f}$  and other contact forces, described by the applied stress  $\mathbf{t}$ . Further, as  $\varepsilon$  is the specific internal energy, the rate of change per unit volume of  $\varepsilon$  is balanced by the energy flux due to heat conduction  $\mathbf{q}$ , the work performed by applied forces ( $\mathbf{t} * \mathbf{D}$ ), and the external source  $\rho r$  of energy (e.g. radiation). The balance law of angular momentum is not written down explicitly, as it is commonly satisfied by requiring the Cauchy stress tensor to be symmetric,  $\mathbf{t} = \mathbf{t}^T$ . The energy balance (5.2.29) corresponds to the first law of thermodynamics. There exists yet a further balance law for the *entropy* of a material, the second law of thermodynamics. All these laws must be fulfilled to describe a valid physical process. However, we will return to the restrictions of the entropy balance at a later stage. The principles and quantities which we have briefly recalled in this section will be used when we set up the constitutive relations for the ice. For a more detailed account and background we point to e.g. Hutter and Jöhnk (2004).

### 5.2.2 Form of Constitutive Relation for Isotropic Materials

The balance laws of mass, linear momentum and energy form five evolution equations involving more than five physical field quantities. To reduce the number of unknowns to the correct number and determine the field equations which form deterministic evolution equations, some field variables must be determined as functionals of others. Such relations are constitutive relations and the dependent variables

in these relations are called constitutive variables. In a general sense, we can express the relations for the constitutive quantities of the Cauchy stress  $\mathbf{t}$ , heat flux  $\mathbf{q}$  and internal energy  $\varepsilon$  in the form

$$C = \hat{C}(S_c), \quad (5.2.30)$$

where  $C$  either stands for  $\mathbf{t}$ ,  $\mathbf{q}$ , or  $\varepsilon$ , and  $S_c$  expresses a set of independent state variables. If the set  $S_c$  is given by  $\mathbf{F}, T$  and  $\mathbf{G} = \text{Grad}(T)$ , and we leave out explicitly listing  $\mathbf{X}$ , we have

$$C = \hat{C}(\mathbf{F}, T, \mathbf{G}), \quad (5.2.31)$$

which defines a very simplified form of constitutive relations for a so-called *simple material*. In (5.2.31), it is understood that  $C$  is evaluated for a particle at time  $t$  in its present configuration. Likewise, the independent state variables of the constitutive function  $\hat{C}(\cdot)$  are evaluated for the same particle also at present time  $t$ . In a more general simple material, the variables  $S_c$  could depend on all times prior to time  $t$ . However, we shall not consider this generality, but later will allow dependence on the history over a vanishingly small past time through current derivatives of the state variables. Moreover, in a simple material, the constitutive quantities in  $S_c$  are only dependent on the immediate neighborhood of a considered particle  $\mathbf{X}$ , expressed by their gradients  $\mathbf{F} = \text{Grad}(\mathbf{x})$  and  $\mathbf{G} = \text{Grad}(T)$ . The relation of the form (5.2.31) is the basis for many material descriptions and is already a very much simplified description of the material behaviour. The full derivation of this concept goes back to Coleman and Noll (1960).

### Material symmetry

The above representation (5.2.31) describes isotropic or anisotropic material behaviour. To obtain a constitutive relation for isotropic materials, additional restrictions need to be imposed. A material may possess certain symmetries which must be reflected by the constitutive relations. If, for example, the *same* deformation (on the macroscopic scale) in the present configuration would result from having deformed a material body either out of the reference configuration  $\kappa$ , or out of another reference configuration  $\hat{\kappa}$  relative to  $\kappa$ , then the transformation which relates  $\kappa$  to  $\hat{\kappa}$  is a symmetry transformation of the considered material body. Configuration  $\hat{\kappa}$  is said to be symmetric to  $\kappa$ . Other such configurations  $\hat{\kappa}_i$  may also exist; all symmetric transformations  $\hat{\kappa}_i$  define a mathematical group of symmetry transformations which then reflects the material symmetry properties. To express this in terms of the constitutive relations, we write (5.2.31) in either configuration  $\kappa$ ,  $\hat{\kappa}$  as

$$\hat{C}^\kappa(\mathbf{F}^\kappa, T^\kappa, \mathbf{G}^\kappa), \quad \text{and} \quad \hat{C}^{\hat{\kappa}}(\mathbf{F}^{\hat{\kappa}}, T^{\hat{\kappa}}, \mathbf{G}^{\hat{\kappa}}), \quad (5.2.32)$$

in which the reference configurations  $\kappa$  and  $\hat{\kappa}$  and the corresponding values of  $\mathbf{F}$ ,  $T$  and  $\mathbf{G}$  in the respective configuration have been made explicit by the superscripts  $(\cdot)^\kappa$  and  $(\cdot)^{\hat{\kappa}}$ , respectively.

Correct constitutive relations respecting a given material symmetry must then satisfy the condition

$$\hat{C}^\kappa(\mathbf{F}^\kappa, T^\kappa, \mathbf{G}^\kappa) = \hat{C}^{\hat{\kappa}}(\mathbf{F}^{\hat{\kappa}}, T^{\hat{\kappa}}, \mathbf{G}^{\hat{\kappa}}), \quad (5.2.33)$$

where  $\mathbf{F}^{\hat{\kappa}}$ ,  $T^{\hat{\kappa}}$ ,  $\mathbf{G}^{\hat{\kappa}}$  in configuration  $\hat{\kappa}$  can be expressed as those in configuration  $\kappa$ , viz.,

$$\mathbf{F}^{\hat{\kappa}} = \mathbf{F}^\kappa \mathbf{P}^{-1}, \quad T^{\hat{\kappa}} = T^\kappa, \quad \mathbf{G}^{\hat{\kappa}} = \mathbf{G}^\kappa \mathbf{P}^{-1}, \quad (5.2.34)$$

and  $\mathbf{P}$  stands for the invertible transformation

$$\mathbf{P} = \frac{\partial \mathbf{X}^{\hat{\kappa}}}{\partial \mathbf{X}^\kappa}. \quad (5.2.35)$$

Note that the scalar quantity of temperature  $T$  does not depend on the configuration, whereas the gradient quantities  $\mathbf{F}^{\kappa, \hat{\kappa}}$  and  $\mathbf{G}^{\kappa, \hat{\kappa}}$  do. We may drop the superscript notation in the argument list of (5.2.33), as

by (5.2.33) and (5.2.34) we automatically stated the formal equality of the two configurations. The symmetry condition then takes the form

$$\hat{C}(\mathbf{F}, T, \mathbf{G}) = \hat{C}(\mathbf{FP}, T, \mathbf{GP}). \quad (5.2.36)$$

The material is said to be *isotropic*, when its constitutive relations fulfill the symmetry condition (5.2.36) for all possible  $\mathbf{P}$ , which belong to the group of full orthogonal transformations, so (5.2.36) becomes

$$C = \hat{C}(\mathbf{F}, T, \mathbf{G}) = \hat{C}(\mathbf{FQ}, T, \mathbf{GQ}), \quad (5.2.37)$$

where  $\mathbf{Q}$  is any general orthogonal transformation. It can easily be verified that for an isotropic material  $C$  must have the dependencies

$$C = \hat{C}(f(\mathbf{B}), T, \mathbf{GF}^{-1}), \quad (5.2.38)$$

where  $\mathbf{B} = \mathbf{FF}^T$ , and  $\mathbf{GF}^{-1} = \text{grad}(T)$ . Indeed, with  $\mathbf{FQ}$  from (5.2.37) we have

$$\mathbf{B} = (\mathbf{FQ})(\mathbf{FQ})^T = \mathbf{FQ}\mathbf{Q}^T\mathbf{F}^T = \mathbf{FF}^T, \quad (5.2.39)$$

$$\mathbf{GF}^{-1} = \mathbf{GQ}\mathbf{Q}^{-1}\mathbf{F}^{-1} = \mathbf{GF}^{-1}, \quad (5.2.40)$$

which are both invariant under the full orthogonal group. The quantity  $f(\mathbf{B})$  is any convenient Eulerian strain measure.

### Rate type materials

In the constitutive relations of the form (5.2.31), there is no dependence on the history of the state variables  $\mathbf{F}$ ,  $T$ , and  $\mathbf{G}$ , but dependence on the immediate past can be incorporated by including truncated Taylor series of the state variables at time  $t$ . Then the functional  $C$  becomes

$$C = \hat{C}(\mathbf{F}, \dot{\mathbf{F}}, \dots, \overset{N_{\mathbf{F}}}{\mathbf{F}}, T, \dot{T}, \dots, \overset{N_T}{T}, \mathbf{G}, \dot{\mathbf{G}}, \dots, \overset{N_{\mathbf{G}}}{\mathbf{G}}), \quad (5.2.41)$$

and the material which is described by such a constitutive relation is said to be of *rate type*  $N_{\mathbf{F}}$ ,  $N_T$ , and  $N_{\mathbf{G}}$  in the variables  $\mathbf{F}$ ,  $T$  and  $\mathbf{G}$ . From the above constitutive form (5.2.41), different material classes arise:

**Thermoelastic material:** If  $N_{\mathbf{F}} = N_T = N_{\mathbf{G}} = 0$ , the resulting constitutive relations for  $\mathbf{t}$ ,  $\mathbf{q}$  and  $\varepsilon$  read

$$\varepsilon = \hat{\varepsilon}(\mathbf{F}, T, \mathbf{G}), \quad \mathbf{q} = \hat{\mathbf{q}}(\mathbf{F}, T, \mathbf{G}), \quad \mathbf{t} = \hat{\mathbf{t}}(\mathbf{F}, T, \mathbf{G}). \quad (5.2.42)$$

Materials which pertain to the above constitutive relations are classified as *thermoelastic materials*.

**Viscous thermoelastic material:** If  $N_{\mathbf{F}} = 1$  and  $N_T = N_{\mathbf{G}} = 0$ , we get

$$\varepsilon = \hat{\varepsilon}(\mathbf{F}, \dot{\mathbf{F}}, T, \mathbf{G}), \quad \mathbf{q} = \hat{\mathbf{q}}(\mathbf{F}, \dot{\mathbf{F}}, T, \mathbf{G}), \quad \mathbf{t} = \hat{\mathbf{t}}(\mathbf{F}, \dot{\mathbf{F}}, T, \mathbf{G}), \quad (5.2.43)$$

which are the basic constitutive relations describing a *viscous thermoelastic or thermo-viscoelastic material*. Thermo-viscoelastic materials are of rate type 1 with respect to the deformation gradient.

### Fluid or solid

The above constitutive relations do not yet tell us whether the material dealt with is a fluid or a solid; they describe a general isotropic material. However, if we explicitly want to express the constitutive relations for an isotropic fluid body, we use the fact that an isotropic fluid has higher degrees of symmetry than a solid material, e.g. consider an experiment where a glass of water has been stirred and the water in it has come to rest again. We will not be able to distinguish between the water in the glass before and

after it has been stirred. However, the motion the water has undergone by the stirring operation is much more general than an orthogonal transformation. Isotropic fluids possess the largest group of symmetry transformations possible, which includes all uni-modular (volume-preserving) transformations. If we consider the symmetry condition (5.2.36) for an isotropic viscous thermoelastic material and choose  $\mathbf{Q}$  to be an uni-modular transformation, e.g.  $\mathbf{Q} = (\det \mathbf{F})^{\frac{1}{3}} \mathbf{F}^{-1}$ , then

$$\begin{aligned} C &= \hat{C}(\mathbf{FQ}, \dot{\mathbf{F}}\mathbf{Q}, T, \mathbf{GQ}) \\ &= \hat{C}(\mathbf{F}(\det \mathbf{F})^{\frac{1}{3}} \mathbf{F}^{-1}, \dot{\mathbf{F}}(\det \mathbf{F})^{\frac{1}{3}} \mathbf{F}^{-1}, T, \mathbf{G}(\det \mathbf{F})^{\frac{1}{3}} \mathbf{F}^{-1}). \end{aligned} \quad (5.2.44)$$

The right-hand side of (5.2.44) can be exploited in more detail if we rewrite the material temperature gradient  $\mathbf{G}$  as

$$\mathbf{G} = \frac{\partial T(\mathbf{X}, t)}{\partial \mathbf{X}} = \frac{\partial T(\mathbf{x}, t)}{\partial \mathbf{x}} \frac{\partial \mathbf{x}}{\partial \mathbf{X}} = \text{grad}(T) \mathbf{F} = \mathbf{gF}. \quad (5.2.45)$$

We use  $\dot{\mathbf{F}} = \mathbf{LF}$  from (5.2.10) and substitute (5.2.45) into (5.2.44), which yields

$$\begin{aligned} C &= \hat{C}(\mathbf{F}, \mathbf{LF}, T, \mathbf{gF}) \\ &= \hat{C}(\mathbf{F}(\det \mathbf{F})^{\frac{1}{3}} \mathbf{F}^{-1}, \mathbf{LF}(\det \mathbf{F})^{\frac{1}{3}} \mathbf{F}^{-1}, T, \mathbf{gF}(\det \mathbf{F})^{\frac{1}{3}} \mathbf{F}^{-1}) \\ &= \hat{C}((\det \mathbf{F})^{\frac{1}{3}}, \mathbf{L}(\det \mathbf{F})^{\frac{1}{3}}, T, \mathbf{g}(\det \mathbf{F})^{\frac{1}{3}}) \\ &= \hat{C}(\det \mathbf{F}, \mathbf{L}, T, \mathbf{g}). \end{aligned} \quad (5.2.46)$$

The constitutive relations for a viscous thermoelastic fluid thus depend on  $\mathbf{F}$  only through  $\det(\mathbf{F})$ . According to (5.2.8), we may use  $\rho = (\det(\mathbf{F}))\rho_0$ , where  $\rho_0$  corresponds to the known density in the reference configuration. We can always compute the actual density  $\rho$  which is proportional to  $\det(\mathbf{F})$ , thus we may substitute the spatial material density  $\rho$  for the dependency on  $\det(\mathbf{F})$ . The constitutive relations for a viscous thermoelastic fluid are consequently equally of the form

$$\boldsymbol{\varepsilon} = \hat{\boldsymbol{\varepsilon}}(\rho, \mathbf{L}, T, \mathbf{g}), \quad \mathbf{q} = \hat{\mathbf{q}}(\rho, \mathbf{L}, T, \mathbf{g}), \quad \mathbf{t} = \hat{\mathbf{t}}(\rho, \mathbf{L}, T, \mathbf{g}). \quad (5.2.47)$$

Note that we thereby have changed the independent constitutive variables to Eulerian quantities.

### Density preserving materials

So far we have considered fluid or solid isotropic bodies, and, based upon their symmetry properties, formulated the corresponding general forms of constitutive relations. We must note that those formulations apply to materials which are compressible, in the sense that their density  $\rho$  may vary through time and motion and is an unknown independent field variable on which the constitutive relations rely. For a density-preserving material this can not be the appropriate description, as we would lose an independent field for constant density  $\rho$ . To accommodate for this, the stress tensor is split into two components as  $\mathbf{t} = \mathbf{t}^0 + \mathbf{t}^E$ , where  $\mathbf{t}^0$  is a diagonal tensor of the form  $\mathbf{t}^0 = -p\mathbf{I}$ . In a figurative sense, the pressure  $p$  is a uniform stress component in all three dimensions, accounting for the constraint condition  $\text{div } \mathbf{v} = v_{i,i} = \text{tr}(\mathbf{L}) = 0$ , which arises due to the reduction of the mass balance for  $\rho = \text{const}$ . The pressure  $p$  does not perform any work on deformations, satisfying the constraint  $\text{tr}(\mathbf{L}) = 0$ . Therefore, the constitutive relation for a density-preserving material is only formulated for the *extra-stress tensor*  $\mathbf{t}^E$ . As a basic field, the density  $\rho$  is replaced by the unknown pressure  $p$ .

### The matter of objectivity

It is demanded that the constitutive relations formally do not differ when one changes the frame of observation. Hence, the functional forms in (5.2.37) can only depend on quantities which transform in an objective manner, where frame-dependent terms vanish and do not influence the transformed variables.

For an Euclidian transformation  $\mathbf{x}^* = \mathbf{O}(t)\mathbf{x} + \mathbf{b}(t)$ , the rotation matrix  $\mathbf{O}(t)$  is orthogonal and  $\mathbf{b}(t)$  is a translation vector. Objectivity is warranted if the dependent variables and also the constitutive quantities transform according to the rules

$$\lambda^* = \lambda, \quad (5.2.48)$$

$$\mathbf{b}^* = \mathbf{O}\mathbf{b}, \quad (5.2.49)$$

$$\mathbf{T}^* = \mathbf{O}\mathbf{T}\mathbf{O}^T, \quad (5.2.50)$$

Here,  $\lambda^*$ ,  $\mathbf{b}^*$  and  $\mathbf{T}^*$  are dependent constitutive variables referred to the frame  $(\cdot)^*$ , whilst  $\lambda$ ,  $\mathbf{b}$  and  $\mathbf{T}$  are those referred to the frame  $(\cdot)$ . Moreover, (5.2.48) is an objective transformation for a scalar quantity, (5.2.49) indicates the objective vector transformation, and (5.2.50) is an objective tensor transformation<sup>2</sup>.

The symmetry condition (5.2.37) and the above transformation rules for objectivity can be combined to yield general restrictions, which the constitutive functions describing an isotropic material must satisfy. Let  $\mu$ ,  $\mathbf{v}$  and  $\mathbf{S}$  be a scalar-valued, vector-valued and tensor-valued physical quantity, for which the constitutive functions are of the form

$$\lambda = \hat{\lambda}(\mu, \mathbf{v}, \mathbf{S}), \quad \mathbf{b} = \hat{\mathbf{b}}(\mu, \mathbf{v}, \mathbf{S}), \quad \mathbf{T} = \hat{\mathbf{T}}(\mu, \mathbf{v}, \mathbf{S}). \quad (5.2.51)$$

The combined conditions of isotropy and objectivity then read

$$\hat{\lambda}(\mu, \mathbf{Q}\mathbf{v}, \mathbf{Q}\mathbf{S}\mathbf{Q}^T) = \hat{\lambda}(\mu, \mathbf{v}, \mathbf{S}) \quad (5.2.52)$$

$$\hat{\mathbf{b}}(\mu, \mathbf{Q}\mathbf{v}, \mathbf{Q}\mathbf{S}\mathbf{Q}^T) = \mathbf{Q}\hat{\mathbf{b}}(\mu, \mathbf{v}, \mathbf{S}) \quad (5.2.53)$$

$$\hat{\mathbf{T}}(\mu, \mathbf{Q}\mathbf{v}, \mathbf{Q}\mathbf{S}\mathbf{Q}^T) = \mathbf{Q}\hat{\mathbf{T}}(\mu, \mathbf{v}, \mathbf{S})\mathbf{Q}^T, \quad (5.2.54)$$

and must hold for the group of all orthogonal transformations  $\mathbf{Q}$ . Constitutive relations obeying these relations then possess a form admissible for isotropic bodies that need no further reductions for solids but may need further reduction for fluids. According to the above requirements, general complex isotropic polynomial expressions in terms of  $\mathbf{v}$  and  $\mathbf{S}$  have been derived for the representations of constitutive isotropic functions  $\mathbf{b}$  and  $\mathbf{T}$ , in which the polynomial coefficients depend on invariant quantities of  $\mathbf{v}$  and  $\mathbf{S}$ . Reduced forms of these functions have the form (see Hutter and Jöhnk, 2004)

$$\begin{aligned} \mathbf{T} = & a\mathbf{I} + b\mathbf{S} + c\mathbf{S}^2 + d\mathbf{v} \otimes \mathbf{v} + e(\mathbf{S}\mathbf{v} \otimes \mathbf{v} + \mathbf{v} \otimes \mathbf{S}\mathbf{v}) \\ & + f(\mathbf{S}^2\mathbf{v} \otimes \mathbf{v} + \mathbf{v} \otimes \mathbf{S}^2\mathbf{v}), \end{aligned} \quad (5.2.55)$$

$$\mathbf{b} = \alpha\mathbf{v} + \beta\mathbf{S}\mathbf{v} + \gamma\mathbf{S}^2\mathbf{v}, \quad (5.2.56)$$

in which  $\mathbf{T}$  and  $\mathbf{S}$  have been assumed symmetric. The coefficients  $a, b, c, d, e, f, \alpha, \beta, \gamma$  are functions of the set  $\mathbb{S}$  of scalar invariants

$$\begin{aligned} \mathbb{S} = & \{I_{\mathbf{S}}, II_{\mathbf{S}}, III_{\mathbf{S}}, \mathbf{v} \cdot \mathbf{v}, \mathbf{v} \cdot \mathbf{S}\mathbf{v}, \mathbf{v} \cdot \mathbf{S}^2\mathbf{v}, \mu\}, \\ \text{where } & I_{\mathbf{S}} = \text{tr}(\mathbf{S}), \quad II_{\mathbf{S}} = \frac{1}{2}\text{tr}(\mathbf{S}^2), \quad III_{\mathbf{S}} = \det(\mathbf{S}). \end{aligned} \quad (5.2.57)$$

In applications, a dependence of  $\mathbf{T}$  on  $\mathbf{v}$ , and of  $\mathbf{b}$  on  $\mathbf{S}$  is often ignored. In those circumstances, (5.2.55) and (5.2.56) reduce to

$$\mathbf{T} = a\mathbf{I} + b\mathbf{S} + c\mathbf{S}^2, \quad (5.2.58)$$

$$\mathbf{b} = \alpha\mathbf{v}. \quad (5.2.59)$$

The coefficients  $a, b, c$  in (5.2.58) and (5.2.59) are now functions of the new set  $\mathbb{S}' = \{I_{\mathbf{S}}, II_{\mathbf{S}}, III_{\mathbf{S}}, \mu\}$ , and  $\alpha$  depends on  $\mu$  and  $\mathbf{v} \cdot \mathbf{v}$ . Note that either set  $\mathbb{S}$  or  $\mathbb{S}'$  is different again for a density-preserving material, as the third invariant  $III_{\mathbf{S}} = 1$ , due to the constraint  $\text{tr}(\mathbf{S}) = 0$  in such case.

<sup>2</sup>The adjective 'objective' means that the transformations (5.2.48) - (5.2.50) hold under the application of Euclidian transformations

### 5.2.3 Glen's flow law for ice

Classically, ice flow behaviour is described by the Glen flow law, motivated by laboratory experiments by Glen (1955) and Steinemann (1958). Nye (1953) formulated the flow law for three-dimensional stress states. It describes the constitutive relation of an incompressible isotropic fluid where the extra stress tensor depends only on the strain rate tensor  $\mathbf{D}$  and temperature  $T$  according to

$$\mathbf{t}^E = \hat{\mathbf{t}}^E(\mathbf{D}, T). \quad (5.2.60)$$

The constitutive function for Glen's flow law is a simplified form of (5.2.58), in which the stress and stretching tensors are collinear to one another. Due to the incompressibility, the first term in (5.2.58) vanishes since  $\mathbf{I}_{\mathbf{D}} = 0$  and it may be written as

$$\mathbf{D} = \alpha(\Pi_{\mathbf{t}^E}, T)\mathbf{t}^E, \quad \text{or} \quad \mathbf{t}^E = \beta(\Pi_{\mathbf{D}}, T)\mathbf{D}. \quad (5.2.61)$$

where the form (5.2.61)<sub>1</sub> is commonly adopted in glaciology. The dependency of the coefficient  $\alpha$  on temperature  $T$  and the second invariant  $\Pi_{\mathbf{t}^E}$  of the extra stress tensor is multiplicatively split

$$\mathbf{D} = \alpha_1(\Pi_{\mathbf{t}^E})\alpha_2(T)\mathbf{t}^E. \quad (5.2.62)$$

So  $\alpha_2(T)$  is identified as the temperature-dependent *rate factor*  $A(T)$  and  $\alpha_1(\Pi_{\mathbf{t}^E})$  is mostly assumed as a power law function with exponent  $n$ , thus in

$$\mathbf{D} = A(T)(\Pi_{\mathbf{t}^E})^{\frac{n-1}{2}}\mathbf{t}^E, \quad (5.2.63)$$

we recognize the classical flow law of Glen (Nye, 1953; Glen, 1955; Steinemann, 1958).

#### Regularization of Glen's flow law

Due to the power law behaviour, there is a singularity in the flow law of Glen, as for very low stresses, the term  $(\Pi_{\mathbf{t}^E})^{(n-1)/2}$  may become zero. To avoid infinite stiff ice at low stresses, (5.2.63) can be slightly modified by adding a constant  $k$  as

$$\mathbf{D} = A(T)(\Pi_{\mathbf{t}^E} + k)^{\frac{n-1}{2}}\mathbf{t}^E, \quad (5.2.64)$$

where  $k$  is called the *regularization parameter* and (5.2.64) is the regularized Glen's flow law (Hutter, 1983). Thus, for low stress regimes, the ice rheology reduces to a linear (Newtonian) stress-strain relation with a slope  $\approx k^{\frac{n-1}{2}}$ . Newtonian behaviour of ice at low stresses is also what Mellor and Smith (1967) have observed.

## 5.3 Ice as a Thermoelastic Modified Second Order Isotropic Material

### 5.3.1 The Modified Second Order Fluid

We begin the analysis with the constitutive relation of the form

$$\mathbf{C} = \hat{\mathbf{C}}(\rho, \mathbf{D}, \dot{\mathbf{D}}, T, \mathbf{g}), \quad (5.3.1)$$

which corresponds to a fluid of rate type 2 with respect to  $\mathbf{D}$ . Indeed,  $\mathbf{D}$  is a strain rate and  $\dot{\mathbf{D}}$  is a strain acceleration. To fulfill the objectivity requirement,  $\mathbf{L}$  and  $\dot{\mathbf{L}}$  have been replaced by their symmetric parts  $\mathbf{D}$  and  $\dot{\mathbf{D}}$ , as the former do not transform in a objective manner. However,  $\dot{\mathbf{D}}$  is not objective, so the frame indifferent equivalents are given by the Rivlin-Ericksen tensors already introduced in (5.2.25). Considering an isotropic fluid, equation (5.3.1) then becomes

$$\mathbf{C} = \hat{\mathbf{C}}(\mathbf{A}_{(1)}, \mathbf{A}_{(2)}, T, \mathbf{g}), \quad (5.3.2)$$

and describes a Rivlin-Ericksen fluid of degree 2. The constitutive relations for the *modified second-order fluids* (MSOF) proposed by Man and Sun (1987) are of the form (5.3.2). They are slightly modified representations of the general Rivlin-Ericksen fluid class derived by Rivlin and Ericksen (1955). The stress-strain relation models proposed by Man and Sun (1987) are

$$\mathbf{t}^I = -p\mathbf{I} + \pi^{\frac{m}{2}} \mu \mathbf{A}_{(1)} + \alpha_1 \mathbf{A}_{(2)} + \alpha_2 \mathbf{A}_{(1)}^2, \quad (I), \quad (5.3.3)$$

$$\mathbf{t}^{II} = -p\mathbf{I} + \pi^{\frac{m}{2}} [\mu \mathbf{A}_{(1)} + \alpha_1 \mathbf{A}_{(2)} + \alpha_2 \mathbf{A}_{(1)}^2], \quad (II), \quad (5.3.4)$$

where

$$\pi = \frac{1}{2} \text{tr} \mathbf{A}_{(1)}^2, \quad (5.3.5)$$

and the parameters  $\mu, \alpha_1, \alpha_2$  are constants for isothermal ice. The isotropic component  $-p\mathbf{I}$  may be interpreted as the constraint pressure for the density-preserving case  $\text{tr}(\mathbf{A}_{(1)}) = 0$  (as Man and Sun have considered). Otherwise, if  $\mathbf{A}_{(1)}$  is not deviatoric, it corresponds to the isotropic stress component similar to  $a\mathbf{I}$  in (5.2.58). Note, that for (5.3.3) and (5.3.4), the isotropic constitutive functions are functions of two symmetric (Rivlin-Ericksen) tensors and therefore have slightly different representation forms than (5.2.58). Man and Sun (1987) have called (I) in (5.3.3), the *modified second order fluid with power law viscosity*, and (II) in (5.3.4), the *power law fluid of grade 2*. However, we will henceforth rather speak of the *modified second order fluid model* (MSOFM) and thereby not (yet) differ between these two models. The important property of the MSOFM is, that for  $\alpha_1 = \alpha_2 = 0$  and  $m = (1 - n)/n$ , it reduces to a Glen-like power law flow model with exponent  $n$ , as (5.2.63). Including a temperature-dependency of the parameter  $\mu = \mu(T)$  would make it correspond to the inverse rate factor  $A(T)$ . The MSOFM of Man and Sun (1987) has been proposed as an improvement of Glen's flow law. It is able to describe general secondary creep of glacier flow, e.g. shearing flow and its corresponding velocity profiles can be reproduced adequately. Moreover, it incorporates primary creep. All this has been shown in detail by Sun (1987), and he confirmed the compatibility of the MSOFM with the second law of thermodynamics. We will not state all the derivations in detail for the MSOFM; by use of the *entropy principle* (Section 5.3.3), only a partial exploration of the thermodynamic restrictions will be carried out for the constitutive relations describing a *thermoelastic modified second order isotropic body*. We will demonstrate that the restrictions and conformity of the MSOFM of Man and Sun hold equally for a thermoelastic modified second order isotropic body under certain assumptions.

### 5.3.2 The Thermoelastic Modified Second Order Isotropic Material

It is difficult to say whether at timescales of flow perturbations of hours to a few days, glacier ice behaves as a solid or fluid-like viscous or viscoelastic isotropic material. In the past, the role of primary creep and/or elastic effects on glacier flow and observed flow anomalies on a scale of hours to a few days has not been investigated. To explore this in detail, we adopt the approach of the MSOFM, in which the ice is treated as a second order viscous fluid, able to reproduce both primary and secondary creep effects with good agreement on the experiments conducted and discussed by Sun (1987). However, we also want to account for elastic properties of the ice by assuming it to behave as an isotropic elastic solid. We therefore extend the constitutive form of the MSOFM by an explicit dependence on the spatial Finger strain tensor and postulate

$$C = \hat{C}(\mathbf{E}, \mathbf{A}_{(1)}, \mathbf{A}_{(2)}, T, \mathbf{g}), \quad (5.3.6)$$

where  $C$  stands for the constitutive quantities of stress  $\mathbf{t}$ , heat flux  $\mathbf{q}$ , specific energy  $\varepsilon$  and entropy  $\eta$ . We call the corresponding material a *thermoelastic modified second order isotropic material* (TMSOIM).

### 5.3.3 Thermodynamic Restrictions

The balance laws (5.2.27) to (5.2.29), upon substitution of appropriate constitutive functions for the quantities of  $\mathbf{t}$ ,  $\eta$ ,  $\varepsilon$  and  $\mathbf{q}$ , form a set of *field equations*. However, we are lacking a balance law for the

entropy  $\eta$ , which must be equally fulfilled in order that the field equations describe a valid thermodynamic process and may be integrable to solve for the unknowns: motion  $\mathbf{x}$ , temperature  $T$  and density  $\rho$ , respectively pressure  $p$  when the material is density-preserving. We use the *entropy principle* to investigate the implications of the second law of thermodynamics. For this, we use the entropy balance in the form of the Clausius-Duhem inequality. Considering the set of constitutive quantities  $\mathbf{t}$ ,  $\varepsilon$ ,  $\eta$ ,  $\mathbf{q}$ , which, for the thermoelastic modified second order isotropic material, are given as the relations (5.3.6), the Clausius-Duhem inequality is given as

$$\rho \dot{\hat{\eta}} + \operatorname{div} \left( \frac{\hat{\mathbf{q}}}{T} \right) - \frac{\rho r}{T} \geq 0, \quad (5.3.7)$$

where  $\hat{\eta}$  is the specific entropy,  $\hat{\mathbf{q}}/T$  is the entropy flux, and  $r/T$  is the entropy supply. We combine the energy balance (5.2.29) and the Clausius-Duhem inequality (5.3.7) to eliminate its source terms,  $r$ , and also replace  $\hat{\mathbf{t}} * \mathbf{D}$  by  $\frac{1}{2} \hat{\mathbf{t}} * \mathbf{A}_{(1)}$ . Thus, the inequality now reads

$$\rho(T\dot{\hat{\eta}} - \dot{\hat{\varepsilon}}) + \frac{1}{2} \hat{\mathbf{t}} * \mathbf{A}_{(1)} - \frac{\hat{\mathbf{q}} \cdot \mathbf{g}}{T} \geq 0. \quad (5.3.8)$$

Using the chain rule of differentiation on  $\hat{\eta}$ ,  $\hat{\varepsilon}$  and collecting respective derivatives, transforms (5.3.8) into

$$\begin{aligned} \rho \left\{ \left( T \frac{\partial \hat{\eta}}{\partial \mathbf{E}} - \frac{\partial \hat{\varepsilon}}{\partial \mathbf{E}} \right) * \dot{\mathbf{E}} + \left( T \frac{\partial \hat{\eta}}{\partial \mathbf{A}_{(1)}} - \frac{\partial \hat{\varepsilon}}{\partial \mathbf{A}_{(1)}} \right) * \dot{\mathbf{A}}_{(1)} + \left( T \frac{\partial \hat{\eta}}{\partial \mathbf{A}_{(2)}} - \frac{\partial \hat{\varepsilon}}{\partial \mathbf{A}_{(2)}} \right) * \dot{\mathbf{A}}_{(2)} \right. \\ \left. + \left( T \frac{\partial \hat{\eta}}{\partial T} - \frac{\partial \hat{\varepsilon}}{\partial T} \right) \dot{T} + \left( T \frac{\partial \hat{\eta}}{\partial \mathbf{g}} - \frac{\partial \hat{\varepsilon}}{\partial \mathbf{g}} \right) \cdot \dot{\mathbf{g}} \right\} + \frac{1}{2} \hat{\mathbf{t}} * \mathbf{A}_{(1)} - \frac{\hat{\mathbf{q}} \cdot \mathbf{g}}{T} \geq 0. \end{aligned} \quad (5.3.9)$$

In this imbalance, the terms  $\dot{T}$ ,  $\dot{\mathbf{A}}_{(2)}$  and  $\dot{\mathbf{g}}$  appear linearly, whilst  $\dot{\mathbf{A}}_{(1)}$  can be expressed in terms of  $\mathbf{A}_{(1)}$ ,  $\mathbf{A}_{(2)}$  and  $\mathbf{L}$  by (5.2.24). The time derivative of the Finger strain tensor can be evaluated as

$$\begin{aligned} \dot{\mathbf{E}} &= \frac{1}{2} (\mathbf{F}\mathbf{F}^T - \mathbf{1})' \\ &= \frac{1}{2} (\mathbf{L}\mathbf{F}\mathbf{F}^T + \mathbf{F}\mathbf{F}^T\mathbf{L}^T) \\ &= \frac{1}{2} (\mathbf{L}(2\mathbf{E} + \mathbf{1}) + (2\mathbf{E} + \mathbf{1})\mathbf{L}^T) \\ &= \mathbf{L}\mathbf{E} + \mathbf{E}\mathbf{L}^T + \frac{1}{2}(\mathbf{L} + \mathbf{L}^T) \\ &= \mathbf{L}\mathbf{E} + \mathbf{E}\mathbf{L}^T + \frac{1}{2}\mathbf{A}_{(1)}, \end{aligned} \quad (5.3.10)$$

and shows an explicit dependence on  $\mathbf{A}_{(1)}$ . Here, we have used  $\mathbf{L} = \dot{\mathbf{F}}\mathbf{F}^{-1}$  from (5.2.10). As the linear variables  $\dot{T}$ ,  $\dot{\mathbf{A}}_{(2)}$  and  $\dot{\mathbf{g}}$  in (5.3.9) may take any value, the prefix terms must vanish to satisfy the inequality (5.3.9), implying<sup>3</sup>

$$T \frac{\partial \hat{\eta}}{\partial \mathbf{A}_{(2)}} - \frac{\partial \hat{\varepsilon}}{\partial \mathbf{A}_{(2)}} \equiv 0, \quad (5.3.11)$$

$$T \frac{\partial \hat{\eta}}{\partial T} - \frac{\partial \hat{\varepsilon}}{\partial T} \equiv 0, \quad (5.3.12)$$

$$T \frac{\partial \hat{\eta}}{\partial \mathbf{g}} - \frac{\partial \hat{\varepsilon}}{\partial \mathbf{g}} \equiv 0. \quad (5.3.13)$$

<sup>3</sup> This inference requires better justification as follows: Inequality (5.3.9) must be obeyed in order to satisfy the field equations, which are the balances of mass, momentum and energy when the constitutive relations are substituted in the respective terms. Because for the exploitation of the Clausius-Duhem inequality in the approach of Truesdell and Noll (2004), the balance laws of linear momentum and energy have external source terms ( $\mathbf{f}$  and  $r$ ), which can be arbitrarily assigned, these laws do not form constraints of this exploitation. Therefore, only the balance of mass remains as a possible constraint; however,  $\mathbf{E}$  is an independent constitutive variable which is temporally updated by (5.3.10), so mass balance is automatically obeyed via  $\rho_0 = \mathbf{J}\rho = (\det \mathbf{B})^{1/2} \rho$ .

These are satisfied as identities. We now cross-differentiate (5.3.11) and (5.3.12) as follows:

$$\frac{\partial}{\partial T} \left\{ T \frac{\partial \hat{\eta}}{\partial \mathbf{A}_{(2)}} - \frac{\partial \hat{\varepsilon}}{\partial \mathbf{A}_{(2)}} \right\} = \frac{\partial \hat{\eta}}{\partial \mathbf{A}_{(2)}} + T \frac{\partial^2 \hat{\eta}}{\partial T \partial \mathbf{A}_{(2)}} - \frac{\partial^2 \hat{\varepsilon}}{\partial T \partial \mathbf{A}_{(2)}} \equiv 0, \quad (5.3.14)$$

$$\frac{\partial}{\partial \mathbf{A}_{(2)}} \left\{ T \frac{\partial \hat{\eta}}{\partial T} - \frac{\partial \hat{\varepsilon}}{\partial T} \right\} = T \frac{\partial^2 \hat{\eta}}{\partial \mathbf{A}_{(2)} \partial T} - \frac{\partial^2 \hat{\varepsilon}}{\partial \mathbf{A}_{(2)} \partial T} \equiv 0. \quad (5.3.15)$$

Subtracting these expressions from each other and using the fact that mixed derivatives of functions are independent of the order of differentiation, yields  $\partial \hat{\eta} / \partial \mathbf{A}_{(2)} \equiv \mathbf{0}$  and consequently,  $\partial \hat{\varepsilon} / \partial \mathbf{A}_{(2)} \equiv \mathbf{0}$ . In an analogous way, we deduce

$$\frac{\partial}{\partial T} \left\{ T \frac{\partial \hat{\eta}}{\partial \mathbf{g}} - \frac{\partial \hat{\varepsilon}}{\partial \mathbf{g}} \right\} = \frac{\partial \hat{\eta}}{\partial \mathbf{g}} + T \frac{\partial^2 \hat{\eta}}{\partial T \partial \mathbf{g}} - \frac{\partial^2 \hat{\varepsilon}}{\partial T \partial \mathbf{g}} \equiv 0, \quad (5.3.16)$$

$$\frac{\partial}{\partial \mathbf{g}} \left\{ T \frac{\partial \hat{\eta}}{\partial T} - \frac{\partial \hat{\varepsilon}}{\partial T} \right\} = T \frac{\partial^2 \hat{\eta}}{\partial \mathbf{g} \partial T} - \frac{\partial^2 \hat{\varepsilon}}{\partial \mathbf{g} \partial T} \equiv 0, \quad (5.3.17)$$

or,  $\partial \hat{\eta} / \partial \mathbf{g} \equiv \mathbf{0}$  and  $\partial \hat{\varepsilon} / \partial \mathbf{g} \equiv \mathbf{0}$ . Therefore,  $\eta$  and  $\varepsilon$  can not depend on  $\mathbf{A}_{(2)}$  and  $\mathbf{g}$ , implying

$$\eta = \hat{\eta}(\mathbf{E}, \mathbf{A}_{(1)}, T), \quad \varepsilon = \hat{\varepsilon}(\mathbf{E}, \mathbf{A}_{(1)}, T), \quad (5.3.18)$$

with the remaining constraint

$$T \frac{\partial \hat{\eta}}{\partial T} = \frac{\partial \hat{\varepsilon}}{\partial T}. \quad (5.3.19)$$

We now return to (5.3.8) and introduce the Helmholtz free energy  $\psi = \varepsilon - T\eta$  as a thermodynamic potential for the entropy  $\eta$ , replacing  $T\hat{\eta} - \hat{\varepsilon}$  by  $-(\hat{\psi} + T\hat{\eta})$ . The Clausius-Duhem inequality in terms of the Helmholtz free energy takes the form

$$-\rho(\hat{\psi} + T\hat{\eta}) + \frac{1}{2} \hat{\mathbf{t}} * \mathbf{A}_{(1)} - \frac{\hat{\mathbf{q}} \cdot \mathbf{g}}{T} \geq 0. \quad (5.3.20)$$

Again we use the chain rule of differentiation for  $\hat{\psi}(\cdot)$  and observe that, in view of (5.3.18), it does not depend on  $\mathbf{A}_{(2)}$ , so that

$$-\rho \left\{ \left( \frac{\partial \hat{\psi}}{\partial \mathbf{E}} * \dot{\mathbf{E}} + \frac{\partial \hat{\psi}}{\partial \mathbf{A}_{(1)}} * \dot{\mathbf{A}}_{(1)} + \frac{\partial \hat{\psi}}{\partial T} \dot{T} + \frac{\partial \hat{\psi}}{\partial \mathbf{g}} \cdot \dot{\mathbf{g}} + T\hat{\eta} \right) \right\} + \frac{1}{2} \hat{\mathbf{t}} * \mathbf{A}_{(1)} - \frac{\hat{\mathbf{q}} \cdot \mathbf{g}}{T} \geq 0. \quad (5.3.21)$$

In rearranged order, incorporating the term  $\frac{1}{2} \hat{\mathbf{t}} * \mathbf{A}_{(1)}$  into the bracketed expression, (5.3.21) reads

$$-\rho \left\{ \left( \underbrace{\frac{\partial \hat{\psi}}{\partial T} + \hat{\eta}}_{=0, (\frac{\partial \hat{\psi}}{\partial T} = -\hat{\eta})} \right) \dot{T} + \frac{\partial \hat{\psi}}{\partial \mathbf{E}} * \dot{\mathbf{E}} + \frac{\partial \hat{\psi}}{\partial \mathbf{A}_{(1)}} * \dot{\mathbf{A}}_{(1)} + \underbrace{\frac{\partial \hat{\psi}}{\partial \mathbf{g}} \cdot \dot{\mathbf{g}} - \frac{1}{2\rho} \hat{\mathbf{t}} * \mathbf{A}_{(1)}}_{=0} \right\} - \frac{\hat{\mathbf{q}} \cdot \mathbf{g}}{T} \geq 0. \quad (5.3.22)$$

This inequality is linear in  $\dot{T}$  and  $\dot{\mathbf{g}}$ , which both may take any values; therefore the associated factors must necessarily vanish which we have indicated by the braces. The entropy production thus reduces to

$$\Gamma := -\rho \left( \frac{\partial \hat{\psi}}{\partial \mathbf{E}} * [\mathbf{LE} + \mathbf{EL}^T + \frac{1}{2} \mathbf{A}_{(1)}] + \frac{\partial \hat{\psi}}{\partial \mathbf{A}_{(1)}} * \dot{\mathbf{A}}_{(1)} - \frac{1}{2\rho} \hat{\mathbf{t}} * \mathbf{A}_{(1)} \right) - \frac{\hat{\mathbf{q}} \cdot \mathbf{g}}{T} \geq 0, \quad (5.3.23)$$

where for  $\dot{\mathbf{E}}$  the expression (5.3.10) was substituted. The remaining conditions are

$$\psi = \hat{\psi}(\mathbf{E}, \mathbf{A}_{(1)}, T), \quad \text{and} \quad \eta = -\frac{\partial \hat{\psi}}{\partial T}. \quad (5.3.24)$$

Consider next a situation of *thermostatic equilibrium*, characterized as a *time-independent process with*

*uniform distributions of temperature and velocity.* For such a process, the time derivative,  $\dot{\mathbf{A}}_{(1)}$  of  $\mathbf{A}_{(1)}$ , and the spatial gradients of the temperature,  $\mathbf{g}$  and velocity  $\mathbf{L}$  are equal to zero. Likewise, in a state of thermostatic equilibrium,  $\Gamma$  also vanishes, viz.,

$$\Gamma|_E := \Gamma(\mathbf{L} = \mathbf{0}, \dot{\mathbf{A}}_{(1)} = \mathbf{0}, \mathbf{g} = \mathbf{0}, T = \text{const}) = 0, \quad (5.3.25)$$

where  $\Gamma|_E$  indicates evaluation of  $\Gamma$  at thermostatic equilibrium. Consequently, the thermostatic equilibrium makes  $\Gamma$  a minimum with value zero:

$$\Gamma|_E = \Gamma|_{\min} = 0. \quad (5.3.26)$$

On the other hand, the extrema of a function may be found where its first derivatives with respect to the independent variables are equal to zero. We may immediately see that this function is  $\Gamma(\mathbf{A}_{(1)}, \dot{\mathbf{A}}_{(1)}, \mathbf{g})$ , thus we request

$$\left. \frac{\partial \Gamma}{\partial \mathbf{A}_{(1)}} \right|_{E=\min} = \left. \frac{\partial \Gamma}{\partial \dot{\mathbf{A}}_{(1)}} \right|_{E=\min} = \left. \frac{\partial \Gamma}{\partial \mathbf{g}} \right|_{E=\min} = \mathbf{0}, \quad (5.3.27)$$

as necessary conditions for the stationarity of  $\Gamma$ . In view of (5.3.23), equation (5.3.27) has the consequence

$$\left. \frac{\partial \psi}{\partial \mathbf{A}_{(1)}} \right|_{E=\min} = \mathbf{0}, \quad \text{and} \quad \mathbf{q}|_{E=\min} = \mathbf{0}. \quad (5.3.28)$$

There remains the term

$$-\rho \left( \frac{\partial \psi}{\partial \mathbf{E}} * [\mathbf{L}\mathbf{E} + \mathbf{E}\mathbf{L}^T + \frac{1}{2}\mathbf{A}_{(1)}] - \frac{1}{2\rho} \hat{\mathbf{t}} * \mathbf{A}_{(1)} \right), \quad (5.3.29)$$

and the condition

$$\left. \frac{\partial \Gamma}{\partial \mathbf{A}_{(1)}} \right|_{E=\min} = \mathbf{0}, \quad (5.3.30)$$

which must be evaluated. To do so, we write the term in parentheses of equation (5.3.29) in index form,

$$\frac{\partial \psi}{\partial E_{ij}} (L_{ik}E_{kj} + E_{ik}L_{jk} + \frac{1}{2}L_{ij} + \frac{1}{2}L_{ji}) - \frac{1}{2\rho} t_{ij} (L_{ij} + L_{ji}), \quad (5.3.31)$$

and differentiate with respect to  $\mathbf{L}$ , which is equivalent to condition (5.3.30), thus

$$\begin{aligned} & \frac{\partial}{\partial L_{uv}} \left( \frac{\partial \psi}{\partial E_{ij}} (L_{ik}E_{kj} + E_{ik}L_{jk} + \frac{1}{2}L_{ij} + \frac{1}{2}L_{ji}) - \frac{1}{2\rho} (t_{ij}L_{ij} + t_{ij}L_{ji}) \right) \\ &= \frac{\partial \psi}{\partial E_{ij}} \left( \delta_{iu}\delta_{vk}E_{kj} + E_{ik}\delta_{ju}\delta_{kv} + \frac{1}{2}\delta_{iu}\delta_{vj} + \frac{1}{2}\delta_{ju}\delta_{iv} \right) - \frac{1}{2\rho} t_{ij} (\delta_{iu}\delta_{vj} + \delta_{ju}\delta_{iv}) \\ &= \frac{\partial \psi}{\partial E_{ij}} (\delta_{iu}E_{vj} + E_{iv}\delta_{ju} + \frac{1}{2}(\delta_{iu}\delta_{vj} + \delta_{ju}\delta_{iv})) - \frac{1}{2\rho} t_{ij} (\delta_{iu}\delta_{vj} + \delta_{ju}\delta_{iv}) \\ &= \frac{\partial \psi}{\partial E_{uj}} E_{vj} + \frac{\partial \psi}{\partial E_{ui}} E_{iv} + \frac{1}{2} \left( \frac{\partial \psi}{\partial E_{uv}} + \frac{\partial \psi}{\partial E_{vu}} \right) - \frac{1}{\rho} t_{uv} = 0, \\ &\Rightarrow 2 \frac{\partial \psi}{\partial \mathbf{E}} \mathbf{E} + \frac{\partial \psi}{\partial \mathbf{E}} - \frac{1}{\rho} \mathbf{t} = \mathbf{0}. \end{aligned} \quad (5.3.32)$$

Solving (5.3.32) for  $\mathbf{t}$ , we can determine the stress in thermostatic equilibrium by the expression

$$\mathbf{t}|_E = \rho \left( 2 \frac{\partial \psi}{\partial \mathbf{E}} \mathbf{E} + \frac{\partial \psi}{\partial \mathbf{E}} \right). \quad (5.3.33)$$

Interestingly, this expression contains a term which is explicitly nonlinear in  $\mathbf{E}$ .

In thermostatic equilibrium, the heat flux  $\mathbf{q}|_E$  vanishes as seen in (5.3.28)<sub>2</sub>, and the equilibrium stress is derived solely from the Helmholtz free energy; and it is a function of the spatial strain tensor, temperature and density according to (5.3.33). To determine how the stress in non-equilibrium is related to its variables, we separate the Cauchy stress tensor additively as

$$\mathbf{t} = \mathbf{t}_E + \mathbf{t}_D, \quad (5.3.34)$$

where  $\mathbf{t}_E$  is the stress  $\mathbf{t}|_E$  as evaluated for values of  $\mathbf{E}$ ,  $T$  and  $\rho$  in the non-equilibrium process (this is the frozen elastic contribution) and  $\mathbf{t}_D$  describes the dissipative stress component necessarily of zero value at equilibrium, thus  $\mathbf{t}_D|_E = 0$ .

We retrieve the thermodynamic conditions for the dissipative stress by re-substituting (5.3.34) into (5.3.23), which yields

$$-\rho \left\{ \frac{\partial \psi}{\partial \mathbf{E}} * [\mathbf{L}\mathbf{E} + \mathbf{E}\mathbf{L}^T + \frac{1}{2}(\mathbf{L} + \mathbf{L}^T)] - \frac{1}{2\rho} (\mathbf{t}_E + \mathbf{t}_D) * \mathbf{A}_{(1)} + \frac{\partial \psi}{\partial \mathbf{A}_{(1)}} * \dot{\mathbf{A}}_{(1)} \right\} - \frac{\mathbf{q} \cdot \mathbf{g}}{T} \geq 0. \quad (5.3.35)$$

We evaluate the above expression using (5.3.33) as

$$\begin{aligned} & -\rho \left\{ \frac{\partial \psi}{\partial \mathbf{E}} * [\mathbf{L}\mathbf{E} + \mathbf{E}\mathbf{L}^T + \frac{1}{2}(\mathbf{L} + \mathbf{L}^T)] \right. \\ & \quad \left. - \frac{1}{2\rho} \left( \left[ 2\rho \frac{\partial \psi}{\partial \mathbf{E}} \mathbf{E} + \rho \frac{\partial \psi}{\partial \mathbf{E}} \right] + \mathbf{t}_D \right) * (\mathbf{L} + \mathbf{L}^T) + \frac{\partial \psi}{\partial \mathbf{A}_{(1)}} * \dot{\mathbf{A}}_{(1)} \right\} - \frac{\mathbf{q} \cdot \mathbf{g}}{T} \geq 0 \\ & = -\rho \left\{ \frac{\partial \psi}{\partial \mathbf{E}} * \mathbf{L}\mathbf{E} + \frac{\partial \psi}{\partial \mathbf{E}} * \mathbf{E}\mathbf{L}^T + \frac{1}{2} \frac{\partial \psi}{\partial \mathbf{E}} * \mathbf{L} + \frac{1}{2} \frac{\partial \psi}{\partial \mathbf{E}} * \mathbf{L}^T \right. \\ & \quad \left. - \left( \left[ \frac{\partial \psi}{\partial \mathbf{E}} \mathbf{E} * \mathbf{L} + \frac{\partial \psi}{\partial \mathbf{E}} \mathbf{E} * \mathbf{L}^T + \frac{1}{2} \frac{\partial \psi}{\partial \mathbf{E}} * \mathbf{L} + \frac{1}{2} \frac{\partial \psi}{\partial \mathbf{E}} * \mathbf{L}^T \right] + \frac{1}{2\rho} \mathbf{t}_D * \mathbf{A}_{(1)} \right) \right. \\ & \quad \left. + \frac{\partial \psi}{\partial \mathbf{A}_{(1)}} * \dot{\mathbf{A}}_{(1)} \right\} - \frac{\mathbf{q} \cdot \mathbf{g}}{T} \geq 0 \\ & = -\rho \left\{ -\frac{1}{2\rho} \mathbf{t}_D * \mathbf{A}_{(1)} + \frac{\partial \psi}{\partial \mathbf{A}_{(1)}} * \dot{\mathbf{A}}_{(1)} \right\} - \frac{\mathbf{q} \cdot \mathbf{g}}{T} \geq 0, \end{aligned} \quad (5.3.36)$$

obtaining the residual inequality condition for the non-equilibrium stress  $\mathbf{t}_D$

$$\frac{1}{2} \mathbf{t}_D * \mathbf{A}_{(1)} - \rho \frac{\partial \psi}{\partial \mathbf{A}_{(1)}} * \dot{\mathbf{A}}_{(1)} - \frac{\mathbf{q} \cdot \mathbf{g}}{T} \geq 0. \quad (5.3.37)$$

Formally, this imbalance represents the same thermodynamic inequality, which holds for the MSOFM by Sun (1987). However, in our case, the material is not a density-preserving fluid without temperature dependence as Man and Sun (1987) have considered. Nonetheless, we may recover the equivalent exploitation of (5.3.37) explicitly worked out by Sun (1987) by introducing the following assumptions:

### Postulates:

We assume that

- (1) the dissipative stress  $\mathbf{t}_D$  neither depends on the temperature gradient  $\mathbf{g}$ , nor on the spatial strain tensor  $\mathbf{E}$ .
- (2) the heat flux vector  $\mathbf{q}$  be not a function of  $\mathbf{E}$ ,  $\mathbf{A}_{(1)}$  and  $\mathbf{A}_{(2)}$ :  $\mathbf{q} = \hat{\mathbf{q}}(T, \|\mathbf{g}\|)$ .
- (3) the functional dependence of the Helmholtz free energy can be additively decomposed as

$$\psi = \hat{\psi}(\mathbf{E}, \mathbf{A}_{(1)}, T) = \hat{\psi}_1(\mathbf{E}, T) + \hat{\psi}_2(\mathbf{A}_{(1)}, T). \quad (5.3.38)$$

(4) the component  $\psi_2$  of the Helmholtz free energy is a convex function of its argument  $\mathbf{A}_{(1)}$ .

With postulates (1) and (2), inequality (5.3.37) is equivalent to the imbalances

$$\mathbf{q} \cdot \mathbf{g} \leq 0, \quad (5.3.39)$$

$$\frac{1}{2} \mathbf{t}_D * \mathbf{A}_{(1)} - \rho \frac{\partial \hat{\psi}_2}{\partial \mathbf{A}_{(1)}} * \dot{\mathbf{A}}_{(1)} \geq 0. \quad (5.3.40)$$

Furthermore, postulate (3) and equation (5.3.33) imply

$$\mathbf{t}|_E = \rho \left( 2 \frac{\partial \hat{\psi}_1}{\partial \mathbf{E}} \mathbf{E} + \frac{\partial \hat{\psi}_1}{\partial \mathbf{E}} \right). \quad (5.3.41)$$

If  $\mathbf{q} = -\kappa(T, \|\mathbf{g}\|) \mathbf{g}$ , the imbalance (5.3.39) implies

$$\kappa(T, \mathbf{0}) = \kappa|_E \geq 0. \quad (5.3.42)$$

Alternatively, (5.3.41) allows, via the postulation of a functional relation for  $\hat{\psi}_1(\mathbf{E}, T)$ , evaluation of the equilibrium stress tensor<sup>4</sup>. The significant inequality is (5.3.40), which, together with postulate (4), is mathematically analogous to a corresponding inequality of Man and Sun for their modified second order fluid model. Sun (1987) formulated the complete exploitation of the thermodynamic compatibility for the MSOFM, following the work of Dunn and Fosdick (1974) who performed the thermodynamic exploitation for general second order fluids.

Since the above postulate establishes mathematically the identical prerequisites for the TMSOIM as that of Sun (1987) for the MSOFM, there is no need to repeat the analysis here as well. We restrict ourselves to present the essential inferences listed in the framed box on page 73.

---

<sup>4</sup>Note however that the entropy is determined by both  $\hat{\psi}_1$  and  $\hat{\psi}_2$ , if  $\hat{\psi}_2$  depends on temperature.

- The Helmholtz free energy  $\psi_2$  is a convex function of  $\mathbf{A}_{(1)}$ ; therefore, possible forms for  $\psi_2$  and correspondingly the entropy  $\eta$  satisfy

$$\begin{aligned} (I), \quad \hat{\psi}_2(T, \mathbf{A}_{(1)}) &= \hat{\psi}_2(T, \mathbf{0}) + \alpha_1(T) \frac{|\mathbf{A}_{(1)}|^2}{4\rho}, \\ (II), \quad \hat{\psi}_2(T, \mathbf{A}_{(1)}) &= \hat{\psi}_2(T, \mathbf{0}) + \alpha_1(T) \frac{|\mathbf{A}_{(1)}|^{2+m}}{2^{1+\frac{m}{2}}(2+m)\rho}, \\ \hat{\eta} &= -\frac{\partial \hat{\psi}(T, \mathbf{A}_{(1)})}{\partial T} = -\frac{\partial}{\partial T} (\hat{\psi}_1(\mathbf{E}, T) + \hat{\psi}_2(T, \mathbf{A}_{(1)})). \end{aligned} \quad (5.3.43)$$

- The coefficients  $\mu(T)$ ,  $\alpha_1(T)$  and  $\alpha_2(T)$  satisfy the conditions

$$\mu(T) \geq 0, \quad \alpha_1(T) \geq 0, \quad \alpha_1(T) + \alpha_2(T) = 0, \quad (5.3.44)$$

for general, *unrestricted motions*. *Slow creep in the neighborhood of thermostatic equilibrium* requires the sum  $|\alpha_1(T) + \alpha_2(T)|$  to be small as

$$\begin{aligned} (I) \quad |\alpha_1(T) + \alpha_2(T)| &\leq \left(\frac{1}{2}\right)^{\frac{m}{2}} \sqrt{6} \frac{\mu(T)}{|\mathbf{A}_{(1)}|^{1-m}}, \\ (II) \quad |\alpha_1(T) + \alpha_2(T)| &\leq \sqrt{6} \frac{\mu(T)}{|\mathbf{A}_{(1)}}. \end{aligned} \quad (5.3.45)$$

- The residual inequality reads as

$$\frac{1}{2} \mathbf{t}_D * \mathbf{A}_{(1)} - \rho \frac{\partial \psi_2}{\partial \mathbf{A}_{(1)}} * \dot{\mathbf{A}}_{(1)} - \frac{\mathbf{q} \cdot \mathbf{g}}{T} \geq 0, \quad (5.3.46)$$

and if  $\mathbf{q}$  is not allowed to be a function of  $\mathbf{E}$ ,  $\mathbf{A}_{(1)}$  and  $\mathbf{A}_{(2)}$ , the Fourier law of heat conduction applies in the form

$$\mathbf{q} = -\kappa(T, \|\mathbf{g}\|) \mathbf{g}, \quad \kappa \geq \kappa|_E = 0. \quad (5.3.47)$$

### 5.3.4 Constitutive Function for the Thermo-Viscoelastic Modified Second Order Isotropic Material (TMSOIM)

We now gather the explicit expressions on the stress-strain relationship for the constitutive function of the TMSOIM. To describe the elastic stress contribution, we consider a polynomial expansion for the Helmholtz free energy part  $\psi_1$  as

$$\psi_1(E_{ij}, T') = \psi_{10} + \psi_{11}^{ij} E_{ij} + \frac{1}{2} \psi_{12}^{ijkl} E_{ij} E_{kl} + \psi_{13} T' + \psi_{14}^{ij} T' E_{ij} + \frac{1}{2} \psi_{15} T'^2, \quad (5.3.48)$$

in which  $\psi_{11}^{ij}$ ,  $\psi_{14}^{ij}$  and  $\psi_{12}^{ijkl}$  are the constant isotropic coefficients

$$\psi_{11}^{ij} = \psi_{11} \delta_{ij}, \quad \psi_{14}^{ij} = \psi_{14} \delta_{ij}, \quad \psi_{12}^{ijkl} = \psi_{12}^{(1)} \delta_{ij} \delta_{kl} + \psi_{12}^{(2)} (\delta_{ik} \delta_{jl} + \delta_{il} \delta_{jk}), \quad (5.3.49)$$

so that

$$\psi_1 = \psi_{10} + \psi_{11} E_{ii} + \frac{1}{2} \left( \psi_{12}^{(1)} E_{ii} E_{kk} + 2 \psi_{12}^{(2)} E_{kj} E_{kj} \right) + \psi_{13} T' + \psi_{14} T' E_{ii} + \frac{1}{2} \psi_{15} T'^2. \quad (5.3.50)$$

In these relations,  $T' = T - T_0$ , is the temperature deviation from a uniform constant reference temperature  $T_0$ . The coefficient functions  $\psi_{10}, \dots, \psi_{15}$  are treated as constants. The elastic stress is now obtained from (5.3.41) and (5.3.50) by evaluating

$$\frac{\partial \psi_1}{\partial E_{pq}} = (\psi_{11} + \psi_{14} T') \delta_{pq} + \psi_{12}^{(1)} E_{kk} \delta_{pq} + 2 \psi_{12}^{(2)} E_{pq}. \quad (5.3.51)$$

This yields in view of (5.3.41)

$$(t|_E)_{ij} = \rho \left\{ \left( \psi_{11} + \psi_{14} T' + \psi_{12}^{(1)} E_{kk} \right) \delta_{ip} + 2 \psi_{12}^{(2)} E_{ip} \right\} \{ 2 E_{pj} + \delta_{pj} \}. \quad (5.3.52)$$

We then rewrite (5.3.52) as

$$(t|_E)_{ij} = \rho \left\{ 2 \left( \psi_{11} + \psi_{14} T' + \psi_{12}^{(1)} E_{kk} \right) E_{ij} + 4 \psi_{12}^{(2)} E_{ip} E_{pj} \right. \\ \left. + \left( \psi_{11} + \psi_{14} T' + \psi_{12}^{(1)} E_{kk} \right) \delta_{ij} + 2 \psi_{12}^{(1)} E_{ij} \right\},$$

and with  $\psi_{12}^{(1)} := \frac{1}{\rho} (\mathbf{K} - \frac{2}{3} \mathbf{G})$  and  $\psi_{12}^{(2)} := \frac{1}{\rho} \mathbf{G}$ , the above expression becomes

$$(t|_E)_{ij} = \rho \left\{ 2 \left( \psi_{11} + \psi_{14} T' + \frac{1}{\rho} (\mathbf{K} - \frac{2}{3} \mathbf{G}) E_{kk} \right) E_{ij} + \frac{4}{\rho} \mathbf{G} E_{ip} E_{pj} \right. \\ \left. + \left( \psi_{11} + \psi_{14} T' + \frac{1}{\rho} (\mathbf{K} - \frac{2}{3} \mathbf{G}) E_{kk} \right) \delta_{ij} + \frac{2}{\rho} \mathbf{G} E_{ij} \right\} \\ = 2 \rho (\psi_{11} + \psi_{14} T') E_{ij} + 2 (\mathbf{K} - \frac{2}{3} \mathbf{G}) E_{kk} E_{ij} + 4 \mathbf{G} E_{ip} E_{pj} \\ + \rho (\psi_{11} + \psi_{14} T') \delta_{ij} + (\mathbf{K} - \frac{2}{3} \mathbf{G}) E_{kk} \delta_{ij} + 2 \mathbf{G} E_{ij} \\ = \rho (\psi_{11} + \psi_{14} T') (2 E_{ij} + \delta_{ij}) + \mathbf{K} E_{kk} \delta_{ij} + 2 \mathbf{G} (E_{ij} - \frac{1}{3} E_{kk} \delta_{ij}) \\ + 2 \mathbf{K} E_{kk} E_{ij} + 4 \mathbf{G} (E_{ip} E_{pj} - \frac{1}{3} E_{kk} E_{ij}),$$

and if we substitute  $B_{ij} = (2 E_{ij} + \delta_{ij})$ ,

$$(t|_E)_{ij} = \underbrace{\rho (\psi_{11} + \psi_{14} T') B_{ij}}_{\text{pre- and thermal stress}} + \underbrace{\mathbf{K} E_{kk} \delta_{ij} + 2 \mathbf{G} (E_{ij} - \frac{1}{3} E_{kk} \delta_{ij})}_{\text{Hooke stress}} \\ + \underbrace{2 \mathbf{K} E_{kk} E_{ij} + 4 \mathbf{G} (E_{ip} E_{pj} - \frac{1}{3} E_{kk} E_{ij})}_{\text{non-linear elastic stress}}, \quad (5.3.53)$$

or,

$$\mathbf{t}|_E = 2 \rho (\psi_{11} + \psi_{14} T') \mathbf{B} + \mathbf{K} \text{tr}(\mathbf{E}) \mathbf{I} + 2 \mathbf{G} (\mathbf{E} - \frac{1}{3} \text{tr}(\mathbf{E}) \mathbf{I}) \\ + 2 \mathbf{K} \text{tr}(\mathbf{E}) \mathbf{E} + 4 \mathbf{G} (\mathbf{E}^2 - \frac{1}{3} \text{tr}(\mathbf{E}) \mathbf{E}). \quad (5.3.54)$$

Evidently, the elastic stress consists of three contributions. The first term on the right-hand side of (5.3.53) is the pre-stress plus thermal stress due to an initial pressure distribution and a temperature variation. As time goes on and the deformation evolves, this term changes as the temperature deviation  $T'$  and the left Cauchy-Green deformation tensor  $B_{ij}$  evolve. The second term is the classical Hooke stress, comprising two components due to compressibility ( $K$ ) and shearing ( $G$ ).  $K$  and  $G$  are called the *bulk* and the *shear modulus*. The bulk and shear modulus can also be related via the Poisson ratio  $\nu$  as

$$K = 2G \frac{(1+\nu)}{3(1-2\nu)}, \quad (5.3.55)$$

and  $\nu$  may vary between 0.3 for perfect elastic behaviour, to 0.5 for ductile incompressible fluid-like behaviour (e.g. Squire et al., 1990). The third term on the right hand side of (5.3.53) describes non-linear elastic behaviour and is neglected. With  $\mathbf{E}' = \mathbf{E} - \frac{1}{3} \text{tr}(\mathbf{E}) \mathbf{I}$  as the deviatoric strain (with  $\text{tr}(\mathbf{E}) = 0$ ), we write the relation (5.3.54) as

$$\begin{aligned} \mathbf{t}_E &= \lambda(T) \mathbf{B} + 2G \frac{(1+\nu)}{3(1-2\nu)} \text{tr}(\mathbf{E}) \mathbf{I} + 2G \left( \mathbf{E} - \frac{1}{3} \text{tr}(\mathbf{E}) \mathbf{I} \right) \\ &= \lambda(T) \mathbf{B} + 2G \left( \frac{1+\nu}{3(1-2\nu)} \text{tr}(\mathbf{E}) \mathbf{I} + \mathbf{E}' \right) \\ &= \lambda(T) \mathbf{B} + \beta \left( \frac{1+\nu}{3(1-2\nu)} \text{tr}(\mathbf{E}) \mathbf{I} + \mathbf{E}' \right). \end{aligned}$$

For simplification, we used  $\beta = 2G$  and the thermo-mechanical pre-stress term in (5.3.54) was condensed as

$$\lambda(T') = 2\rho (\psi_{11} + \psi_{14} T'). \quad (5.3.56)$$

The elastic stress contribution is now inserted in the constitutive equations (5.3.3) and (5.3.4) of the MSOFM to obtain the constitutive equations for the TMSOIM. They read

$$(I), \quad \mathbf{t} = -p \mathbf{I} + \eta(\mathbf{A}_{(1)}) \mathbf{A}_{(1)} + \alpha_1 \mathbf{A}_{(2)} + \alpha_2 \mathbf{A}_{(1)}^2 + \lambda(T') \mathbf{B} + \beta \left( \mathbf{E}' + \frac{1+\nu}{3(1-2\nu)} \text{tr}(\mathbf{E}) \mathbf{I} \right), \quad (5.3.57)$$

$$(II), \quad \mathbf{t} = -p \mathbf{I} + \eta(\mathbf{A}_{(1)}) (\mathbf{A}_{(1)} + \alpha_1 \mathbf{A}_{(2)} + \alpha_2 \mathbf{A}_{(1)}^2) + \lambda(T') \mathbf{B} + \beta \left( \mathbf{E}' + \frac{1+\nu}{3(1-2\nu)} \text{tr}(\mathbf{E}) \mathbf{I} \right), \quad (5.3.58)$$

with the power-law viscosity

$$\eta(\mathbf{A}_{(1)}) = \mu \left( \frac{1}{2} \text{tr} \mathbf{A}_{(1)}^2 \right)^{\frac{m}{2}}, \quad (5.3.59)$$

and the material parameters  $\mu$ ,  $m$ ,  $\alpha_1$ ,  $\alpha_2$ ,  $\lambda$ ,  $G$ , and  $\nu$ .

### Model parameter identifications

In the TMSOIM equations (5.3.57) and (5.3.58), the parameter set can readily be reduced by one due to the thermodynamic constraint  $\alpha_2 = -\alpha_1$ . Several authors have made attempts to identify the elastic constants of ice, of which R othlisberger (1972) gives a summary. From Hutter (1983) we extract a temperature-dependent estimate of the elastic shear modulus  $G$ , computed from the collected data in R othlisberger (1972) as

$$G(T) = 3500 \times (1 - 0.00146T) \text{ MPa}, \quad (5.3.60)$$

where temperature  $T$  is in centigrades. However, the variation with temperature is small and can be neglected (Hutter, 1983). Schulson and Duval (2009) also give an estimate of the shear modulus as  $G = 3500$  MPa. The pre-stress parameter  $\lambda(T')$  describes a certain boundary/initial configuration and the influence of temperature. It may be put to zero if any preceding loading conditions and thermal effects are to be ignored.

Model	$\mu$	$\alpha_1$
(I)	2.41 MPa d <sup>1/3</sup>	161.0 MPa d <sup>2</sup>
(II)	2.43 MPa d <sup>1/3</sup>	3.0 MPa d <sup>4/3</sup>

Table 5.1: Mean least-square estimates on the parameters  $\mu$  and  $\alpha_1$  for the MSOF models (I) and (II) for fixed  $m = -2/3$  and the condition  $\alpha_1 + \alpha_2 = 0$ .

Considering the viscous material parameters, Kjartason (1986) conducted pressure meter experiments. In a pressure meter, a small cylindrical cavity inside a large cylindrical body of ice is pressurized and the increase of the cavity radius due to ice creep is measured. Multiple experiments at  $T = -2^\circ\text{C}$  and different cavity pressures have been conducted, each lasting one day. Sun (1987) first estimated the parameters  $\mu$  and  $m$  from Kjartason by using nonlinear regression methods on the experimental creep function in a steady-state and secondary creep phase data and obtained

$$\mu = 9114 \text{ kPa}(\text{min})^{1+m}, \quad \text{and} \quad m = -0.7111. \quad (5.3.61)$$

He then used the fixed values of  $\mu$  and  $m$  to fit a third-order in time polynomial function to the experimental results in the primary creep phase and calculated  $\alpha_1$  for both models (I) and (II) as

$$\alpha_1^I = 2.562 \times 10^8 \text{ kPa}(\text{min})^2, \quad (I), \quad (5.3.62)$$

$$\alpha_1^{II} = 1.255 \times 10^5 \text{ kPa}(\text{min})^{1+m}, \quad (II). \quad (5.3.63)$$

By the nature of the pressure meter experiments, it is not possible to determine the parameter  $\alpha_2$ . McTigue et al. (1985) carried out triaxial experiments, where a prolate cylindrical ice sample under ambient pressure is loaded by an axial stress and its change in length is measured. Again, from the experimental setup, a characteristic creep function can be determined. McTigue et al. performed the parameter identifications of  $\mu$ ,  $\alpha_1$ , and  $\alpha_2$  for the case of a second order fluid model with  $m = 0$ . However, their results have been criticized to be insufficient and may suffer from over-parametrization. Man and Sun (1987) have overcome this problem by fixing the parameter  $m = -2/3$ , corresponding to an exponent  $n = 3$  in GLEN's flow law. Further, in using the thermodynamic restrictions for creep close to equilibrium, the sum  $|\alpha_1 + \alpha_2|$  is considered to be small, hence the related terms in the experimental creep function were neglected. A minimization routine on the creep data under the conditions of  $m = -2/3$  and  $\alpha_1 + \alpha_2 = 0$  was performed to obtain least square estimates for  $\mu$  and  $\alpha_1$ . The resulting mean estimates of the four experiments of McTigue et al. are given in Tab. 5.1 for the MSOFM (I) and (II).

In summary, we impose a priori the following restrictions on the set of parameters:

$$\alpha_2 = -\alpha_1, \quad \nu = 0.5, \quad m = -\frac{2}{3}, \quad (5.3.64)$$

A poisson ratio of  $\nu = 0.5$  will lead to a vanishing trace of the strain tensor  $\mathbf{E}$ . Thus, only deviatoric strains are considered and elastic deformations are limited to shearing.

## 5.4 Summary

We briefly recapitulated the basic tools of describing the behavior and deformation of a material in terms of Continuum Mechanics. We pointed out the concepts of objectivity (frame-indifference) and material symmetry which are fundamental in setting up a valid constitutive relation for various classes of materials by using the corresponding correct objective measures of stress, strain and deformation. From our observations on the lake drainage of Gornergletscher and the rapid changes in ice flow we conjecture the importance of rapid changes of strain. Thus, we use the constitutive formulation of Sun (1987) of two modified second order fluid models which relate stress to strain rates and strain accelerations as a basis for describing the ice rheology. The modified second order fluid models of Sun (1987) incorporate an

objective material derivative of the stretching tensor and its quadratic form, which results in a non-coaxial state between the stress and stretching tensor. This constitutive relation is able of reproducing primary creep, secondary creep and second order effects (e.g. normal stress differences, see Man and Sun, 1987). This is contrary to the usually employed constitutive relation of Glen, where stress and stretching tensor are collinear. However, the modified second order fluid models of Sun (1987) reduce to power law type relations according to Glen's flow law, when ignoring second grade properties.

To include possible relaxation of the ice and test the hypothesis of elastic effects being partly responsible for our observations, we extended the constitutive relation of Sun (1987) to also explicitly depend on strain. Exploring the entropy principle in form of the Clausius-Duhem inequality for the extended constitutive class has shown that the elastic stress contribution can be determined as a function of strain and thermodynamic potential. We retrieved the essential thermodynamic residual imbalance, which is a function of strain rates, strain accelerations, heat flux, temperature and dissipative stress (the non-elastic stress contribution). The residual inequality is very similar to that derived by Sun (1987) for the modified second order fluid models. To obtain complete agreement, we have therefore postulated important attributes of the constitutive quantities of dissipative stress, heat flux and thermodynamic potential to simplify and reduce the further exploration of the imbalance to the same case as the modified second order fluid models of Sun (1987). As one of these postulates, the thermodynamic potential (here as the Helmholtz free energy) must be a sum of the contributions to the entropy production by strain and strain rate. The part depending on strain rate is thus a function of the strain rates (the Rivlin-Ericksen tensor  $\mathbf{A}_{(1)}$ ) alone and is given in the form derived by Sun (1987). For the component of the thermodynamic potential arising from strain, we proposed an appropriate function of the Finger strain tensor  $\mathbf{E}$  and subsequently recovered the elastic stress-deformation relation. The constitutive relation for the elastic contribution consists of three terms of which we keep the two linear terms in  $\mathbf{E}$ ; a Hooke-type elasticity law and a term describing thermoelastic effects and boundary conditions. However, we must note that the elastic law is linear in the strain tensor  $\mathbf{E}$ , but not in the displacement, as  $\mathbf{E}$  is a non-linear function of the deformation gradient  $\mathbf{F}$ . Combination of the elasticity relation and the modified second order fluid relation yields the constitutive relation for the Thermoelastic Modified Second Order Isotropic Material, given in (5.3.54). It relates stress to strain, strain rates, strain accelerations and temperature, where we consider heat conduction in the form of Fourier's law. The advantage of the constitutive function for the Thermoelastic Modified Second Order Isotropic Material (TMSOIM) is its decoupled formulation. The effects of elasticity and transient viscous behaviour of first and second grade, and their influence with temperature variation can all be studied either separately or combined, allowing us to determine the exact implications of the respective material property on the rapid changes of ice flow in terms of the observations.

The TMSOIM is a very general constitutive equation of a thermo-viscoelastic material. The theory was outlined for the inclusion of thermo-mechanical effects which may also significantly impact the material behaviour besides the complexity of a viscoelastic ice rheology with transient effects. However, in the subsequent chapter the constitutive relation is solved numerically. As a simplification, we ignore the temperature-dependency of the constitutive equation and constrict the process under consideration to isothermal conditions at uniform temperature. The focus is thus put on the transient effects generated by the proposed relation, and the constitutive function of the Cauchy stress tensor will then only be a function of  $\mathbf{E}$ ,  $\mathbf{A}_{(1)}$ , and  $\mathbf{A}_{(2)}$ , whereas the dependency on  $T$  and  $\mathbf{g}$  is ignored. This simplification of the TMSOIM is referred to as elastic modified second order isotropic material (EMSOIM), and is described in the following chapter (Sect. 6.3).



## Chapter 6

# Creep responses of the viscoelastic model in uni-directional shearing flow

This chapter is published in a slightly modified form. Original title and citation are:

Riesen, P., Hutter, K., and Funk, M.: A viscoelastic Rivlin-Ericksen material model applicable to glacier ice (2010), *Nonlin. Processes Geophys.*, 17, 673-684, doi:10.5194/npg-17-673-2010.

**Abstract** We present a viscoelastic constitutive relation which describes transient creep of a modified second grade fluid enhanced with elastic properties of a solid. The material law describes a Rivlin-Ericksen material and is a generalization of existing material laws applied to study the viscoelastic properties of ice. The intention is to provide a formulation tailored to reproduce the viscoelastic behavior of ice ranging from the instantaneous elastic response, to recoverable deformation, to viscous, stationary flow at the characteristic minimum creep rate associated with the deformation of polycrystalline ice. We numerically solve the problem of a slab of material shearing down a uniformly inclined plate. The equations are made dimensionless in a form in which elastic effects and/or the influence of higher order terms (i.e., strain accelerations) can be compared with viscous creep at the minimum creep rate by means of two dimensionless parameters. We discuss the resulting material behavior and the features exhibited at different parameter combinations. Also, a viable range of the non-dimensional parameters is estimated in the scale analysis.

### 6.1 Introduction

Creep of ice is an inevitable issue when dealing with glaciers and terrestrial ice masses. From the pioneering work in the 1950s (Glen, 1952; Nye, 1953; Steinemann, 1958), the viscous constitutive relation for stationary creep of ice has emerged, which, in the glaciology community, is referred to as Glen's flow law. The Glen flow law is a generalized Newtonian material model (e.g. Crochet et al., 1984) with power-law viscosity and is widely used when modeling the flow of glaciers, ice streams and ice sheets at any spatial and temporal scale, in spite of its constraint to only predict a stationary stress/strain rate relation at the minimum creep rate observed in laboratory creep experiments. However, laboratory experiments on creep of ice conducted in the past consistently revealed non-stationary creep of ice (e.g. Jellinek and Brill, 1956; Mellor and Cole, 1982; Jacka, 1984).

Several attempts were made to describe the transient creep of polycrystalline ice observed in laboratory creep experiments by viscoelastic constitutive equations, relating strain rates, strain, stress and time in different ways. Nonlinear, time-dependent constitutive relations describing creep behavior observed in uni-axial compression tests at constant load were given by Sinha (1978) and Le Gac and Duval (1980), and reviewed in Ashby and Duval (1985). The work of Szyszkowski and Glockner (1985) considered a nonlinear constitutive equation based on spring and dash-pot elements. A description of the transient strain rate as a nonlinear power-law function of stress and strain was proposed by Azizi (1989). Shyam-

Sunder and Wu (1989a,b) published a differential flow model, and in Shyam-Sunder and Wu (1990) it was compared with the models of Sinha, and Le Gac and Duval. Later on, Meyssonier and Goubert (1994) took up the models of Le Gac and Duval, and Shyam-Sunder and Wu and proposed some modifications. While the early attempts of the aforementioned models describe only uni-axial creep responses, and lack an obvious generalization to multi-axial creep states (e.g. Sinha), the more recent models of Le Gac and Duval; Shyam-Sunder and Wu, and Meyssonier and Goubert, include one or more state variables which must be modeled by additional differential equations. Morland (1979) and Morland and Spring (1981) proposed constitutive equations of rate type (Lockett, 1972; Hutter, 1983) to describe the viscoelastic responses of isotropic polycrystalline ice. They considered constitutive relations which relate stress and stress rates to either strain rates and strain accelerations, which is a fluid type model (Morland and Spring, 1981), or else to strain and strain rates, i.e. a solid type model (Spring and Morland, 1982). These models are capable of reproducing idealized decelerating (primary), stationary (secondary) and accelerating (tertiary) creep responses, but were not applied to real creep data. If stress rates are excluded from the constitutive relation and the stress is considered only a function of the strain rates, strain accelerations, and possibly higher order derivatives, the relation then describes a fluid of differential type (Rivlin and Ericksen, 1955). These fluids are also known as fluids of grade  $N$  (e.g. Joseph, 1990), or, order fluids (Owens and Phillips, 2002). The incompressible second grade fluid model (fluid of grade 2) was first applied to creep experiments and ice mechanics by McTigue et al. (1985), who investigated the relevance of normal stress differences in shearing flow. However, the second grade fluid model has no strain rate-dependent viscosity. Man and Sun (1987) thereupon postulated a modified second grade fluid with power-law viscosity. The relation of Man and Sun describes primary and secondary creep, and the material behavior asymptotes to a Glen-like power-law fluid model for vanishing second order terms. For ice, Sun estimated the phenomenological coefficients for the modified second grade fluid model with power-law viscosity from triaxial laboratory creep experiments (see also Sections 5.3.4 and 5.4).

In recent field observations on an Alpine glacier (Gornergletscher, Switzerland), repeated near-reversal of flow, accompanied by reversed displacement direction was observed (Sugiyama et al., 2007a, 2008). The change of motion takes place within a few days during the periodical drainage of a supra-glacial lake, and is possibly related to the unloading and stress redistribution during the rapid drainage. The question was raised whether the retrograde movement may be attributed to viscoelastic recovery properties of the ice. To elaborate on this hypothesis, an appropriate viscoelastic constitutive model for glacier ice is needed, preferably applicable to multi-axial deformations. No attempt has been made so far to take into account transient, recoverable deformation effects when an external load (e.g. a forming and draining lake) is applied to and removed from a glacier. This was our motivation to construct a simple constitutive formulation with a material response varying smoothly in between the limits of ice behaving as a viscous fluid on long time scales, and ice behaving as an elastic solid on short time scales. We here propose a constitutive model able to predict instantaneous elastic strain followed by recoverable, transient strain fading into a steady creep response associated with the stationary minimum creep rate of ice, based on a further generalization of the modified second grade fluid of Man and Sun (1987). A tertiary response with increasing strain rate after the minimum strain rate is not considered. Ultimately, we target to corroborate whether glacier ice allows for deformations such as those observed. By now, we develop the constitutive relation aimed for, and investigate it in a numerical example. The possible range of parameters is collected and the characteristics which can be exhibited by the rheological model are illustrated.

## 6.2 Constitutive relations

In our description we use the Eulerian notation. The kinematic measures used are summarized in Table 6.1, following Lockett (1972) and Hutter and Jöhnk (2004). Before we discuss the proposed generalized constitutive relation, we now quote the relations for the already mentioned material laws. In general, the ice is assumed an incompressible material, which introduces the pressure as an independent

	Symbol	Measure
(i)	$\mathbf{X} = (X, Y, Z)$	Particle coordinates in the reference configuration
(ii)	$\mathbf{x} = (x, y, z)$	Position coordinates in the present configuration
(iii)	$\mathbf{F} = \partial\mathbf{x}/\partial\mathbf{X}$	Deformation gradient
(iv)	$\mathbf{B} = \mathbf{F}\mathbf{F}^T$	Left Cauchy-Green deformation tensor
(v)	$\mathbf{E} = \frac{1}{2}(\mathbf{B} - \mathbf{I})$	Finger strain tensor
(vi)	$\mathbf{L} = \text{grad}(\mathbf{v}) = \dot{\mathbf{F}}\mathbf{F}^{-1}$	Velocity gradient
(vii)	$\mathbf{D} = \frac{1}{2}(\mathbf{L} + \mathbf{L}^T)$	Strain rate (Stretching) tensor
(viii)	$\mathbf{A}_{(n)} = \dot{\mathbf{A}}_{(n-1)} + \mathbf{A}_{(n-1)}\mathbf{L} + \mathbf{L}^T\mathbf{A}_{(n-1)}$	$n$ -th Rivlin-Ericksen tensor
(ix)	$\text{tr}(\cdot)$	The trace of a measure, i.e. $\text{tr}(\mathbf{D}) = D_{ii}$

Table 6.1: Definition of kinematic tensor quantities in Eulerian notation. In index notation, the tensor quantity is non-bold and indexed (i.e.  $\mathbf{L} \hat{=} L_{ij}$ ). The material derivative ( $\dot{\cdot}$ ) is given as  $\frac{\partial(\cdot)}{\partial t} + v_j \cdot (\cdot)_{,j}$ , where  $\mathbf{v} \hat{=} v_j$  is the velocity. Note that for (viii), we have  $\mathbf{A}_{(0)} = \mathbf{I}$ , and  $\mathbf{A}_{(1)} = 2\mathbf{D}$ .

field, absorbing any isotropic stress contribution.

### 6.2.1 Glen's flow law

In Glen's flow law, the Cauchy stress tensor  $\mathbf{t}$  is given by the relation

$$\mathbf{t} = -p\mathbf{I} + \hat{\eta}(\mathbf{D})\mathbf{D}, \quad \text{where} \quad \hat{\eta}(\mathbf{D}) = B \left( \frac{1}{2} \text{tr}(\mathbf{D}^2) \right)^{\frac{1-n}{2n}}. \quad (6.2.1)$$

Here,  $p$  is the pressure due to the incompressibility constraint,  $\mathbf{I}$  is the identity tensor,  $\hat{\eta}(\mathbf{D})$  the strain rate-dependent power-law viscosity,  $B$  a constant, and  $n$  the power-law exponent. For  $n \neq 1$ , the material model becomes non-Newtonian. This relation is valid for all times; obviously it can merely describe stationary creep. For the monotonic secondary creep regime of ice, a value of  $n = 3$  is commonly used. The parameter  $B$  is in the range of 1.2 to 2.9 MPa d<sup>3</sup> for ice at temperatures between 0 °C and -10 °C, as recommended by Paterson (1994).

### 6.2.2 The modified second order fluid model

The *modified second order fluid model with power-law viscosity* (MSOFM) was introduced by Man and Sun (1987) as

$$\mathbf{t} = -p\mathbf{I} + \eta(\mathbf{A}_{(1)})\mathbf{A}_{(1)} + \alpha_1\mathbf{A}_{(2)} + \alpha_2\mathbf{A}_{(1)}^2, \quad (6.2.2)$$

where  $\mathbf{A}_{(1,2)}$  are the first and second Rivlin-Ericksen tensors, describing the current strain rate and strain accelerations (Rivlin and Ericksen, 1955). The first Rivlin-Ericksen tensor in terms of the spatial velocity gradient is  $\mathbf{A}_{(1)} = \mathbf{L} + \mathbf{L}^T = 2\mathbf{D}$ . The strain acceleration tensor  $\mathbf{A}_{(2)}$ , and higher order tensors are constructed via the recurrence relation (viii) in Table 6.1. The coefficients  $\alpha_{1,2}$  are termed normal stress coefficients. The viscosity  $\eta(\mathbf{A}_{(1)})$  follows a power-law relation of the form

$$\eta(\mathbf{A}_{(1)}) = \mu \left( \frac{1}{2} \text{tr}(\mathbf{A}_{(1)}^2) \right)^{\frac{m}{2}}. \quad (6.2.3)$$

In Sun (1987), the MSOFM was proposed as an improvement on Glen's flow law to include non-stationary creep. Glen's flow law is contained in Eq. (6.2.2) as the asymptotic limit after transient creep has died out. Or else, with use of (vii) and (viii) (Table 6.1), Eq. (6.2.1) is recovered when  $\alpha_1 = \alpha_2 = 0$  in Eq. (6.2.2),  $m = (1 - n)/n$ , and  $\mu = 2^{-1/n}B$ , is substituted in Eq. (6.2.3). If  $m = 0$ , the MSOFM becomes the second order fluid model. Clearly, Eq. (6.2.2) is a generalization of the second order fluid model. A good summary on related generalizations of the second order model and the MSOFM is given in Massoudi and Vaidya (2008).

Sun (1987) performed the exploitation of the second law of thermodynamics (Clausius-Duhem inequality) for the MSOFM and deduced the restrictions on the stress function and its parameters  $\mu$ ,  $\alpha_1$  and  $\alpha_2$ . There is much controversy on the second order fluid models. Experimental observation and mathematical analyzes on the fluid model and its stability properties do not share the same consequences on the sign of the normal stress coefficient  $\alpha_1$  (see e.g. Dunn and Fosdick, 1974; Joseph, 1976; Müller and Wilmanski, 1986; Joseph, 1990; Rajagopal and Srinivasa, 2008). A review on this topic is given by Dunn and Rajagopal (1995). Here, we follow the work of Sun (1987), who used the restrictions (i)  $\alpha_1 + \alpha_2 = 0$ , and (ii)  $m = -2/3$ , corresponding to  $n = 3$  in Glen's flow law, Eq. (6.2.1). Sun determined mean values of  $\mu = 2.41 \text{ MPa d}^{\frac{1}{3}}$  and  $\alpha_1 = 161 \text{ MPa d}^2$  from fitting the model to the data of triaxial (McTigue et al., 1985), and pressure-meter (Kjartason, 1986) creep experiments.

### 6.3 The elastic modified second order isotropic material model (EMSOIM)

In the past, the role of primary creep and elastic effects on glacier flow and observed flow anomalies on a scale of hours to a few days has scarcely been investigated. To strike a new path in this direction, we adopt the MSOFM, in which the ice is able to reproduce both primary and secondary creep effects with good agreement on the creep experiments analyzed by Sun (1987). However, we further require the material to exhibit two contrasting properties: (1) viscous stationary creep of a fluid on long time scales, and (2) elasticity of a solid when the time scale under consideration becomes short, allowing elastic strain jumps and reversible creep. The material law needs to include properties of an isotropic elastic solid. We propose to extend the constitutive form of the MSOFM by an explicit dependence on the Finger strain tensor (Table 6.1), postulating

$$\mathbf{t} = \hat{\mathbf{t}}(\mathbf{E}, \mathbf{A}_{(1)}, \mathbf{A}_{(2)}), \quad (6.3.1)$$

as a frame-invariant functional relation for the stress. We call the corresponding material an *elastic modified second order isotropic material* (EMSOIM). The functional form (6.3.1) is a further generalization of the MSOFM, and belongs to the class of Rivlin-Ericksen materials (Rivlin and Ericksen, 1955).<sup>1</sup>

We now restrict the constitutive model (6.3.1) by ad-hoc assumptions to make the mathematical proof of the thermodynamic behavior performed by Sun (1987) applicable to the EMSOIM. In this way, we preserve the essential properties, namely (i) inclusion of elasticity effects, which, paired with the viscous effects, allow for relaxation phenomena, and (ii) use of the MSOFM concept to account for the primary and secondary creep regimes, in the context of an extended Glen flow law.

For an isothermal process with a body at uniform temperature the thermodynamic analysis of Sun (1987) is recovered for the EMSOIM (Eq. 6.3.1) if the following postulates hold:

1. The Cauchy stress tensor  $\mathbf{t}$  can be additively composed as

$$\mathbf{t} = \mathbf{t}_E + \mathbf{t}_D = \hat{\mathbf{t}}_E(\mathbf{E}) + \hat{\mathbf{t}}_D(\mathbf{A}_{(1)}, \mathbf{A}_{(2)}), \quad (6.3.2)$$

where  $\hat{\mathbf{t}}_D$  is a dissipative stress component that does not depend on  $\mathbf{E}$ , and  $\hat{\mathbf{t}}_E$  is an elastic stress contribution.

2. The functional dependence of the Helmholtz free energy may be additively decomposed as

$$\psi = \hat{\psi}(\mathbf{E}, \mathbf{A}_{(1)}) = \hat{\psi}_1(\mathbf{E}) + \hat{\psi}_2(\mathbf{A}_{(1)}). \quad (6.3.3)$$

3. The component  $\hat{\psi}_2$  of the Helmholtz free energy is a convex function of its argument  $\mathbf{A}_{(1)}$ .

<sup>1</sup>In chapter 5, the thermo-viscoelastic modified second order isotropic model (TMSOIM) was elucidated, which generalizes the MSOFM. The elastic modified second order isotropic material (EMSOIM) is a sub-form of the TMSOIM, but nevertheless a generalization of the MSOFM, since the constitutive relation of the Cauchy stress tensor is expanded by a dependence on the Finger strain tensor  $\mathbf{E}$ .

EMSOIM	Glen's flow law (Paterson, 1994)	MSOFM (Sun, 1987)
$m$	$-2/3$	$-2/3$
$\mu$	$1.4\text{--}2.3 \text{ MPa d}^{\frac{1}{3}}$	$2.41 \text{ MPa d}^{\frac{1}{3}}$
$\alpha$		$161 \text{ MPa d}^2$
$\beta_0$		$7000 \text{ MPa}^*$

Table 6.2: Values for the parameters of the Glen flow law and MSOFM, available from the referenced literature, expressed for the generalized EMSOIM constitutive relation. (\*) The value for the modulus  $\beta_0$  corresponds to  $2G$ , where  $G = 3500 \text{ MPa}$  is the shear modulus of ice (Schulson and Duval, 2009).

#### 4. The conditions

$$\mu \geq 0, \quad \alpha_1 \geq 0, \quad \alpha_1 + \alpha_2 = 0, \quad (6.3.4)$$

must be met.

We refrain from carrying out the complete thermodynamic analysis here as the problem which we consider in the following is an isothermal process and does not require an energy balance to be solved. An admissible form of the elastic stress contribution  $\mathbf{t}_E$  for an incompressible material with elastic deformation limited to shearing is the relation

$$\mathbf{t}_E = \beta(\mathbf{E}') \mathbf{E}', \quad (6.3.5)$$

where

$$\mathbf{E}' = \mathbf{E} - \frac{1}{3} \text{tr}(\mathbf{E}) \mathbf{I}, \quad (6.3.6)$$

is the deviatoric strain tensor, and  $\beta$  is a variable shear modulus of the form

$$\beta(\mathbf{E}') = \beta_0 \exp(-c \frac{1}{2} \text{tr}(\mathbf{E}'^2)), \quad (6.3.7)$$

with initial rigidity  $\beta_0 = 2G$ , where  $G = 3500 \text{ MPa}$  corresponds to the shear modulus of ice (Schulson and Duval, 2009). The constant  $c \geq 0$  is referred to as ‘‘fading elasticity factor’’. The purpose of the exponential dependence of the shear modulus on strain evolution is the ability to destroy elasticity on long time scales. It introduces an exponentially fading strength of elasticity with increasing strain accumulation. This is analogous to an exponentially fading memory of the material’s elastic properties with increasing deformation. This should not be confused with the concept of materials with fading memory (Coleman and Noll, 1960).

Thus, in the EMSOIM, the Cauchy stress tensor  $\mathbf{t}$  takes the form

$$\mathbf{t} = -p \mathbf{I} + \eta(\mathbf{A}_{(1)}) \mathbf{A}_{(1)} + \alpha(\mathbf{A}_{(2)} - \mathbf{A}_{(1)}^2) + \beta(\mathbf{E}') \mathbf{E}', \quad (6.3.8)$$

where  $\alpha = \alpha_1 = -\alpha_2$  was used. This representation is a fairly general form of a material law containing the modified second order fluid model by Man and Sun (1987), the Glen flow law and a Hooke-type elasticity relation with vanishing bulk modulus for an incompressible isotropic material of the class of materials of differential type (Rivlin and Ericksen, 1955). A similar, even more general constitutive relation is discussed by Zhou (1991).

In Table 6.2 we summarize values of the parameters  $m$ ,  $\mu$ ,  $\alpha$  and  $\beta_0$  which are available from the literature and experimental data. The values of  $n$  and  $B$  in Glen’s flow law, given in Sect. 6.2.1, are expressed in terms of  $m$  and  $\mu$ .

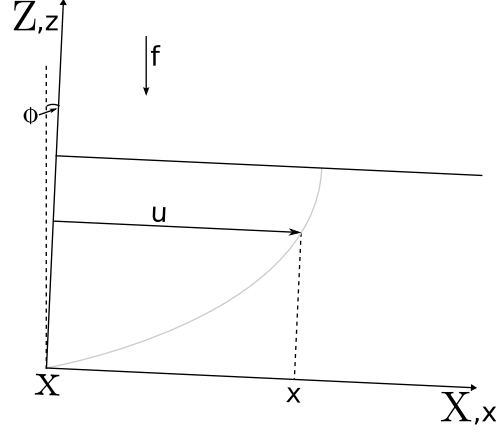


Figure 6.1: Problem geometry of one-directional shearing flow of a slab of material down a uniformly inclined plate (UIP). The coordinate systems of the reference ( $\mathbf{X}$ ) and present ( $\mathbf{x}$ ) configurations are oriented concordant, inclined by some angle  $\phi$  relative to the gravitational force  $\mathbf{f}$  acting in the vertical.

## 6.4 Unidirectional flow of the EMSOIM

We solve the balance equations for incompressible, isothermal Stokes (creeping) flow with the EMSOIM law. The governing equations are

$$-\operatorname{div}(\mathbf{t}) + \rho \mathbf{f} = 0, \quad (6.4.1)$$

$$\operatorname{div}(\mathbf{v}) = 0, \quad (6.4.2)$$

$$\mathbf{t} = -p\mathbf{I} + \eta(\mathbf{A}_{(1)})\mathbf{A}_{(1)} + \alpha(\mathbf{A}_{(2)} - \mathbf{A}_{(1)}^2) + \beta(\mathbf{E}')\mathbf{E}', \quad (6.4.3)$$

$$\eta(\mathbf{A}_{(1)}) = \mu \left( \frac{1}{2} \operatorname{tr}(\mathbf{A}_{(1)}^2) \right)^{\frac{m}{2}}, \quad (6.4.4)$$

$$\beta(\mathbf{E}') = \beta_0 \exp(-c \frac{1}{2} \operatorname{tr}(\mathbf{E}'^2)). \quad (6.4.5)$$

Equation (6.4.1) is the momentum balance, where  $\rho$  is the (constant) material density and  $\mathbf{f}$  an external force. Equation (6.4.2) is the mass balance, which requires the velocity  $\mathbf{v}$  to be solenoidal. The remaining equations describe the constitutive relation of the EMSOIM.

To solve the system forward in time, the set of equations must be complemented by an evolution equation for the Finger strain tensor  $\mathbf{E}$  from the present time  $t$ . Differentiation of  $\mathbf{E}$ , using (vi) from Table 6.1 yields

$$\begin{aligned} \dot{\mathbf{E}} &= \frac{1}{2} (\mathbf{F}\mathbf{F}^T - \mathbf{I})' \\ &= \frac{1}{2} (\mathbf{L}\mathbf{F}\mathbf{F}^T + \mathbf{F}\mathbf{F}^T\mathbf{L}^T) \\ &= \mathbf{L}\mathbf{E} + \mathbf{E}\mathbf{L}^T + \frac{1}{2}(\mathbf{L} + \mathbf{L}^T), \end{aligned}$$

or,

$$\dot{\mathbf{E}} - \mathbf{L}\mathbf{E} - \mathbf{E}\mathbf{L}^T = \frac{1}{2}\mathbf{A}_{(1)}, \quad (6.4.6)$$

which follows as an identity.

As a benchmark example, we consider one-directional shearing flow of a slab of material down a uniformly inclined plate (UIP), as illustrated in Fig. 6.1. Congruent to the two-dimensional spatial Cartesian coordinate system  $(x, z)$  depicted in Fig. 6.1, we define the particular reference configuration  $\mathbf{X} = (X, Z)$ . The plate is considered infinite in the downstream direction  $(X, x)$ , and the slab thickness is monotonic. The flow is driven by a gravitational force  $\mathbf{f} = (g \sin \phi, -g \cos \phi)$  where  $\phi$  is the inclination angle of the plate. We seek the velocity profile  $\mathbf{v} = (v(z), 0)$  which varies with the thickness of the slab.

In this rectilinear flow problem, the following relations exist between present and reference configuration:

$$x = X + u, \quad z = Z, \quad (6.4.7)$$

where  $u$  is a spatial displacement in the flow direction. The deformation gradient is then

$$\mathbf{F} = \frac{\partial \mathbf{x}}{\partial \mathbf{X}} = \begin{pmatrix} 1 & \partial u / \partial Z \\ 0 & 1 \end{pmatrix}. \quad (6.4.8)$$

We note that

$$\frac{\partial u}{\partial Z} = \frac{\partial u}{\partial z} \frac{\partial z}{\partial Z} = \frac{\partial u}{\partial z},$$

so that the Finger strain tensor is given by

$$\mathbf{E} = \frac{1}{2} \begin{pmatrix} (\partial u / \partial z)^2 & \partial u / \partial z \\ \partial u / \partial z & 0 \end{pmatrix}. \quad (6.4.9)$$

It may appear appropriate to use a geometrically linearized strain tensor, i.e., neglecting terms less than  $O((\partial u / \partial z)^2)$ . However, this would render the use of a variable modulus inconsistent, as  $\text{tr}(\mathbf{E}^2) \propto (\partial u / \partial z)^2$ . Thus, the geometrical linearization implies explicitly that one only moves little away from the reference configuration; the material's elastic properties would remain unchanged in that range of deformation. Since we require degradation of material elasticity, terms less than  $O((\partial u / \partial z)^2)$  should be retained in the formulation for consistency.

The 1st Rivlin-Ericksen tensor is determined from the spatial velocity gradient as

$$\mathbf{A}_{(1)} = \mathbf{L} + \mathbf{L}^T = \begin{pmatrix} 0 & \partial v / \partial z \\ \partial v / \partial z & 0 \end{pmatrix}. \quad (6.4.10)$$

The evaluation of Eq. (6.4.6) brings up the relation between velocity  $v$  and displacement  $u$  as

$$\frac{\partial v}{\partial z} = \frac{\partial^2 u}{\partial t \partial z} = \frac{\partial}{\partial z} \frac{\partial u}{\partial t}, \quad (6.4.11)$$

which, in this unidirectional case, is simply  $v = \partial u / \partial t$ . We keep  $v$  and  $u$  separate and insert Eq. (6.4.3), together with Eqs. (6.4.9) and (6.4.10) into the momentum equation (6.4.1). The stress divergence yields two equations as

$$\begin{aligned} -\mu \frac{\partial}{\partial z} \left( \left| \frac{\partial v}{\partial z} \right|^m \frac{\partial v}{\partial z} \right) - \alpha \frac{\partial}{\partial z} \left( \frac{\partial^2 v}{\partial t \partial z} \right) \\ - \beta_0 \frac{\partial}{\partial z} \left( \exp \left( -c \frac{1}{4} \left[ \left( \frac{\partial u}{\partial z} \right)^2 + \frac{1}{4} \left( \frac{\partial u}{\partial z} \right)^4 \right] \right)^{\frac{1}{2}} \frac{\partial u}{\partial z} \right) = \rho g \sin \phi, \end{aligned} \quad (6.4.12)$$

$$-\alpha \frac{\partial}{\partial z} \left( \frac{\partial v}{\partial z} \right)^2 + \beta_0 \frac{\partial}{\partial z} \left( \frac{1}{2} \frac{\partial u}{\partial z} \right)^2 + \frac{\partial p}{\partial z} = -\rho g \cos \phi, \quad (6.4.13)$$

with the velocity  $v$ , displacement  $u$ , and pressure  $p$  as unknowns.

Note, the pressure equation (6.4.13) is decoupled from the flow equation (6.4.12). Equation (6.4.13) is interesting as it obviously describes deviations from a hydrostatic stage (linear pressure variation with slab thickness) which arise from second order effects and elasticity. These normal stress contributions due to second order effects (term associated with  $\alpha$ ) and elasticity (term associated with  $\beta_0$ ) in Eq. (6.4.13) carry opposite signs. If we would have used a geometrically linearized strain tensor, elastic normal stresses, i.e., the second term in Eq. (6.4.13) would be absent.

In the following, we will only be concerned with the solution of the flow problem of Eq. 6.4.12. We now non-dimensionalize problem (Eq. 6.4.12) by replacing the relevant fields on the basis of a characteristic time scale as

$$t = \bar{t}[\mathbf{T}] = \bar{t}[\mathbf{L}][\mathbf{V}]^{-1}, \quad z = \bar{z}[\mathbf{L}], \quad v = \bar{v}[\mathbf{V}], \quad (6.4.14)$$

where each bracketed term represents a characteristic scale of the respective field. For Eq. (6.4.12), upon inserting Eq. (6.4.14) and dividing by the load  $\rho g$  and rearranging, we obtain

$$\begin{aligned} -\Pi_1 \frac{\partial}{\partial \bar{z}} \left( \left| \frac{\partial \bar{v}}{\partial \bar{z}} \right|^m \frac{\partial \bar{v}}{\partial \bar{z}} \right) - \Pi_2 \frac{\partial}{\partial \bar{z}} \left( \frac{\partial^2 \bar{v}}{\partial \bar{t} \partial \bar{z}} \right) \\ - \Pi_3 \frac{\partial}{\partial \bar{z}} \left( \exp \left( -c \frac{1}{4} \left[ \left( \frac{\partial u}{\partial z} \right)^2 + \frac{1}{4} \left( \frac{\partial u}{\partial z} \right)^4 \right] \right)^{\frac{1}{2}} \frac{\partial \bar{u}}{\partial \bar{z}} \right) = \sin \phi \end{aligned} \quad (6.4.15)$$

with the  $\Pi$ -coefficients

$$\Pi_1 = \frac{\mu[V]^{m+1}}{[L]^{m+2} \rho g}, \quad \Pi_2 = \frac{\alpha[V]^2}{[L]^3 \rho g}, \quad \Pi_3 = \frac{\beta_0}{[L] \rho g}. \quad (6.4.16)$$

The coefficients  $\Pi_{1-3}$  contain  $\rho g$  to the first power. This means that only two  $\Pi$ -products are independent, namely  $\mathbb{H} = \Pi_2/\Pi_1$  and  $\mathbb{K} = \Pi_3/\Pi_1$ , evaluated as

$$\mathbb{H} = \frac{\alpha}{\mu} [\Gamma]^{m-1}, \quad \mathbb{K} = \frac{\beta_0}{\mu} [\Gamma]^{m+1}. \quad (6.4.17)$$

The non-dimensional number  $\mathbb{H}$  measures the significance of strain accelerations, while  $\mathbb{K}$  is the initial rigidity modulus. The non-dimensionalization emphasizes the parameters' relationship to transient effects. Dropping the superscript bars, the non-dimensional form of the initial/boundary value problem takes the form

$$\begin{aligned} -\frac{\partial}{\partial z} \left( \left| \frac{\partial v}{\partial z} \right|^m \frac{\partial v}{\partial z} \right) - \mathbb{H} \frac{\partial}{\partial z} \left( \frac{\partial^2 v}{\partial z \partial t} \right) \\ - \mathbb{K} \frac{\partial}{\partial z} \left( \exp \left( -c \frac{1}{4} \left[ \left( \frac{\partial u}{\partial z} \right)^2 + \frac{1}{4} \left( \frac{\partial u}{\partial z} \right)^4 \right] \right)^{\frac{1}{2}} \frac{\partial u}{\partial z} \right) = \sin \phi, \end{aligned} \quad (6.4.18)$$

$$v = \frac{\partial u}{\partial t}, \quad (6.4.19)$$

$$v(z=0, t) = u(z=0, t) = 0, \quad (6.4.20)$$

$$u(z, t=0) = u_0(z), \quad v(z, t=0) = v_0(z), \quad (6.4.21)$$

where Eq. (6.4.20) is the Dirichlet boundary condition, assuming that the slab adheres to the plate, and Eq. (6.4.21) describes a set of initial conditions with  $u_0(z) = v_0(z) = 0$ , at  $z = 0$ , due to Eq. (6.4.20).

We have now reduced the set of coefficients to the parameters  $\mathbb{H}$  and  $\mathbb{K}$  as measures on viscoelastic, transient effects (strain acceleration and/or elasticity) relative to the purely viscous power-law material, i.e., the first term of Eq. (6.4.18).

### 6.4.1 Numerical implementation

The field equations are numerically implemented using the DOLFIN/FFC finite element software (Kirby and Logg, 2006; Logg and Wells, 2010). We solve the flow problem of Eqs. (6.4.18), (6.4.19) together with the homogeneous boundary condition (6.4.20) and the initial conditions (6.4.21) in a mixed problem. The weak form of the discrete Galerkin formulation is to find  $(u_h, v_h) \in \mathcal{U}_h \times \mathcal{V}_h$ , such that

$$\begin{aligned} F(u_h, v_h; b_h, w_h) := & \left( \frac{\partial w_h}{\partial z}, \left| \frac{\partial v_h}{\partial z} \right|^m \frac{\partial v_h}{\partial z} \right) + \mathbb{H} \left( \frac{\partial w_h}{\partial z}, \frac{\partial^2 v_h}{\partial z \partial t} \right) \\ & + \mathbb{K} \left( \frac{\partial w_h}{\partial z}, \exp \left( -c \frac{1}{4} \left[ \left( \frac{\partial u_h}{\partial z} \right)^2 + \frac{1}{4} \left( \frac{\partial u_h}{\partial z} \right)^4 \right] \right)^{\frac{1}{2}} \frac{\partial u_h}{\partial z} \right) \\ & - \left( w_h, \sin \phi \right) + \left( b_h, \frac{\partial u_h}{\partial t} - v_h \right) = 0, \end{aligned} \quad (6.4.22)$$

for all admissible  $(b_h, w_h) \in \mathcal{U}_h \times \mathcal{V}_h$ . Here,  $F$  is a bilinear form, where  $(\cdot, \cdot)$  is an  $L^2(\Omega)$  inner product for scalars defined with respect to the partition of the bounded domain  $\Omega$  of  $\mathbb{R}^1$  into finite elements, and

the subscript  $h$  is a discretization parameter. The finite element spaces  $\mathcal{U}_h$  and  $\mathcal{V}_h$  are appropriate spaces of square integrable basis functions with derivatives also being square integrable. We use continuous Galerkin elements with Lagrange polynomials of second order. The time derivatives are discretized using the implicit backward Euler scheme. We apply Newton's method to solve the resulting system of nonlinear algebraic equations.

Note that Eq. (6.4.22) results in a system of nonlinear differential-algebraic equations (DAEs) of the form  $G(t, u, v, \partial v/\partial t) = 0$ . It contains the initial value problem of satisfying a consistent set of initial conditions for the  $N$ -dimensional vectors of unknowns  $u_0(z)$  and  $v_0(z)$  at  $t = 0$  (e.g. Brown et al., 1998). Initially, the creep rate of ice is larger than in the stationary creep regime and it is decelerating (primary creep). Thus, to compute a consistent  $v_0(z)$ , we solve one time step with  $\mathbb{H} = 0$  using a very small step size. In this way, we obtain a valid steady solution  $(u_s(z), v_s(z))$ . The velocity is then increased above the steady solution by a constant  $a$ , i.e.  $(u_0(z), v_0(z)) = (u_s(z), av_s(z))$ . Using  $a = 2.5$  and then solving another (tiny) time step with  $\mathbb{H}$  specified, yields a vector  $u_0(z)$  consistent with  $v_0(z)$ , so that the actual computation can be started with  $(u_0(z), v_0(z))$  as consistent initial conditions. If  $\mathbb{K} = 0$ , we reset the displacement  $u_0(z) = 0$  as no initial instantaneous elastic displacement occurs. If  $\mathbb{K} > 0$ ,  $u_0(z)$  also served as initial condition.

## 6.5 Results

### 6.5.1 Creep under step function load

The UIP problem may be interpreted in analogy to a shear creep experiment. At time  $t < 0$ , the load is zero and the material has been at rest for a long time. For  $t \geq 0$ , we assume the load to be constant, i.e., equal to  $\sin \phi$ . However, as we are also interested in the unloading phase, we artificially remove the (gravitational) load after some time, so we define the modified load  $\sin \phi(t)$  with

$$\phi(t) = (H(t) - H(t - t_r)) \phi_c, \quad (6.5.1)$$

where  $\phi_c = 12^\circ$ ,  $H(\cdot)$  is the Heaviside function, and  $t_r$  is a portion of the experiment run-time (60% of the total run-time). Of the solutions, we display velocity (creep rate) and displacement (creep) at the surface of the slab as functions of time. In Figs. 6.2 to 6.4 we elucidate results for different parameter combinations.

If second order (creep accelerations) and elasticity effects are absent, i.e.  $\mathbb{H} = \mathbb{K} = 0$ , the purely viscous flow problem, equivalent to the Glen power-law is solved. In that case, the material simply shears down the plate with steady creep rate (velocity). As the load is removed at  $t = 0.9$ , the creep rate instantaneously drops to zero. This case is depicted by the black solid curve in Fig. 6.2a. In Fig. 6.2b, the corresponding creep curve is depicted. The displacement increases linearly with time with a slope corresponding to the creep rate (Fig. 6.2b). At unloading ( $t = 0.9$ ), the creep curve remains at a constant level of permanent creep experienced so far.

For increasing (decreasing) power-law exponent  $m$ , the constant creep rate increases (decreases) proportionally. However, the creep rate is fixed for a constant load, and no transient behavior occurs. In all the following computations, we used  $m = -2/3$  ( $n = 3$ ).

In Fig. 6.2a, b, we have  $0 \leq \mathbb{H} \leq 10$ , while  $\mathbb{K} = 0$ . Here, the material initially deforms rapidly with high creep rate. For  $\mathbb{H} \leq 1.0$ , the creep rate decays rapidly and asymptotically reaches the steady creep rate (the solution with  $\mathbb{H} = 0$ , Fig. 6.2a, black solid). If  $\mathbb{H} = 5$  or 10, the creep rate decelerates significantly, but does not reach stationary creep until  $t = 0.9$ . When the load is removed at that time, the creep rates do not drop instantaneously to zero, but further decay for all  $\mathbb{H} > 0$ . For small  $\mathbb{H}$ , the creep curves in Fig. 6.2b are composed of four sections; an initial interval of decelerating (primary) creep followed by monotonically increasing, stationary creep, and a recurring interval of decelerating creep, which then goes over into  $u = \text{const}$ . However, as  $\mathbb{H}$  is increased, the sequence of these different creep intervals is blurred and the displacement function transforms into a single interval of almost permanently decelerating (primary) creep (see  $\mathbb{H} = 10$ , Fig. 6.2b). Note that the decelerating creep at  $t > 0.9$  is particularly

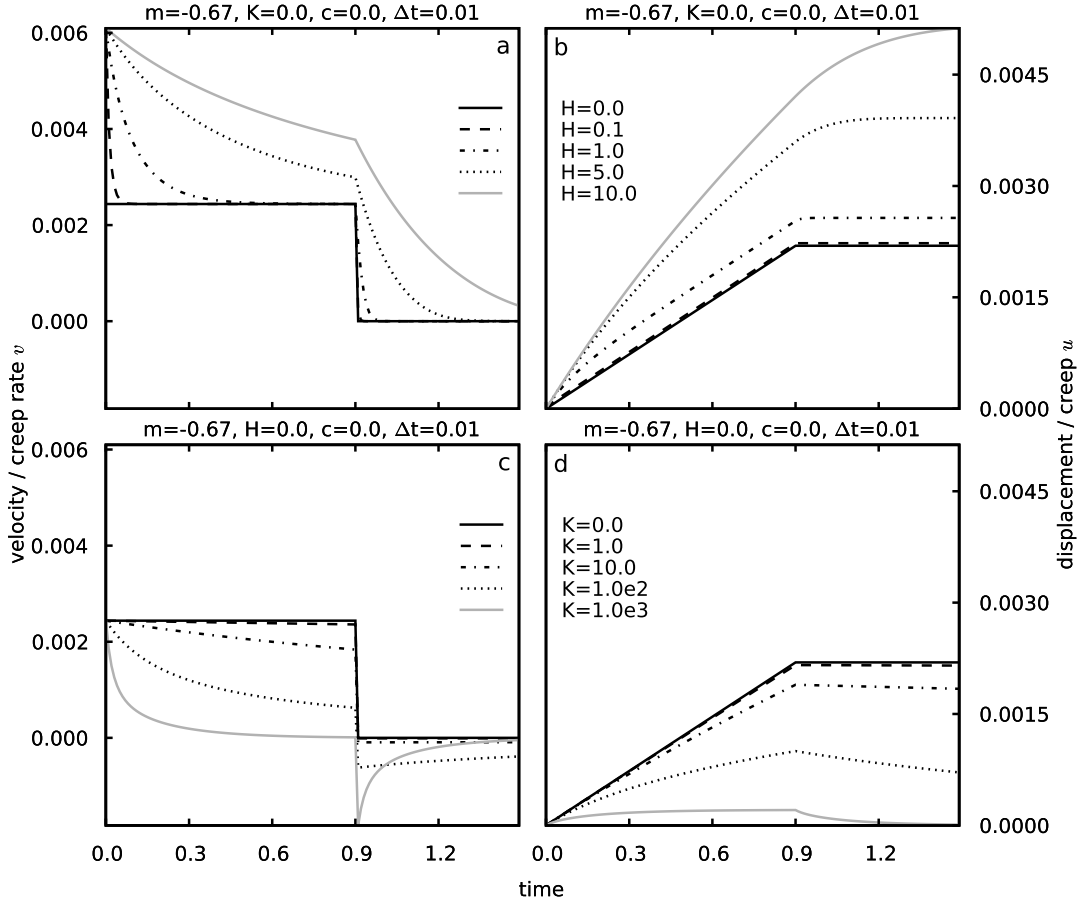


Figure 6.2: (a, c) Velocity (creep rate)  $v$  at the slab surface as function of time. (b, d) Displacement (creep)  $u$  at the slab surface as function of time. In (a, b), solutions of  $v$  and  $u$  are displayed for different values of the dimensionless number  $\mathbb{H}$  while  $\mathbb{K} = 0$ . In (c, d), solutions of  $v$  and  $u$  are displayed with  $\mathbb{H} = 0$  and varying  $\mathbb{K}$ . Other parameters are as displayed in the plot headers. All fields ( $u, v, t$ ) are non-dimensional.

interesting since the material now exhibits, after removal of the load, continued decelerating creep. This situation indicates a retardation of the material's response to the removal of the load; with increasing  $\mathbb{H}$  the creep rate decays increasingly slower. The creep undergone by the material is not recoverable, so the material is a viscous fluid with the ability to experience transient creep, according to the MSOFM.

In Fig. 6.2c, we now impose elastic properties with  $\mathbb{K} > 0$  and set  $\mathbb{H} = 0$ . For any  $\mathbb{K}$  the material immediately starts to creep with initial velocity as the solution with  $\mathbb{K} = 0$ . All creep rates then decay asymptotically to zero; the time it takes to reach zero depends on  $\mathbb{K}$ . At the removal of the load ( $t = 0.9$ ), the creep rates instantaneously jump to negative values, which indicates that creep starts to recover. In Fig. 6.2d, the increase of displacements decelerates with increasing time  $t$  and eventually the individual displacement solution approaches an asymptotic limit (e.g.  $\mathbb{K} = 10^3$  in Fig. 6.2d). At unloading time  $t = 0.9$ , the displacements start to decrease again quasi-exponentially and re-approach zero. Thus, for  $\mathbb{K} > 0$ , the material becomes elastic and rigid, which prevents permanent creep but allows complete recovery of the displacement.

In Fig. 6.3, we display the material behavior when elastic and second order effects are both activated with nonzero  $\mathbb{H}$  and  $\mathbb{K}$ . We show solutions for  $\mathbb{H} = 2.0$  and varying  $\mathbb{K}$  (Fig. 6.3a, b), and for  $\mathbb{K} = 10^2$  with variable  $\mathbb{H}$  (Fig. 6.3c, d). When  $\mathbb{H} > 0$ , the slab starts to creep with initially high creep rate. If  $\mathbb{K}$  is very small, i.e.,  $\mathbb{K} = 1.0$ , the decay of the creep rate slows down and becomes almost constant (Fig. 6.3a). At removal of the load ( $t = 0.9$ ), the decay of the creep rate speeds up again and approaches zero fast. If  $\mathbb{K} = 10^2$ , the creep rate initially decays rapidly but slows down considerably after  $t \sim 0.3$ . If  $\mathbb{K} = 10^3$ ,

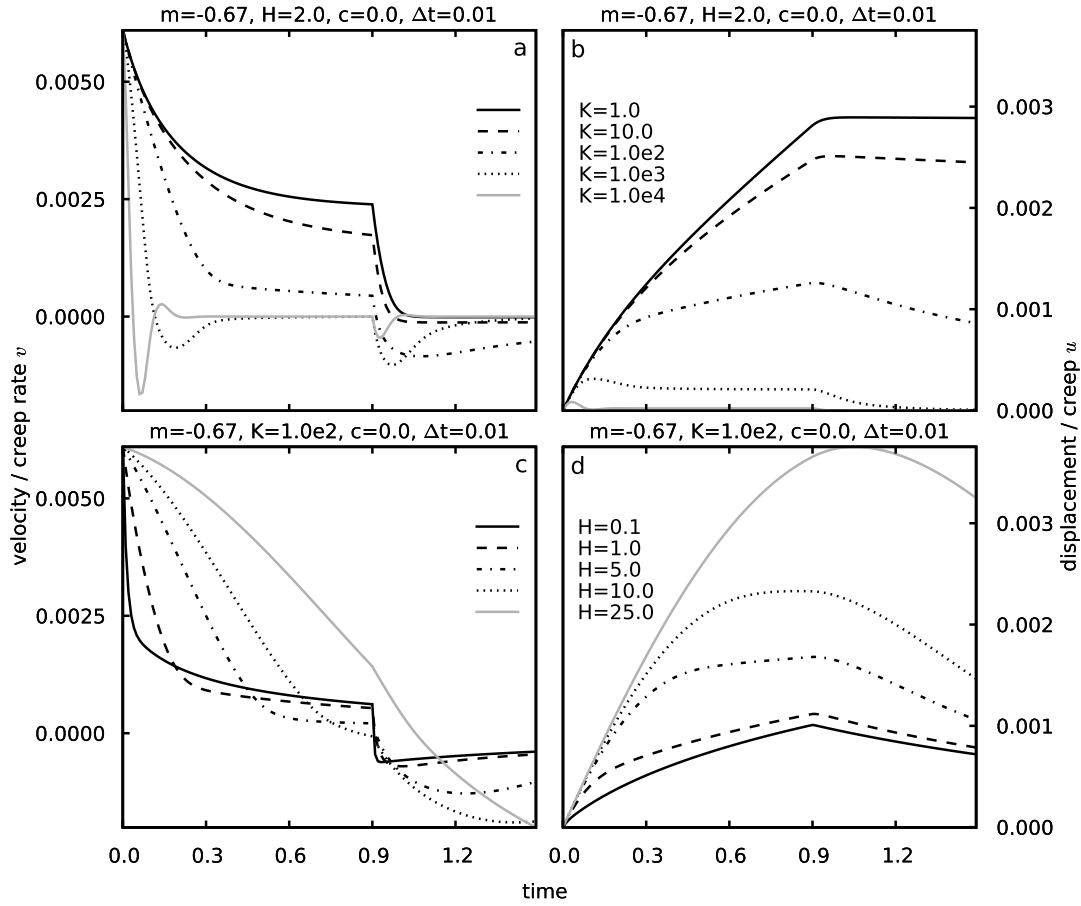


Figure 6.3: (a, c) Velocity (creep rate)  $v$  at the slab surface as function of time. (b, d) Displacement (creep)  $u$  at the slab surface as function of time. In (a, b) solutions of  $v$  and  $u$  are displayed for  $\mathbb{H} = 2$  and variable  $\mathbb{K}$ , while in (c, d) solutions of  $v$  and  $u$  are shown for  $\mathbb{K} = 10^2$  and different values of  $\mathbb{H}$ . Other parameters are as displayed in the plot headers. All fields ( $u, v, t$ ) are non-dimensional.

or larger, the creep rates decay very rapidly and even drop below zero and then increase again. So, the creep rates begin to oscillate and fade to zero afterward. If the load is removed, the creep rates drop, oscillate and fade again to zero. Thus, since  $\mathbb{K} \gg 0$  and  $\mathbb{H} \neq 0$ , the material is strongly elastic and able to respond to creep accelerations; the material behavior becomes resilient. The corresponding creep curves show decelerating creep reaching a maximum at increasingly earlier time, at which time recovery is also activated (Fig. 6.3b).

In Fig. 6.3c, we observe how the creep rate decays increasingly less rapidly with increasing  $\mathbb{H}$ . The material response gets strongly delayed. If  $\mathbb{H}$  is small, the creep rate quickly decays asymptotically to zero. At unloading ( $t = 0.9$ ), it jumps to negative values and again asymptotically returns to zero. If  $\mathbb{H} = 1$  or 5, the creep rate first decreases fast and then the decay slows down rather quickly. For large  $\mathbb{H} \geq 10$ , the creep rate decreases slowly and unloading at  $t = 0.9$  has almost no effect. In this case, for increasing  $\mathbb{H}$  and fixed  $\mathbb{K}$ , the material experiences increasingly more creep until at unloading, the creep decreases (recovers) again (Fig. 6.3d).

### 6.5.2 Fading elasticity

As already mentioned, when  $\mathbb{K} > 0$  (Figs. 6.2c, d and 6.3), the material is essentially a viscoelastic solid which can only experience limited, though fully recoverable creep. It is obvious that these properties of a viscoelastic solid dominate the material behavior for all times  $t$ . However, viscous creep of a fluid should be the dominating material behavior for  $t \gg 0$ , thus with increasing time  $t$ , the material needs to forget its

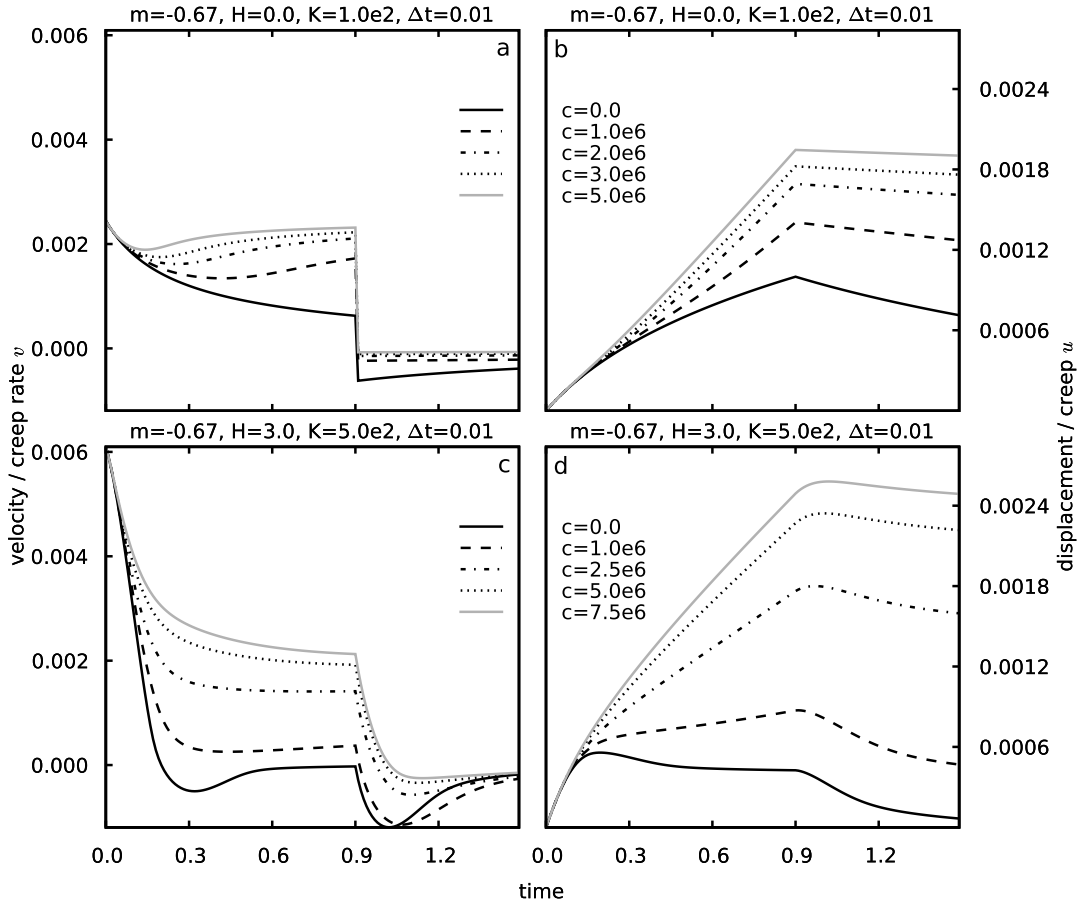


Figure 6.4: (a, c) Velocity (creep rate)  $v$  at the slab surface as a function of time. (b, d) Displacement (creep)  $u$  at the slab surface as a function of time. In (a, b) solutions of  $v$  and  $u$  are displayed for different values of the memory damping factor  $c$  while  $\mathbb{H} = 0$ . In (c, d) solutions of  $v$  and  $u$  are shown for various values of  $c$  and  $\mathbb{H} = 3.0$ . Other parameters are as displayed in the plot headers. All fields ( $u$ ,  $v$ ,  $t$ ) are non-dimensional.

elastic properties. This is achieved by adjusting the fading elasticity factor  $c$ . In our creep experiment, if  $\mathbb{K} > 0$  and the load  $\sin\phi(t)$  is applied, the displacement approaches some asymptotic limit for increasing time. In that case, i.e.,  $t \gg 0$ , the last term on the left-hand side of Eq. (6.4.18), associated with  $\mathbb{K}$ , becomes dominant at  $t \gg 0$ , while due to  $v \rightarrow 0$  the other terms diminish. Setting  $c \geq 0$  exponentially attenuates the growth of that term with increasing displacement (i.e., strain). This is equivalent to an exponential decay of the initial dimensionless modulus  $\mathbb{K}$  with increasing displacement/strain. Note that this results in a temporal response of the material behavior, however it is not an explicit time-dependent response, as the change in the phenomenological parameter is linked to the deformation. This response can be physically interpreted as a change in resistance of the material, which e.g. Ashby and Duval (1985) and Castelnau et al. (2008) associate with a change in the internal stress field of the material.

We display the associated material behavior in Fig. 6.4. If second order effects are left aside ( $\mathbb{H} = 0$ ) we observe the material creep rate to decay towards zero and then increase again (Fig. 6.4a). The larger  $c$  is, the earlier the decay of the creep rate will be interrupted and the creep rate increases again, approaching some constant nonzero value. For such cases, the creep decelerates and then accelerates again, increasing gradually with time. When the load is removed at  $t = 0.9$ , some recovery of creep takes place where the displacements decrease and approach some constant value again, corresponding to the amount of permanent viscous creep acquired (Fig. 6.4b). The larger  $c$  is, the more permanent viscous creep and the less recovery of creep occurs. If second order effects are taken into account, e.g.  $\mathbb{H} = 3$ , primary creep is activated again and oscillating creep rates (re-)appear. The increase of  $c$  in such cases dampens the

oscillations and prevents the creep rate from decaying to or below zero, maintaining increasing viscous creep with increasing  $c$ .

## 6.6 Discussion

### 6.6.1 Viable ranges of $\mathbb{H}$ and $\mathbb{K}$

The EMSOIM includes three relevant material parameters, i.e.,  $\mu$ ,  $\alpha$ , and  $\beta_0$ . The parameters  $\mu$  and  $\alpha$  have been determined based on laboratory experiments and creep function fitting. McTigue et al. performed the parameter identifications of  $\mu$ ,  $\alpha_1$ , and  $\alpha_2$  for a second order fluid model with  $m = 0$ . Sun (1987) re-fitted the creep data of McTigue et al. for the MSOFM, under the conditions of  $m = -2/3$ , ( $n = 3$  in Glen's flow law) and  $\alpha_1 + \alpha_2 = 0$  (thermodynamic constraint). The resulting mean estimates of Sun were listed in Table 6.2. We now use  $m$  and  $\alpha$  as determined by Man and Sun (1987, see Table 6.2) and insert them into the definition of  $\mathbb{H}$  (first equation of Eqs. 6.4.17). In Fig. 6.5, we plot the variation of  $\mathbb{H}$  as a function of time scale. The limits of the abscissa encompass the approximate range over which the experiments of Mellor and Cole (1982) and Jacka (1984) lasted. The time scales shaded in light grey range from 1 to 10 days, and correspond to the durations of the creep experiments analyzed by Sun (1987), from which he estimated the parameters  $\mu$  and  $\alpha$ . The value of  $\mu$  deduced by Sun is in the range of  $\mu$  expected from the Glen flow law (Paterson, 1994). Considering a variation of  $\mu$  according to the range given in Table 6.2, the change of  $\mathbb{H}$  with increasing time scale and fixed  $\alpha = 161 \text{ MPa d}^2$  is given by the dark grey bar in Fig. 6.5a. The range of expected  $\mathbb{H}$  is the intersection of the grey bar with the time scale interval shaded in light grey, which is  $1.5 \leq \mathbb{H} \leq 115$ . For a time scale of 5 d,  $\mathbb{H}$  is  $\approx 5$ . In Fig. 6.5b, the change of  $\mathbb{K}$  with increasing time scale, according to the second equation of (6.4.17), is shown. Here, the dark grey bar indicates the value of  $\mathbb{K}$  for  $\beta_0 = 7000 \text{ MPa}$ , and  $1.4 \leq \mu \leq 2.4 \text{ MPa d}^{1/3}$ . Expected values of  $\mathbb{K}$  for a time scale between 1 to 10 d lie in the interval of  $2.9 \cdot 10^3 \leq \mathbb{K} \leq 2 \cdot 10^4$ , with  $\mathbb{K} \approx 8 \cdot 10^3$  at  $[T] = 5 \text{ d}$ .

We note that there is a considerable variation of  $\mathbb{H}$  of two orders of magnitude with increasing  $[T]$ , whereas  $\mathbb{K}$  changes only one order of magnitude across the time scales of 1 to 10 d. In this range, the absolute value of  $\mathbb{K}$  is about two orders larger than that of  $\mathbb{H}$  at a given time scale. Thus, the solid elastic properties are the prominent feature of the ice at any time scale. Since the value of  $\mathbb{H}$  shows strong variation across  $[T]$ , the behavior of a strongly elastic material (large  $\mathbb{K}$ ) is expected to vary quite significantly, depending on  $\mathbb{H}$ . The occurrence of oscillating creep (Sect. 6.5) is a striking indication to this.

### 6.6.2 Relevance of acceleration effects ( $\mathbb{H} > 0$ )

As pointed out, the magnitude of  $\mathbb{H}$  obviously varies strongly, depending on the scales considered. The interpretation is that the strain acceleration term in the constitutive relation can alter the material behavior considerably, as demonstrated by the appearance of oscillating creep rates with increasing  $\mathbb{H}$  and large  $\mathbb{K}$ . The oscillating creep questions consideration of second order effects (i.e., strain accelerations) in a creeping (Stokes) flow problem. Nevertheless, if no creep accelerations are considered, i.e.,  $\alpha$  ( $\mathbb{H}$ ) is zero, it is not possible to reproduce primary creep rates which are up to two orders larger than the steady secondary creep rate (e.g. Jacka, 1984; Castelnuovo et al., 2008). For  $\mathbb{K} > 0$ , but  $\mathbb{H} = 0$ , there is no solution with creep rates larger than the viscous, stationary creep rate ( $\mathbb{K} = 0$ ). The strain accelerations with  $\mathbb{H} > 0$  are necessary to capture the primary creep regime with the deceleration of the creep rate. However, in the EMSOIM constitutive equation, the significant decrease of strain rate in the primary creep regime will also be influenced by the evolving elasticity of the material and not only by strain accelerations, as in the MSOFM. Presumably, the actual value of  $\alpha$  as a material parameter in the EMSOIM is smaller than it can be expected on the basis of the MSOFM. Thus, strain accelerations and decay of elasticity in the EMSOIM should be designed in such way that the interference does not result in oscillating creep behavior.

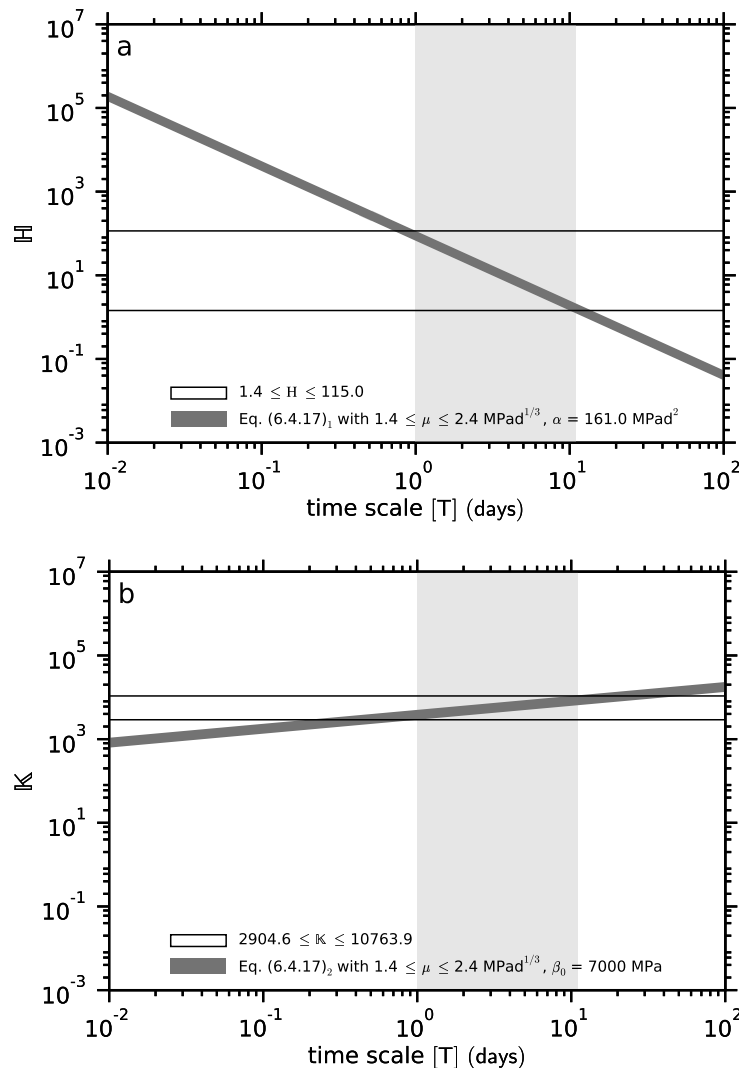


Figure 6.5: Change of the dimensionless numbers  $\mathbb{H}$  and  $\mathbb{K}$  of Eq. (6.4.17) as functions of the time scale and the parameters from Table 6.2.

## 6.7 Final remarks

We applied a viscoelastic material law in a simple unidirectional flow problem and studied the influences of the various material parameters. The EMSOIM relates stress to strain and its derivatives up to second order, i.e. strain rates and strain accelerations. As the EMSOIM is a generalized material law incorporating the Glen flow law, the MSOFM and a nonlinear elasticity relation, depending on the choice of parameters, it reproduces material behavior with respect to either a single or multiple of the incorporated constitutive relations.

For unidirectional flow considered here, the set of field equations was substantially reduced, however, the constitutive model was capable of producing complex material responses. Such characteristics, including total or partial recovery of deformation and enhanced viscous deformation with non-stationary creep rates, may be possibly encountered in the observations on Gornergletscher. Such a multi-dimensional situation makes the problem much more challenging and besides the difficulties associated with the viscoelastic theory and material behavior, numerically dealing with the problem in the context of finite elements becomes more involved. Nevertheless, we target on considering further applications of the EMSOIM constitutive model and the investigation of viscoelastic properties of glacier ice.

## 6.8 Addendum: Fit of the EMSOIM to experimental uni-axial creep data

In Section 6.4 a uni-directional shear flow problem obeying the EMSOIM viscoelastic constitutive equation was developed. Transient responses of velocity and displacements were analyzed in a constant load/sudden unloading situation for selected parameter combinations and in the results a broad spectrum of material behavior was illustrated (Sect. 6.5). However, no particular response or certain parameter combination was identified for a representative ice rheology, only estimates on the parameters  $\mathbb{H}$  and  $\mathbb{K}$  based on the variation of an arbitrary process time scale  $[\mathbb{T}]$  were given. In this section, I seek a set of non-dimensional model parameters  $\mathbb{H}$ ,  $\mathbb{K}$  and  $c$ , which generate a viscoelastic response describing the primary and secondary creep stages of the creep of polycrystalline ice. To this end, the model is tested on experimental data on the creep deformation of ice.

Most creep experiments conducted in the past considered uni-axial compression tests. Specimens of artificial isotropic polycrystalline ice, prepared in the laboratory, were subjected to constant loading at relatively low stresses over long time, and strain rates and strains were measured on the specimen. The experiments of Mellor and Cole (1982, abbreviated MC82) and Jacka (1984, abbrev. JA84) are well known and include repeated compression tests performed at different temperatures and at different stresses (loads). The tests of MC82 covered a stress range of 0.8 to 3.8 MPa and were carried out at  $-5^\circ\text{C}$ . In the tests of JA84 different loads in the axial stress range of 0.11 to 2.54 MPa were applied, and four sets of experiments were carried out at temperatures of  $[-5, -10.6, -17.2, -32.5]^\circ\text{C}$ . The results of MC82 and JA84 were compiled as creep curves in log-log plots of strain rate versus time or strain. Example creep curves extracted from MC82 and JA84 are displayed in Figure 6.6. The three distinct creep regimes of primary creep (decaying strain rate), secondary creep (minimum strain rate), and tertiary creep (increasing strain rate) are easily discernible. In all curves displayed, the minimum strain rate ( $\dot{\epsilon}_{min}$ ) is reached at  $\sim 1\%$  strain ( $\hat{=} 0.6\%$  octahedral strain). The creep curves are not exactly geometrically similar as indicated by Mellor and Cole (1983), but nevertheless do resemble each other remarkably. Ashby and Duval (1985) scrutinized the analogy of the creep curves from constant load experiments in more detail. They showed that normalized creep curves (strain rate vs. strain, or strain rate vs. time) can be adequately represented by a single, non-dimensional master relation. The scaling of creep data proposed by Ashby and Duval was the result of a dimensional analysis of a constitutive equation proposed, and, indeed, the experimental creep data strongly supported such dimensional affinity. In Ashby and Duval (1985), the basis of normalization of strain, strain rate and time data was the relation

$$[\dot{\epsilon}] = \frac{[e]}{[\mathbb{T}]}, \quad (6.8.1)$$

where  $[\cdot]$  represents a characteristic scale for each of the creep variables of strain,  $e$ , strain rate  $\dot{\epsilon}$ , and time  $t$ . Plots of strain rate as a function of time in both Mellor and Cole (1982, 1983) and Jacka (1984) indicate that  $\dot{\epsilon}_{min}$  and the time required to develop the minimum strain rate, denoted as  $t_{min}$ , are related as

$$\dot{\epsilon}_{min} \propto \frac{1}{t_{min}}. \quad (6.8.2)$$

This allows normalization of creep variables by the measured minimum strain rate as

$$\begin{aligned} \bar{\epsilon} &= \dot{\epsilon}/[\dot{\epsilon}] = \dot{\epsilon}/\dot{\epsilon}_{min}, \\ \bar{t} &= \bar{t}/[\mathbb{T}] = t \dot{\epsilon}_{min}, \end{aligned} \quad (6.8.3)$$

with the time scale

$$[\mathbb{T}] = 1/\dot{\epsilon}_{min}. \quad (6.8.4)$$

In this scaling,  $[e] = 1$ , i.e. no additional scaling of strain is used in equation (6.8.1). Ashby and Duval (1985) used a slightly different scaling, where  $[e] \approx 10^{-4}$ , the strain scale having the order of an initial elastic strain. In that case, the scaling reflects a normalization of initial strain/primary creep stage data. However, the scaling (6.8.3) is a normalization with respect to the secondary creep regime at minimum

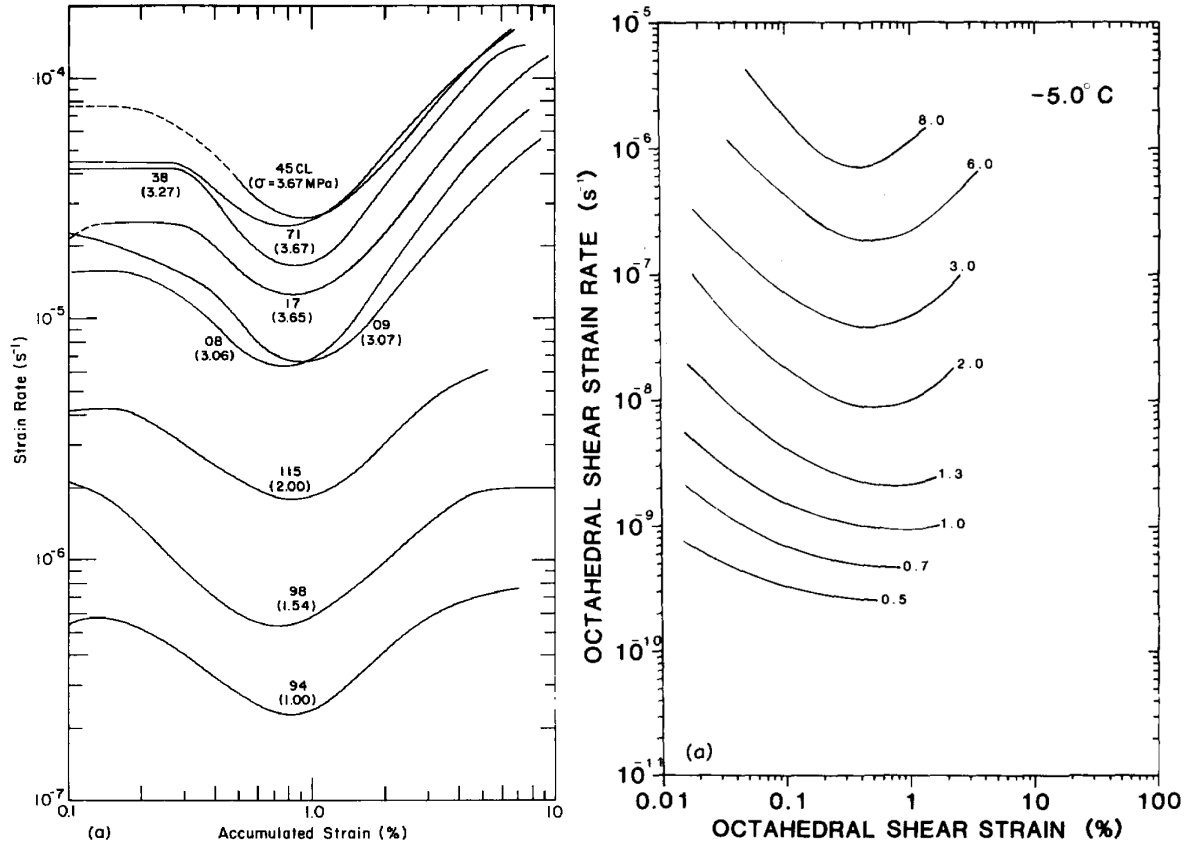


Figure 6.6: Creep curves (strain rate versus strain) from constant load experiments (Curve labels refer to stress loading in MPa). Reproduced from (Mellor and Cole, 1982, left), and (Jacka, 1984, right).

strain rate. By way of design, the uni-directional model (equation (6.4.18)) considers transient creep relative to the creep at the minimum strain rate by means of the parameters  $\mathbb{H}$  and  $\mathbb{K}$  (and  $c$ ). Consequently, a single master creep curve from experimental data normalized according to (6.8.3) can be predicted with the EMSOIM model. Assuming a constant elastic modulus ( $c = 0$ ), the non-dimensional uni-directional shearing problem (6.4.18) can be written as

$$-\frac{\partial}{\partial z} \left( \left| \frac{\partial v}{\partial z} \right|^m \frac{\partial v}{\partial z} + \mathbb{H} \frac{\partial^2 v}{\partial t \partial z} + \mathbb{K} \frac{1}{2} \frac{\partial u}{\partial z} \right) = 1. \quad (6.8.5)$$

If  $e = \partial u / \partial z$  is a non-dimensional shear strain and  $\dot{e} = \partial v / \partial z$  a non-dimensional shear rate, model (6.8.5) becomes

$$-\frac{\partial}{\partial z} \left( |\dot{e}|^{m+1} + \mathbb{H} \dot{e} + \frac{1}{2} \mathbb{K} e \right) = 1. \quad (6.8.6)$$

Since we now have identified an appropriate measure for  $[T]$ , we can renew the estimates for  $\mathbb{H}$  and  $\mathbb{K}$  based on equation (6.4.17). If we take the mean of all minimum strain rates from the creep experiments of MC82 and JA84, we obtain  $|\dot{e}_{min}| = 0.54 \text{ d}^{-1}$ . Using (6.8.2) and (6.4.17), we estimate  $\mathbb{H} = 24$  and  $\mathbb{K} = 1.8 \cdot 10^3$ . From the calculations performed in Section 6.5, values of  $\mathbb{H} \approx 5$  and  $\mathbb{K} \approx 10^4$  were expected for  $[T] = 5 \text{ d}$ .

In the fitting trial,  $\mathbb{K}$  was kept as estimated,  $c$  was chosen in order that elasticity ( $\mathbb{K}$ ) vanishes shortly after reaching the minimum shear rate, while  $\mathbb{H}$  could be used to correctly match the shear strain at minimum shear rate. Note that the experimental strain rate/strain data from the compression tests of MC82 and JA84 is converted to values corresponding to a simple shearing situation according to Budd (1969). In Figure 6.7, the thick solid dotted line depicts shear rate versus time (Fig. 6.7a) and shear rate versus shear strain (Fig. 6.7b) computed with equation (6.4.12). Shear rate and shear strains correspond to maximum

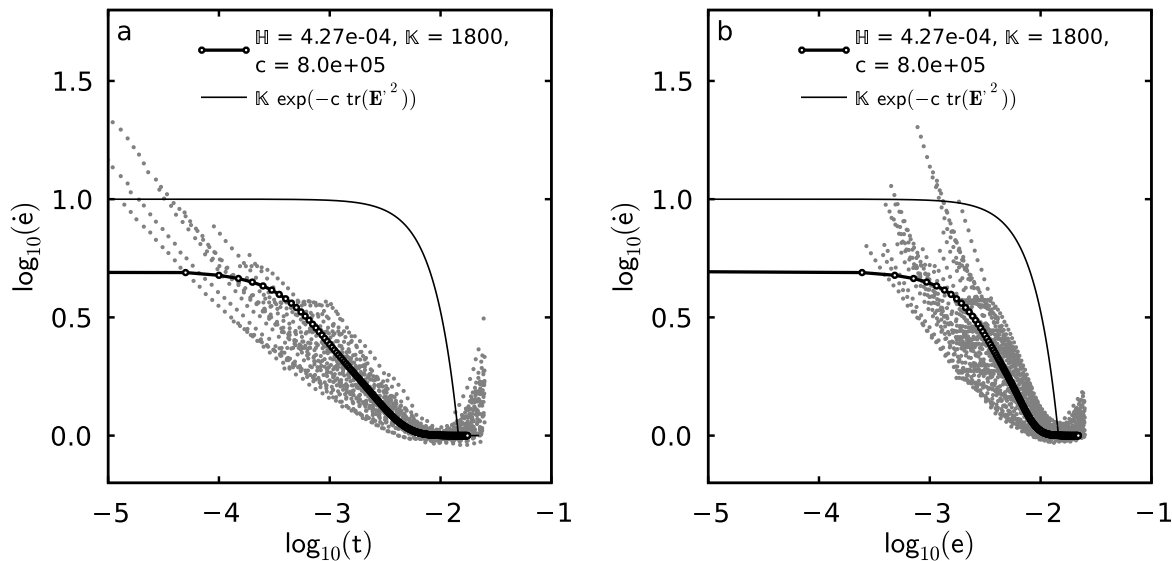


Figure 6.7: Non-dimensional creep relations (thick solid-dotted line) of shear rate as a function of time (a) and shear rate as a function of shear strain (b), modelled using the uni-directional flow equation (6.4.18). The model creep curves are compared to normalized primary/secondary creep data (background grey dots) of Mellor and Cole (1982) and Jacka (1984). The thin solid line is the normalized exponential decay function of the modulus  $\mathbb{K}$ .

values occurring at the bottom of the shearing slab. The parameters  $\mathbb{H} = 4.27 \cdot 10^{-4}$ ,  $\mathbb{K} = 1.8 \cdot 10^3$ , and  $c = 8 \cdot 10^5$  give a consistent fit to the experimental data of MC82 and JA84 (background grey dots) for both shear rate vs. time and shear rate vs. shear strain relations. Apart from the very high strain rates at initial small strain, the decrease of shear strain rates in the primary regime down to the minimum creep rate is well captured in the model. The (logarithmic) decay of the non-dimensional modulus  $\mathbb{K}$  (the non-dimensional equivalent of equation 6.4.5) is also drawn in Figures 6.7a, b (thin solid line). The decay of  $\mathbb{K}$  cancels elastic effects and recoverable strain approximately when the secondary creep regime is reached, while shear strain during primary creep remains fully recoverable.

Unexpectedly, the value of  $\mathbb{H}$  is more than 4 orders smaller than anticipated. Numerical failure of fitting the creep data using the expected  $\mathbb{H}$  and  $\mathbb{K}$  (occurrence of high-frequency oscillating creep), identifies a certain incompatibility of strain accelerations and elastic properties. The MSOFM model of Sun (1987) considers decaying strain rate (primary creep) as a deceleration response, i.e., a second-order effect. Our intent was to retain the MSOFM concept of primary and secondary creep and annihilate the sole viscous nature of the MSOFM by including elasticity, rendering elapsed creep reversible. However, this concept can only be maintained under two circumstances: either elastic properties are kept weak ( $\mathbb{K}$  small) or else strong elastic properties ( $\mathbb{K}$  large) must vanish before interfering with second order effects, i.e. before the primary creep response of ice. This would mean, that the MSOFM can be enhanced with elastic effects only for an initial (small) elastic response; the material may pertain only very weak elastic properties while the primary creep response (strain rate deceleration) is generated via second-order effect. Else, one abandons the concept of a modified second grade fluid enhanced with elastic properties and switches the interpretation, and regards the material as a viscoelastic solid enhanced with higher-order effects. In that case, the primary creep response will be generated primarily by elasticity (increased resistivity of the material, strain-hardening) and higher-order strain accelerations take on a minor role, creating initial strain rates larger than the stationary creep rate, and, equivalently, second-order effects will vanish in the early stage of the primary creep response. The conclusion is that the desired response of ice in the primary and secondary creep regimes can only be represented by one of these effects, and the other one must take on a minor role. Which of the two effects is to be suppressed depends on the objective

of the material law. Since we are concerned with elastic effects and recoverable creep, we choose the interpretation as a viscoelastic solid model, abandoning the MSOFM interpretation.

An appropriate response fitting the experimental creep data was presented and values for  $\mathbb{H}$ ,  $\mathbb{K}$  and  $c$  were determined. The value of  $\mathbb{H}$  indicates that the model parameter  $\alpha$  takes on a value radically different than expected on the basis of the MSOFM and the parameter estimation of Sun (1987). Indeed, the primary creep response is generated either by second grade effects (large  $\mathbb{H}$ ), or by means of elasticity alone. The non-zero  $\mathbb{H}$  merely initiates the creep at a shear rate higher than the minimum shear rate and has a minor impact elsewhere.

# Chapter 7

## Simulating reversing ice motion as viscoelastic recoverable creep

A recurring feature was the observation of ice motions drifting off the usual trajectory, or almost completely reversing the flow direction. In the first chapter of this thesis, a selection of ice flow motions occurring during different drainages of Gornersee was illustrated. Several of the referenced ice displacement trajectories not only exhibited increased flow velocities and/or noticeable vertical motion, but also particular departures from the expected flow paths. Moreover, the departures were retrograde; after a certain increase of time and displacement, the movement changed direction, and markers (and thus ice) resumed the trend of motion preceding the anomalous excursion. In Sugiyama et al. (2007a), the anomalous reversing motions in the periphery of Gornersee are discussed. The considered motions correspond to the type L1 of the drainage O1 (see Fig. 2.5a1). In Sugiyama et al. (2010) the side-ways (N-S) motions towards the margins below the confluence of Gornergletscher are treated, which correspond to the L3/L4 motions (see Figs. 2.7a1 and 2.8a1).

In chapter 3, the ice-flow changes occurring in the vicinity of Gornersee were scrutinized for the cases of the O1 and O2 drainages (A comparison of drainages 2004 and 2006). Due to the absence of a profound subglacial impact of the O2 drainage, the inspection successfully identified the presence and action of the lake water pressure on the surrounding ice. The lake water pressure is an extra load on the ice in the vicinity of the lake. The lake water exerts pressure on the sub-aqueous and lake-marginal ice, and is a comprehensible initiator of changing stress conditions. During the filling of Gornersee, the pressure increases gradually and ice flow within the vicinity of Gornersee reacts accordingly. This is the interpretation established in Chapter 3. The magnitude of the pressure depends on the depth, and possibly, on the surface area of the lake. During the lake drainage, the water pressure reduces again. The discharge of (lake) water determines the change of lake water level, which in turn determines the change of the pressure imposed on the ice. The forces acting upon the lake-marginal ice increase with increasing depth of the lake water. Thus, only a sufficiently deep (i.e. high water level) and large lake may be able to generate a substantial stress affecting the motion of the ice surrounding the lake. From this situation, it may be conjectured that a sufficient (and sufficiently fast) decrease of lake water pressure may allow the ice to temporarily reverse the displacement direction. The interplay between magnitude, rate of release of force imposed on the ice, and the transient response of the ice would then determine the possibility of such a reverse motion event. These relations will be explored in the following by simple simulations using the viscoelastic model (EMSOIM) presented.

### 7.1 Observed ice motions with reversing displacement component

The simulations will be based on the motion events observed. The superficial ice-motion events from two different O1-drainages exhibiting a recursive motion component are collected in Figure 7.1. Panels (a) depict the horizontal ice displacement (thick black solid). Along this trajectory, the symbols indicate

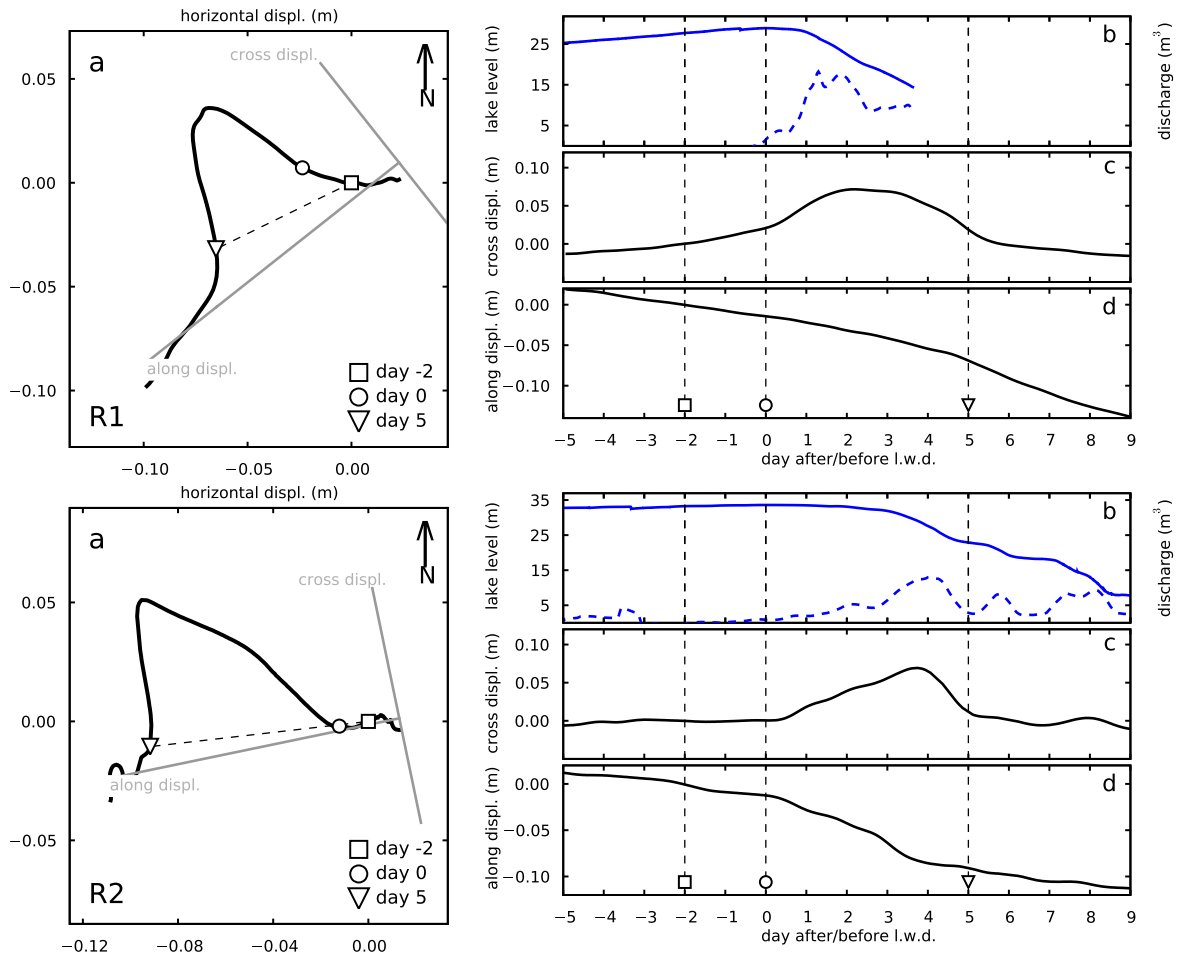


Figure 7.1: Panels R1a and R2a display horizontal ice displacement trajectories (solid black), with dates indicated. Grey lines labelled 'along displ.' refer to approximate motion trend lines computed from the trajectory data  $<$  day -2 and  $>$  day 5, while the lines labelled 'cross displ.' are normal thereto. Panels R1b/R2b display lake water level (blue solid) and lake discharge (blue dashed) as functions of time (l.w.d. = lake water level decrease). Panels R1c d/R2c d display transformed horizontal ice displacement; the displacement is separated into cross (c) and along-flow (d) components and plotted against time.

the direction of motion as they mark the positions at days -2, 0, and 5 (corresponding to the interval between 2 days prior to the highest lake water level and 5 days afterward). From the motion prior to day -2 and later than day 5, linear trend lines for each motion R1 and R2 were estimated, which are the solid grey lines labelled 'along displ.' in Figure 7.1, R1a and R2a. A coordinate transformation was then applied to the horizontal displacement trajectory, aligning one coordinate axis with the trend line, and the other axis normal thereto. Thus, the original horizontal displacement trajectory was separated into along-flow and cross-flow components, the new coordinate directions being indicated by the grey solid lines in Figure 7.1, R1a and R2a. The resulting time series of the along- and cross-displacements are depicted in the sub-panels R1c-d and R2c-d. Additionally, the sub-panels R1b and R2b in Figure 7.1 display the evolution of lake water level and lake discharge. The lake discharge was computed based on melt modeling studies by Huss et al. (2007). Vertical dashed lines and corresponding symbols refer again to the days -2, 0 and 5 of the drainages. The coordinate transformation isolates each of the two reversing motions. They now appear exclusively on one displacement component (i.e., on the cross-component, Fig. 7.1, R1c and R2c), whereas on the other component (Fig. 7.1, R1d and R2d), only an approximately linear displacement trend remains. Note that the along-flow directions in Figure 7.1 are oriented approximately in line with the lake boundary, whereas the cross-flow direction corresponds to directions normal to the lake boundary.

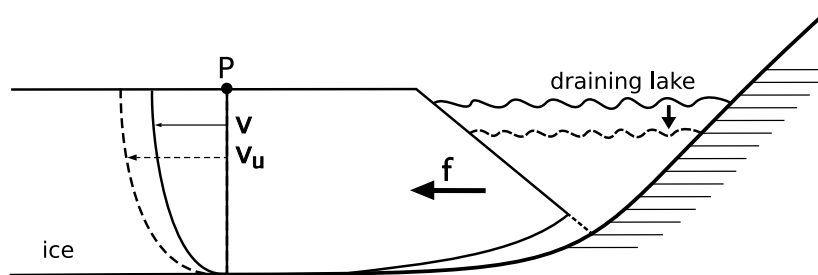


Figure 7.2: Use of uni-directional shearing model for creep recovery simulation.

If the reversing motion would solely be caused by the decrease of lake water pressure, one would expect the cross displacement in Figure 7.1R1c to follow the decrease of the lake water level (Fig. 7.1, R1b). However, this is not true for the first two days 1-2 of the drainage. In fact, when the lake water level starts to decrease on day 0, the ice displacement increases further and the ice moves away from the lake at accelerated rate (Fig. 7.1, R1c). At day 3, when the lake water level has already dropped about 10 m (Fig. 7.1, R1b), the cross displacement reverses and decreases again (which corresponds to the ice moving again towards the lake). The same applies for the R2-motion (Fig. 7.1, R2b, c).

## 7.2 Modelled reversing deformation in uni-directional shearing

With use of the EMSOIM uni-directional shearing model (equation (6.4.18)), a modelling experiment as depicted in Figure 7.2 is pursued. On a line normal to the lake, we consider the vertical shearing flow profile across the depth of the ice column. The lake is situated upstream the measurement point  $P$ , which refers to the location where the reversible motion events R1 and R2, depicted in Figure 7.1, were observed. The effect of the lake water and drainage is considered as a modulation of the loading component  $f$ , i.e. the right-hand side of the equation (6.4.18). Variations of basal motion can not be considered, as the use of basal motion as a specified boundary condition directly transfers to the surface in the 1-D model. Further, implementation of a basal boundary condition generating a basal velocity is avoided. The purpose of the computational experiment is to answer the following question: What load and subsequent release across what time is needed to create reversible displacements similar to the observations at the surface of the ice column if the ice is considered the sole actuator. Thus, the objective is to test the conditions under which a reversing displacement can be caused purely by the ice rheology reacting to changing stress conditions. If the model generates a deformation response with reasonable material parameters on time and stress scales expected for the situation of Gornensee, we may suppose that viscoelastic flow effects are acting (at least amongst other processes). If no acceptable creep response is deduced, the hypothesis of viscoelastic recovery of deformation is rejected. Then, the reversible ice motion is declared a consequence of other influences, such as enhanced basal motion and/or vertical uplifting etc.

In the simulations, the load function  $f$  is taken as a sinusoidal signal. For a non-dimensional load  $\bar{f}$  with peak load equal to unity,

$$\begin{aligned} \bar{f} &= \sin(\pi(t/t_{max})^p), & \text{for } t \leq t_{max}, \\ \bar{f} &= 0, & \text{for } t > t_{max}, \end{aligned} \quad (7.2.1)$$

where  $t$  is the non-dimensional experiment run-time,  $t_{max}$  is a limit time to normalize the half-period of the sinusoidal signal, i.e. the sinusoidal load then becomes zero at  $t = t_{max}$ . The sinusoidal load is needed to apply an increasing force component and reproduce the initial increase of displacement; the displacement reverses direction with a delay of about 1-3 days from day 0. For an exponent  $p > 1$ , the load function is asymmetric; the increase of the load is slowed, while the decrease of the load is hastened. In Figure 7.3a, a set of symmetric, non-dimensional loading curves with  $p = 1$  in equation (7.2.1) are displayed. The total run-time was  $T = 1.1$ , and  $t_{max}$  was incrementally changed from  $0.2T$  to  $0.8T$  for

S1-S7, respectively. In Figure 7.3b, the resulting transient displacement responses at the surface of the ice column are depicted. For these responses, the parameter values of  $\mathbb{H} = 4.27 \cdot 10^{-4}$ ,  $\mathbb{K} = 1800$ , and  $c = 8 \cdot 10^5$ , as estimated in Section 6.8, were used. Thus, the curves depict various superficial recovery responses for increasing time of loading. For increasing loading time, the slope of deformation on the recovering part becomes less steep, i.e. the creep recovers less quickly. This is an influence of material weakening due to the memory factor  $c$ . To estimate scales  $[L]$  and  $[T]$  required to normalize the real observations fitting into the range of non-dimensional creep recovery responses displayed, the definitions (6.4.16) and (6.4.17) are suitable. The most important relation is

$$\mu[T]^{-(m+1)} = [L][f]. \quad (7.2.2)$$

Thus, given  $\mu$ ,  $[T]$  and  $[L]$  by the real data, where  $[T]$  represents a time interval of the lake drainage and  $[L]$  an appropriate measure for the ice thickness at the location, we may immediately deduce the dimensional load required to produce the according dimensional response. However, the load is a measure of force per unit volume. Note that  $[f][L]$  has the more practical dimension of stress,  $[\sigma]$ , thus we may consider (7.2.2) as

$$[\sigma] = [f][L] = \mu[T]^{-(m+1)}. \quad (7.2.3)$$

From Figure 7.1 (R1c and R2c) it is observed that the major increase and subsequent decrease of the ice displacement takes place during the first five days of the drainage (day 0 to day 5). The time scale can thus be set as  $[T] = 5$  d. The thickness of the ice column at the location of interest is roughly  $[L] = 150$  m. Using equation (7.2.3) with a standard value of the viscosity  $\mu = 2.41 \text{ MPa d}^{\frac{1}{3}}$ , the stress scale is estimated as  $[\sigma] = 1.4 \text{ MPa}$ . The modelled non-dimensional displacements functions displayed in Figure 7.3b can now be re-dimensionalized using the aforementioned scales for time,  $[T]$ , and length,  $[L]$ . The range of the non-dimensional displacements is  $0.0012 \leq u \leq 0.0018$ , which, multiplied by  $[L]$ , corresponds to the physical range  $0.18 \leq u \leq 0.27$  m. The maximum non-dimensional time in Figure 7.3b is 1.0, which corresponds to 5 d. Thus, the modelled displacements as functions of time shown in Figure 7.3b, re-dimensionalized with the scales  $[T] = 5$  d and  $[L] = 150$  m, indicate that for an applied stress of  $[\sigma] = [f][L] = 1.4 \text{ MPa}$ , up to 0.27 m of displacement can be fully recovered. The amplitude of reversing displacements of the motions R1c and R2c is about 0.1 m (see Fig. 7.1, R1c and R2c), thus the range of the modelled displacement functions covers the observed motions R1c and R2c when appropriately rescaled. However, the corresponding stress scale (1.4 MPa) required to produce these displacements is rather large. A possible source to account for the stress required to deform the ice is the lake water pressure acting on the ice surrounding the lake. The pressure generated by Gornerssee is determined by its depth  $d$ , which is  $d \approx 30$  m. Thus, the lake water pressure is expected as  $p_{lake} = \rho g d \approx 0.3 \text{ MPa}$ , where  $\rho = 1000 \text{ kg/m}^3$  is the density of water and  $g = 9.82 \text{ m/s}^2$  is the gravitational acceleration. The stress which can be caused by the lake water pressure is about five times lower than the required stress  $[\sigma] = 1.4 \text{ MPa}$ . Further, by use of (6.4.17)<sub>2</sub>, the elastic modulus is estimated as  $\beta_0 = \mathbb{K}[\sigma] = 2520 \text{ MPa}$ , which appears too low, as it is only about a third of the theoretically expected modulus  $\beta_0$  for ice (Tab. 6.2). Nevertheless, the displacements can be generated on the same time scale  $[T] = 5$  d but at a lower stress level of  $[\sigma] = 0.3 \text{ MPa}$ , if the ice is considered to be much weaker. This can be achieved by lowering the viscosity to a fifth, i.e.  $\mu = 0.5 \text{ MPa d}^{\frac{1}{3}}$ . With the set of scales as  $[T] = 5$  d,  $[L] = 150$  m,  $[\sigma] = 0.3 \text{ MPa}$  and  $\mu = 0.5 \text{ MPa d}^{\frac{1}{3}}$ , identical displacements functions as in Figure 7.3b are generated in the model. However, weakening the ice viscosity has the disadvantage that the corresponding elastic modulus becomes very low. In this case,  $\beta_0 = \mathbb{K}[\sigma] = 540 \text{ MPa}$  for the value of  $\mathbb{K} = 1800$  as used in the computations, and the anticipated stress of 0.3 MPa. Only with a remarkable increase of the elasticity number  $\mathbb{K}$  to  $\mathbb{K} = 2.3 \cdot 10^4$  is the expected elastic modulus of  $\beta_0 = 7000 \text{ MPa}$  recovered. On the other hand, if both the elastic modulus and ice viscosity retain the theoretically predicted values  $\beta_0 = 7000 \text{ MPa}$  and  $\mu = 2.41 \text{ MPa d}^{\frac{1}{3}}$ , an even larger stress as  $[\sigma] = 3.9 \text{ MPa}$  is required to generate appropriate displacements. This stress level is more than ten times larger than the (maximum) expected lake water pressure.

In Figure 7.4 the reversing motions R1 and R2 were reproduced using the shearing model. The scales and parameters which apply to the depicted results were as follows:  $[L] = 180$  m,  $[T] = 4.6$  d,  $\mathbb{H} = 10^{-4}$ ,

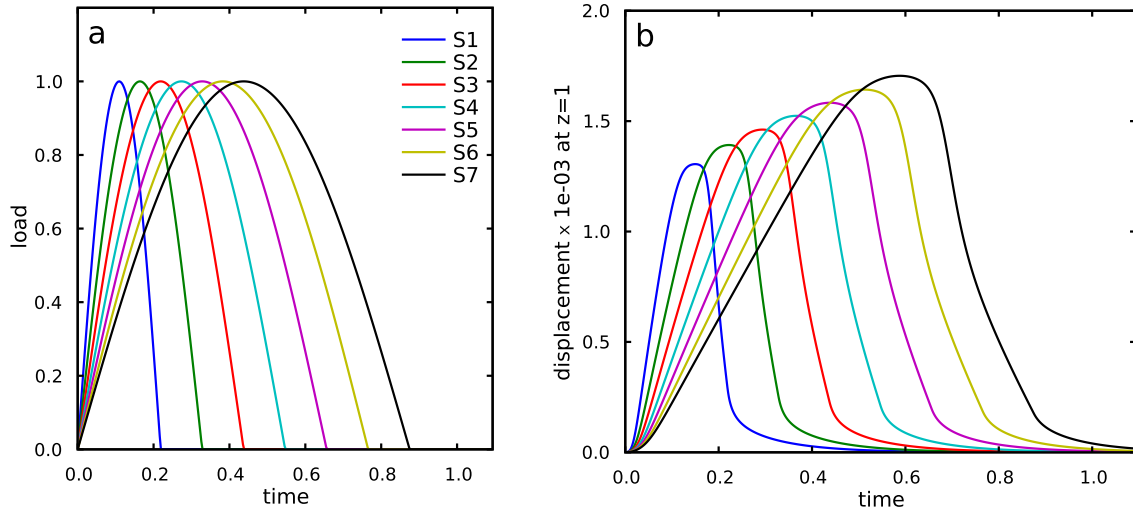


Figure 7.3: (a) Loads as functions of time, according to equation (7.2.1). (b) Resulting displacement as function of time (at surface  $z = 1$ ). Parameters used in the model:  $\mathbb{H} = 4.27 \cdot 10^{-4}$ ,  $\mathbb{K} = 1800$ , and  $c = 8 \cdot 10^5$  (as estimated in Section 6.8).

$\mathbb{K} = 2500$ ,  $c = 0$ . Using equation (7.2.3), the corresponding stress is  $[\sigma] = 0.3$  MPa if the ice is considered to have a viscosity of  $\mu = 0.5$  MPa d $^{\frac{1}{3}}$ . The reversing motions can be modelled adequately under these circumstances. Although, as mentioned beforehand, if  $\mu = 0.5$  MPa d $^{\frac{1}{3}}$ , a value of the parameter  $\mathbb{K} = 2.5 \cdot 10^4$  is required to guarantee an elastic modulus of  $\beta_0 = 7000$  MPa. To reproduce the displacements according to the measurements (Fig. 7.4), the elasticity number  $\mathbb{K}$  had to be adjusted, and sufficient agreement between model and measurements was only achieved with  $\mathbb{K} = 2500$ , which is one order lower than anticipated. The corresponding elastic modulus is  $\beta_0 = 750$  MPa, which is significantly below the theoretically expected value. Thus, the model results are not altogether consistent. The stresses required to reproduce the reversing ice motions are about five to ten times larger than the lake water pressure if expected values of the elastic modulus of about 3500-7000 MPa are considered for the glacier ice. Even if the ice is drastically softened, the reversing displacements can not be adequately reproduced without a considerable decrease of the elastic modulus. To allow displacements at envisaged low stress levels below 1 MPa, a rather low elastic modulus of less than 1000 MPa is required. If the viscosity of the ice is not changed at all, the ice can only be deformed appropriately by such low stresses if it experiences the applied stress across a much longer time scale. According to equation (7.2.2), this would imply  $[T] = 400$  d. However, further numerical computations using  $[T] = 400$  d together with  $[L] = 180$  m and  $\mu = 2.41$  MPa d $^{\frac{1}{3}}$  could not account for the discrepancy of about one order of magnitude on the elastic parameter  $\mathbb{K}$ . Further, the recovery of the displacements starts to lag strongly behind the release of the imposed load, and a quick recovery of the displacements within 1-3 days as observed (Fig. 7.4) is not possible.

### 7.3 Discussion

It appears difficult to provide a consistent suite of scales and parameters which would generate satisfactory results of reversing ice motion. No set of scales for applied stress, time and elastic modulus allowed a reasonable explanation of the reversing displacements. Either the stresses required to reproduce displacements of correct magnitude are too large, or else the elastic properties of the ice must be considerably weaker. Thus, it does not seem plausible to generate reversing motions solely by considering the impact of the lake water pressure and transient rheological properties of the ice. Even if the glacier ice can be characterized by an elastic modulus as low as 1000 MPa, stresses at the order of at

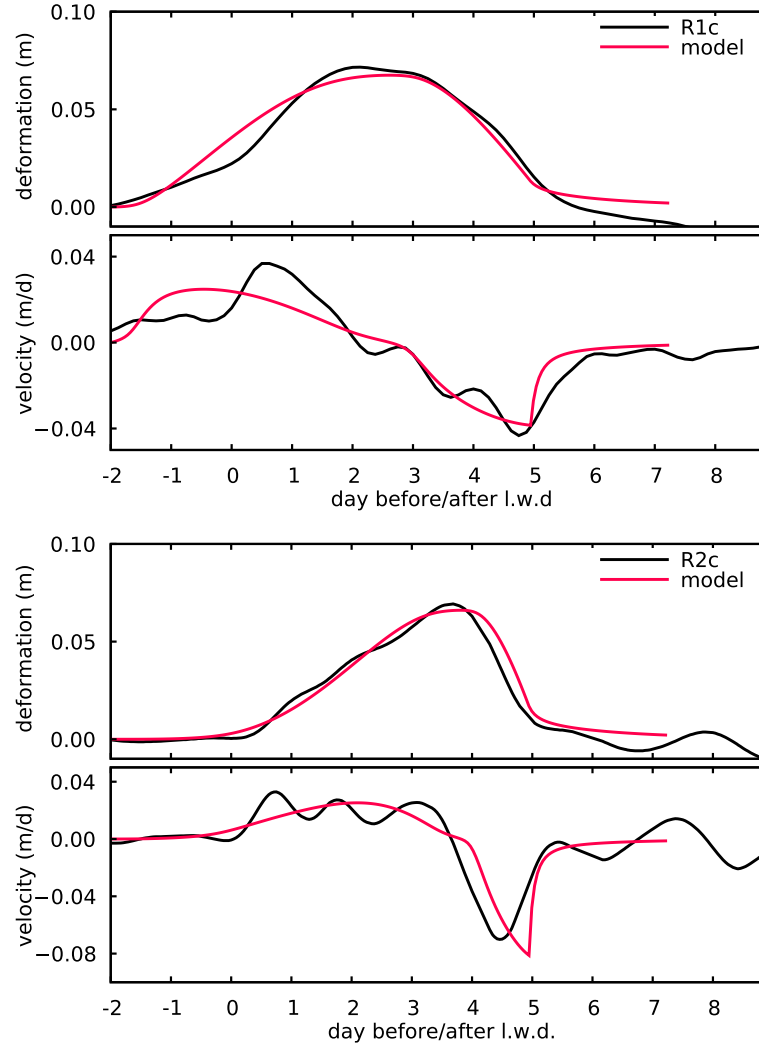


Figure 7.4: Reversing ice motion of Figure 7.1 reproduced using the uni-directional shearing model. Parameters and scales are:  $[L] = 180$  m,  $[T] = 4.6$  d,  $\mathbb{H} = 10^{-4}$ ,  $\mathbb{K} = 2500$ ,  $c = 0$ .

least 1 MPa are needed to yield sufficiently large displacements. Thus, under a reasonable ice rheology with an elastic modulus larger than 1000 MPa, the effect of the lake water pressure appears too weak, providing no sufficient explanation. Further, it can not account for the initially enhanced displacement of the ice, which occurs after day 0 (the begin of lake water level decrease), and before the ice reverses the direction of displacement (at  $\sim$ day 3). Sugiyama et al. (2007a) tried to explain the reversing motion as a purely elastic process. It was argued that the reversing motion can only be explained if the applied stresses do not exceed  $\sim 0.001$  MPa. At higher stress scales, the recovery of displacements could only be explained by inclusion of viscoelastic creep effects, which would allow the material to recover from displacements much larger than the purely elastic response, due to the existence of delayed elastic strain. The lake water pressure creates stresses of about 0.3 MPa, which are about  $300\times$  larger than the elastic stress limit suggested by Sugiyama et al. (2007a). Due to the solid character of the viscoelastic model (EMSOIM), every deformation is rendered fully recoverable, especially when no weakening of the elastic properties is considered ( $c = 0$ ). However, in the model, no consistency between time, stress and displacement explaining the measurements was achieved. The numerical experiments suggest that the reversing displacements can only be explained when considering even higher stresses than the lake water pressure. Note that in the model, the stress scale can be replaced fully by the time scale due to relation (7.2.2); however, it actually does not even have to be considered for the modelling. However, inconsistencies with the corresponding elastic shear modulus which can be recovered from the time scale by

equation (6.4.17)<sub>2</sub> still exist. Thus, the reversing motion is not explained solely by viscoelastic relaxation of deformation experienced by the ice.

The required stress of about 1-1.5 MPa corresponds approximately to the overburden pressure of a column of ice of about 150-180 m thickness. It is known that the ice was lifted by small amounts of ~2-5 cm during the time of reversing motions R1 and R2 (see also Fig. 2.5b1). This means that one may expect that the ice was nevertheless subjected to large stresses in the range of 1-1.5 MPa. Such large stresses and resulting vertical motion is better explained by high basal water pressure approaching the ice-overburden pressure than solely by the lake water pressure imposed on the ice by a 30 m deep lake basin as in Figure 7.2. Such drastically increased basal water pressure in the vicinity of the lake can be explained if the lake water is hydraulically connected to the water at the base of the glacier; or else, if increasing discharge of lake water to the basal environment over-stresses the subglacial drainage system. Between days 0 to 5, the reversing motion R2 correlates with the increase and decrease of the discharge of lake water (Fig. 7.1b, c). This would support the latter interpretation of a blockage of the subglacial drainage system of Gornergletscher by the increasing discharge of lake water. In that case, the increasing basal water pressure may produce the required stress of 1-1.5 MPa at which vertical lifting is enabled. Further, under the same conditions, basal displacement of the ice is very likely and can not be precluded. Therefore, the interpretation of the reversing ice motion being a secondary deformation accompanying the lowering of the initially uplifted ice as a consequence to the decrease of the subglacial discharge of lake water is likely more realistic.



# Chapter 8

## Conclusions

Monitoring the surface ice motion of a glacier is still one of the most frequent methods used in basic glaciology. The measurements of the flow of ice are needed to further understand the behaviour of glaciers under changing boundary conditions such as weather, climate, local topography and conditions at the glacier bed. The motion of glacier ice is tightly coupled to glacier hydrology. Subglacial distribution and transport of water modulates basal motion of the glacier ice, which is directly transferred and reflected in the ice motion at the surface of the glacier. In that sense, the dramatic impact of the subglacial drainages of the ice-marginal Gornersee on the surface ice flow regime of Gornergletscher was expected. The measurements of ice displacements, flow velocities and heave or lowering of the ice surface showed that the impact of the subglacial lake drainages on the ice flow of adjacent Gornergletscher is highly variable both spatially and temporally. This has been illustrated by the compilation of flow measurements and inspection of the ice motions induced by the differential impacts of the Gornersee drainages on the ice flow of Gornergletscher on the local and regional scales (Chapter 2). It became evident, that the various ice flow changes did not react in similar ways in every drainage. Where the ice of Gornergletscher was displaced and uplifted severely in the periphery of Gornersee in the years 2004 and 2007 (type O1), the same ice was left almost unaffected when the lake drained early in the years 2005 and 2008 (drainage types O3). Thus, the impact of the lake drainages on the surface ice flow of Gornergletscher was highly diversified. If the character of subglacial lake drainages varies similarly at other locations and other glaciers, it is expected that the damming glacier reacts equivalently in very distinguished ways to different lake drainages. Therefore, the character of the lake drainage can be established solely from the analysis of featured ice flow changes induced by the lake drainage.

The particular, very calm lake drainage of 2006 (type O2) made it possible to identify a previously neglected process. The increase and decrease of lake water pressure imposed on the ice was shown to have the potential to change the ice motion in the vicinity of the Gornersee, which had not been previously considered. The impact of the lake water pressure was not readily deducible from the individual trajectories indicating the ice movements at the marker locations but only became evident by appropriate analysis of the flow velocities (Chapter 3).

During one selected drainage of Gornersee (2008, type O3), the surface ice displacements of Gornergletscher were recorded by a novel interferometric radar device. The recording of the surface ice displacements by the interferometer was successfully accomplished. Unfortunately, due to the absence of anticipated flotation of ice peripheral to Gornersee, the ice displacements in the periphery of Gornersee were not scrutinized in more detail. Rather, the radar results provided an autonomous confirmation of the side-ways ice motions towards the margins which occurred about 2 km down-glacier of Gornersee. This was only possible due to the large coverage of the radar device, which allowed a survey of almost the entire area of Gornergletscher downstream of Gornersee. This coverage was a prominent feature of the interferometer.

To a large part, this thesis has focused on the construction of a sound viscoelastic constitutive model for the ice rheology. The viscoelastic model presented incorporates the complete response of ice expected

for short-time to medium-time loading conditions: an initial elastic strain and delayed elastic strain with primary creep fading into a steady creep response at the minimum creep rate observed in laboratory experiments. Such a model was first applied to a non-laboratory situation on an Alpine glacier within this study. However, the relevant processes could not be explained, as anticipated, by the recovery of deformation exhibited by a viscoelastic ice rheology. The required stresses are much larger than the stress imposed on the ice due to the presence of the lake water. Therefore, the impact of the lake water pressure modulating the ice motion is not sufficient to justify considering viscoelastic effects in the ice rheology. The effects of a viscoelastic rheology only become relevant at sufficiently large scales of either stress, time or length dimension. At the base of the glacier, normal stress conditions in the viscoelastic range  $>1$  MPa can be exceeded, as vertical uplifting of the glacier ice during the lake drainage indicates. The subglacial discharge of lake water blocking the basal drainage system is a possible cause of the elevated stresses. However, in such cases, increased basal motion of the ice is very likely to contribute to the surface ice motion. Consequently, the stress does not necessarily imply creep deformation of the ice, but may simply imply basal (rigid-body) displacement of the ice, in which case viscoelastic recovery of deformation is redundant.

### **Future prospects of modeling a viscoelastic ice rheology**

This outcome was partially expected and became apparent during the occupation with the EMSOIM viscoelastic model. Other numerical experiments were conducted, in which also two-dimensional flow situations were treated. But not all experiments conducted were promising. Chapter 7 can thus be regarded as the most simple case which indicates that the proposed hypothesis of viscoelastic reversible ice motion is insufficient. This outcome may seem somewhat unfruitful after a great deal of work has been put into the derivation and implementation of the EMSOIM model. However, this work was additionally motivated by the fact that the knowledge of the viscoelastic rheological properties of ice beyond the laboratory scale is insufficient. Moreover, it is not clear what further effects a viscoelastic ice rheology would generate and where or how these effects may be captured or revealed in actual flow measurements. It is therefore important to assess possible flow effects generated by an appropriate viscoelastic ice rheology. Comparison of horizontal and vertical profiles of stress, pressure, strain and strain-rates in conventional but natural flow situations using a viscous ice rheology on the one hand and an enhanced viscoelastic rheology on the other, would help to corroborate knowledge about the rheology of the ice of glaciers and ice sheets beyond laboratory situations. The EMSOIM viscoelastic model is a feasible candidate for such studies. Within this thesis, a robust numerical suite for the viscoelastic EMSOIM model with about 7000 lines of code emerged. The code supports two-dimensional computations and was extensively tested. Thus, a tool for future analysis of viscoelastic flow effects for a non-linear viscoelastic ice rheology is available (<http://bitbucket.org/riesen/emsoim>).

## References

- Anderson, R. S., Walder, J. S., Anderson, S. P., Trabant, D. C., and Fountain, A. G. (2005). The dynamic reponse of Kennicott Glacier, Alaska, USA, to the Hidden Creek Lake outburst flood. *Annals of Glaciology*, 40:237,242.
- Ashby, M. F. and Duval, P. (1985). The creep of polycrystalline ice. *Cold Regions Science and Technology*, 11:285–300.
- Azizi, F. (1989). Primary creep of polycrystalline ice under constant stress. *Cold Regions Science and Engineering Monograph*, 16:159–165.
- Bamber, J. L., Hardy, R. J., and Joughin, I. (2000). An analysis of balance velocities over the Greenland ice sheet and comparison with synthetic aperture radar interferometry. *Journal of Glaciology*, 46(152):67–74.
- Bamler, R. and Hartl, P. (1998). Synthetic aperture radar interferometry. *Inverse Problems*, 14:R1–R54.
- Bassi, A. (1999). Messungen der Oberflächengeschwindigkeitsänderungen des Unteraargletscher, Berner Alpen, mit hoher räumlicher und zeitlicher Auflösung. Master's thesis, ETH Zürich.
- Björnsson, H. (1992). Jökulhlaups in Island: Prediction, characteristics and simulation. *Annals of Glaciology*, 16:95–106.
- Brown, P. N., Hindmarsh, A. C., and Petzold, L. R. (1998). Consistent initial condition calculation for Differential-Algebraic Systems. *SIAM Journal on Scientific and Statistical Computing*, 19(5):1495–1512.
- Bucher, C. (2007). Geodätische Überwachungsmessung am Gornergletscher. Master's thesis, ETH Zürich.
- Budd, W. F. (1969). The dynamics of ice masses. Australian National Antarctic Research Expedition, Scientific Report 108, Melbourne, Australia.
- Castelnau, O., Duval, P., Montagnat, M., and Brenner, R. (2008). Elastoviscoplastic micromechanical modeling of the transient creep of ice. *Journal of Geophysical Research*, 113(B11203).
- Chen, G. (1998). *Positioning for the airborne laser altimetry at Long Valley, California*. PhD thesis, MIT.
- Coleman, B. D. and Noll, W. (1960). An approximation theorem for functionals, with applications in continuum mechanics. *Archive for Rational Mechanics and Analysis*, 6(1):355–370.
- Crochet, M. J., Davies, A. R., and Walters, K. (1984). *Numerical Simulation of Non-Newtonian Flow*, volume 1 of *Rheology Series*. Elsevier Science Publishers B.V.
- Dunn, J. and Rajagopal, K. (1995). Fluids of differential type: critical review and thermodynamic analysis. *International Journal of Engineering Science*, 33:689–729.
- Dunn, J. E. and Fosdick, R. L. (1974). Thermodynamic stability of boundedness of fluids of complexity 2 and fluids of second grade. *Archive for Rational Mechanics and Analysis*, 56:191–252.

- Eisen, O., Bauder, A., Lüthi, M., Riesen, P., and Funk, M. (2009). Deducing the thermal structure in the tongue of Gornergletscher, Switzerland, from radar surveys and borehole measurements. *Annals of Glaciology*, 50(51):63–70.
- ESA (2007). *InSAR Principles: Guidelines for SAR Interferometry Processing and Interpretation*. European Space Agency (ESA), TM-19 edition.
- Estey, L. H. and Meertens, C. M. (1999). TEQC: The Multi-Purpose Toolkit for GPS/GLONASS data. *GPS Solutions*, 3(1):42–49.
- Fahnestock, M. A., Bindschadler, R. A., Kwok, R., and Jezek, K. (1993). Greenland ice sheet surface properties and ice dynamics from ERS-1 SAR imagery. *Science*, 262(5139):1530–1534.
- Glen, J. W. (1952). Experiments on the deformation of ice. *Journal of Glaciology*, 2(12):111–114.
- Glen, J. W. (1955). The creep of polycrystalline ice. *Proceedings of the Royal Society of London, Ser. A*, 228(1175):519–538.
- Gudmundsson, G. H. (1994). Converging glacier flow — a case study: the Unteraarglacier. Mitteilung 131, Versuchsanstalt für Wasserbau, Hydrologie und Glaziologie der ETH Zürich, Gloriastrasse 37-39, ETH Zürich, CH-8092 Zürich. pp. 120.
- Gudmundsson, G. H. (1999). A three-dimensional numerical model of the confluence area of Unteraargletscher, Bernese Alps, Switzerland. *Journal of Glaciology*, 45(150):219–230.
- Gudmundsson, G. H., Bassi, A., Vonmoos, M., Bauder, A., Fischer, U. H., and Funk, M. (2000). High-resolution measurements of spatial and temporal variations in surface velocities of Unteraargletscher, Bernese Alps, Switzerland. *Annals of Glaciology*, 31:63–68.
- Helbing, J. (2005). *Glacier dynamics of Unteraargletscher: Verifying theoretical concepts through flow modeling*. Dissertation No 16303, ETH Zürich.
- Hofmann-Wellenhof, B., Lichtenegger, H., and Collins, J. (2001). *Global Positioning System: Theory and Practice*. Springer-Verlag.
- Huss, M., Bauder, A., Werder, M., Funk, M., and Hock, R. (2007). Glacier-dammed lake outburst events of Gornersee, Switzerland. *Journal of Glaciology*, 53(181):189–200.
- Hutter, K. (1983). *Theoretical glaciology; material science of ice and the mechanics of glaciers and ice sheets*. D. Reidel Publishing Company/Tokyo, Terra Scientific Publishing Company.
- Hutter, K. and Jöhnk, K. (2004). *Continuum methods of physical modeling : continuum mechanics, dimensional analysis, turbulence*. Springer, Berlin, Germany.
- Iken, A. (1977). Variations of surface velocities of some Alpine glaciers measured at intervals of a few hours. Comparison with Arctic Glaciers. *Zeitschrift für Gletscherkunde und Glazialgeologie*, 13:23–35.
- Iken, A. (1981). The effect of the subglacial water pressure on the sliding velocity of a glacier in an idealized numerical model. *Journal of Glaciology*, 27(97):407–421.
- Iken, A. and Bindschadler, R. A. (1986). Combined measurements of subglacial water pressure and surface velocity of Findelengletscher, Switzerland: Conclusions about drainage system and sliding mechanism. *Journal of Glaciology*, 32(110):101–119.
- Iken, A., Röthlisberger, H., Flotron, A., and Haerberli, W. (1983). The uplift of the Unteraargletscher at the beginning of the melt season – a consequence of water storage at the bed? *Journal of Glaciology*, 29(101):28–47.

- Iken, A. and Truffer, M. (1997). The relationship between subglacial water pressure and velocity of Findelengletscher, Switzerland, during its advance and retreat. *Journal of Glaciology*, 43(144):328–33.
- Jacka, T. H. (1984). The time and strain required for development of minimum strain rates in ice. *Cold Regions Science and Technology*, 8(3):261–268.
- Jellinek, H. H. G. and Brill, R. (1956). Viscoelastic Properties of Ice. *Journal of Applied Physics*, 27(10).
- Joseph, D. D. (1976). *Stability of Fluid Motions*, volume 27 and 28 of *Springer Tracts in Natural Philosophy*. Springer, Berlin.
- Joseph, D. D. (1990). *Fluid dynamics of viscoelastic liquids*, volume 84 of *Applied mathematical sciences*. Springer-Verlag.
- Joughin, I., Winebrenner, D., Fahnestock, M., Kwok, R., and Krabill, W. (1996). Estimation of ice-sheet motion using satellite radar interferometry: method and error analysis with application to Humbolt Glacier, Greenland. *Journal of Glaciology*, 42(142):564–575.
- Joughin, I. R., Kwok, R., and Fahnestock, M. A. (1998). Interferometric estimation of three-dimensional ice-flow using ascending and descending passes. *IEEE Transactions on Geoscience and Remote Sensing*, 36(1):25–37.
- Joughin, I. R., Winebrenner, D. P., and Fahnestock, M. A. (1995). Observations of ice-sheet motion in greenland using satellite radar interferometry. *Geophysical Research Letters*, 22(5):571–574.
- Kalman, R. E. (1960). A new approach to linear filtering and prediction problems. *Transactions of the ASME—Journal of Basic Engineering*, 82(Series D):35–45.
- King, M. (2004). Rigorous GPS data-processing strategies for glaciological applications. *Journal of Glaciology*, 50(171):601–607.
- Kirby, R. C. and Logg, A. (2006). A compiler for variational forms. *ACM Transactions on Mathematical Software*, 32(3):417–444.
- Kjartason, B. (1986). *Pressure meter creep testing in laboratory ice*. PhD thesis, University of Manitoba, Winnipeg, Manitoba, Canada.
- Le Gac, H. and Duval, P. (1980). *Constitutive relations for the non-elastic deformation of polycrystalline ice*. In Tryde, P., *International Union of Theoretical and Applied Mechanics*, chapter Physics and Mechanics of Ice, pages 51–59. Springer-Verlag.
- Lockett, F. J. (1972). *Nonlinear Viscoelastic Solids*. Academic Press Inc., London.
- Logg, A. and Wells, G. N. (2010). DOLFIN: Automated finite element computing. *ACM Transactions on Mathematical Software*, 37(2):20:1–20:28.
- Man, C.-S. and Sun, Q.-X. (1987). On the significance of normal stress effects in the flow of glaciers. *Journal of Glaciology*, 33(115):268–273.
- Marc (2005). *MSC.Marc/Mentat 2005 User's Manual*. MARC Software Corporation, 2 MacArthur Place, Santa Ana, CA 92707, 2005 edition.
- Massoudi, M. and Vaidya, A. (2008). On some generalizations of the second grade fluid model. *Nonlinear Anal. R. World Appl.*, 9:1169–1183.
- McTigue, D. F., Passman, S. L., and Jones, S. J. (1985). Normal stress effect in the creep of ice. *Journal of Glaciology*, 31(108):120–126.

- Mellor, M. and Cole, D. (1982). Deformation and failure of ice under constant stress or constant strain-rate. *Cold Regions Science and Technology*, 5(3):201–219.
- Mellor, M. and Cole, D. (1983). Stress/strain/time relations for ice under uniaxial compression. *Cold Regions Science and Technology*, 6(3):207–230.
- Mellor, M. and Smith, J. (1967). Creep of Snow and Ice. In Oura, H., editor, *Physics of snow and ice*, International conference on low temperature science, pages 843–855, The Institute of Low Temperature Science Hokkaido University.
- Mellor, M. and Testa, R. (1969). Creep of ice under low stress. *Journal of Glaciology*, 8(52):147–152.
- Meyssonnier, J. and Goubert, A. (1994). Transient creep of polycrystalline ice under uniaxial compression: an assessment of internal state variable models. *Annals of Glaciology*, 19:55–62.
- Mohr, J., Reeh, N., and Madsen, S. N. (1998). Three-dimensional glacial flow and surface elevation measured with radar interferometry. *Nature*, 391.
- Morland, L. W. (1979). Constitutive laws for ice. *Cold Regions Science and Technology*, 1(2):101–108.
- Morland, L. W. and Spring, U. (1981). Viscoelastic fluid relation for the deformation of ice. *Cold Regions Science and Technology*, 4(3):255–268.
- Müller, I. and Wilmanski, K. (1986). Extended thermodynamics of a non-newtonian fluid. *Rheol. Acta*, 25:335–349.
- Natural Resources Canada (2008). Online Precise Point Positioning (CSRS-PPP) manual. Technical report, Natural Resources Canada (Canadian Spatial Reference System, CSRS). <http://www.geod.nrcan.gc.ca>.
- Nye, J. F. (1953). The flow law of ice from measurements in glacier tunnels, laboratory experiments and the Jungfraufirn borehole experiment. *Proceedings of the Royal Society of London, Ser. A*, 219(1193):477–489.
- Nye, J. F. (1976). Water flow in glaciers: jökulhlaups, tunnels and veins. *Journal of Glaciology*, 17(76):181–207.
- Owens, R. and Phillips, T. (2002). *Computational Rheology*. Imperial College Press. ISBN 1-86094-186-9.
- Paterson, W. S. B. (1994). *The Physics of Glaciers*. Pergamon, New York, third edition.
- Rajagopal, K. and Srinivasa, A. (2008). On the development of fluid models of the differential type within a new thermodynamic framework. *Mechanics Research Communications*, pages 483–489.
- Raymond, M. J. and Gudmundsson, G. H. (2005). On the relationship between surface and basal properties on glaciers, ice sheets, and ice streams. *Journal of Geophysical Research*, 110(B08411).
- Riesen, P., Bauder, A., and Eisen, O. (2006). Dual-frequency radar investigations on an alpine valley glacier. *Geophysical Research Abstracts*, 8(02289).
- Riesen, P., Sugiyama, S., and Funk, M. (2010). The influence of the presence and drainage of an ice-marginal lake on the ice flow of Gornergletscher, Switzerland. *Journal of Glaciology*, 56(196):278–286.
- Rivlin, R. S. and Ericksen, J. L. (1955). Stress-deformation relations for isotropic materials. *Journal for Rational Mechanics and Analysis*, 4:523–532.

- Röthlisberger, H. (1972). Seismic exploration in cold regions. *Cold Regions Science and Engineering Monograph*, II-A2a:139.
- Schoof, C. (2010). Ice-sheet acceleration driven by melt supply variability. *Nature*, 468:803–806.
- Schulson, E. and Duval, P. (2009). *Creep and Fracture of Ice*. Cambridge University Press. ISBN 978-0-521-80620-6.
- Shyam-Sunder, S. and Wu, M. S. (1989a). A differential flow model for polycrystalline ice. *Cold Regions Science and Technology*, 16:45–62.
- Shyam-Sunder, S. and Wu, M. S. (1989b). A multiaxial differential model of flow in orthotropic polycrystalline ice. *Cold Regions Science and Technology*, 16:223–235.
- Shyam-Sunder, S. and Wu, M. S. (1990). On the constitutive modeling of transient creep in polycrystalline ice. *Cold Regions Science and Technology*, 18:267–294.
- Sinha, N. K. (1978). Short-term rheology of polycrystalline ice. *Journal of Glaciology*, 21(85):457–473.
- Spring, U. and Morland, L. (1982). Viscoelastic solid relations for the deformation of ice. *Cold Regions Science and Technology*, 5:221–234.
- Squire, V. A., Hosking, R. J., Kerr, A. D., and Langhorne, P. J. (1990). *Moving Loads on Ice Plates*, volume 45 of *Solid Mechanics and its applications*. Kluwer Academic Publishers.
- Steinemann, S. (1958). Experimentelle Untersuchungen zur Plastizität von Eis. Geotechnische Serie Nr. 10, Beiträge zur Geologie der Schweiz, Kommissionsverlag Kümmerli & Frey AG, Geographischer Verlag, Bern.
- Sugiyama, S., Bauder, A., Huss, M., Riesen, P., and Funk, M. (2008). Triggering and drainage mechanisms of the 2004 glacier-dammed lake outburst in Gornergletscher, Switzerland. *Journal of Geophysical Research*, 113:F04019.
- Sugiyama, S., Bauder, A., Riesen, P., and Funk, M. (2010). Surface ice motion deviating toward the margins during speed-up events at Gornergletscher, Switzerland. *Journal of Geophysical Research*, 115(F03010). doi:10.1029/2009JF001509.
- Sugiyama, S., Bauder, A., Weiss, P., and Funk, M. (2007a). Reversal of ice motion during the outburst of a glacier-dammed lake on Gornergletscher, Switzerland. *Journal of Glaciology*, 53(181):172–180.
- Sugiyama, S., Bauder, A., Zahno, C., and Funk, M. (2007b). Evolution of Rhonegletscher, Switzerland, over the past 125 years and in the future: application of an improved flowline model. *Annals of Glaciology*, 46:268–274.
- Sugiyama, S. and Gudmundsson, G. H. (2004). Short-term variations in glacier flow controlled by subglacial water pressure at Lauteraargletscher, Bernese Alps, Switzerland. *Journal of Glaciology*, 50(170):353–362.
- Sun, Q.-X. (1987). *On two special Rivlin-Ericksen fluid models generalizing Glen's flow law for polycrystalline ice*. PhD thesis, University of Manitoba, Canada.
- Szyszkowski, W. and Glockner, P. G. (1985). Modelling the time-dependent behavior of ice. *Cold Regions Science and Technology*, 11:3–21.
- Truesdell, C. and Noll, W. (2004). *The non-linear field theories of mechanics*. Springer Verlag, Berlin, 3rd edition. edited by Stuart S. Antman, ISBN:3540027793.

- Vieli, A., Funk, M., and Blatter, H. (2000). Tidewater glaciers: frontal flow acceleration and basal sliding. *Annals of Glaciology*, 31:217–221.
- Walder, J. S., Trabant, D. C., Cunico, M., Anderson, S. P., Anderson, R. S., Fountain, A. G., and Malm, A. (2005). Fault-dominated deformation of an ice dam during annual filling and drainage of a marginal lake. *Annals of Glaciology*, 40:174–178.
- Walder, J. S., Trabant, D. C., Cunico, M., Fountain, A. G., Anderson, S. P., Anderson, R. S., and Malm, A. (2006). Local response of a glacier to annual filling and drainage of an ice-marginal lake. *Journal of Glaciology*, 52(178):440–450.
- Walter, F. (2009). *Seismic Activity on Gornergletscher during Gornersee Outburst Floods*. PhD thesis, ETH Zürich. No. 18184.
- Walter, F., Deichmann, N., and Funk, M. (2008). Basal icequakes during changing subglacial water pressures beneath Gornergletscher, Switzerland. *Journal of Glaciology*, 54(186):511–532.
- Welch, G. and Bishop, G. (2006). An introduction to the Kalman filter. Technical report, Department of Computer Sciences, University of North Carolina, Chapel Hill, NC 27599-3175.
- Werder, M. A. (2009). *Dye tracing and modelling jökulhlaups*. PhD thesis, ETH Zürich. No. 18293.
- Werder, M. A. and Funk, M. (2009). Dye tracing a jökulhlaup: II. Testing a jökulhlaup model against flow speeds inferred from measurements. *Journal of Glaciology*, 55:899–908.
- Werder, M. A., Loye, A., and Funk, M. (2009). Dye tracing a jökulhlaup: I. Subglacial water transit speed and water-storage mechanism. *Journal of Glaciology*, 55:889–898.
- Werner, C., Strozzi, T., Wiesmann, A., and Wegmuller, U. (2008). A real-aperture radar for ground-based differential interferometry. In *Geoscience and Remote Sensing Symposium, 2008. IGARSS 2008. IEEE International*, volume 3, pages III –210 –III –213.
- Zhou, Z. (1991). Creep and recovery on nonlinear viscoelastic materials of the differential type. *Int. J. Engng. Sci.*, 29(12):1661–1672.

# Acknowledgements

This work would not have been completed without the help and support of a great deal of persons whose names did not appear in any of the lines of this manuscript so far. This page is dedicated to those people and their encouragement is greatly acknowledged.

I very much thank Prof. Martin Funk, my *Doktorvater*, for the opportunity of this PhD work. It was a great pleasure to return from Japan in 2007 and immediately start off working on this project. I enjoyed the field measurements on Gornergletscher very much. Without Prof. Martin Funk, it would not have been possible to repeatedly visit Gornersee and conduct all the ice-flow measurements. Prof. Martin Funk also provided financial support for conferences and meetings I attended, which is also highly appreciated. I thank Prof. Martin Funk for providing a pleasant working environment in the glaciology group of VAW and his open ears to my considerations and possible problems.

This research was funded by the Swiss National Science Foundation grants 200021-103882/1, 200020-111892/1 and 200020-129514. Thanks are given to the International Foundation of High Altitude Research at Gornergrat (HFSJG) for providing facilities and support during the field surveys on Gornergletscher.

I am also very indebted to Prof. Kolumban Hutter and his lectures (which were most times private lectures) on continuum mechanics and constitutive modelling of ice. I was thrown in at the deep end of constitutive theory and Prof. Kolumban Hutter inspired me strongly to eventually understand the subject and get acquainted with tensors and constitutive equations. I thank him very much therefore. Further, I thank Prof. A. Puzrin and Prof. L. W. Morland for being part of the thesis examination committee and accepting it. Their comments and suggestions improved the final thesis manuscript considerably and are very much acknowledged.

During the field work on Gornergletscher I enjoyed the company of two other PhD students working on different topics related to Gornergletscher and Gornersee: Fabian Walter and Mauro Werder. I gladly remember working together on Gornergletscher. Unfortunately, we did not succeed to prompt the drainage(s) of Gornersee by celebrating nightly fire spectacles. However, these were good times. Mauro Werder is also thanked for guidance on the sporadic mountaineering and snowboarding tours I joined. Fabian Walter and me witnessed a spectacular calving event where large chunks of ice broke off the lake margin. It was one of the rare times when Fabian was not as cool as a cucumber like I used to know him. I enjoyed this time very much. Both Mauro Werder and Fabian Walter were also office buddies, and there was nothing to complain about their presence next to my office.

Bruno Nedela generously committed himself to the cooking and kitchen work during the time in the field, which is greatly acknowledged. Within this work, Martin Lüthi provided support for the surface regression method used for calculation of horizontal flow velocities and strain-rates. Hilmar Gudmundssen is responsible for the initial design of the Kalman filtering routine. Shin Sugiyama also provided support and contributed to Chapter 3. I thank them all very heartily.

When Fabian Walter and Mauro Werder finished their dissertations, new PhD students moved in to the offices next to me. I very much enjoyed the company of Claudia Ryser, Pierre Dalban, Arne Keller, Jed Brown and Daniel Farinotti. I thank Claudia Ryser for the great support and help with borehole drilling in the field season of 2008. The socializing, chatting and occasional snacks provided by Pierre, Arne and Daniel were good reliefs to the work in the office. Jed Brown provided invaluable support

at compiling and installing mathematical software on my workstation. Regardless that I never payed the coffee expenses on time, Thomi Wyder always offered me new coffee beans when the machine was running short of it, thank you Thomi!

Soon after I began this PhD, I moved to Zurich and left my parents. However, I regularly return for the Sunday evening dinner. I always enjoyed the meals and the watching of the recent blockbuster together, and I am extremely grateful for their continuous support and love while giving me so much freedom of self-realization. I also like to thank my sister, Nathalie, for her support. Further, I send many thanks to my friends Daniel Figi (personal certified sports instructor), Sarah Clavadetscher (Gelsemium sempervirens), Mario Gysi (I sing!) and Christoph Jans (lunch, coffees and snowboarding and much more) for being my friends in good and bad times during the last four years and more. Last but not least, Gabriela Brunner was a source of substantial support and motivation. She always had a word left to make me feel happy and save me from the feeling of having failed the world. For this I adore her and owe her my gratitude.

Patrick Riesen